Doctorate Dissertation
博士論文

The nature of Lyα emitters: SFR, stellar mass, and dark matter halo mass

（Lyα輝線銀河の性質:
星形成率、星質量、ダークマターハロー質量）

A Dissertation Submitted for Degree of Doctor of Philosophy, December 2018
平成30年12月　博士（理学）申請

Department of Astronomy, Graduate School of Science, The University of Tokyo
東京大学大学院　理学系研究科　天文学専攻

Haruka Kusakabe
日　下　部　晴　香

Supervisor:
Associate Prof. Kazuhiro Shimasaku : Department of Astronomy, School of Science, The University of Tokyo

Abstract

Low-mass galaxies in the past Universe are "building blocks" of present-day galaxies in terms of hierarchical structure formation. It means that they play a key role in galaxy formation and evolution. One of the most representative high-z low-mass galaxies are Lyα emitters (LAEs), which are characterized by strong Lyα emission. Thanks to remarkable progress in observations and intensive studies, LAEs are found to have low stellar masses ($M_\star \lesssim 10^9$ M$_\odot$) and to reside in low-mass dark matter halos ($M_\mathrm{h} \sim 10^{10}$–$10^{12}$ M$_\odot$). They are also confirmed to have spatially extended diffuse Lyα emission, called Lyα halos (LAHs), which are not negligible because they are as bright as the central Lyα emission.

However, since their M_h, SFR, $M_\star$, and LAH luminosities have not been estimated at the same time with a high enough accuracy to place them in the framework of hierarchical structure formation, we still have two basic unknowns: (1) the star forming activity of LAEs: star formation mode, stellar to halo mass ratio ($M_\star/M_\mathrm{h}$, SHMR), and baryon conversion efficiency (SFR/baryon accretion rate, BCE) and (2) the origin of LAHs of LAEs, whose candidates are the cold streams (gravitational cooling), satellite star formation, and resonant scattering in the circum-galactic medium (CGM). The properties such as M_h, SFR, $M_\star$, and LAH luminosities can be most reliably measured at $z \sim 2$. This is because this redshift is high enough to conduct a wide-field LAE survey with ground-based telescopes, which is critical for measuring M_h and LAH properties from clustering analysis and stacked NB images, respectively. Another reason is that deep mid-infrared (MIR) and far-infrared (FIR) data are available to investigate the amount of dust attenuation (A_{1600}) and thus SFR as well as an appropriate dust attenuation curve. Deep rest-frame near-infrared (NIR) photometry is also possible, which is essential to derive $M_\star$ from SED fitting.

In this thesis, we use 1248 narrow-band-selected LAEs at $z \sim 2$ from four deep survey fields with a total area of $\simeq 1$ deg^2. Among them, 213 LAEs with deep MIR/FIR data are used to measure the dust emission of LAEs and to obtain an appropriate dust attenuation curve. We perform SED fitting to stacked imaging data of LAEs to measure stellar population parameters including SFR, A_{1600}, and $M_\star$, while we derive M_h from clustering analysis. We divide 891 LAEs in two fields with deep broadband data into subsamples to discuss the origin of LAHs. We investigate star formation mode (or SFR–$M_\star$ relation), SHMR, BCE, and the relation between LAH luminosity and mass to discuss the origin of star forming activity and the origin of LAHs of LAEs.

We find that the stacked LAEs have the 3σ IR luminosity $L_\mathrm{TIR}^{3\sigma} = 1.1 \times 10^{10} L_\odot$ and $A_{1600} = 0.9$ mag, preferring an SMC-like attenuation curve. We perform SED fitting with

an assumption of an SMC-like attenuation curve. The mean of each stellar parameter over the four fields is: $M_\star$ = 10.2 ± 1.8 × 10^8 $M_\odot$, A_{1600} = 0.6 ± 0.1 mag, Age= 3.8 ± 0.3 × 10^8 yr, and SFR= 3.4 ± 0.4 $M_\odot$ yr^{-1} for LAEs with $NB387 \leq 25.5$ mag. They are found to be located near an extrapolation of the consensus relation of IRX–$M_\star$, where IRX is an indicator of dustiness and is defined as the ratio of infrared luminosity to ultraviolet (UV) luminosity. They are also found to be normal star forming galaxies lying on the star formation main sequence (the average SFR–$M_\star$ relation of star forming galaxies).

From clustering analysis, we find that the same LAE sample with $NB387 \leq 25.5$ mag has an effective bias of $1.22^{+0.16}_{-0.18}$. We derive an average dark matter halo mass, $M_{\rm h} \sim 4.0^{+5.1}_{-2.9} \times 10^{10}$ $M_\odot$, from the effective bias. Combining the $M_{\rm h}$, $M_\star$, and SFR, our LAEs are suggested to lie above a simple lower-mass extrapolation of the average $M_\star$–$M_{\rm h}$ and BCE–$M_{\rm h}$ relations with $SHMR = 0.02^{+0.07}_{-0.01}$ and $BCE = 1.6^{+6.0}_{-1.0}$. Thus, our LAEs have been converting baryons into stars more efficiently than average galaxies with similar $M_{\rm h}$ both in the past and at the observed epoch but with a moderate star formation similar to average galaxies. Galaxies with weak SN feedback or small halos' spin parameters possibly have such properties according to a semi-analytic model. The obtained $M_{\rm h}$ also suggests that at $z = 0$ our LAEs are embedded in dark matter halos with a median halo mass similar to the mass of the Large Magellanic Cloud (LMC) from the extended Press-Schehter model. If their star-formation is largely suppressed after the observed time until $z = 0$ similar to the star-formation history of the LMC, they would have a similar $SHMR$ to the present-day LMC.

With regard to LAHs, we find that ten LAE subsamples divided in accordance with UV, Lyα, K-band properties have similar LAH luminosities, $L({\rm Ly}\alpha)_{\rm H} \sim 2 \times 10^{42}\,{\rm erg\,s^{-1}}$, and total Ly$\alpha$ luminosities, $L({\rm Ly}\alpha)_{\rm tot} \sim 2 \times 10^{42}$–$4 \times 10^{42}\,{\rm erg\,s^{-1}}$. Their $L({\rm Ly}\alpha)_{\rm H}$ and $L({\rm Ly}\alpha)_{\rm tot}$ remain almost unchanged or even decrease when $M_\star$ increases by factor 2–5. They are also nearly independent of SFR, $E(B-V)_\star$, and $M_{\rm h}$, although the uncertainties in $M_{\rm h}$ are large. We also find that Hα emitters in Matthee et al. (2016) also have non-increasing $L({\rm Ly}\alpha)_{\rm H}$ and $L({\rm Ly}\alpha)_{\rm tot}$. These results are inconsistent with the cold stream scenario and the satellite star formation scenario both of which predict a nearly linear scaling of $L({\rm Ly}\alpha)_{\rm H}$ with mass and a relatively low $L({\rm Ly}\alpha)_{\rm H}$. The most likely is the resonant scattering scenario because it can naturally explain these results as well as a weak positive correlation between $M_\star$ and $L({\rm Ly}\alpha)_{\rm H}/L({\rm Ly}\alpha)_{\rm tot}$, where $L({\rm Ly}\alpha)_{\rm H}/L({\rm Ly}\alpha)_{\rm tot}$ indicates the efficiency of resonant scattering in the CGM. We also discuss the origin of bright observable Lyα emission of LAEs (i.e., high Lyα escape fraction) considering all the results obtained in this work.

Acknowledgments

I would like to express my sincere gratitude to my supervisor, Dr. Kazuhiro Shimasaku, whose enormous support and insightful comments were invaluable during the course of my PhD. Without his instructions on the analysis, discussion, presentation, and writing, I would not be able to accomplish my research. I also owe a very important debt to Dr. Masami Ouchi, whose valuable data, essential comments, and encouragement made enormous contribution to my work. He also taught me how to lead international collaborations.

My heartfelt appreciation goes to Dr. Kimihiko Nakajima, who provided source catalogs and gave me invaluable comments kindly. I also would like to to express my gratitude to Dr. Takuya Hashimoto, who gave me various instruction and constructive comments. I have always looked up to them. They assisted me as essential research collaborators even when they worked overseas. Thanks to their kind host at and invitation to Lyon observatory, Geneva observatory, and ESO in 2015, I could have opportunities to collaborate with people there. Without their support, I could not have completed the work presented in this thesis.

For completing our work during my Masters and PhD, I feel especially thankful for researchers below. I am grateful to Dr. Yoshiaki Ono for passionate guidance of SED fitting and basic codes. His warm encouragement supports me. I am also grateful to Dr. Rieko Momose, who gave me invaluable comments and encouraged me a lot. I was so excited when she moved to our group. I really appreciate her kindness and exciting discussion.

I would like to thank Dr. Jeremy Blaizot and Dr. Johan Richard in Lyon observatory for giving me wonderful memories. I really appreciate their kind host and exciting discussion during my stay in Lyon, for three months in 2018. I like my life in Lyon very much so that I wish I had extended my stay. I also thankful to Dr. Anne Verhamme in Geneva observatory, who encouraged me and gave me amazing memories during conferences as well as my short-time visit in Geneva. I have admired her since I met her for the first time in 2015. She showed me how to play an active role in international collaborations and juggle work and family. I can not wait to start working with her there. I feel thankful to my collaborators of this thesis: Dr. Roland Bacon, Dr. John D. Silverman, Dr. Peter L. Capak, Dr. Thibault Garel, Dr. Hanae Inami, Dr. Alyssa Drake, Dr. Akira Konno, Mr. Ryosuke Goto, and Dr. Yuichi Harikane, who gave me constructive comments and

always supported me a lot. It has been a great pleasure to work with them. I hope we will continue our collaboration in future research.

In addition to them, I am grateful to Dr. Lihwai Lin and Dr. Li-Ting Hsu for kindly providing us with J, H and Ks images of the HDFN field and their data plotted in figures in this thesis. I would like to show our appreciation to Dr. Takashi Hamana for helpful comments on cosmic variance and computer programs of the covariance of dark matter angular correlation function and the EPS model. I am grateful to Dr. Kazuyuki Ogura and Dr. Masahiro Nagashima for kindly providing ν^2GC data and giving helpful comments. I thank Dr. Giulia Rodighiero, Dr. David Sobral, Dr. Naveen A. Reddy, Dr. Alex Hagen, Dr. Jorryt Matthee, Dr. Shogo Ishikawa, and Dr. Ken-ichi Tadaki for kindly providing their data plotted in figures and invaluable comments. I would like to express to my gratitude to Dr. James E. Rhoads, and Dr. Peter S. Behroozi for useful comments on their results. I also acknowledge Dr. Eric Gawiser, Dr. Richard S. Ellis, Dr. Cai-Na Hao, Dr. Kyoung-Soo Lee, Dr. Richard Bower, Dr. Richard M. Bielby, Dr. Edmund Christian Herenz, Dr. Tsutomu T. Takeuchi, Dr. Hidenobu Yajima, Dr. Ikkoh Shimizu, Dr. Ken Mawatari, Dr. Koki Kakiichi, Dr. Ichi Tanaka, Dr. Rhythm Shimakawa, Dr. Masao Hayashi, Dr. Tomoko Suzuki, Dr. Hikari Shirakata, Ms. Moegi Yamamoto, Dr. Mana Niida, Dr. Hiroko Niikura, Dr. Tomonari Michiyama, Dr. Yuki Yamaguchi, Dr. Seiji Fujimoto, Dr. Koki Terao, Dr. Yuki Kimura, Mr. Yuki Yoshimura, Mr. Sergio Santos, and Mr. Joao Calhau for insightful discussion. Their fruitful comments were an enormous help to me.

I thank the referees, Dr. Nobunari Kashikawa (chair), Dr. Tadayuki Kodama, Dr. Kotaro Kohno, Dr. Akio K. Inoue, and Dr. Michiko Fujii for helpful comments and suggestions, which improved my thesis greatly. I really enjoyed the discussion with them.

I greatly appreciate the helps by and daily interactions with members of our laboratory, Mr. Shingo Shinogi, Dr. Ryota Kawamata, Mr. Taku Okamura, Mr. Kazushi Irikura, Mr. Makoto Ando, and Ms. Hinako Goto. I am indebted to Dr. Ituski Sakon, Dr. Mark Hammonds, Dr. Ronin Wu, and Dr. Tamami I. Mori for useful discussions and comments. My heartfelt appreciation goes to Scarlet S. Elgueta, my regalona. I can not imagine my PhD life without her. I also thank Dr. Taichi Uyama, Mr. Shotaro Yamasaki, and Dr. John Livingston for daily live in Hongo campus. I appreciate the member of department of Astronomy in the University of Tokyo for daily supports. Especially, Ms. Yuko Asakawa, Ms. Etsuko Nagayama, and Mr. Shin Fujieda have always supported me a lot. I feel thankful to astronomers in Lyon: Dr. Floriane Leclercq, Dr. Anna Feltre, Dr. David Carton, Dr. David Lagattutta, Dr. Benjamin Clement, Dr. Peter Mitchell, Dr. Simon Conseil, and Dr. Mohammad Akhlaghi, for extensive helps with my work and my daily live there.

This thesis is based on observations taken by the Subaru Telescope which is operated by the National Astronomical Observatory of Japan. I really wish to recognize and acknowledge the very significant cultural role and reverence that the summit of Maunakea has always had within the indigenous Hawaiian community. Based on data products from observations made with ESO Telescopes at the La Silla Paranal Observatory under ESO programme ID 179.A-2005 and on data products produced by TERAPIX and the Cambridge Astronomy Survey Unit on behalf of the UltraVISTA consortium. These researchs made use of IRAF, which is distributed by NOAO, which is operated by AURA under a cooperative agreement with the National Science Foundation and of Python packages for Astronomy: Astropy, Colossus, CosmoloPy and PyRAF, which is produced by the Space Telescope Science Institute, which is operated by AURA for NASA. This work is supported in part by KAKENHI (16K05286) Grant-in-Aid for Scientific Research (C) through the JSPS. I also acknowledges support from the JSPS through the JSPS Research Fellowship for Young Scientists.

As the last of this section, I would like to express my gratitude to my family. I am deeply grateful to my parents, Den Kusakabe and Midori Kusakabe, and my sister, Yasuha Kusakabe, for their moral support, kind understanding, and warm encouragements for this 27 years. I greatly appreciate my husband, Naoya Takeishi, who understands me and my career in academia. He always supports me deeply. I have really enjoyed my life with him and hope to live together again in the near future. I would like to thank my grand parents, Kiyoshi Kusakabe, Teruko Kusakabe, Kunihiro Ono, and Mitsuko Ono, for their warm encouragements. Finally, I am very grateful to my husband's parents, Yoshihito Takeishi and Tomoko Takeishi, for their sweet support and warm caring.

Contents

List of Figures

List of Tables

Chapter 1

Introduction

1.1 The history of the Universe and galaxy evolution

1.1.1 The history of the Universe and galaxies

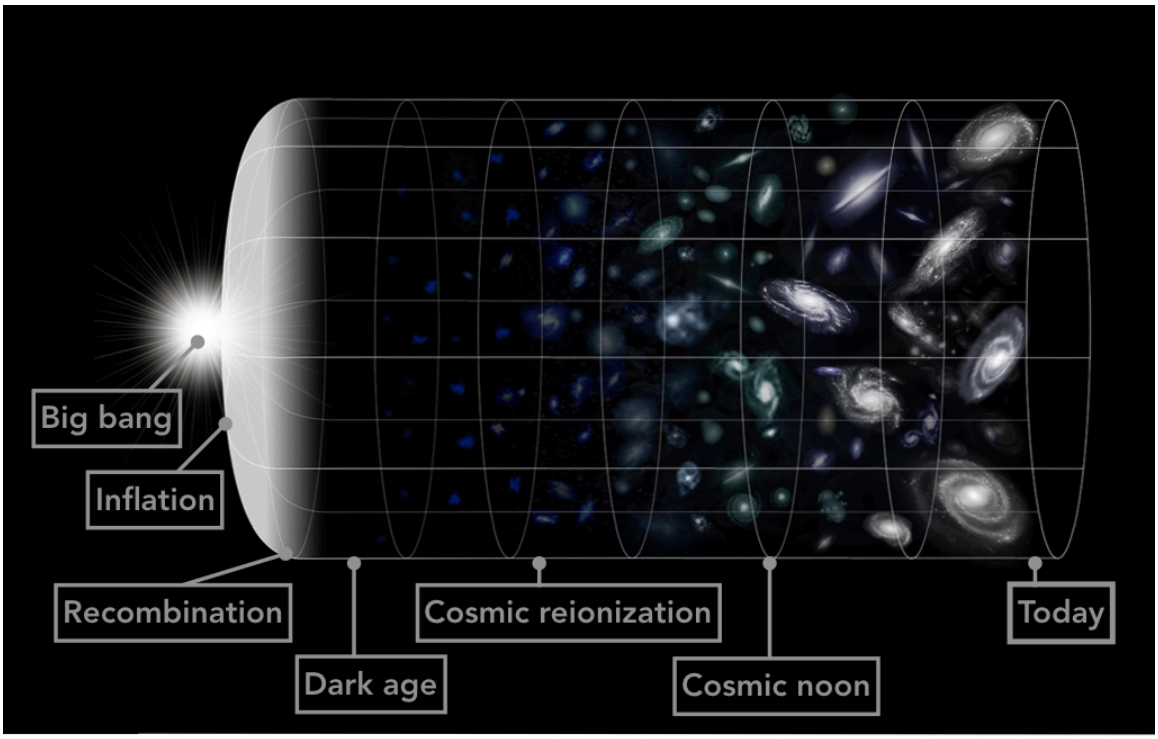

Figure 1.1 The history of the Universe and the evolution of galaxies.

The Universe has been expected to begin through phenomena of rapid expansion and incredible heating known as "inflation" and "the Big Bang" about 14 billion years ago as shown in figure 1.1. About 380 thousand years after the Big Bang, the temperature in the Universe decreased below $\sim 3,000K$ due to the expansion, and gas in the Universe became completely neutral (called, "recombination").

The Universe has expanded until the present day. Thanks to the expansion and the constant speed of light, we can see objects in the past Universe directly using the relation

between distance and time. The expansion of the Universe increases distances between two objects fixed in space. It causes an observer to see more distant objects moving away faster, with the wavelength of the arriving radiation being shifted to longer values. The amount of the shift of the observed wavelength with respect to the rest-frame wavelength is called "redshift" (z). Space itself expands, causing objects to become separated without changing their positions in space.

Following a period of darkness of about a few hundred million years (the dark age), the first objects formed and flooded the Universe with light. They ionized the neutral gas in the intergalactic medium (IGM). This phenomenon is called "cosmic reionization". A plausible candidate for the main source of reionization is young galaxies, whose ionizing radiation, called 'Lyman Continuum' (LyC, $\lambda < 912$Å), from massive stars is expected to leak to the IGM (e.g., Robertson et al., 2015; Livermore et al., 2017). Other candidates, quasi-stellar objects (QSOs) and active galactic nuclei (AGNs) (e.g., Giallongo et al., 2015; Madau & Haardt, 2015), are recently indicated to contribute to less than $\sim 10\%$ of the ionizing photons to keep the IGM ionized (over a UV magnitude range of -18 to -30 mag; Matsuoka et al., 2018). Previous studies suggest that cosmic reionization has been completed by $z \sim 6$ from the Gunn-Peterson absorption trough in quasar spectra (e.g., Gunn & Peterson, 1965; Fan et al., 2006) and in gamma-ray burst spectra (e.g., Totani et al., 2006; McGreer et al., 2015) as well as the evolution of the Lyα luminosity function (e.g., Kashikawa et al., 2006; Hu et al., 2010; Konno et al., 2018; Itoh et al., 2018) and the Lyα emitter fraction (e.g., Stark et al., 2011; Pentericci et al., 2011; Schenker et al., 2014). After that, the IGM of the Universe was full of low density ionized hydrogen and has been nearly transparent to photons until today.

Multi-wavelength observations have revealed the cosmic star formation history of galaxies as a function of redshift (e.g., Hopkins & Beacom, 2006, see also Madau & Dickinson 2014 and references therein) and the evolution of the number density of AGNs/QSOs (e.g., Hopkins et al., 2007; Niida et al., 2016), as well as the evolution of cosmic dust attenuation (e.g., Burgarella et al., 2013). The cosmic star formation rate density (SFRD) has been found to increase from high redshift ($z \sim 11$; Oesch et al., 2015) to $z \sim 1.5$–3 and then to decrease to $z \sim 0$. Interestingly, the cosmic dust attenuation also shows an inverted V-shaped evolution, and the peak is found to be located at a similar z or to be delayed from the peak of the cosmic SFRD (at $z \sim 1.2$; Burgarella et al., 2013). It is also coeval with the peak (plateau) of the number density of QSOs (e.g., Niida et al., 2016). The peak (plateau) of the cosmic SFRD of galaxies is called "cosmic noon", which is regarded as one of the most active eras in the Universe.

In the local Universe, at $z \sim 0$, although the activities of star forming galaxies and AGNs/QSOs are modest compared with those at high redshift, we can observe various astronomical objects with a wide dynamic range. Clusters of galaxies are the largest self-gravitating structures in the Universe, whose virial masses reach more than $10^{14}\ M_\odot$ (e.g., Fornax and Coma clusters; Drinkwater et al., 2001; Kubo et al., 2007), while dwarf galaxies are the smallest whose stellar masses are often as low as $10^6 M_\odot$ (e.g., Dwarf Galaxy Survey; Madden et al., 2013). Galaxies also show a variety in their appearance.

Their morphologies are classified into Elliptical, S0 galaxies ("early type"), spiral and irregular galaxies ("late type") according to the Hubble sequence (Hubble, 1936). The Milky Way galaxy is classified as a spiral galaxy, while the Large Magellanic Cloud (LMC) and the Small Magellanic Cloud (SMC), both are satellites of the Milky Way galaxy, are classified as irregular galaxies. Early-type galaxies tend to be bright and massive with suppressed (or quenched) star formation and red colors, while late-type galaxies are generally faint and less massive with star formation, rich gas content, and blue colors. It is still unkown how galaxies evolved to have various properties observed in the present Universe from the past Universe.

Through the long history of $\sim$ 14 billion years, galaxies are a basic component of the Universe. The formation and evolution of galaxies is one of the fundamental topics in astronomy and *still* raises essential questions to us.

1.1.2 Galaxy evolution

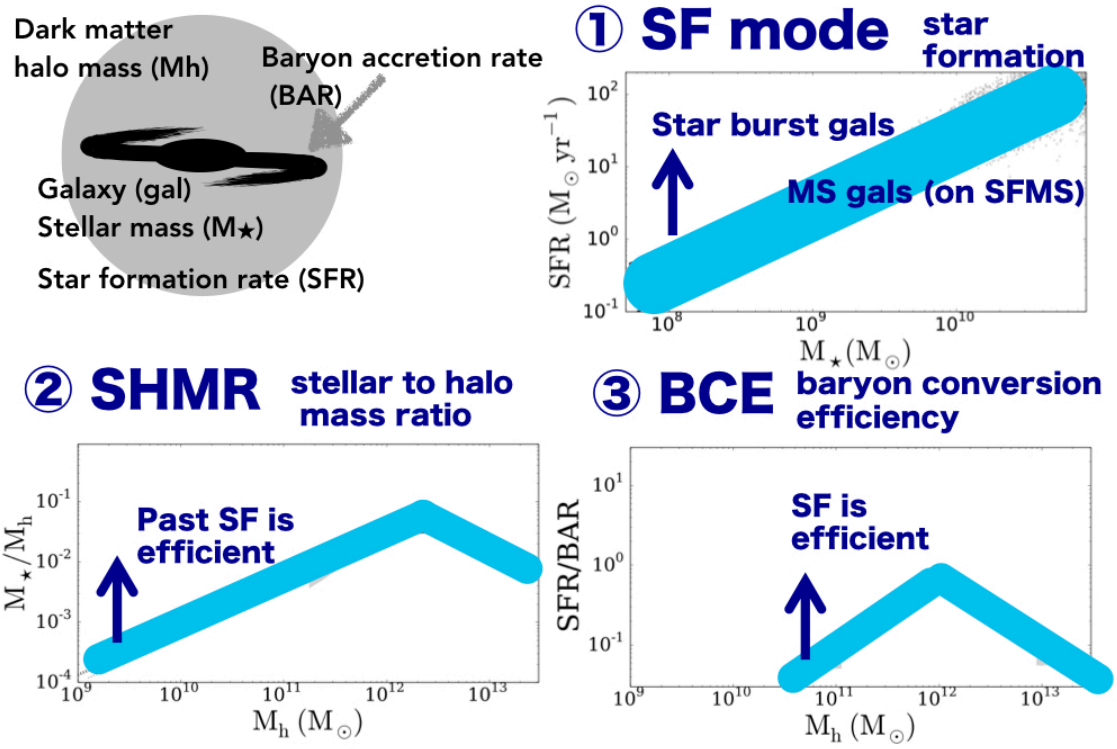

Figure 1.2 Illustration of a galaxy embedded in a dark matter halo and three key properties of star formation activity: star formation mode, stellar to halo mass ratio, and baryon conversion efficiency.

Galaxies form and evolve over cosmic time. They are self-gravitating systems composed of stars, gas, dust, and dark matter. Galaxies assemble their stellar mass through star formation and galaxy merging under the gravitational influence of their host dark matter halos, which also grow through mass accretion and merging (e.g., Somerville & Davé, 2015).

To understand the growth (i.e., star forming activity) of galaxies in the framework of hierarchical structure formation, the star formation mode, the stellar to halo mass ratio, and the baryon conversion efficiency are three key properties.

Star formation mode

The mode of star formation in star-forming galaxies can be divided into two categories: the normal star formation (or main-sequence, MS) mode and the starburst mode. The MS mode where galaxies form stars at moderate rates makes a well-defined sequence in the diagram of star formation rate (SFR) versus stellar mass ($M_\star$) (e.g., Noeske et al., 2007; Elbaz et al., 2007; Speagle et al., 2014). It is called "star formation main sequence" (SFMS). The starburst mode where galaxies have much higher specific star formation rates ($= SFR/M_\star$: $sSFRs$) than MS galaxies with similar masses (e.g., Rodighiero et al., 2011). The star formation (SF) mode also tells us the nature of star formation in terms of stellar mass growth. The SFR–$M_\star$ relation is measured over a wide range of redshift, $z \sim 0$ to ~ 6, and shows higher SFR at a fixed $M_\star$ at higher redshift (e.g., Santini et al., 2017).

Stellar to halo mas ratio

The stellar to halo mass ratio ($= M_\star/M_\mathrm{h}$: $SHMR$) indicates the efficiency of star formation in dark matter halos integrated over time from the onset of star formation to the observed epoch, which we refer to as the integrated SF efficiency. The $SHMR$ as a function of halo mass is known to have a peak and the halo mass at the peak (pivot mass) is $\simeq 2-3\times10^{12}$ $\mathrm{M}_\odot$ at $z \sim 2$ (e.g., Behroozi et al., 2013; Moster et al., 2013). The shape of the average relation shows almost no evolution at $z \sim 0$–5, although the behavior of the $SHMR$ at low M_h is still uncertain.

Baryon conversion efficiency

The baryon conversion efficiency (BCE) is defined as $BCE = \dot{M}_\star/\dot{M}_\mathrm{b}$, where $\dot{M}_\mathrm{b}$ is the baryon accretion rate (BAR). It measures the efficiency of star formation in dark matter halos at the observed time with an assumption that most of the accreting baryons are in a (cold) gas phase (i.e., the BAR is equal to the inflow rate of cold gas). The average BAR at a fixed halo mass is proportional to the halo mass accretion rate that is estimated as a function of redshift and halo mass from cosmological simulations (Dekel et al., 2009a). Previous studies show a tight relation between BCE and M_h over a wide range of redshift (at $z \sim 0$–8; e.g., Behroozi et al., 2013; Moster et al., 2013; Rodríguez-Puebla et al., 2017).

These relations are usually given as the average relations in the literature thus presented here as such. Figure 1.2 illustrates the three key properties of star forming activity.

In addition to these relations, star-forming galaxies have a positive correlation that more

massive ones have higher IRX, which is an indicator of dustiness (e.g., Reddy et al., 2010; Whitaker et al., 2014). IRX is defined as $\equiv L_{\rm IR}/L_{\rm UV}$, where $L_{\rm IR}$ and $L_{\rm UV}$ are infrared (IR; 8–1000μm) and ultraviolet (UV; $\sim$ 1500Å) luminosities, respectively. The location of a galaxy in a diagram of IRX versus $M_\star$ gives us information of dust enrichment (or the evolution of dust contents) of the galaxy in terms of system size.

Dark matter halo mass is also useful to track the evolution of galaxies since the growth of dark matter halos is statistically predicted by the extended Press-Schehter (EPS: Press & Schechter, 1974; Bond et al., 1991; Bower, 1991) model. It allows us to connect galaxies in a snapshot at a redshift to the present-day descendants.

Gas masses ($M_{\rm g}$) in a galaxy and in the circum-galactic medium (CGM) are also important parameters as well as SFR, $M_\star$, and $M_{\rm h}$. As is well known, a tight correlation between SFR surface density and gas surface density (in a galaxy) has been established (the Kennicutt-Schmidt law; e.g., Schmidt, 1959; Kennicutt & Evans, 2012, and references therein). The CGM is also linked to galaxy formation and evolution since a sufficient gas reservoir in the CGM can sustain star formation of the central galaxies (e.g., Lilly et al., 2013). Gas inflows into (outflows from) a galaxy are expected to trigger starburst (suppress star formation) (e.g., Dekel et al., 2009b; Muratov et al., 2015).

1.1.3 Low-mass "building blocks"

From the point of view of hierarchical structure formation, low-mass galaxies in the past Universe are "building blocks" of present-day galaxies over a wide range of mass (Rauch et al., 2008; Dressler et al., 2011). It means that they play a key role in galaxy formation and evolution. Moreover, young low-mass galaxies at high redshift are important as a plausible candidate for the main source of reionization as described in section 1.1. However, it has been challenging to investigate the properties and evolution of high-z low-mass galaxies because of their faint luminosities. Nebular emission lines are useful to detect faint (or low-mass) galaxies at high redshift, among which the hydrogen Lyα line has been used most commonly. Thus, Lyα emitters (LAEs) are one of the most popular high-z low-mass galaxies.

1.2 Lyα emitters

1.2.1 Theoretical predictions and discoveries of Lyα emitters

A Lyα photon is emitted when an electron jumps from the state of the principle quantum number of $n = 2$ and the azimuthal quantum number of $l = 0$ (i.e., 2p) to that of $n = 1$ and $l = 0$ (i.e., 1s) with an energy difference of 10.2 eV ($\lambda_{\rm rest} = 1215.67$Å). It is produced in HII regions by recombination radiation following hydrogen photoionization by young massive stars (i.e., O- and B- type stars, Partridge & Peebles, 1967). Since about 68% of hydrogen ionization yields a Lyα photon in case B recombination (e.g., Osterbrock & Ferland, 2006), the Lyα emission line is intrinsically the brightest feature in the nebula spectrum of star forming galaxies. However, Lyα photons can not escape from a galaxy

with rich dust and neutral hydrogen gas (HI) contents due to resonant scattering by HI gas, which causes an asymmetric Lyα line profile (e.g., Dijkstra, 2014).

In 1967, Partridge & Peebles (1967) have theoretically predicted that galaxies with bright Lyα emission are candidates of very young galaxies at $z \sim$ 10–30. About 30 years later, several candidates of LAEs around an AGN at $z = 4.6$ have been detected with the University of Hawaii 2.2-meter telescope, and two of them have been identified spectroscopically with the Keck 10-m telescope (Hu & McMahon, 1996). In the same year, five LAEs around a radio galaxy at $z = 2.39$ have been also identified spectroscopically with the Multiple Mirror Telescope (Pascarelle et al., 1996). Blank field surveys of LAEs have been conducted with narrow band (NB) images of ground-based telescopes such as the Keck 10-m telescope, the Mayall 4-meter telescope, and the Subaru telescope at $z = 3.6$–4.8 (e.g., Cowie & Hu, 1998; Rhoads et al., 2000; Ouchi et al., 2003). They have used the Lyα technique to select LAEs with a color excess of a narrow band targeting redshifted Lyα emission against far UV (FUV) continuum. Thanks to the remarkable progresses of observations, tens of thousands of LAEs have been studied so far with narrowband imaging ($z \sim$ 2–7: e.g., Malhotra & Rhoads, 2002; Taniguchi et al., 2005; Shimasaku et al., 2006; Gronwall et al., 2007; Ota et al., 2008; Ouchi et al., 2008; Guaita et al., 2010; Hayes et al., 2010; Hu et al., 2010; Ouchi et al., 2010; Ciardullo et al., 2012; Nakajima et al., 2012; Yamada et al., 2012; Konno, 2014; Sandberg et al., 2015; Ota et al., 2017; Shimakawa et al., 2017; Shibuya et al., 2018a; Itoh et al., 2018) and/or with spectroscopic identification ($z \sim$ 0–7: e.g., Shapley et al., 2003; Kashikawa et al., 2006; Reddy et al., 2008; Cowie et al., 2010; Blanc et al., 2011; Dressler et al., 2011; Kashikawa et al., 2011; Curtis-Lake et al., 2012; Mallery et al., 2012; Nakajima et al., 2013; Erb et al., 2014; Hayes et al., 2014; Hashimoto et al., 2013; Hathi et al., 2016; Karman et al., 2017; Shibuya et al., 2018b). Consequently, they are one of the most representative populations of high-z star forming galaxies because of scientific importance as well as historical reasons like the attractive observational efficiency.

1.2.2 Typical properties of Lyα emitters

Typical LAEs at high redshifts have low stellar masses ($M_\star \lesssim 10^9$ M$_\odot$: Ono et al., 2010a; Guaita et al., 2011; Hagen et al., 2016; Shimakawa et al., 2017). They are also dust poor (Lai et al., 2008; Blanc et al., 2011) and metal poor (Nakajima et al., 2012, 2013; Nakajima & Ouchi, 2014; Kojima et al., 2017), and have young stellar populations (Pirzkal et al., 2007; Gawiser et al., 2007; Hagen et al., 2014), although a small fraction of them are attributed to dusty galaxies with high stellar masses (Nilsson & Møller, 2009; Ono et al., 2010b; Pentericci et al., 2010; Oteo et al., 2012), which implies diversity of LAEs (see also Shapley et al., 2001). They are found to reside in low-mass dark matter halos from clustering analysis ($M_\mathrm{h} \sim 10^{10}$–$10^{12}$ M$_\odot$ over $z \sim$ 2–7: e.g., Ouchi et al., 2005; Kovač et al., 2007; Gawiser et al., 2007; Shioya et al., 2009; Guaita et al., 2010; Ouchi et al., 2010; Bielby et al., 2016; Diener et al., 2017; Ouchi et al., 2018).

LAEs are found to have spatially extended Lyα emission, called, Lyα halos (LAHs; e.g., Hayashino et al., 2004; Momose et al., 2014; Wisotzki et al., 2016), which are suggested to

have information of the CGM (e.g., Dijkstra & Kramer, 2012). LAHs are not negligible because they are as bright as the central Lyα emission (Momose et al., 2014; Leclercq et al., 2017).

So far, remarkable progresses in observations and intensive studies have enabled us to extend our knowledge of LAEs and low-mass galaxies towards $M_\star \lesssim 10^8$– 10^9 $M_\odot$. However, we still have two big unknows in the framework of hierarchical structure formation.

1.2.3 Two basic unknowns of Lyα emitters

We still have two basic issues:

(1) the star forming activity of LAEs: the star formation mode, the stellar to halo mass ratio, and the baryon conversion efficiency, and
(2) the origin of the LAHs of LAEs.

For LAEs, M_h, SFR, and $M_\star$ are most reliably measured at $z \sim 2$. This is because of three reasons below. First, this redshift is high enough that the Lyα line is redshifted into the optical regime where a wide-field ground-based Lyα survey is possible. It is critical for measuring M_h from clustering analysis. A large sample constructed from wide-field surveys is also essential to measure properties of LAHs with NB images. Second, deep mid-infrared (MIR) and far-infrared (FIR) data are available to measure dust emission of galaxies at $z \sim 2$, which is essential for deriving the amount of dust attenuation (A_{1600}) and thus SFR. It enables us to derive total SFR from dust obscured SFR observed in the FIR/MIR regime and dust unobscured SFR in the FUV regime. An appropriate dust attenuation curve as well as A_{1600} is also key to derive stellar population parameters such as SFR and $M_\star$ from spectral energy distribution (SED) fitting. Third, the redshift is low enough that deep rest-frame near-infrared (NIR) photometry is still possible with Spitzer/IRAC. It is critical for deriving $M_\star$ from SED fitting of faint galaxies like LAEs. Moreover, this redshift is also scientifically interesting because star-formation of galaxies in the Universe is at the global maximum as described in section 1.1.1.

However, even at $z \sim 2$, their star forming activity (the issue (1)) has not been interpreted in the framework of structure formation, since M_h, SFR, and $M_\star$ of LAEs have not been derived for the same sample with a high accuracy as described below (section 1.3). With regard to the issue (2) about LAH, a large number of previous studies on the origin of LAHs have obtained neither conclusive, nor consistent results with each other (see section 1.4 for more detail). It might be better to approach from a different angle to the issue. Understanding the origin of LAHs enables us to estimate the escape fraction of Lyα emission from central galaxies correctly. We will also describe the mechanisms of Lyα escape in section 1.5.

1.3 Star forming activity of Lyα emitters

To understand the star forming activity of LAEs in the framework of hierarchical structure formation, the star formation mode, the stellar to halo mass ratio, and the baryon con-

version efficiency are three key properties (see section 1.1.2). Even at $z \sim 2$, only Guaita et al. (2010) and Guaita et al. (2011) succeeded in deriving SFR, $M_\star$, and M_h for the same LAE sample. In the following sections, we first of all describe the dust attenuation of LAEs, which is closely connected with the measurement of SFR, and then describe the star formation mode, $SHMR$, and BCE of LAEs at $z \sim 2$.

1.3.1 Dust attenuation and IRX at a fixed $M_\star$

At high redshift, because of the limited sensitivities of existing IR telescopes, IR luminosities have been measured only for relatively luminous galaxies ($L_\mathrm{TIR} \gtrsim 10^{11} L_\odot$ at $z \gtrsim 2$, see, e.g., Elbaz et al., 2011; Magnelli et al., 2013) except for a small number of less luminous, lensed galaxies (e.g., Sklias et al., 2014) and for stacked objects (e.g., Reddy et al., 2012a).

Previous studies on LAEs have failed to individually detect dust emission except for rare objects with (U)LIRG-like luminosities (Pentericci et al., 2010; Nilsson et al., 2011; Oteo et al., 2012). Wardlow et al. (2014) have stacked Herschel/SPIRE 250–500μm and LABOCA 870 μm images of typical LAEs at $z \gtrsim 2.8$ to obtain 3σ upper limits of $L_\mathrm{TIR} \sim$ 2–$3 \times 10^{11} L_\odot$, but they have not discussed the amount of dust attenuation. Although, usually, SED fitting has thus been used to derive A_{1600} for LAEs, A_{1600} values from SED fitting are sensitively dependent on the dust attenuation curve assumed. All of the previous studies of LAEs have assumed the Calzetti curve (Calzetti et al., 2000) and obtained a relatively wide range of $A_{1600} \lesssim 3$ magnitude (see Table 2 of Vargas et al., 2014). Since $M_\star$ and $E(B-V)$ of LAEs in Guaita et al. (2011) are estimated to be $\sim 4 \times 10^8$ $M_\odot$ and ~ 0.22 (i.e., $A_{1600} \sim$ 2 mag), respectively, their LAEs are indicated to have higher IRXs than expected from the average IRX–$M_\star$ relation. It implies that LAEs are dust-enriched galaxies at a fixed $M_\star$, which is not matched with a general intuition of their dust-poor contents.

Recent observations (e.g., Reddy et al., 2006; Nordon et al., 2013; Reddy et al., 2018) have found that some high-redshift galaxies favor an SMC extinction curve (e.g., Gordon et al., 2003) as the dust attenuation curve, which may question the use of the Calzetti curve for LAEs. Therefore, we need to measure the dust emission or A_{1600} of LAEs with deep MIR/FIR observations and then discuss an appropriate dust attenuation curve for the LAEs using a relation between IRX and UV slope (β) (e.g., Meurer et al., 1999).

1.3.2 Star formation mode

Guaita et al. (2011) derive the $M_\star$ and SFR of LAEs from SED fitting. Their LAEs have too large errors in $M_\star$ and SFR to distinguish the star formation mode although they are consistent with the MS mode. In addition, their SED model does not include nebulae emission and adopts the Calzetti curve. Nebular emission enhances luminosities of galaxies especially at rest optical wavelengths. For these reasons, their $M_\star$ and SFR are possibly overestimated, though the uncertainties caused by their methods are not included in their error bars.

Hagen et al. (2016) have found that spectroscopically-selected individual LAEs with a bright Lyα luminosity ($\gtrsim 1 \times 10^{43}\,\mathrm{erg\,s^{-1}}$, Hagen et al., 2014) and NB-selected individual LAEs with a typical Lyα luminosity of $\sim 1 \times 10^{42}\,\mathrm{erg\,s^{-1}}$ that have a counterpart in the 3D-HST catalog (Guaita et al., 2010; Vargas et al., 2014) lie along or above the SFMS, though they also assume the Calzetti curve. Meanwhile, Shimakawa et al. (2017) have found that fainter NB-selected individual LAEs with an NB luminosity brighter than $\sim 4 \times 10^{41}\,\mathrm{erg\,s^{-1}}$ lie on the SFMS assuming the Calzetti curve. Note that the stellar masses are derived from SED fitting without IRAC photometry.

Because of this situation, the star formation mode of typical LAEs has not been discussed accurately yet. Recent observations have revealed that the stellar properties of LAEs are similar to those of other emission line galaxies at $z \sim 2$ (Hagen et al., 2016). Shimakawa et al. (2017) have also found that LAEs at $M_\star \lesssim 10^{10}$ $\mathrm{M_\odot}$ obey the same $M_\star$-size relation as Hα emitters (HAEs) at $z = 2.5$. These results imply a possibility that LAEs are normal star-forming galaxies in the low stellar mass regime at high redshift.

To discuss the star formation mode of LAEs, deep FIR/MIR observations as well as deep IRAC photometry are required. It is also essential to include nebular emission into the SED fitting model (e.g., Ono et al., 2010a) and to estimate an appropriate dust attenuation curve for LAEs from the IRX–β relation.

1.3.3 Dark matter halo mass, SHMR, and BCE

To date, there is only one clustering study carried out at $z \sim 2$ by Guaita et al. (2010) with 250 LAEs in a ~ 0.3 deg^2 field. They obtain a relatively high halo mass of $\log(M_\mathrm{h}/\mathrm{M_\odot}) \sim 11.5^{+0.4}_{-0.5}$ compared with the other work for LAEs at $z \sim 3$–7 (e.g., Gawiser et al., 2007; Bielby et al., 2016; Diener et al., 2017; Ouchi et al., 2018). Their M_h implies an $SHMR$ comparable to or lower than the average relations by Behroozi et al. (2013) and Moster et al. (2013) at the same dark matter halo mass. Their LAEs are estimated to have a comparable BCE with the average relation by Behroozi et al. (2013) but its uncertainty is as large as $\sim$ 1 dex. However, this halo mass estimate may suffer from statistical uncertainties due to a small sample size ($N \sim 250$) and systematic uncertainties from cosmic variance due to a small survey area (~ 0.3 deg^2). Moreover, true uncertainties are probably larger, since their $M_\star$ and SFR are possibly overestimated without including systematic uncertainties into the error bars as described in 1.3.2.

Their result of M_h also suggests that their LAEs at $z \sim 2$ could be progenitors of present-day $L_\star$ galaxies like the Milky Way and that they could also be descendants of $z \sim 3$ LAEs (Guaita et al., 2010). Note that LAEs at $z \sim 3$, which are progenitors of present-day $L_\star$ galaxies, are suggested not to evolve into LAEs at $z \sim 2$ from SED fitting (Acquaviva et al., 2012). Measurements of M_h also provide us the duty cycle of LAEs defined as the fraction of dark matter halos hosting an LAE. The LAEs in Guaita et al. (2010) are suggested to have a high duty cycle, 43^{+113}_{-30} % compared with those of previous studies at $z \sim 3$, a few tenths to a few percent (e.g., Gawiser et al., 2007; Ouchi et al., 2010). An accurate measurement of the duty cycle is useful to discuss the physical mechanisms which determine the star forming activity and the Lyα escape fraction of

LAEs.

To overcome the above problems due to the large uncertainty in the$M_{\rm h}$ measurement, a larger number of sources from a larger survey area with deep multi-wavelength data is needed.

1.4 Lyα halos

1.4.1 The ubiquitous presence of Lyα halos

A Lyα halo (LAH) is a diffuse, spatially extended structure of Lyα emission seen around star-forming galaxies. It is expected to trace neutral hydrogen gas in the CGM of galaxies, which is closely linked to galaxy formation and evolution. Cosmological simulations have predicted that Lyα halos are common in galaxies especially at high redshift (e.g., Zheng et al., 2011; Rosdahl & Blaizot, 2012; Dijkstra & Kramer, 2012).

LAHs around local galaxies, as well as around AGNs and QSOs, can be detected individually because they are relatively bright (e.g., Keel et al., 1999; Kunth et al., 2003; Hayes et al., 2005; Goto et al., 2009; Östlin et al., 2009; Hayes et al., 2013; Matsuda et al., 2011, and references therein). LAHs around high-z galaxies are much fainter, but they have been detected in stacked narrow-band images (tuned to redshifted Lyα emission) of $\sim 100 - 4000$ star-forming galaxies at $z \sim 2$–6 (e.g., Hayashino et al., 2004; Steidel et al., 2011; Matsuda et al., 2012; Feldmeier et al., 2013; Momose et al., 2014, 2016; Xue et al., 2017, see also a stacking study of spectra of ~ 80 LAEs at $z \sim 2$–4 by Guaita et al. 2017). Very recently, LAHs around ~ 170 star forming galaxies at $z \sim 3$–6 have been detected individually by deep integral field spectroscopy with VLT/MUSE (Wisotzki et al., 2016, 2018; Leclercq et al., 2017). Thanks to the intense observations of Lyα halos for more than 20 years, the existence of LAHs has now been established. The next question is what is their physical origin(s).

1.4.2 Theoretical candidates of the origin of Lyα halos

Theoretical studies have proposed several physical origins of LAHs: resonant scattering in the CGM, cold streams (gravitational cooling radiation), star formation in satellite galaxies (one-halo term), fluorescence (photo-ionization), shock heating by gas outflows, and major mergers (e.g., Haiman et al., 2000; Taniguchi & Shioya, 2000; Cantalupo et al., 2005; Mori & Umemura, 2006; Laursen & Sommer-Larsen, 2007; Zheng et al., 2011; Rosdahl & Blaizot, 2012; Yajima et al., 2013; Lake et al., 2015; Mas-Ribas & Dijkstra, 2016). The former three are generally considered for high-z star-forming galaxies (e.g., Lake et al., 2015), while the latter three are preferred for giant Lyα nebulae (Lyα blobs; LABs) and/or bright QSOs (e.g., Kollmeier et al., 2010; Mori & Umemura, 2006; Yajima et al., 2013).

In the cold stream scenario, the accreting relatively dense and cold ($\sim 10^4$ K) gas releases the gravitational energy (called, cold streams; e.g., Fardal et al., 2001; Kereš et al., 2005; Dekel & Birnboim, 2006) and emits Lyα photons (e.g., Haiman et al., 2000;

Furlanetto et al., 2005; Dijkstra & Loeb, 2009). Cold streams are suggested to produce an extended Lyα halo without (extended) UV continuum emission (Lake et al., 2015). The Lyα luminosity due to cold streams is suggested to increase with the $M_{\rm h}$ of host galaxies (Dijkstra & Loeb, 2009; Faucher-Giguère et al., 2010; Rosdahl & Blaizot, 2012).

Meanwhile, in the satellite star formation scenario, Lyα photons are produced through star formation (recombination) in satellite galaxies. If it contributes to LAHs, they would involve extended UV emission from the star formation (Shimizu et al., 2011; Zheng et al., 2011; Lake et al., 2015; Mas-Ribas et al., 2017). According to the local observations, the number of disk (i.e., star-forming) satellite galaxies correlates with the host dark matter halo mass of the central galaxy (e.g., Trentham & Tully, 2009; Wang et al., 2014), and such properties can be reproduced by theoretical models (e.g., Nickerson et al., 2013; Sales et al., 2014). The Lyα luminosity from satellite star formation can be interpreted as a function of the $M_{\rm h}$ and $M_\star$ of the central galaxy. Note that recent detailed models for this scenario have been examined with a few galaxies not with a large sample from a cosmological simulation (e.g., Mas-Ribas et al., 2017).

In the resonant scattering scenario, Lyα photons that have escaped from the main body of the galaxy are scattered away by HI gas in the CGM (Laursen & Sommer-Larsen, 2007; Barnes & Haehnelt, 2010; Zheng et al., 2011; Dijkstra & Kramer, 2012; Verhamme et al., 2012). It is suggested to produce an extended Lyα halo without (extended) UV continuum emission (e.g., Mas-Ribas et al., 2017). The relation between $M_{\rm h}$ (or $M_\star$) of the central galaxy and the Lyα luminosity is probably determined by the balance between the efficiency of resonant scattering, and the amount of dust attenuation, if we assume that intrinsic Lyα luminosity correlates with SFR and thus mass.

Understanding the origin of LAHs provides crucial information on the CGM, which is closely linked to galaxy formation and evolution. A sufficient gas reservoir in the CGM can sustain the star formation of the central galaxy (e.g., Lilly et al., 2013). Gas inflows into and outflows from a galaxy are expected to trigger starburst and suppress star formation, respectively (e.g., Dekel et al., 2009b; Muratov et al., 2015). It also enables us to estimate the escape fraction of Lyα emission from central galaxies correctly. If resonant scattering mainly drives LAHs, the Lyα luminosity of LAHs should be included in the calculation of the Lyα escape fraction. LAHs are also important for studies of cosmic reionization because their spatial extent can be used as a probe of the IGM ionization fraction (Verhamme et al. in prep).

1.4.3 Previous observational work on the origin of LAHs

Lyman α emitters (LAEs) are suitable objects for studying the nature of LAHs because a large sample of LAEs at a fixed redshift as needed for a stacking analysis can be constructed relatively easily from a narrow-band imaging survey (Matsuda et al., 2012; Feldmeier et al., 2013; Momose et al., 2014, 2016; Xue et al., 2017). LAEs are typically low-stellar-mass young galaxies with low metallicities and low-dust contents hosted in low-mass dark matter halos (e.g., Pirzkal et al., 2007; Lai et al., 2008; Ono et al., 2010a; Nakajima & Ouchi, 2014; Kojima et al., 2017; Ouchi et al., 2018, and reference therein).

They are detected owing to efficient Lyα escapes, which are suggested to stem partly from these physical properties such as low-dust attenuation (e.g., Finkelstein et al., 2009).

Matsuda et al. (2012) have found that LAEs in a large-scale overdense region at $z = 3.1$ have large ($\sim$ 100–200 Å) EWs if LAH components are included. They suggest that those LAHs may partly originate from shock heating due to gas outflows or cold streams, although they have not ruled out other possibilities. On the other hand, Momose et al. (2016) have stacked $\sim$ 3600 LAEs in field regions at $z \sim 2$ to find that some subsamples have relatively small Lyα EWs fully consistent with pop II star formation, suggesting that the cold stream scenario is not preferred. Finding no correlation between the spatial extent (the scale length, r_s) and the surface number density for LAEs at $z \sim 3$–4, Xue et al. (2017) have suggested that star formation in satellite galaxies is not the dominant contributor to LAHs (see however, Matsuda et al., 2012). They have also found that the radial profile of LAHs is very close to that predicted by models of resonant scattering in Dijkstra & Kramer (2012), leaving only little room for the contribution from satellites galaxies and cold streams modeled by Lake et al. (2015). Note, however, that Lake et al. (2015)'s model reproduces the radial profile of LAHs seen in LAEs at $z \sim 3$ in Momose et al. (2014). More recently, Leclercq et al. (2017) have measured LAH properties of $\sim$ 150 individual LAEs at $z \sim 3$–6 using VLT/MUSE. They argue that a significant contribution from star formation in satellite galaxies is somewhat unlikely since the UV component of LAEs is compact and not spatially offset from the center of their LAHs, while having not given a firm conclusion on other origins. To summarize, although there are a number of observational studies on the origin of LAHs, their results are not very conclusive, nor consistent with each other (Matsuda et al., 2012; Feldmeier et al., 2013; Momose et al., 2016; Wisotzki et al., 2016; Xue et al., 2017; Leclercq et al., 2017, see also Steidel et al. 2011).

1.4.4 Open a new way for revealing the origin of LAHs

So far, correlations of LAH properties with properties of central galaxies have not been fully studied. To obtain further information, it might be better to approach from a different angle, which enables us to compare more directly with theoretical predictions. Especially important may be correlations with the dark matter halo mass and stellar mass of central galaxies, because they can be directly compared with theoretical predictions (e.g., Rosdahl & Blaizot, 2012). Although Leclercq et al. (2017) have discussed a correlation between the Lyα luminosity of LAHs and the UV luminosity of central galaxies, they have not estimated those masses. $SFRs$ and dust attenuation are also important quantities to discuss the scattering origin of LAHs.

Another problem is that r_s, the scale-length of LAHs that is often used to discuss the origin of LAHs in previous studies, is not robust against measurement errors. Indeed, the dependence of r_s on Lyα luminosity found in individually detected MUSE LAEs is not consistent with the average dependence obtained by Momose et al. (2016) from stacked images. In contrast, as we will see later, relations between the Lyα luminosity of central galaxies and that of LAHs found in Momose et al. (2016) is in good agreement with

those seen in individual MUSE-LAEs in Leclercq et al. (2017). This suggests that Lyα luminosity is more robust against systematic errors from stacking.

A large sample size of NB-selected LAEs enables us to investigate the dependence of LAH luminosity on stellar properties and dark matter halo mass. This is one of the studies that make the best use of Subaru/Hyper Suprime-Cam (HSC: Miyazaki et al., 2012) and even Subaru/Suprime-Cam (SC: Miyazaki et al., 1998).

1.5 The origin of bright Lyα emission

The bright Lyα emission arises from high Lyα escape fractions. The mechanisms for high Lyα escape fractions ($f_{\rm esc}$(Lyα)) are directly related to the origin of LAEs as a galaxy population.

Previous studies have not taken account of LAHs when calculating the Lyα escape fraction (e.g., Song et al., 2014; Hayes et al., 2011). However, if the dominant origin of LAHs is scattering in the CGM, we can obtain more accurate values including LAHs. The diagram of $f_{\rm esc}$(Lyα) versus $E(B-V)$ is useful, since additional mechanisms are needed to make $f_{\rm esc}$(Lyα) higher or lower than that expected from $E(B-V)$.

The possible origins for a high $f_{\rm esc}$(Lyα) of LAEs are categorized to: (i) less efficient resonant scattering in a uniform interstellar medium (ISM), (ii) less efficient resonant scattering in a clumpy ISM, (iii) additional Lyα sources, and (iv) hard ionizing spectra. In a uniform ISM where dust and gas are well mixed, Lyα photons have a higher chance of dust absorption than continuum photons because of resonant scattering. To reduce the efficiency of resonant scattering in a uniform ISM, one needs to reduce column density of HI gas ($N_{\rm HI}$) or scattering cross section ($\sigma_{\rm Ly\alpha}$) (e.g., Duval et al., 2014; Garel et al., 2015). On the other hand, in the clumpy ISM, Lyα photons are not attenuated by dust if dust is confined in HI clumps (Neufeld, 1991; Hansen & Peng Oh, 2006). Candidates of additional Lyα sources are AGNs and cold streams in the central part of galaxies. Hard ionizing spectra are suggested for high-z LAEs at $z \sim 2$–7, and it means that the production efficiency of ionizing photons compared to the UV luminosity is higher than the fiducial value (e.g., Nakajima et al., 2016; Harikane et al., 2018).

1.6 Overview of this thesis

In this thesis, we will study galaxy evolution with a representative high-z low-mass galaxy, LAEs, in the framework of structure formation. Especially we investigate the two basic issues:

(1) star forming activity of LAEs: the star formation mode, the stellar to halo mass ratio, and the baryon conversion efficiency, and
(2) the origin of LAHs of LAEs.

We use $\sim$ 1250 NB-selected LAEs from four deep survey fields with a total area of $\simeq 1$ deg^2. Among them, 213 LAEs with deep MIR/FIR data are used to measure the dust

emission of LAEs and to obtain an appropriate dust attenuation curve (Kusakabe et al., 2015). We perform SED fitting to stacked imaging data to measure stellar population parameters including SFR, A_{1600}, and $M_\star$, while we derive M_h from clustering analysis (Kusakabe et al., 2018b,a). We divide our LAEs into subsamples to discuss the origin of LAHs (Kusakabe et al., 2018a). The layout of this thesis are below.

In chapter 2, we describe the sample selection of our LAEs in the four survey fields, the fraction of interlopers in our sample, photometric data used in this thesis, and subsample criteria. For the IR study, we only use LAEs in a field covered by one of the deepest public MIR and FIR data, while we use LAEs in the whole fields to discuss their star forming activity. We divide our LAEs with deep optical/NIR data into subsamples.

In chapters 3 and 4, we present the methods of SED fitting: stacking analysis, photometry, and details of the SED fitting model, and the methods of clustering analysis: how to measure angular correlation functions, biases, and dark matter halo masses. We also describe how to estimate cosmic variance analytically. In chapter 5, we explain methods to estimate Lyα luminosities of LAHs.

Chapter 6 is devoted to show results in this thesis: IR luminosity and dust attenuation curve, results of SED fitting, results of clustering analysis, IRX-$M_\star$ relation, star formation mode, $SHMR$ and BCE, LAH luminosity, and Lyα escape fraction.

In chapter 7, we discuss the physical origin of star forming activity, the origin of dust attenuation, and the present-day descendants of the LAEs. We also discuss the origin of LAHs of the LAEs in chapter 8. Chapter 9 is devoted to discuss the mechanisms for high Lyα escape fractions. Conclusions are given in chapter 10.

In Appendices A to C, we show auxiliaries for methods and results of SED fitting, clustering analysis, and LAH luminosity estimation in chapters 4 to 6, respectively. We also mention the details of estimation of cosmic variance in appendix C. The star formation modes derived from different assumptions are shown in appendix D. In appendix E, we show details of a study on the LAE fraction at $z \sim 3$ to 6 with VLT/MUSE data, which are used in the discussion of LAE fraction in chapter 9.

Throughout this thesis, we adopt a flat cosmological model with the matter density $\Omega_\mathrm{m} = 0.3$, the cosmological constant $\Omega_\Lambda = 0.7$, the baryon density $\Omega_b = 0.045$, the Hubble constant $H_0 = 70\ \mathrm{km\,s^{-1}Mpc^{-1}}$ ($h_{100} = 0.7$), the power-law index of the primordial power spectrum $n_\mathrm{s} = 1$, and the linear amplitude of mass fluctuations $\sigma_8 = 0.8$, which are consistent with the latest Planck results (Planck Collaboration, 2016). We assume a Salpeter initial mass function (IMF: Salpeter, 1955) with a mass range of 0.1–100 $M_\odot$[*1]. Magnitudes are given in the AB system (Oke & Gunn, 1983) and coordinates are given in J2000. Distances are expressed in comoving units, while galaxy sizes are expressed in the physical scale. We use "log" to denote a logarithm with a base 10 ($\log_{10}$).

[*1] To rescale stellar masses in previous studies assuming a Chabrier or Kroupa IMF (Kroupa, 2001; Chabrier & Chabrier, 2003), we divide them by a constant factor of 0.61 or 0.66, respectively. Similarly, to convert SFRs in the literature with a Chabrier or Kroupa IMF, we divide them by a constant factor of 0.63 or 0.67, respectively.

Chapter 2

Data and Sample Selection

Here we describe sample selection of our LAEs in four survey fields, the fraction of interlopers in our sample, photometric data used in this thesis, and subsample criteria. For IR study, we only use LAEs in a field covered by one of the deepest public MIR and FIR data. While We use LAEs in the whole fields for discussion of their star forming activity, we only use our LAEs in two fields covered by deep rest UV to NIR data to divide into subsamples for discussion of the origin of LAHs.

2.1 Sample selection

Our LAE samples are constructed in four deep survey fields, the Subaru/XMM-Newton Deep Survey (SXDS) field (Furusawa et al., 2008), the Cosmic Evolution Survey (COSMOS) field (Scoville et al., 2007), the Hubble Deep Field North (HDFN: Capak et al., 2004), and the Chandra Deep Field South (CDFS: Giacconi et al., 2001, or The Great Observatories Origins Deep Survey South (GOODS-S) in Dickinson et al. (2003)). We select LAEs at $z = 2.14$–2.22 using the narrow band $NB387$ (Nakajima et al., 2012) as described in selection papers (Nakajima et al., 2012, 2013; Kusakabe et al., 2015; Konno et al., 2016). The threshold of rest-frame equivalent width, EW_0, of Lyα emission is $EW_0(\mathrm{Ly}\alpha) \geq 20$–$30$Å (Konno et al., 2016). The threshold varies from 20 to 30 Å because the response curves of the selection bands U (or u^*) and B are slightly different among the four fields. Two-color diagrams of B–$NB387$ versus U (or $u^\star$)–$NB387$ for selection in each of the four fields are shown in figure 1 in Konno et al. (2016). We overview the sample selection of our LAEs in the four fields below (see a flowchart of our (sub)samples shown in figure 2.1).

2.1.1 SXDS field

SXDS field consists of five sub-fields: SXDS–Center (SXDS–C), SXDS–North (SXDS–N), SXDS–South (SXDS–S), SXDS–West (SXDS–W), and SXDS–East (SXDS–E). We do not use the $NB387$ image in SXDS–E sub-field due to the relatively larger PSF FWHM ($\sim 2''.0$) than those in the other sub-fields ($\sim 0''.7$–$1''.2$). The total (effective) area is 2003 arcmin^2 and 934 LAEs are selected (Nakajima et al., 2012, see also Konno et al.

2016). In this thesis, we do not use LAEs in SXDS-W because the $NB387$ image is ~ 0.6 mag shallower than those in the other sub-fields. The $5\,\sigma$ depth in a $2''$ diameter aperture is $\simeq 25.7$ mag in the three subregions (after corrected zero point offset described below).

These LAEs include those in low S/N regions of the $NB387$ images setting brighter limiting magnitudes according to S/N ratios in order to maximize the sample size. The 5 σ limiting magnitudes of the low S/N regions are 25.2 – 25.3 mag. This low S/N regions exists due to the limited number of dithering (i.e., short net exposure times) and bright objects in $NB387$ images. Clustering analysis requires a sample with a uniform detection rate over the entire area for accurate measurements, since the difference in the depth in sub regions can enhance apparent clustering strength artificially. We also remove the LAEs in regions with short net exposure times. In SXDS field (SXDS–C, N, and S), we use the overlapping regions to examine if there exists an offset in the $NB387$ zero point for the previous selection. A non-negligible offset of 0.06 mag is found in SXDS–N and appropriately corrected. Note that such correction values change the Lyα luminosities only slightly. We remove LAEs with counter parts in X-ray and radio catalogs (Ueda et al., 2008; Simpson et al., 2006) and in UV images from the Multimission Archive at STScI as interlopers (see also section 2.2 for more details on interlopers). Finally, we obtain 601[*2] star-forming LAEs with total $NB387$ magnitude ($NB387_{\rm tot}$, i.e., aperture-corrected magnitude) brighter than 25.5 mag in ~ 1240 arcmin^2 region (Kusakabe et al., 2018b,a). We use the SXDS sample to study the star forming activity and the origin of LAH of LAEs (in chapters 3, 4, and 5).

2.1.2 COSMOS field

In Nakajima et al. (2013), 642 LAEs are selected in 846 arcmin^2 (see also Konno et al., 2016, for details). The $5\,\sigma$ depth in a $2''$ diameter aperture is $\simeq 26.1$ mag.

For accurate clustering analysis, we remove LAEs in regions with short net exposure times. We examine the $NB387$ zero point for the previous selection using the colors of the Galactic stars from Gunn & Stryker (1983) and do not find significant offsets. We remove LAEs with counter parts in X-ray and radio catalogs (Elvis et al., 2009; Schinnerer et al., 2007) and UV images from the Multimission Archive at STScI (see also Zamojski et al., 2007) as interlopers (see also section 2.2 for more details on interlopers). Finally, we obtain 526 star-forming LAEs with $NB387_{\rm tot} \leq 25.8$ mag in ~ 740 arcmin^2 area (Kusakabe et al., 2018b,a). We use the COSMOS sample to study the star forming activity and the origin of LAH of LAEs (in chapters 3, 4, and 5).

[*2] The number of LAEs divided into subsamples is slightly different (600) since we use $NB387$ images before PSF matching to other selection-band images for photometry (Kusakabe et al., 2018a).

	IR study	SED fitting: samples with NB_{tot}≤25.5mag	clustering analysis: samples with NB_{tot}≤26.3mag	SED fitting: subsamples	clustering analysis and Lyα halo luminosity: subsamples
SXDS	-	93 "IRAC-clean" LAEs	601 LAEs NB_{tot}≤25.5mag	514 (99) LAEs with UV-NIR photometry ("IRAC-clean" LAEs)	595 LAEs with NB_{tot}≤25.5mag and UV/Lyα properties*2
COSMOS	-	21 "IRAC-clean" LAEs	526 LAEs NB_{tot}≤25.8mag (297 LAEs with NB_{tot}≤25.5mag)	296 (22) LAEs with UV-NIR photometry ("IRAC-clean" LAEs)	296 LAEs with NB_{tot}≤25.5mag and UV/Lyα properties
HDFN	-	56 "IRAC-clean" LAEs	588 LAEs NB_{tot}≤25.8mag (299 LAEs with NB_{tot}≤25.5mag)	-	-
CDFS	213 LAEs with MIR/FIR data	4 "IRAC-clean" LAEs	222 LAEs NB_{tot}≤26.3mag (51 LAEs with NB_{tot}≤25.5mag)	-	-
total	213 LAEs with MIR/FIR data	174 "IRAC-clean" LAEs	1937 LAEs NB_{tot}≤26.3mag (1248 LAEs with NB_{tot}≤25.5mag)	810 (121) LAEs with UV-NIR photometry ("IRAC-clean" LAEs)	891 LAEs with NB_{tot}≤25.5mag and UV/Lyα properties

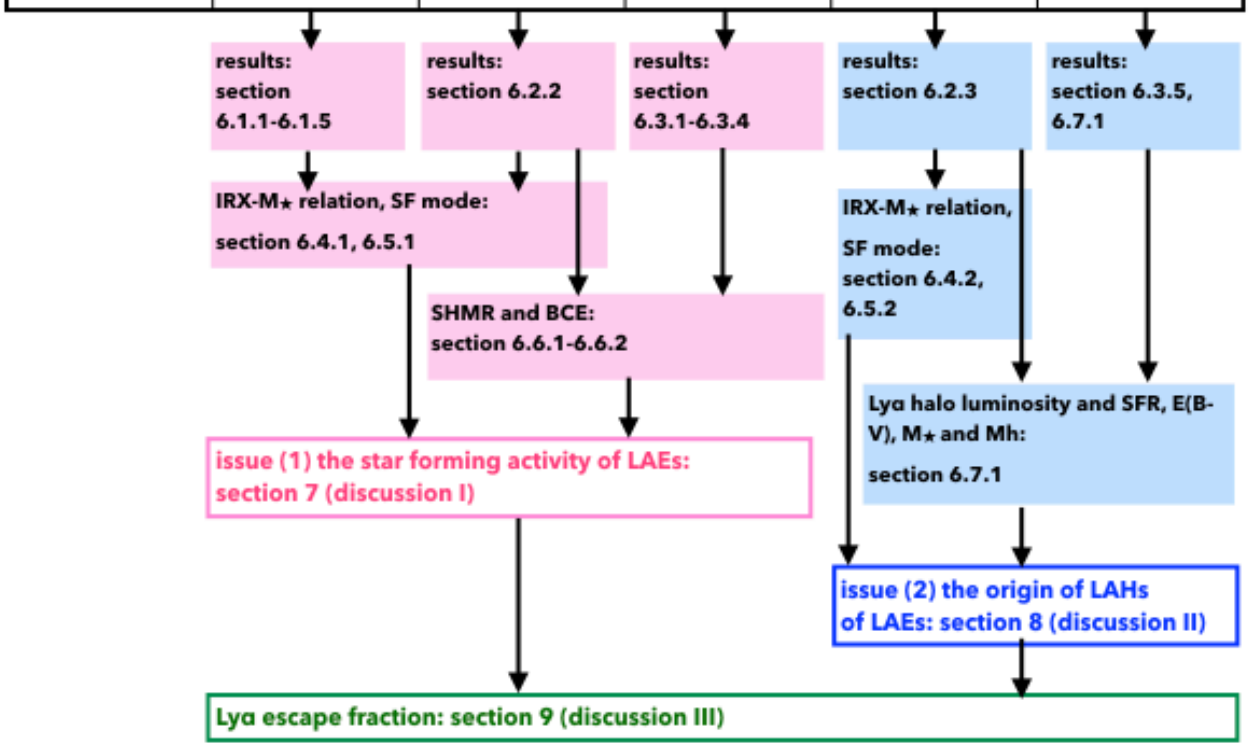

Figure 2.1 Flowchart of our (sub)samples. The number of LAEs in each (sub)sample is also shown (see sections 2.1, 2.4, and 2.5 for more details).

2.1.3 HDFN field

In Nakajima et al. (2013), 967 LAEs are selected in 913 arcmin^2 (see also Konno et al., 2016, for details). The $5\,\sigma$ depth in a $2''$ diameter aperture is $\simeq 26.4$ mag.

For accurate clustering analysis, we remove LAEs in regions with short net exposure times. We do not find significant offset of $NB387$ zero point from the colors of the Galactic stars from Gunn & Stryker (1983). We remove LAEs with counter parts in X-ray catalog (Alexander et al., 2003) and UV images from the Multimission Archive at STScI as interlopers (see also section 2.2 for more details on interlopers). Finally, we obtain 588 star-forming LAEs with $NB387_{\rm tot} \leq 25.8$ mag in ~ 780 arcmin^2 area (Kusakabe et al., 2018b). We use the HDFN sample to study the star forming activity of LAEs (in chapters 3 and 4).

2.1.4 CDFS field

LAEs in this field are once selected with wide but shallow U band image of MPG 2.2m telescope/WFI (Gawiser et al., 2006; Cardamone et al., 2010) to construct a large sample as described in Nakajima et al. (2013). However, IR study is sensitive to contaminants due to poor resolution and sensitivity of FIR and MIR telescopes. In order to construct a secure sample, we replace the U band data to VLT/VIMOS U-band (Nonino et al., 2009) combining with MPG 2.2m telescope/WFI B-band data (Hildebrandt et al., 2006). We construct an LAE sample with 423 sources in 577 arcmin^2 area in Kusakabe et al. (2015), whose details including selection criteria are described in Konno et al. (2016). The $5\,\sigma$ depth in a $2''$ diameter aperture is $\simeq 26.6$ mag (after corrected zero point offset described below).

In this field, one of the deepest publicly available deep Spitzer/MIPS 24 μm and Herschel/PACS images exist (Magnelli et al., 2011; Lutz et al., 2011; Elbaz et al., 2011; Magnelli et al., 2013). Moreover, deep HST and IRAC data, from optical to mid infrared, for SED fitting are also available in this field (Giavalisco et al., 2004; Damen et al., 2011; Grogin et al., 2011; Koekemoer et al., 2011; Brammer et al., 2012; Skelton et al., 2014). We use the LAE sample in this field for IR study in this thesis (Kusakabe et al., 2015). We remove a small number of interlopers with a spectroscopic redshift outside of the range probed by NB387 ($z = 2.14 - 2.22$) ($\sim 6\%$) and Galactic stars ($\sim 0.4\%$) using the GOODS-MUSIC (Santini et al., 2009), the MUSYC (Cardamone et al., 2010), GMASS (Kurk et al., 2013), and X-ray (Chandra 4Ms; Xue et al., 2011) catalogs and AGNs ($\sim 2\%$) detected in X-ray or radio (VLA 1.4-GHz source catalog; Miller et al., 2013). The fraction of interlopers is expected to be low (see section 2.2 for more details). We obtain a large sample of 213 LAEs in the area covered by the MIR and FIR images (hereafter, "IR-study sample"). Our LAEs are as faint as $M_{\rm UV} = -18.7$ mag in average with $\sigma = 0.6$ mag. Among them, ~ 44 percent are within the coverage of deep HST images from the GOODS and CANDELS surveys. We use 52 objects with uncontaminated IRAC images for SED fitting with stacked SEDs and compare the results with those derived with IR

data (Kusakabe et al., 2015).

On the other hand, we use the LAE sample in the whole field of $\sim$ 580 arcmin^2 for clustering analysis and SED fitting with ground-based telescopes to study the star forming activity (in chapters 3 and 4). Following zeropoint check of $NB387$ in the other fields, we find a 0.1 mag offset using the colors of the Galactic stars from Gunn & Stryker (1983). We apply a 0.1 mag correction to LAEs used for clustering analysis and SED fitting. Note that we do not apply it to LAEs used for the IR study in section 3.1 and that such correction values change the Lyα luminosities only slightly. The whole $\sim$ 580 arcmin^2 area do not include regions with short net exposure times, resulting from the dither pattern. We remove interlopers as described above and obtain 222 star-forming LAEs with $NB387_{\rm tot} \leq 26.3$ mag in $\sim$ 580 arcmin^2 area (Kusakabe et al., 2018b).

2.1.5 Summary of our sample

Our sample basically consists of 1937 LAEs with $NB387_{\rm tot} \leq 26.3$ mag from $\simeq$ 1 square degrees in the four fields (see the flowchart of our (sub)samples shown in figure 2.1). Each survey area size is shown in tables 2.1 to 2.4 in section 2.3. We use all of them for the clustering analysis to examine the halo mass dependence on $NB387_{\rm tot}$ (see figure 2.2 and table 2.5 in section 2.4). However, since not all the fields reach $NB387_{\rm tot} = 26.3$ mag, 1248 LAEs with $NB387_{\rm tot} \leq 25.5$ mag are used to calculate the four-field average effective bias (see section 4.2) and hence to derive stellar parameters from SED fitting for discussion of the star forming activity. With regard to subsample study for Lyα halo, we only use 897 LAEs with $NB387_{\rm tot} \leq 25.5$ mag in $\sim$ 1980 square arcminutes in COSMOS and SXDS fields, where deep optical to MIR data exist (see section 2.3.3 for more details). Among them, 891 LAEs can be divided into subsamples in accordance with UV, Lyα, K-band properties. We do not use the HDFN sample because the V-band and R-band images in this filed are not deep enough to derive the UV slope for faint LAEs. We also do not use the CDFS sample because I, z, and H data are too shallow to perform reliable SED fitting. For the IR study of LAEs, we use 213 LAEs in CDFS covered by the MIR and FIR images. Note that we only use isolated LAEs with uncontaminated IRAC images for SED fitting, which is described in chapter 3.

2.2 Contamination fraction

Possible interlopers in our LAE samples are categorized into (i) spurious sources without continuum, (ii) AGNs, (iii) low-z line emitters whose line emission (not Lyα) is strong enough to meet our color selection, (iv) low-z line emitters with weaker emission lines which happen to meet the color selection owing to photometric errors in the selection bands, (v) low-EW ($\lesssim 20-30$ Å) LAEs at our target redshift selected owing to photometric errors in the selection bands, and (vi) continuum sources at any redshifts selected as LAEs owing to photometric errors in the selection bands. We describe each in further detail here.

(i) Spurious sources without continuum are possibly included in our LAE sample even after visual inspection was performed as described in the original papers based on selection. About $\sim 2\%$ of all 1937 LAEs have neither U (or u^*) nor B band detection at more than $2\,\sigma$, and this fraction reduces to 0.2% for the 1248 objects with $NB387 \leq 25.5$.

(ii) All sources detected in either X-ray, UV, or radio are regarded as AGNs and have been removed as described in section 2.1. Their fraction of the entire sample is about 2%. Obscured faint AGNs at these wavelengths may contaminate our sample, although heavily obscured AGNs are unlikely to have emission lines strong enough to pass our color selection. Following (Guaita et al., 2010), we estimate the possible fraction of obscured AGNs in our LAE sample to be $\sim 2\%$, i.e. similar to that of X-ray, UV, or radio detected AGNs (i.e., Xue et al., 2010; Stern et al., 2012; Heckman & Best, 2014; Aird et al., 2018; Ricci et al., 2017).

(iii) Candidate emitters are [O II] $\lambda\,3727$ emitters at $z \simeq 0.04$, Mg II $\lambda\,2798$ emitters at $z \simeq 0.4$, and CIV$\lambda\,1550$ and CIII] $\lambda\,1909$ emitters at $z \simeq 1.5$. However, the survey volume of [O II] emitters at $z \simeq 0.04$ is three orders of magnitude smaller than that of LAEs at $z = 2.2$. Moreover, the EW_0([O II]) of the vast majority of [O II] emitters is too small (~ 8 Å) to meet our color selection of $EW_0([\mathrm{O\,II}]) \geq 70$ Å (see Konno et al., 2016; Ciardullo et al., 2013). [O II] emitters with such a large EW_0([O II]) should be AGNs. Mg II, CIV and CIII] emitters which satisfy our selection criteria are also likely to be AGNs. X-ray, UV, or radio detected AGNs have been removed. Therefore, the fraction of contaminants (iii) is expected to be negligibly small and is included in the possible fraction of obscured AGNs as described in category (ii).

(iv), (v), (vi) We evaluate the contamination fraction contributed by (iv), (v) and (vi) sources that do not satisfy the selection criteria if they have no photometric error (hereafter, intrinsically unselected sources) using Monte Carlo simulations. We create a mock catalog with intrinsic and observed (i.e., added photometric errors) values of $NB387$ magnitudes and two colors in the color-color selection diagram, U (or u^*) –$NB387$ and $B - NB387$, down to the 5σ limiting magnitude of $NB387$ in each of the four fields (as shown in figure 2.2). Hereafter, we assume that the distribution of the two colors for $NB387$-detected objects is unchanged with $NB387$ magnitude intrinsically. For each mock source in a given field, an intrinsic $NB387$ magnitude is randomly selected from the $NB387$ distribution of the $NB387$-detected objects, and its $NB387$ photometric error is assigned by random selection from the Gaussian distribution of $NB387$ photometric errors in the given field. Meanwhile, a pair of intrinsic two colors is randomly selected from those of bright $NB387$-detected objects with $NB387 \leq 24.0$ mag where photometric errors are negligible in the three selection bands of U (or u^*), B, and $NB387$ in the four fields. Photometric errors of the three selection bands are also added to the mock intrinsic colors.

We then apply the same selection as for the real catalog to obtain the number of objects passing the selection. The contamination fraction is calculated by dividing the number of intrinsically unselected sources passing the selection by the number

of all sources passing the selection. The latter are a mixture of real LAEs with $EW_0(\mathrm{Ly}\alpha) \geq$ 20–30 Å and intrinsically unselected sources passing the selection (i.e., (iv), (v) and (vi)). We find that the contamination fraction at $NB387 \leq 25.5$ is 10–20% for all four fields. This contamination fraction is conservative in the sense that (v) real LAEs with $EW_0(\mathrm{Ly}\alpha) \leq$ 20–30 Å are categorized as intrinsically unselected sources, whose fraction is expected to be significantly higher than that of (iv).

To summarize, the fractions of possible interlopers (i), (ii), and (iii) are negligibly small and those of (iv), (v), and (vi) are estimated to be 10–20% in total for all four fields.

Spectroscopic follow-up observations of Lyα emission of bright LAEs in our sample ($NB387 \leq 24.5$ mag) have also been carried out with Magellan/IMACS, MagE, and Keck/LRIS by Nakajima et al. (2012), Hashimoto et al. (2013), Shibuya et al. (2014b), Hashimoto et al. (2015), Hashimoto et al. (2017a), and M. Rauch et al. (2019, in preparation). In total, more than 40 LAEs are spectroscopically confirmed and no foreground interlopers such as [OII] emitters at $z = 0.04$ are found (Nakajima et al., 2012). Although faint LAEs cannot be confirmed spectroscopically, the contamination fraction is probably not high. Indeed, Konno et al. (2016) have not applied contamination correction in deriving luminosity functions. On the basis of the results of the Monte Carlo simulations and the spectroscopic follow-up observations, 0–20%, we conservatively adopt 10 ± 10% for the contamination fraction. This value is similar to a previous result for NB-selected LAEs at $z \sim 2$, 7 ± 7%, which is a sum of (i), (ii), (iii) and (vi) (Guaita et al., 2010). The effect of contamination sources is taken into account in clustering analysis (in section 4.1). On the other hand, it is negligible in SED fitting for median-stacked (sub)samples (in sections 3.1 and 3.2).

2.3 Imaging data and catalogs

We describe the data and catalogs used in the IR study and SED fitting below.

2.3.1 The data used in the IR study

We study on the infrared luminosity of LAEs with the LAE subsample in CDFS field in section 6.1. We use the deep Spitzer/MIPS 24 μm data from the GOODS survey (Magnelli et al., 2011) and Herschel/PACS/70 μm, 100 μm, and 160 μm data from the PEP (Lutz et al., 2011) and GOODS-Herschel (Elbaz et al., 2011) surveys (Magnelli et al., 2013). The FWHM of the PSF of the MIPS/24 μm band are $5''.9$, while those of PACS/70 μm, 100 μm, and 160 μ are $4''.7$, $6''.7$, and $11''$. The aperture radius and the aperture correction factor for the MIPS/24 μm band are $3''.0$ and 2.87, respectively. The aperture radius of PACS/70 μm, 100 μm, and 160 μ are $3''.2$, $4''.5$, and $7''.4$ with an aperture correction factor of 2.45, 1.96, and 1.92, respectively. We also use catalogs of the MIPS[*3] and the

[*3] http://irsa.ipac.caltech.edu/cgi-bin/Gator/nph-scan?mission=irsa&submit=Select&projshort=SPITZER

PACS (Magnelli et al., 2013) to find counterparts of the LAEs in section 6.1.1.

2.3.2 The data used in SED fitting for the IR-study sample

We perform SED fitting for our LAEs within the coverage of deep HST images from the GOODS and CANDELS surveys (in CDFS field). The images used for stacking are: the WFI B (Hildebrandt et al., 2006), the HST/ACS F606W, F775W, F850LP (Giavalisco et al., 2004)[*4], the HST/WFC3 F125W, F140W, F160W (Grogin et al., 2011; Koekemoer et al., 2011; Brammer et al., 2012; Skelton et al., 2014), and the Spitzer/IRAC 3.6 μm, 4.5 μm, 5.8 μm, 8.0 μm (Damen et al., 2011). The aperture radius and the aperture correction for the B band are $1''.0$ and 0.147 mag, respectively, following Ono et al. (2010a). The aperture radius for IRAC bands are $1''.5$ with the aperture correction of 0.52, 0.55, 0.74, and 0.86 mag for ch1 to ch4, respectively, which are given by MUltiwavelength Survey by Yale-Chile[*5] (MUSYC: Taylor et al., 2009; Cardamone et al., 2010). The aperture radius for the ACS/WFC images is set to $0''.9$ with an aperture correction of 0.029 mag (Skelton et al., 2014).

2.3.3 The data used in SED fitting for the sample with $NB387_{\rm tot} \leq 25.5$ mag

We use ten broadband images for SED fitting of our LAEs with $NB387_{\rm tot} \leq 25.5$ mag: five optical bands – B, V, R (or r), i (or i') and z (or z'); three NIR bands – J, H and K (or Ks); and two mid-infrared (MIR) bands – IRAC ch1 and ch2. The PSFs of the images are matched in each field (not in each sub-field). The aperture corrections for converting $3''$ MIR aperture magnitudes to total magnitudes are taken from Ono et al. (2010a, see tables 2.1–2.4). For each field, a K-band or NIR detected catalog is used to obtain secure IRAC photometry in section 3.2.2. To derive the stellar parameters of the LAE subsamples accurately for the study on the origin of LAH, we use the latest released data of NIR imaging (Kusakabe et al., 2018a), while we use the other version of NIR imaging data for the study on the star forming activity (Kusakabe et al., 2018b). Here we summarize the data used in SED fitting and IRAC cleaning in the four fields. The FWHM of the PSF, aperture diameters, and aperture corrections are summarized in tables 2.1–2.4.

SXDS field

The images used for SED fitting are as follows: B, V, R, i', and z' images with Subaru/Suprime-Cam from the Subaru/XMM-Newton Deep Survey project (Furusawa et al., 2008, SXDS); J, H, and K images from the data release 8 or 11 of the UKIRT/WFCAM UKIDSS/UDS project (Lawrence et al., 2007, Almaini et al. in prep.); Spitzer/IRAC 3.6 μm (ch1) and 4.5 μm (ch2) images from the Spitzer Large Area Survey with Hyper-Suprime-Cam (SPLASH) project (SPLASH: PI: P. Capak; Mehta et al., 2018). We use the latest release data of J, H, and K images, the data release 11 for the

[*4] The F450W image is not used because it is contaminated by Lyα emission at $z \simeq 2.18$.
[*5] http://data.spitzer.caltech.edu/popular/simple/20070601_enhanced/doc/00README_photometry

Table 2.1 Details of the data in SXDS field.

band	SXDS ($\sim 1240\,\mathrm{arcmin}^2$)			
	PSF ($''$)	aperture diameter ($''$)	aperture correction (mag)	5σ limit (mag)
	(1)	(2)	(3)	(4)
$NB387$	0.88	2.0	0.17	25.7
B	0.84	2.0	0.17	27.5–27.8
V	0.8	2.0	0.15	27.1–27.2
R	0.82	2.0	0.16	27.0–27.2
i'	0.8	2.0	0.16	26.9–27.1
z'	0.81	2.0	0.16	25.8 – 26.1
$J^{(a)}$	0.85	2.0	0.15	24.9
$H^{(a)}$	0.85	2.0	0.15	24.2
$K^{(a)}$	0.85	2.0	0.16	24.6
$J^{(b)}$	0.85	2.0	0.15	25.6
$H^{(b)}$	0.85	2.0	0.15	25.1
$K^{(b)}$	0.85	2.0	0.16	25.3
IRAC ch1	1.7	3.0	0.52	$24.9^{(c)}$
IRAC ch2	1.7	3.0	0.55	$24.9^{(c)}$

Note. — (1) The FWHM of the PSF, (2) aperture diameter in photometry, (3) aperture correction, and (4) 5σ limiting magnitude with a $2''$ diameter aperture are shown for each band. Values in parentheses show the area used in clustering analysis. (a) We use these data (release 8) for SED fitting of the whole sample. (*b*) We use these data (release 11) for SED fitting of the subdivided sample. (*c*) The limiting magnitude measured in areas with no sources (see Mehta et al., 2018).

LAE subsamples (Kusakabe et al., 2018a), while we use those of the the data release 8 for the whole sample (Kusakabe et al., 2018b). All images are publicly available except the SPLASH data. The aperture corrections for optical and NIR images are given in Nakajima et al. (2013). The catalog used to clean IRAC photometry (in section 3.2.2) is constructed from the K-band image of the UKIDSS/UDS data release 11 (Almaini et al. in prep.)

COSMOS field

We use the publicly available B, V, r', i', and z' images with Subaru/Suprime-Cam by the Cosmic Evolution Survey (COSMOS: Capak et al., 2007; Taniguchi et al., 2007) and J, H, and Ks images with the VISTA/VIRCAM from the first or third data release of the UltraVISTA survey (McCracken et al., 2012). We use the third data release of J, H, and Ks images for the LAE subsamples (Kusakabe et al., 2018a), while we use those of the the first release for the whole sample (Kusakabe et al., 2018b). We also use Spitzer/IRAC ch1 and ch2 images from the SPLASH project. The aperture corrections for the optical images are derived in Nakajima et al. (2013) and those for the NIR images

Table 2.2 Details of the data in COSMOS field.

band	COSMOS ($\sim 740\,\mathrm{arcmin}^2$) PSF ($''$) (1)	aperture diameter ($''$) (2)	aperture correction (mag) (3)	5σ limit (mag) (4)
$NB387$	0.95	2.0	0.25	26.1
B	0.95	2.0	0.12	27.5
V	1.32	2.0	0.33	26.8
r'	1.04	2.0	0.19	26.8
i'	0.95	2.0	0.12	26.3
z'	1.14	2.0	0.25	25.4
$J^{(a)}$	0.79	2.0	0.3	24.7
$H^{(a)}$	0.76	2.0	0.2	23.9
$Ks^{(a)}$	0.75	2.0	0.2	23.7
$J^{(b)}$	0.79	2.0	0.3	24.6–24.8
$H^{(b)}$	0.76	2.0	0.2	24.3–24.4
$Ks^{(b)}$	0.75	2.0	0.2	23.9–24.6
IRAC ch1	1.7	3.0	0.52	$25.4^{(c)}$
IRAC ch2	1.7	3.0	0.55	$25.1^{(c)}$

Note. — (1) The FWHM of the PSF, (2) aperture diameter in photometry, (3) aperture correction, and (4) 5σ limiting magnitude with a $2''$ diameter aperture are shown for each band. Values in parentheses show the area used in clustering analysis. (a) We use these data (the first releas) for SED fitting of the whole sample. (*b*) We use these data (the third release) for SED fitting of the subdivided sample. (c) The limiting magnitude measured in areas with no sources (see Laigle et al., 2016).

follow McCracken et al. (2012). The catalog used to clean IRAC photometry (in section 3.2.2) is from Laigle et al. (2016), for which sources have been detected in the $z'YJHKs$ images.

HDFN field

The images used for SED fitting are: B, V, R, I, and z' images with Subaru/Suprime-Cam from the Hubble Deep Field North Survey (HDFN: Capak et al., 2004); J (Lin et al., 2012), H (Hsu et al., 2019), and Ks (Wang et al., 2010) images with CFHT/WIRCAm (PI of the J & H imaging observations: L. Lin); Spitzer/IRAC ch1 and ch2 images from the Spitzer Extended Deep Survey (SEDS: Ashby et al., 2013). We use reduced J-band and Ks-band images given in Lin et al. (2012). All images are publicly available. The aperture corrections for the optical images are given in Nakajima et al. (2013). Those of the NIR images with a $2''$ radius aperture are evaluated using bright and isolated point sources in each band. We measure fluxes for 20 bright point sources in a series of apertures from $2''$ with an interval of $0''.1$ and find that the fluxes level off for $> 7''.8$ apertures. We measure the difference in magnitude between the $2''$ and $7''.8$ apertures of 100 bright

Table 2.3 Details of the data in HDFN field.

band	HDFN ($\sim 780\,\mathrm{arcmin}^2$)			
	PSF ($''$)	aperture diameter ($''$)	aperture correction (mag)	5σ limit (mag)
	(1)	(2)	(3)	(4)
$NB387$	0.89	2.0	0.14	26.5
B	0.77	2.0	0.15	26.3
V	1.24	2.0	0.20	25.7
R	1.18	2.0	0.22	26.0
I	0.80	2.0	0.13	25.2
z'	0.81	2.0	0.15	24.9
J	0.84	2.0	0.17	24.7
H	0.84	2.0	0.17	24.2
Ks	0.84	2.0	0.18	24.4
IRAC ch1	1.7	3.0	0.52	$\sim$25
IRAC ch2	1.7	3.0	0.55	$\sim$25

Note. — (1) The FWHM of the PSF, (2) aperture diameter in photometry, (3) aperture correction, and (4) 5σ limiting magnitude with a $2''$ diameter aperture are shown for each band. Values in parentheses show the area used in clustering analysis.

and isolated sources and perform Gaussian fitting to the histogram of differences. We adopt the best-fit mean as the aperture correction term. The catalog used to clean IRAC photometry (in section 3.2.2) is constructed from the K-band image (Wang et al., 2010). As we described in section 2.1.5, the V-band and R-band images are not deep enough to derive the UV slope for faint LAEs individually to dived them into subsamples.

CDFS field

We use the publicly available B, V,R, and I images with the MPG 2.2m telescope/WFI by the Garching-Bonn Deep Survey (GaBoDS: Hildebrandt et al., 2006; Cardamone et al., 2010), the z image with the CTIO 4m Blanco telescope/Mosaic-II camera from the MUSYC survey (Taylor et al., 2009; Cardamone et al., 2010), the H image with the ESO-NTT telescope/SofI camera by the MUSYC (Moy et al., 2003; Cardamone et al., 2010), and the J and Ks images by the Taiwan ECDFS Near-Infrared Survey (TENIS: Hsieh et al., 2012). We also use the Spitzer/IRAC ch1 and ch2 images from the Spitzer IRAC/MUSYC Public Legacy Survey in the Extended CDF-South (SIMPLE: Damen et al., 2011). The aperture corrections for optical and NIR photometry are derived in a similar manner to those in HDFN. The catalog used to clean IRAC photometry (in section 3.2.2) is from Hsieh et al. (2012), for which sources have been detected in the J image. As we described in section 2.1.5, the i, z, and H data are too shallow to perform reliable SED fitting for subsamples.

Table 2.4 Details of the data in CDFS field.

band	CDFS ($\sim 580\,\mathrm{arcmin}^2$) PSF ($''$) (1)	aperture diameter ($''$) (2)	aperture correction (mag) (3)	5σ limit (mag) (4)
$NB387$	0.85	2.0	0.13	26.4
B	1.0	2.0	0.20	26.5
V	0.94	2.0	0.18	26.3
R	0.83	2.0	0.16	26.4
I	0.95	2.0	0.22	24.3
z	1.1	2.0	0.24	23.7
J	0.70	2.0	0.18	25.3
H	1.5	2.0	0.55	22.5
Ks	0.70	2.0	0.18	25.3
IRAC ch1	1.7	3.0	0.52	23.8
IRAC ch2	1.7	3.0	0.55	23.6

Note. — (1) The FWHM of the PSF, (2) aperture diameter in photometry, (3) aperture correction, and (4) 5σ limiting magnitude with a $2''$ diameter aperture are shown for each band. Values in parentheses show the area used in clustering analysis.

2.4 Subsamples divided by $NB387$ magnitude

The distribution of $B - NB387$ as a function of total $NB387$ magnitude, $NB387_{\mathrm{tot}}$, is shown in figure 2.2. To examine the dependence of halo mass on the total $NB387$ magnitude, we divide our LAE sample of each field in up to five cumulative subsamples with different limiting magnitudes, as shown in table 2.5 and figure 2.2. There are 1937 LAEs with $NB387_{\mathrm{tot}} \leq 26.3$ mag used in the clustering analysis.

Table 2.5 Number of objects in each subsample.

	$NB387_{\mathrm{tot}}$ magnitude limit (mag)				
Field	25.0	25.3	25.5	25.8	26.3
SXDS	161	368	601 (93)	-	-
COSMOS	119	205	297 (21)	526	-
HDFN	119	200	299 (56)	588	-
CDFS	27	41	51 (4)	92	222
Total	426	814	1248 (174)	1206	

Note. — The value in parentheses shows the number of objects used for SED fitting.

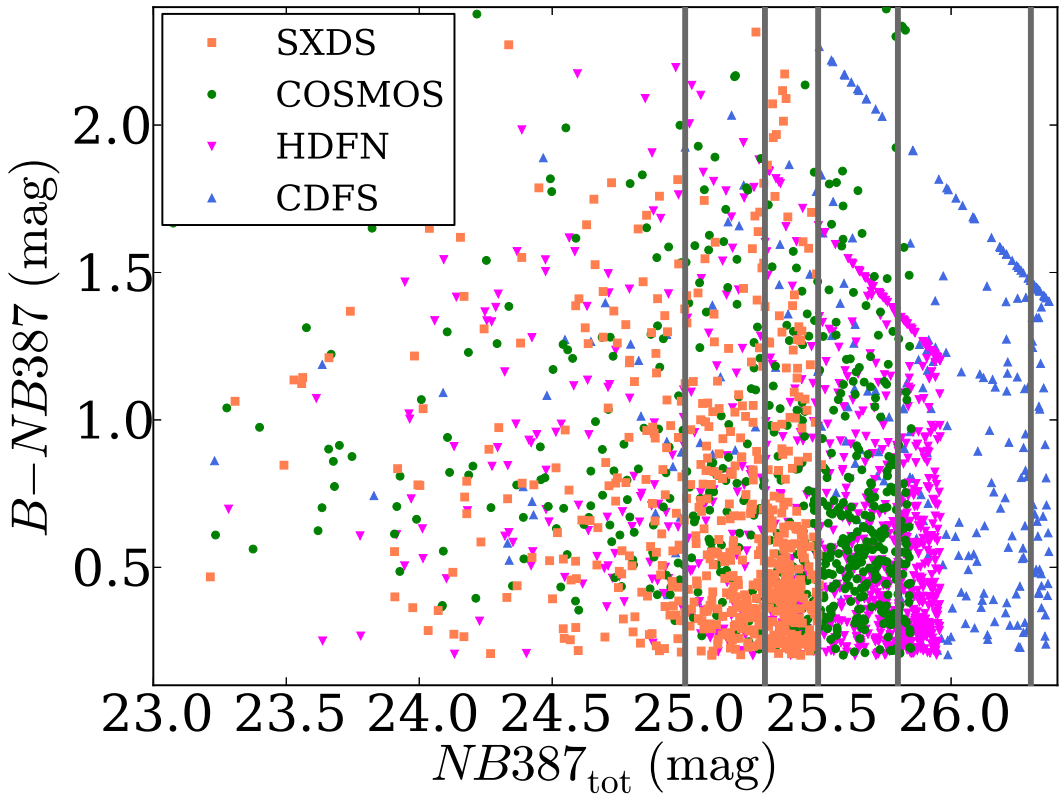

Figure 2.2 $B-NB387$ ($NB387$ excess) plotted against $NB387$ total magnitude. Orange, green, magenta, and blue points show LAEs in SXDS, COSMOS, HDFN, and CDFS, respectively. LAEs are divided into cumulative subsamples with different limiting magnitudes shown by gray solid lines: $NB387_{\rm tot} \leq$ 25.0 mag, 25.3 mag, 25.5 mag, 25.8 mag, and 26.3 mag.

2.5 Subsamples divided by UV, Lyα and K–band properties

A vast majority of our LAEs are too faint to estimate stellar masses on individual basis. To study how LAH luminosity depends on stellar and dark matter halo masses, we therefore divide the entire sample into subsamples in accordance with the following five quantities which are expected to correlate with stellar mass, and perform a stacking analysis on each subsample. (i) K-band apparent magnitude, $m_{\rm K}$, known as a good tracer of stellar mass (e.g., Daddi et al., 2004). (ii) Rest-frame UV absolute magnitude, $M_{\rm UV}$, which is related to SFR and hence expected to trace stellar mass through the star formation main sequence (e.g., Speagle et al., 2014). (iii) UV spectral slope β ($f_\lambda \propto \lambda^\beta$), an indicator of dust attenuation and may correlate with stellar mass (e.g., Reddy et al., 2010). (iv) Lyα luminosity L(Lyα) and (v) rest-frame Lyα equivalent width EW_0(Lyα), both of which possibly anti-correlate with stellar mass according to Ando relation (Ando et al., 2006, 2007, see also Shimakawa et al. 2017).

While only 30–40% of our LAEs are detected in the K band with $m_{\rm K} \lesssim 25.0$ (see section 2.5.2), the other four quantities can be measured for almost all objects because they need only optical imaging data, which are deep enough as shown in tables 2.1 and 2.2. We divide the whole sample of each field into two subsamples in accordance with each of $m_{\rm K}$, $M_{\rm UV}$, β, $L({\rm Ly}\alpha)$, and $EW_0({\rm Ly}\alpha)$; further division makes stacked SEDs too noisy to do reliable SED fitting. Among the five quantities, m_K and $M_{\rm UV}$ are expected to correlate with $M_\star$ most tightly. The subsamples by β, $L({\rm Ly}\alpha)$, and $EW_0({\rm Ly}\alpha)$ are useful to check the results obtained for the m_K and $M_{\rm UV}$ subsamples, because these three quantities are affected by the NB selection bias differently from m_K and $M_{\rm UV}$ as discussed in appendix C.1 (see figure 2.3). As shown later, all five subsample pairs give similar results.

2.5.1 UV and Lyα properties

For each object, we measure $M_{\rm UV}, \beta, L({\rm Ly}\alpha)$, and $EW_0({\rm Ly}\alpha)$ from $NB387$, B, V, and R magnitudes in the following manner. First, we approximate the UV SED of the object by a simple SED composed of a power-law continuum and a Lyα line centered at rest-frame 1216 Å:

$$f_\nu({\rm erg\,s^{-1}\,cm^{-2}\,Hz^{-1}}) = A\,10^{-0.4(m_{{\rm UV}(1+z)}+48.60)} \left(\frac{\nu_{\lambda=UV(1+z)}}{\nu}\right)^{\beta+2} + F_{{\rm Ly}\alpha}\,\delta(\nu-\nu_{\lambda=1216(1+z)}), \tag{2.1}$$

where A, $m_{{\rm UV(1+z)}}$, and $F_{{\rm Ly}\alpha}$ are the IGM attenuation factor from Madau (1995), the apparent UV magnitude (corresponding to $M_{\rm UV}$), and the Lyα flux (erg s^{-1} cm^{-2}), respectively. The apparent magnitude of the model SED in a given band i is calculated from its transfer function $T_i(\lambda)$ as below:

$$m_{i,model} = -2.5\log_{10}\left(\frac{\int f_\nu c/\lambda^2 T_i(\lambda)d\lambda}{\int c/\lambda^2 T_i(\lambda)d\lambda}\right) - 48.6, \tag{2.2}$$

where c is the speed of light.

We fit this model SED to the apparent magnitudes of the object with $M_{\rm UV}$, β, and $F_{{\rm Ly}\alpha}$ as free parameters. We search for the best-fit parameter values that minimize

$$\chi^2 = \Sigma_{i=NB,B,V,R}\left(\frac{m_i - m_{i,model}}{\sigma m_i}\right)^2, \tag{2.3}$$

where m_i and σm_i are the i-th band apparent magnitude and its 1 σ error, respectively. We calculate apparent magnitudes from 2″ diameter aperture magnitudes assuming that our LAEs are point sources in all four bands including $NB387$ which detects Lyα emission. We also assume that their Lyα lines are located at the peak of the response function of $NB387$ and do not correct for flux loss. The best-fit $F_{{\rm Ly}\alpha}$ is obtained by solving $\frac{\partial\chi^2}{\partial F_{{\rm Ly}\alpha}} = 0$. Hereafter, we refer to the $L({\rm Ly}\alpha)$ and $EW_0({\rm Ly}\alpha)$ obtained with the assumption of point sources as $L({\rm Ly}\alpha)_{ps}$ and $EW_{0,ps}({\rm Ly}\alpha)$. Since the best-fit $EW_0({\rm Ly}\alpha)$ is derived from the other three parameters, the degree of freedom is one.

Among the 897 LAEs, six sources are undetected in at least one of the three broad bands. We do not use these objects in the following analyses because the four quantities derived from the SED fitting are highly uncertain.

2.5.2 Subsample construction

Since we divide LAEs into two subsamples in accordance with each of the five quantities, we have a total of ten subsamples for each field. The boundaries of the subsamples are defined from the distribution of the five quantities, which is shown in figure 2.3.

Our LAEs are widely distributed over the four UV and Lyα properties as shown in panels (a) – (d) of this figure. The distribution of $M_{\rm UV}$, β, $L({\rm Ly}\alpha)_{ps}$, and $EW_{0,ps}({\rm Ly}\alpha)$ is different between the two fields. This is possibly because of systematic offsets of the zero-point magnitudes (ZPs) of the optical images adopted in the original papers[*6] as discussed in Yagi et al. (2013) and Skelton et al. (2014). However, these two papers often claim opposite error directions (see section 3.2.3 for more details). Another possible reason for the different distribution is field-to-field variance from large scale structure (cosmic variance). In this thesis, we use the original ZPs and include ZP uncertainties in the flux-density errors in the calculations given in sections 2.5.1 and 3.2.3. Although the causes of the different distributions and the correct ZPs remain to be unclear, a pair of subsamples (with the same definition) from the two fields give consistent SED fitting results and Lyα luminosities in most cases (see figure 6.7, figure 6.9, and table 6.6).

We define the boundary for the four UV and Lyα quantities so that the two subsamples have roughly comparable sizes:

$$M_{\rm UV} = -19.2\,{\rm mag}, \tag{2.4}$$

$$\beta = -1.6, \tag{2.5}$$

$$L({\rm Ly}\alpha)_{ps} = 1.2 \times 10^{42}\,{\rm erg\,s^{-1}}, \tag{2.6}$$

and

$$EW_{0,ps}({\rm Ly}\alpha) = 34\,{\rm \AA} \tag{2.7}$$

as indicated by black lines in figures 2.3 (a) – (d). The numbers of the LAEs in the eight subsamples are shown in table 2.6.

For each field, we also construct two subsamples divided by $m_{\rm K}$. The K-band catalog mentioned in section 2.3.3 effectively include sources with $m_{\rm K} \lesssim 25$ mag. Indeed, the 5σ limiting magnitude of the SXDS K-band image is 25.3 mag and the detection image for the COSMOS catalog, a combined $z'YJHKs$ image, reaches deeper than 25.3 mag (5σ). As a result, about 30–40% of the LAEs in each field have a K-band counterpart with $m_{\rm K} < 25.0$ as shown in panel (e). Therefore, we define the K-magnitude boundary as:

$$m_{\rm K} = 25.0\,{\rm mag}. \tag{2.8}$$

[*6] ZP offsets of optical broad bands can shift the relation between $M_{\rm UV}$ and β (figure 2.3 [f]). They have a larger effect on smaller-$EW_{0,ps}({\rm Ly}\alpha)$ objects in the $EW_{0,ps}({\rm Ly}\alpha)$ vs. $M_{\rm UV}$ plot (figure 2.3 [e]), since the contribution of the UV continuum flux in $NB387$ is larger for such objects. Because of the NB-selection bias (see also appendix C.1), small-$EW_{0,ps}({\rm Ly}\alpha)$ objects tend to have bright $M_{\rm UV}$.

Table 2.6 Subsample definition.

subsample	criteria	COSMOS	SXDS	total
bright UV (MuvB)	$M_{UV} \leq -19.2\,\mathrm{mag}$	123 (123, 9)	293 (257, 52)	416 (380, 61)
faint UV (MuvF)	$M_{UV} > -19.2\,\mathrm{mag}$	173 (173, 13)	302 (257, 47)	475 (430, 60)
blue β (betaB)	$\beta \leq -1.6$	80 (80, 5)	389 (334, 74)	469 (414, 79)
red β (betaR)	$\beta > -1.6$	216 (216, 17)	206 (180, 25)	422 (396, 42)
bright Lyα (lyaB)	$L(\mathrm{Ly}\alpha)_{ps} \geq 1.2 \times 10^{42}\,\mathrm{erg\,s^{-1}}$	211 (211, 14)	236 (218, 41)	447 (429, 55)
faint Lyα (lyaF)	$L(\mathrm{Ly}\alpha)_{ps} < 1.2 \times 10^{42}\,\mathrm{erg\,s^{-1}}$	85 (85, 8)	359 (296, 58)	444 (381, 66)
large EW (ewL)	$EW_{0,\,ps}(\mathrm{Ly}\alpha) \geq 34\,\text{Å}$	222 (222, 16)	228 (205, 35)	450 (427, 51)
small EW (ewS)	$EW_{0,\,ps}(\mathrm{Ly}\alpha) < 34\,\text{Å}$	74 (74, 6)	367 (309, 64)	441 (383, 70)
bright K (KB)	$m_{\mathrm{K}} \leq 25\,\mathrm{mag}$	112 (112, 11)	178 (177, 35)	290 (144, 46)
faint K (KF)	$m_{\mathrm{K}} > 25\,\mathrm{mag}$	184 (184, 11)	417 (337, 64)	601 (236, 75)

Note. — The selection criterion and the numbers of objects for each subsample. The number outside the bracket indicates the number of objects for clustering analysis, while the numbers in the bracket are for SED fitting: the left one corresponds to objects with UV to NIR photometry and the right one to those with clean ch1 and ch2 photometry.

Note that the COSMOS K image is composed of Deep and Ultradeep stripes. Since this could add an artificial pattern in the sky distribution of K-divided subsamples, we do not use the K-divided subsamples for clustering analysis.

We derive the four UV and Lyα quantities for each subsample from a median-stacked SED (see section 3.2.3) in the same manner as in section 2.5.1. We then calculate average values over the two field, e.g., the average M_{UV} of the two faint-M_{UV} subsamples, as shown by red symbols in panels (f) – (k). They are located in the middle of the distribution of individual sources (orange and green points), implying that the average SEDs of the subsamples represent well individual LAEs. We find that the subsamples with red β, faint $L(\mathrm{Ly}\alpha)_{ps}$, small $EW_{0,ps}(\mathrm{Ly}\alpha)$, and bright m_{K} as well as bright M_{UV} have bright M_{UV} as shown by red open symbols. Note that the lower left part in panels (g) and (h) and the upper left part in panel (k) show a selection bias: LAEs with faint M_{UV} can be detected only if they have bright $L(\mathrm{Ly}\alpha)_{ps}$.

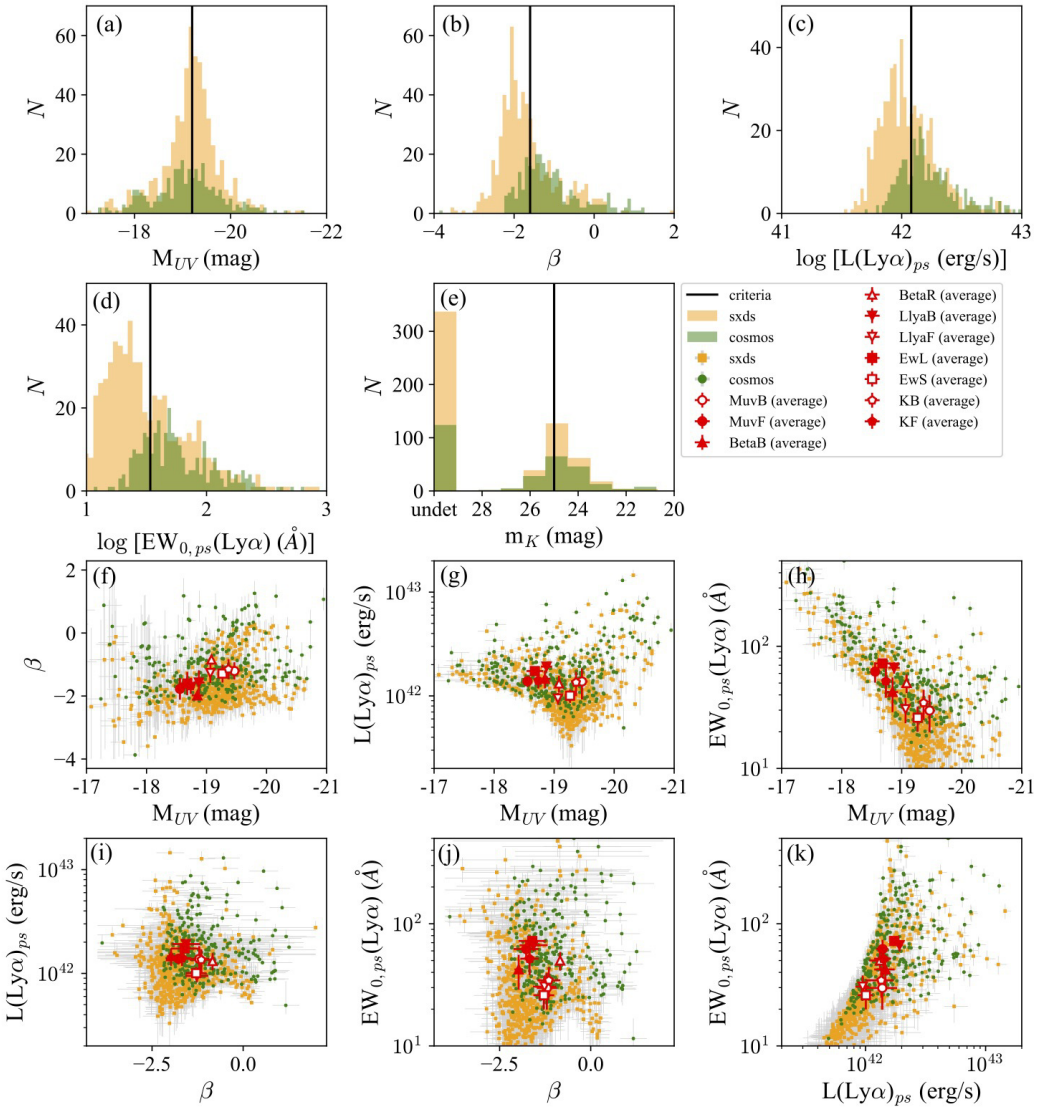

Figure 2.3 The distribution of the five quantities used to divide our LAEs into subsamples. Panels (a) – (e) show histograms: (a) $M_{\rm UV}$, (b) β, (c) $L({\rm Ly}\alpha)_{ps}$, (d) $EW_{0,ps}({\rm Ly}\alpha)$, and (e) $m_{\rm K}$, with orange and green colors corresponding to SXDS and COSMOS fields, respectively. Black lines indicate the boundaries of the two subsamples. Panels (f) – (k) are scatter plots: (f) β vs. $M_{\rm UV}$, (g) $L({\rm Ly}\alpha)_{ps}$ vs. $M_{\rm UV}$, (h) $EW_{0,ps}({\rm Ly}\alpha)$ vs. $M_{\rm UV}$, (i) $L({\rm Ly}\alpha)_{ps}$ vs. β, (j) $EW_{0,ps}({\rm Ly}\alpha)$ vs. β, and (k) $EW_{0,ps}({\rm Ly}\alpha)$ vs. $L({\rm Ly}\alpha)_{ps}$, with the same color coding as panels (a)–(d). Red symbols represent averages over the two fields, where different symbols correspond to different classifications: open (filled) circles for bright (faint) $M_{\rm UV}$, open (filled) triangles for red (blue) β, open (filled) inverted triangles for faint (bright) $L({\rm Ly}\alpha)_{ps}$, open (filled) squares for large (small) EW, and open (filled) pentagons for bright (faint) $m_{\rm K}$.

Chapter 3

SED fitting

We derive parameters that characterize the stellar populations of our LAEs by fitting SEDs based on stacked multi-band images. We only use some parts of the entire sample that have data in ten or eleven broadband filters in rest-frame UV, optical, and NIR and are not contaminated by other objects in the IRAC images to obtain secure IRAC photometry. Recently, some prescriptions are adopted in previous studies (e.g., Guaita et al., 2011; Vargas et al., 2014; Malkan et al., 2017). We also have been developing methods that are suitable for our faint objects as described in sections 3.1.1 and 3.2.2.

The procedure for photometry of the IR-study sample in CDFS field, and the other (sub)samples are described in sections 3.1 and 3.2, respectively. In section 3.3, SED models and fitting methods are described. Below we adopt a dust attenuation curve according to the results of IR study shown in chapter 6.1.

3.1 Photometry for the IR-study sample in CDFS field with HST data

3.1.1 Stacking analysis

As we described in section 2.1.4, $\sim 44\%$ of our LAEs are within the coverage of deep HST images from the GOODS and CANDELS surveys. We only use 52 LAEs that are not uncontaminated by other objects in the IRAC images since the IRAC images have much worse spatial resolutions compared with the other band images [*7].

Images of size $50'' \times 50''$ are cut out at the position of HST/ACS F606W counterparts of the LAEs with IRAF/imcopy task in each of the Subaru/$NB387$, WFI/B, HST/ACS F606W, F775W, F850LP, the HST/WFC3 F125W, F140W, F160W, and the Spitzer/IRAC ch1, ch2, ch3, ch4 bands. We use the task IRAF/imcombine to create a HST F606W-centered, median-stacked image (i.e., image-stacked) from optical to MIR

[*7] We match our LAEs with objects in a source lists of IRAC images and perform a visual inspection. We do not adopt a detailed method described in section 3.2.2. We discuss the IRX at a fixed $M_\star$ and star formation mode of our LAEs based on the results with the detailed methods and compare it with the results with the simple IRAC-clean method here in chapter 6 .

Table 3.1 Broadband photometry from optical to MIR for the stacked IR sample in CDFS field.

B	$F606W$	$F775W$	$F850LP$	$F125W$	$F140W$	$F160W$	[3.6]	[4.5]	[5.8]	[8.0]
0.092	0.11	0.12	0.15	0.21	0.25	0.26	0.24	0.18	0.13	0.09
(0.007)	(0.005)	(0.008)	(0.01)	(0.01)	(0.03)	(0.02)	(0.05)	(0.05)	(0.2)	(0.1)

Note. — All flux densities are total flux densities in μJy with 1σ errors shown in parentheses. The SED of the stacked IR sample is shown in figure 6.2.

wavelengths. While a stacked SED is not necessarily a good representation of individual objects (Vargas et al., 2014), stacking is still useful for our faint objects to obtain an SED covering rest-frame $\sim$ 1000–10000 Å. Note that $NB387$ flux is not included in our SED fitting.

3.1.2 Photometry

An aperture flux is measured for each stacked image using the task PyRAF/phot. We use an aperture radius of $1''$ for the $NB387$ and B, and $1''.5$ for IRAC ch1 to ch4, which are determined following the procedure of Ono et al. (2010a). We set it to $0''.9$ for the ACS/WFC images (Skelton et al., 2014). We use the original zero-point magnitudes (ZP) from references given in Section 2.3.2. All aperture magnitudes are corrected for Galactic extinction, E(B − V) of 0.008 (in CDFS field, Schlegel et al., 1998). The aperture magnitudes are then converted into total magnitudes using the aperture correction values summarized in section 2.3.2.

The errors are a quadratic sum of the photometric error and error in zero point. To measure a photometric error in each stacked image, we randomly distribute 15,000 apertures of a given size and use them to make a histogram of sky noise. We then fit the negative part of the histogram with a Gaussian, whose standard deviation (σ) is used to estimate the photometric errors. As the negative part is not easy to define, the fitting range is set from 53.5% to 53.5%, 58.5%, 63.5%, 68.5%, 73.5%, 78.5%, 83.5%, and 88.5% of the sky noise histograms from the small value side. For these eight ranges, the best fit Gaussian σ is obtained analytically using the least-squares-fit with weights derived from poisson errors for individual bins. Finally, we check the eight best fits and choose one conservatively as its photometric error. We adopt 0.05 mag as the ZP error for $NB387$ and B (typical value for ground-based $NB397$, and optical bands; Nakajima et al., 2012) as well as IRAC bands. It is notable that the dominant uncertainties in IRAC bands are photometric errors. Table 3.1 shows the total flux densities of the stacked SED and its 1σ uncertainties.

s

3.2 Photometry for the sample with $NB387_{\rm tot} \leq 25.5$ mag with ground-based telescope data

3.2.1 Samples

We derive parameters that characterize the stellar populations of LAEs in each of the four fields and subdivided LAEs in SXDS and COSMOS field by fitting SEDs based on stacked multiband ground-based images (see section 2.3). We adopt a threshold of $NB387_{\rm tot} \leq 25.5$ mag to LAEs in each of the four fields since it is the same as that adopted in the clustering analysis to determine the average halo masses. We only use 170 objects ($\sim 14\%$ of the entire sample, 1248) that have data in ten broadband filters (B, V, R, i, z, J, H, K, ch1, and ch2) and are not contaminated by other objects in the IRAC images (see table 2.5, Kusakabe et al., 2018b). Here we exclude LAEs that have either one or more neighbors or a high sky background through a two-step cleaning process. to obtain secure IRAC photometry.

With regard to subdivided LAEs (Kusakabe et al., 2018a), we use 810 LAEs ($\sim 91\%$ of the entire sample, 891) that have data in all ten broadband filters (B, V, R, i, z, J, H, K, ch1, and ch2). After adopting the two-step cleaning process for secure IRAC photometry, we are thus left with 121 LAEs for stacking of ch1 and ch2 images. For stacking of optical to NIR images, we also use objects with a close neighbor or at a high sky background in the IRAC image to earn a high signal to noise ratio. The procedure to select 'IRAC-clean' objects, to stack the images, and to measure flux are described in the following sections.

3.2.2 Selection of IRAC-clean objects

The IRAC images have lower spatial resolution (i.e., larger FWHMs of the PSF) compared with images in other bands. Moreover, they have large-scale residual backgrounds (contaminated sky regions) around bright objects and in crowded regions due to the extended profile of the IRAC PSF. Contamination by nearby objects and large-scale sky residuals can give significant systematic errors in the photometry of stacked images because our LAEs are expected to have very low stellar masses, or very faint IRAC magnitudes. To minimize such contamination, we select clean LAEs through a two-step process.

First, we exclude all LAEs which have one or more neighbors. Assuming that objects bright in IRAC are similarly bright in the K band, we exclude all LAEs that have one or more K-detected objects with a separation between $0''.85$ and $4''.5$; an object within $0''.85$ separation is considered to be the counterpart to the LAE conservatively (the typical separation is $\sim 0''.2$; see section 2.3.3 for the K-detected catalogs)[*8]. $4''.5$ is 2.5 times larger than the PSF size of IRAC ch1.

Second, we exclude all LAEs with a high sky background as determined in the following

[*8] $0''.85$ is the largest PSF FWHM among the K (or K_s) bands shown in tables 2.1 to 2.4.

manner. For each field, we randomly select 5,000 positions with no K-band objects within $4''.5$ (i.e., passing the first step) and measure the sky background in an annular region of $3''.5$ radius centered at these positions. We then make a histogram of the sky background values, which is skewed toward higher values because of contamination by bright or crowded objects outside of the $4''.5$ radius. We fit a Gaussian to the low-flux side (including the peak) of the histogram and obtain its average, μ_{rand}, which we consider to be the true sky background. If cutout images at all the random positions are median-stacked, its annular-region sky background will be brighter than μ_{rand}. A similar systematic sky-background difference will also be seen when all LAEs are stacked, possibly introducing some systematic errors in photometry. The sky background of the median-stacked random image becomes equal to μ_{rand} if positions whose sky background is higher than a certain threshold, sky_{thres}, are removed, where sky_{thres} can be determined so that the total number of the remaining positions (i.e., positions with faint sky background below sky_{thres}) is twice as large as the number of positions below μ_{rand}. Thus, we conservatively remove LAEs with a higher annular-region sky background than sky_{thres}, and are left with 93, 21, 56, and 4 IRAC-clean LAEs in SXDS, COSMOS, HSFN and CDFS, respectively. The stacked flux densities of the IRAC-clean LAEs in the B to K bands are mostly consistent with those of the all LAEs before cleaning.

3.2.3 Stacking analysis and photometry

We perform a stacking analysis for each subsample in almost the same manner as described in section 3.1.1 and as in Nakajima et al. (2012). Images of size $50'' \times 50''$ are cut out at the position of LAEs in the $NB387$ image with IRAF/imcopy task. For each of the B to K bands of SXDS field, PSFs are matched to the largest among the SXDS-Center, North, and South sub-fields using IRAF/gauss task (see table 2.1). We use the task IRAF/imcombine to create the median stacked broadband images at the $NB387$ source positions

An aperture flux is measured for each stacked image using the task PyRAF/phot. Following Ono et al. (2010a), we use an aperture diameter of $2''$ for the $NB387$, optical, and NIR band images and $3''$ for the MIR (IRAC) images. For the $NB387$- to K-band images, the inner radius of the annulus to measure the sky flux is set to twice the FWHM of the largest PSF among these images[*9], and the area of the annulus is set to five times larger than that of the aperture. For each of the ch1 and ch2 images, we obtain the net $3''$-aperture flux density of LAEs by subtracting the offset, between the annular-region and the $3''$-aperture flux densities of the stacked image of IRAC-clean random positions generated in the previous subsection, from the $3''$-aperture flux density of the LAE image (output of the PyRAF/phot task)[*10].

[*9] The PSF size of the CDFS H-band image is exceptionally large, and we determine the radius of the annulus for this image independently.

[*10] The sky background value on a $3''.5$-radius annulus placed at the image center is consistent between the stacked LAE images and the stacked images of IRAC-clean random positions. For stacked images of random positions, annular-region sky flux densities are brighter than aperture-region sky

We use the original zero-point (ZP) magnitudes from references given in section 2.3.3, although some previous work argues that some ZPs need to be corrected (e.g., Yagi et al., 2013; Skelton et al., 2014). The offset (correction) values given by Yagi et al. (2013) are opposite to those by Skelton et al. (2014) in optical bands in SXDS field (Furusawa et al., 2008). Moreover, the ZP corrections based on Yagi et al. (2013) make β redder, while those based on Skelton et al. (2014) make β bluer. Yagi et al. (2013) obtained the offset values using stars with SDSS photometry and this method seems to be reliable. On the other hand, Skelton et al. (2014) obtained the offset values by requiring that observed magnitudes of galaxies be consistent with magnitudes of their best-fit model SEDs. This method is indirect compared with that of Yagi et al. (2013) and thus may be less reliable. However, the values obtained by Skelton et al. (2014) are applied to all 3D-HST data including those in the four fields. Skelton et al. (2014) also argue that the ZP magnitudes of NIR and MIR images also need to be corrected. No work has checked the NIR and MIR image using stellar magnitudes. In this controversial situation, we adopt the original zero points for the optical images in this thesis. All aperture magnitudes are corrected for Galactic extinction, E(B − V), of 0.020, 0.018, 0.012, and 0.008 for SXDS, COSMOS, HDFN, and CDFS fields, respectively (Schlegel et al., 1998).

The aperture magnitudes are then converted into total magnitudes using the aperture correction values summarized in tables 2.1 – 2.4 in section 2.3.3. The 1σ uncertainty in the total magnitudes include photometric errors and errors in aperture correction and the ZP. For the ch1 and ch2 data, errors in sky subtraction, $\sim$ 0.02–0.17 mag, are also included. The photometric errors are determined by the same procedure described in section 3.1.2. The aperture correction errors in the $NB387$, optical, and NIR bands are estimated to be less than 0.03 mag, and those in the ch1 and ch2 bands are set to 0.05 mag. We adopt 0.1 mag as the ZP error for all bands, which is the typical value of the offsets of the images used in this paper (e.g., Yagi et al., 2013; Skelton et al., 2014) and is twice as large as those adopted in previous studies (e.g., Nakajima et al., 2012). The stacked SEDs thus obtained for (sub)samples are shown in figures 6.2, 6.3, A.3 and A.4.

3.3 SED models

We perform SED fitting on the stacked SEDs to derive stellar population parameters in a similar manner to Ono et al. (2010a). Nebular emission (lines and continuum) is added to the stellar population synthesis model of GALAXEV (Bruzual & Charlot, 2003) with constant star formation history (SFH) and $0.2Z_{\odot}$ stellar metallicity following previous SED studies of LAEs (Ono et al., 2010a; Vargas et al., 2014). We do not consider different kinds of SFH (like exponentially decreasing and rising SFH) and metallicity. The age of galaxies (defined since the onset of star formation) highly depends on SFH (e.g., see section 4.3 in de Barros et al., 2014), but it is not discussed as a key property of LAEs in this thesis. Color excess (or attenuation) depends on SFH. A decreasing SFH with an

flux densities with differences corresponding to $\sim$ 7–28% of the aperture fluxes of median-stacked LAEs.

old age (longer than the variable time scale of SF) gives lower attenuation than that with constant SFH, while a decreasing SFH with a younger age gives higher attenuation as well as a rising SFH (de Barros et al., 2014). However, as we will show in sections 6.2.1 and 6.4, the average attenuation of our LAEs derived with the assumption of constant SFH is consistent with that derived from IR and UV observations. Meanwhile, to first order, the current SFR (with time scales of ~ 100 Myr) and $M_\star$ are independent of SFH since SFR and $M_\star$ are determined only from rest-frame UV and NIR luminosities, respectively (e.g., see section 3.6.1 (figure 5) in Reddy et al., 2015). With regard to metallicity, it is found that our LAEs have $12 + \log \mathrm{O/H} \simeq 8.2 \pm 0.1$ (gas metallicity) in average from stacking analysis of spectroscopic data (Nakajima et al., 2012) and that our bright LAEs have $12 + \log \mathrm{O/H} \simeq 8.0 - 8.8$ from individual spectroscopic measurements (Nakajima & Ouchi, 2014). Since metallicity is not easily constrained by SED fitting of broadband photometry (e.g., de Barros et al., 2014), we adopt $0.2 Z_\odot$ stellar metallicity that is roughly consistent with their gas metallicity. We assume an SMC-like dust extinction model for the attenuation curve (hereafter an SMC-like attenuation curve; Gordon et al., 2003), which is suggested to be more appropriate for LAEs at $z \sim 2$ than the Calzetti curve (Calzetti et al., 2000) in section 6.1.6 (Kusakabe et al., 2015). It is also suggested for low-mass star forming galaxies at $z \geq 2$ in Reddy et al. (2018)[*11]. We also examine the case of the Calzetti attenuation curve for comparison (see section 6.2 and appendices A.1 and A.2). We also assume $\mathrm{E(B-V)}_{\mathrm{gas}} = \mathrm{E(B-V)}_\star$ (Erb et al., 2006), where $\mathrm{E(B-V)}_{\mathrm{gas}}$ and $\mathrm{E(B-V)}_\star$ are the color excess for the nebular gas component and the color excess for the stellar component, respectively. The Lyman continuum escape fraction, $f_{\mathrm{esc}}^{\mathrm{ion}}$, is fixed to 0.2 for sample with $NB387_{\mathrm{tot}} \leq 25.5$ mag and subsamples (in section 3.2) considering recent observations of $f_{\mathrm{esc}}^{\mathrm{ion}} \sim 0.1$–$0.3$ for $z \sim 3$ LAEs by Nestor et al. (2013). This means that 80% of ionizing photons produced are converted into nebular emission (see Ono et al., 2010a). We also perform SED fitting with models without nebular emission, $f_{\mathrm{esc}}^{\mathrm{ion}} = 1$, to examine to what extent $SFRs$ and $M_\star$ change in appendix A.1. For the IR-study sample with HST data in CDFS (in section 3.1), we include $f_{\mathrm{esc}}^{\mathrm{ion}}$ in free parameters to validate the effect of dust attenuation curves on $f_{\mathrm{esc}}^{\mathrm{ion}}$.

For each field's stacked SED, we search for the best-fitting model SED that minimizes χ^2 and derive the following stellar parameters: $M_\star$, $\mathrm{E(B-V)}_\star$ (or UV attenuation of A_{1600}), age, ($f_{\mathrm{esc}}^{\mathrm{ion}}$), and SFR. Stellar masses are calculated by solving $\frac{\partial \chi^2}{\partial M_\star} = 0$ since it is the amplitude of the model SED. SFR is not a free parameter in the fit but determined from $M_\star$ and age. The degree of freedom is 7 for each of the (sub)sample. The 1σ confidence interval in each stellar population parameter is obtained from the range of the values giving $\chi^2 \leq \chi^2_{\mathrm{min}} + 1$, where χ^2_{min} is the minimum χ^2 value.

In section 6.2.1, we show the results of SED fitting to the IR-study sample in CDFS field

[*11] While Hagen et al. (2017) have found that the SMC indeed has a flatter extinction curve in average than the classical (Pei, 1992; Gordon et al., 2003) curve, we adopt the classical curve which is consistent with recent observations of high-z galaxies including LAEs. Reddy et al. (2018) find that galaxies at $z = 1.5$–2.5 prefer an SMC-like attenuation curve combined with sub-solar metallicity stellar population models.

in table 6.1 and figure 6.2 and compare the results with an SMC-like attenuation curve and the Calzetti curve. The results of SED fitting to stacked LAEs with $NB387_{\rm tot} \leq 25.5$ mag in the four fields are shown in table 6.2 in section 6.2.2 (table A.1 in appendix A.1) and figure 6.3 (figure A.1 in appendix A.1) with the assumption of an SMC-like attenuation curve (the Calzetti curve). We also discuss the result with models without nebular emission, $f_{\rm esc}^{\rm ion} = 1$, in appendix A.1.2. With regard to subsamples in accordance with UV, Lyα, and K-band properties, the results of SED fitting in SXDS and COSMOS fields are shown in appendix A.2.

Chapter 4

Clustering analysis

We derive the angular two-point correlation functions (ACFs) of our (sub)samples from clustering analysis and convert the correlation lengths into the bias factors and then into the dark matter halo masses. The sky distributions of the LAEs in the four fields are shown in figure 4.1[*12]. We describe our methods below.

4.1 Angular correlation function

We measure the angular two-point correlation function (ACF), $\omega_{\rm obs}(\theta)$, for a given (sub) sample using the calculator given in Landy & Szalay (1993):

$$\omega_{\rm obs}(\theta) = \frac{DD(\theta) - 2DR(\theta) + RR(\theta)}{RR(\theta)}, \tag{4.1}$$

where DD(θ), RR(θ), and DR(θ) are the normalized numbers of galaxy-galaxy, galaxy-random, and random-random pairs, respectively:

$$DD(\theta) = \frac{2DD_0(\theta)}{N_{\rm D}(N_{\rm D}-1)}, \tag{4.2}$$

$$RR(\theta) = \frac{2RR_0(\theta)}{N_{\rm R}(N_{\rm R}-1)}, \tag{4.3}$$

$$DR(\theta) = \frac{DR_0(\theta)}{N_{\rm D}\,N_{\rm R}}, \tag{4.4}$$

Here, N is the total number of pairs with subscripts "D" and "R" indicating galaxies and random points, respectively, and subscript "0" indicates the raw number of pairs. We use a random sample composed of 100, 000 sources with the same geometrical constraints

[*12] In COSMOS field, Matthee et al. (2016, hereafter M16) find an overdense region in their HAE sample at $z = 2.231 \pm 0.016$ (see their figure 2) and a part of their survey region overlaps with that of our LAEs at $z = 2.14$–2.22. In their overdense region, two X-ray sources at $z = 2.219$ and $z = 2.232$ have bright Lyα emission. The first one is roughly at the center of the overdense region but just outside of our $NB387$ image coverage (ID:1139: see figure 2 and table 2 in M16). The second one is included in our coverage but not selected by our color-color criteria probably because its redshift is too large (ID:1037). Indeed, we do not find, by eye inspection, any overdense region in figure 4.1(d) as significant as the one discovered by M16.

as the data sample (see figure 4.1). The $1\,\sigma$ uncertainties in ACF measurements are estimated as:

$$\Delta\omega_{\rm obs}(\theta) = \frac{1+\omega(\theta)}{\sqrt{DD_0(\theta)}} \tag{4.5}$$

following Guaita et al. (2010). While Norberg et al. (2009) find that Poisson errors underestimate the $1\,\sigma$ uncertainties in ACF measurements and that bootstrapping errors overestimate them 40% using a large number of sources ($\sim 10^5$–10^6), Khostovan et al. (2018) show that Poisson errors and bootstrapping errors are comparable in the case of a small sample size using ~ 200 Hβ + [O III] emitters at $z \sim 3.2$ (see also our footnote *14 and figure 6.6(b)).

We approximate the spatial correlation function of LAEs by a power law:

$$\xi(r) = \left(\frac{r}{r_0}\right)^{-\gamma}, \tag{4.6}$$

where r, r_0, and γ are the spatial separation between two objects in comoving scale, the correlation length, and the slope of the power law, respectively (Totsuji & Kihara, 1969; Zehavi et al., 2004). We then convert $\xi(r)$ into the ACF, $\omega_{\rm model}(\theta)$, following Simon (2007), and describe it as:

$$\omega_{\rm model}(\theta) = C\,\omega_{\rm model,\,0}(\theta), \tag{4.7}$$

where $\omega_{\rm model,\,0}(\theta)$ is the ACF in the case of $r_0 = 1\ h_{100}^{-1}$Mpc and C is a normalization constant:

$$C = \left(\frac{r_0\ h_{100}^{-1}{\rm Mpc}}{1\ h_{100}^{-1}{\rm Mpc}}\right)^{\gamma}. \tag{4.8}$$

The correlation amplitude of the ACF at $\theta = 1''$, A_ω, is

$$A_\omega = C\,\omega_{\rm model,\,0}(\theta = 1'') \tag{4.9}$$

An observationally obtained ACF, $\omega_{\rm obs}(\theta)$, includes an offset due to the fact that the measurements are made over a limited area. This offset is given by the integral constraint (IC),

$$\omega(\theta) = \omega_{\rm obs}(\theta) + IC, \tag{4.10}$$

$$IC = \frac{\Sigma_\theta RR(\theta)\,C\,\omega_{\rm model,\,0}(\theta)}{\Sigma_\theta RR(\theta)}, \tag{4.11}$$

where $\omega(\theta)$ is the true ACF. We fit the $\omega_{\rm model}(\theta)$ to this $\omega(\theta)$ over $\sim 40'' - 1000''$ by minimizing χ^2:

$$\chi^2 = \Sigma_\theta \left(\frac{\omega_{\rm obs}(\theta) + IC - \omega_{\rm model}(\theta)}{\Delta\omega_{\rm obs}(\theta)}\right)^2 \tag{4.12}$$

$$= \Sigma_\theta \left(\frac{\omega_{\rm obs}(\theta) + C\,(IC_0 - \omega_{\rm model,0}(\theta))}{\Delta\omega_{\rm obs}(\theta)}\right)^2, \tag{4.13}$$

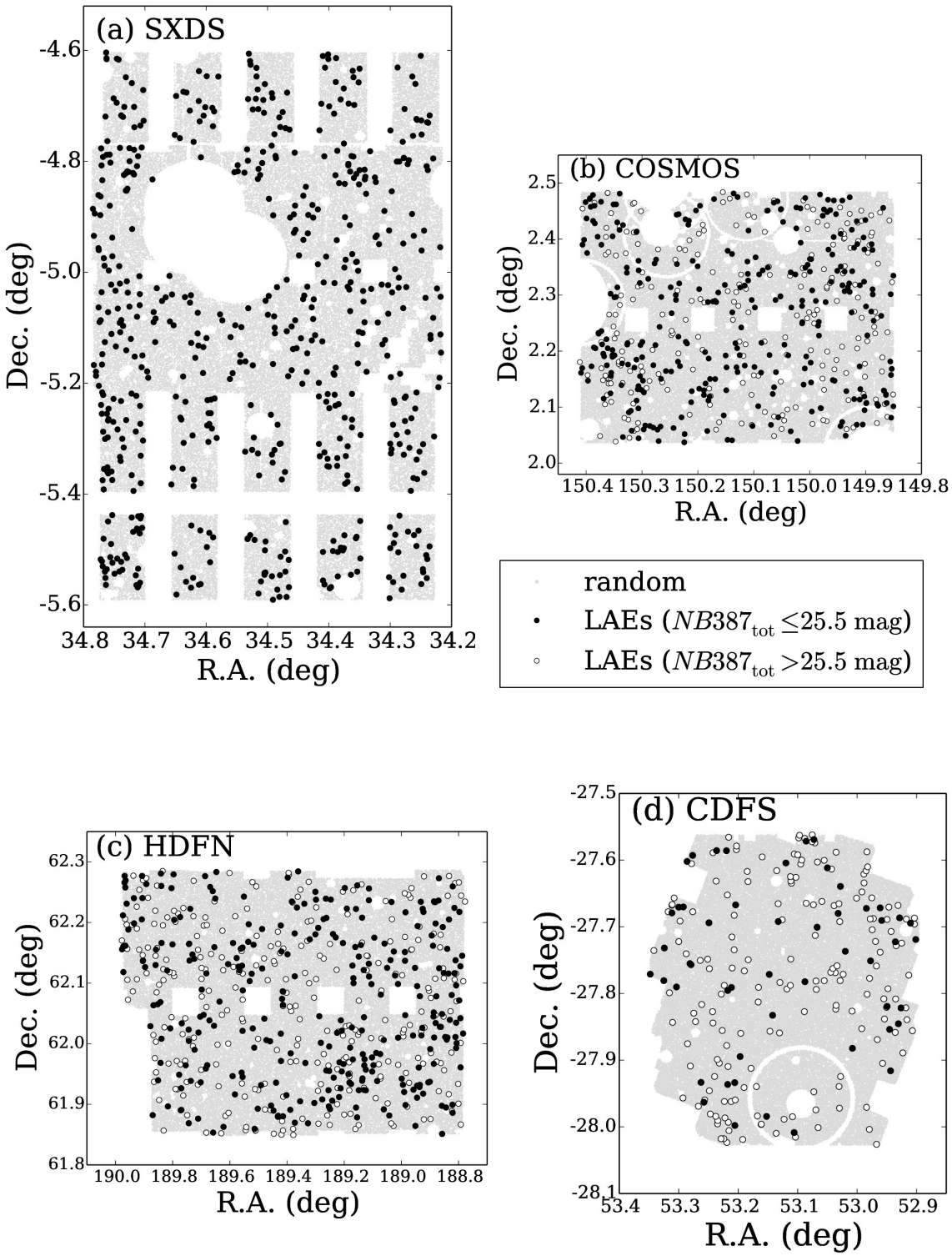

Figure 4.1 Sky distribution of LAEs in SXDS (panel [a]), COSMOS ([b]), HDFN ([c]), and CDFS ([d]). Filled and open black circles represent objects with $NB_{\rm tot} \leq 25.5$ mag and $NB_{\rm tot} > 25.5$ mag, respectively. Gray points indicate 100, 000 random sources used in the clustering analysis. Masked regions are shown in white.

where $IC_0 = IC/C$. This θ range is determined conservatively avoiding the one-halo term at small scales and large sampling noise at large scales. We fix γ to the fiducial value 1.8 following previous clustering analyses (e.g., Ouchi et al., 2003). The analytic solution of the best-fit correlation amplitude is

$$A_\omega = \frac{\Sigma_\theta \left(\frac{\omega_{\rm obs}(\theta)(\omega_{\rm model,0}(\theta) - IC_0)}{\Delta\omega_{\rm obs}(\theta)^2} \right)}{\Sigma_\theta \left(\frac{IC_0 - \omega_{\rm model,0}(\theta)}{\Delta\omega_{\rm obs}(\theta)} \right)^2} \omega_{\rm model,\,0}(\theta = 1'').$$ (4.14)

The $1\,\sigma$ fitting error in A_ω, ΔA_ω, is estimated from $\chi^2_{\rm min} + 1$, where $\chi^2_{\rm min}$ is the minimum χ^2 value. We also derive, for each limiting magnitude, the field-average correlation amplitude over the four survey fields by minimizing the summation of χ^2 over the four fields:

$$A_{\omega,ave} = \frac{\Sigma_{\theta,i=field} \left(\frac{\omega_{{\rm obs},i}(\theta)(\omega_{\rm model,0}(\theta) - IC_{0,i})}{\Delta\omega_{{\rm obs},i}(\theta)^2} \right)}{\Sigma_{\theta,i=field} \left(\frac{IC_{0,i} - \omega_{\rm model,0}(\theta)}{\Delta\omega_{{\rm obs},i}(\theta)} \right)^2} \omega_{\rm model,\,0}(\theta = 1'').$$ (4.15)

The field-average correlation amplitude for subsamples of UV, Lyα, and K-band properties over SXDS and COSMOS fields are also calculated similarly for each UV, Lyα, and K-band subsamples. The best-fit ACFs are shown in figure 6.4 in section 6.3.1 and figure 6.4 in appendix B.1 for the $NB387$ limiting magnitude samples and the subsamples, respectively.

Contaminations by randomly-distributed foreground and background interlopers dilute the apparent clustering amplitude. The correlation amplitude corrected for randomly distributed interlopers, $A_{\omega,\,\rm corr}$, is given by

$$A_{\omega,\,\rm corr} = \frac{A_\omega}{(1 - f_{\rm c})^2},$$ (4.16)

where $f_{\rm c}$ is the contamination fraction. The contamination fraction of our LAEs is estimated to be $10 \pm 10\%$ (0–20%) conservatively from the Monte Carlo simulations and the spectroscopic follow-up observations (see section 2.2). This $A_{\omega,\,\rm corr}$ is the maximum permitted value because interlopers themselves are also clustered in reality. Indeed, some previous clustering studies (e.g., Khostovan et al., 2018) have not applied any contamination correction. In this study, we apply this equation assuming $f_{\rm c} = 10 \pm 10\%$ so that the error range in $A_{\omega,\,\rm corr}$ include both the no correction case and the maximum correction case. The $1\,\sigma$ error in the contamination-corrected correlation amplitude, $\Delta A_{\omega,\,\rm corr}$, is derived by summing the $1\,\sigma$ error in the ACF fitting, ΔA_ω, and the uncertainty in the contamination estimate, $\Delta f_{\rm c} = 0.1$, in quadrature (error propagation):

$$\frac{\Delta A_{\omega,\,\rm corr}}{A_{\omega,\,\rm corr}} \simeq \sqrt{\left(\frac{\Delta A_\omega}{A_\omega} \right)^2 + \left(\frac{2\Delta f_{\rm c}}{f_{\rm c}} \right)^2}.$$ (4.17)

The value of the contamination-corrected correlation length, $r_{0,\,\rm corr}$ and its $1\,\sigma$ error are calculated from $A_{\omega,\,\rm corr}$ and $\Delta A_{\omega,\,\rm corr}$. Table 6.4 in section 6.3.1 and table 6.5 in section 6.3.5 summarize the results of the clustering analysis for the $NB387$ limiting magnitude samples and the subsamples, respectively.

4.2 Bias factor

The galaxy-matter bias, $b_{\rm g}$, is defined as

$$b_{\rm g}(r) = \sqrt{\frac{\xi(r)}{\xi_{\rm DM}(r,z)}}, \tag{4.18}$$

where $\xi_{\rm DM}(r,z)$ is the spatial correlation function of underlying dark matter,

$$\xi_{\rm DM}(r,z) = \int \frac{k^2 dk}{2\pi^2} \frac{\sin(kr)}{kr} P_m(k,z), \tag{4.19}$$

where $P_m(k,z)$ is the linear dark matter power spectrum as a function of wave number, k, at redshift z (Eisenstein & Hu, 1999) with the Eisenstein & Hu (1998) transfer function. We estimate the effective galaxy-matter bias, $b_{\rm g,\,eff}$, at $r = 8\,h_{100}^{-1}$Mpc following previous clustering analyses (e.g., Ouchi et al., 2003) using a suite of cosmological codes called Colossus (Diemer & Kravtsov, 2015). The obtained effective bias for the $NB387$ limiting magnitude samples is shown in figure 6.5 and table 6.3.1. That for each UV, Lyα, and K mag subsample is listed in table 6.5 in section 6.3.5.

4.3 Dark matter halo mass

We estimate the effective dark matter halo masses from $b_{\rm g,\,eff}$ directly assuming that each halo hosts only one galaxy and that our sample has a narrow range of dark matter halo mass. We use the formula of bias and peak height in the linear density field, ν, given in Tinker et al. (2010), which is based on a large set of collisionless cosmological simulations in flat ΛCDM cosmology. The obtained ν is converted to the effective dark matter halo mass with the top-hat window function and the linear dark matter power spectrum (Eisenstein & Hu, 1998, 1999) using a cosmological package for Python called CosmoloPy[*13]. The effective halo mass ($M_{\rm h}$) of each (sub)sample is listed in tables 6.4 and 6.5.

4.4 Cosmic variance on bias factor

Biases and thus dark matter halo masses derived from limited survey areas possibly suffer from cosmic variance due to spatial variations in the ACF of dark matter. We analytically estimate cosmic variance in the bias value of high-redshift galaxies derived from clustering analysis for the first time. With the ACF the galaxy-matter bias can be expressed as $b(\theta) = \sqrt{\omega_{\rm gal}(\theta)/\omega_{\rm DM}(\theta)}$. Assuming that the cosmic variance in b originates solely from the spatial variation of the dark matter ACF, we can express the b of a given galaxy

[*13] http://roban.github.com/CosmoloPy/

sample in a given survey field as:

$$b(\mathrm{field}) = \sqrt{\frac{\omega_{\mathrm{DM}}(\mathrm{field})}{\langle\omega_{\mathrm{DM}}\rangle}\frac{\omega_{\mathrm{gal}}(\mathrm{field})}{\omega_{\mathrm{DM}}(\mathrm{field})}} = \sqrt{\frac{\omega_{\mathrm{DM}}(\mathrm{field})}{\langle\omega_{\mathrm{DM}}\rangle}}b_{\mathrm{int}}, \tag{4.20}$$

where $\langle\omega_{\mathrm{DM}}\rangle$ is the cosmic average of the dark matter ACF, $\omega_{\mathrm{DM}}(\mathrm{field})$ is the dark matter ACF in the field, $\omega_{\mathrm{gal}}(\mathrm{field})$ is the observed galaxy ACF in the field, and

$$b_{\mathrm{int}} \equiv \sqrt{\frac{\omega_{\mathrm{gal}}(\mathrm{field})}{\omega_{\mathrm{DM}}(\mathrm{field})}} \tag{4.21}$$

is the intrinsic bias of this galaxy population which we assume to be unchanged from field to field (parameter θ is omitted for clarity). This assumption is the same as the one assumed to predict cosmic variance in number density (e.g., Moster et al., 2011), as explained below. Field to field fluctuations of number density, $\sigma_{\mathrm{ND,\,g'}}$, are assumed to come from field to field fluctuations of dark matter distribution (i.e., cosmic variance in the density of dark matter), $\sigma_{\mathrm{ND,\,DM}}$, as

$$\sigma_{\mathrm{ND,\,g'}} = b_{\mathrm{g'}}\ \sigma_{\mathrm{ND,\,DM}}, \tag{4.22}$$

where the intrinsic galaxy bias, $b_{\mathrm{g'}}$, is uniform and independent of fields by definition. We also assume that $\omega^2_{\mathrm{gal}}(\mathrm{field})$ is proportional to $\omega^2_{\mathrm{DM}}(\mathrm{field})$ by a factor of b_{int}.

The covariance in ω_{DM} between two angular separations for area Ω_{s} is given by the first term of equation 19 of Cohn (2006)[*14]:

$$\mathrm{Cov}(\omega_{\mathrm{DM}}(\theta),\ \omega_{\mathrm{DM}}(\theta')) = \frac{1}{\pi\Omega_{\mathrm{s}}}\int \mathrm{K}\ \mathrm{dK} J_0(\mathrm{K}\theta)\ {}_0(\mathrm{K}\theta')\ \mathrm{P}_2^2(\mathrm{K}), \tag{4.23}$$

where K, $P_2(\mathrm{K})$ and $J_0(\mathrm{K}\theta)$ are the Fourier transform of θ, the projected power spectrum calculated using the redshift distribution defined by the filter, and the zeroth-order Bessel function of the first kind, respectively. With this equation we calculate ω_{DM} and its standard deviation, σ_{DM}, for the three angular bins used to determine the A_ω of our LAEs. We then fit a power-law correlation function to those values in the same manner as for observed data but also considering the intrinsic covariance given in equation (4.23), and obtain the relative uncertainty in A_ω due to the variation in ω_{DM}, $\frac{\Delta\omega_{\mathrm{DM}}}{\omega_{\mathrm{DM}}}$. According to equation 4.23, the relative uncertainty in A_ω depends on Ω_{s} as:

$$\frac{\Delta\omega_{\mathrm{DM}}}{\omega_{\mathrm{DM}}} \propto \Omega_{\mathrm{s}}^{-0.5}, \tag{4.24}$$

as shown by a light gray solid line in figure 6.6 (a) in section 6.3.3. We compare the analytic solution of $\frac{\Delta\omega_{\mathrm{DM}}}{\omega_{\mathrm{DM}}}$ with $\frac{\Delta\omega_{\mathrm{DM}}}{\omega_{\mathrm{DM}}}$ estimated empirically in Sobral et al. (2010) in section 6.3.3. We also derive $\frac{\Delta\omega_{\mathrm{DM}}}{\omega_{\mathrm{DM}}}$ for our sample in each field and total field as well as for LAEs in Guaita et al. (2010) and then discuss bias values.

[*14] Cohn (2006)'s equation (19) corresponds to the full covariance including those due to a discrete sampling with a finite number of objects; the second term is proportional to $P_2(K)/N\Omega_{\mathrm{S}}$, where N is the number density of objects, and the subsequent terms correspond to the uncertainty shown in our equation 4.5. Inclusion of the second term in our equation 4.23 increases $\Delta\omega_{\mathrm{DM}}$ by $\sim 30\%$ for our LAE survey, although in this study we neglect this term and only consider cosmic variance not dependent on N. See appendix B.2 for more details.

Chapter 5

Lyα halo luminosity

To discuss the origin of Lyα halos (LAHs) of LAEs, we derive the Lyα luminosities for subsamples in accordance with UV, Lyα, and K–band properties as we described in section 1.4.4. The Lyα luminosities of LAHs are estimated from a stacked observational relation obtained in Momose et al. (2016). We do not perform a stacking analysis of LAHs on our own subsamples since their sample sizes, which are one ninth to one half of the subsample sizes (~ 700 each) in Momose et al. (2016), are not large enough to obtain reliable results. Note that parameters that characterize stellar populations and the mass of dark matter halos are derived from SED fitting and clustering analysis as we mention in chapters 3 and 4, respectively.

5.1 Definitions of Lyα luminosities

The LAHs of LAEs have been studied either by a stacking analysis of large samples or using individually detected objects. Momose et al. (2016) have used stacked images of ~ 700 LAEs in each subsample (in total ~ 3600) at $z \sim 2$ to compare Lyα luminosities within $r = 40$ kpc ($\sim 5''$) to those within $r = 1''$ (~ 8 kpc). Their ~ 3000 LAEs are the parent sample of our ~ 900 LAEs, and they have estimated an empirical relation between the two Lyα luminosities. On the other hand, Leclercq et al. (2017) have measured Lyα luminosities for $3 \leq z \leq 6$ LAEs with an individually detected LAH by fitting a two component model consisting of halo and continuum-like components. We define three kinds of Lyα luminosities as below.

$L(\mathrm{Ly}\alpha)_\mathrm{C}$ Lyα luminosity at the central part, i.e., the main body of the object where stars are being formed. In Leclercq et al. (2017), it corresponds to the continuum-like component of Lyα luminosities. We assume that the Lyα luminosities within $r = 1''$ in 2D images in Momose et al. (2016) are approximately equal to $L(\mathrm{Ly}\alpha)_\mathrm{C}$. The aperture size $r = 1''$ (~ 8 kpc) is often used in photometry with ground-based telescopes for point sources, since it is comparable to their typical PSF size and hence $r = 1''$ fluxes are nearly equal to total fluxes. Leclercq et al. (2017) show that the scale length of the continuum-like component of LAEs is typically smaller than 1 kpc, ensuring our assumption that LAEs are point sources.

$L(\mathrm{Ly}\alpha)_\mathrm{H}$ Lyα luminosity of the LAH. In Leclercq et al. (2017), it approximately corre-

sponds to the halo component of Lyα luminosity. We assume that the Lyα luminosities falling in the annulus of $8 \leq r \leq 40$ kpc in Momose et al. (2016) approximately equal to $L(\mathrm{Ly}\alpha)_{\mathrm{H}}$. In Momose et al. (2016), the typical r_s of the stacked Lyα emission including the LAH component is ~ 10 kpc, and LAHs are found to extend up to $r \sim 40$ kpc.

$L(\mathrm{Ly}\alpha)_{\mathrm{tot}}$ Total Lyα luminosity. In Leclercq et al. (2017), it corresponds to a sum of $L(\mathrm{Ly}\alpha)_{\mathrm{C}}$ and $L(\mathrm{Ly}\alpha)_{\mathrm{H}}$. we assume that the Ly$\alpha$ luminosities within 40 kpc in Momose et al. (2016) approximately equal to $L(\mathrm{Ly}\alpha)_{\mathrm{tot}}$.

Momose et al. (2016) have found that LAEs with fainter $L(\mathrm{Ly}\alpha)_{\mathrm{C}}$ have a higher $L(\mathrm{Ly}\alpha)_{\mathrm{tot}}$ to $L(\mathrm{Ly}\alpha)_{\mathrm{C}}$ ratio, $\mathrm{X}(L_{\mathrm{Ly}\alpha})_{\mathrm{tot/C}}$, as shown in their figure 14. This means that the relative contribution of the halo component to the total Lyα luminosity increases with decreasing $L(\mathrm{Ly}\alpha)_{\mathrm{C}}$. The best-fitting linear function between $\mathrm{X}(L_{\mathrm{Ly}\alpha})_{\mathrm{tot/C}}$ and $L(\mathrm{Ly}\alpha)_{\mathrm{C}}$, shown as their equation 2 is:

$$\mathrm{X}(L_{\mathrm{Ly}\alpha})_{\mathrm{tot/C}} = 103.6 - 2.4 \log_{10}[L(\mathrm{Ly}\alpha)_{\mathrm{C}}\,(\mathrm{erg/s})]. \tag{5.1}$$

This equation is valid over $41.5 < \log_{10}(L(\mathrm{Ly}\alpha)_{\mathrm{C}}) < 42.7$[*15] and is shown in figure 5.1(b).

5.2 Previous studies on Lyα halo luminosity

Leclercq et al. (2017) have used the MUSE Hubble Ultra Deep Field survey data to detect LAHs for 145 star forming galaxies (essentially all are LAEs) at $3 \leq z \leq 6$ individually. They have measured the size and $L(\mathrm{Ly}\alpha)_{\mathrm{H}}$ of Lyα halos as well as $L(\mathrm{Ly}\alpha)_{\mathrm{C}}$. They do not find a significant evolution of the LAH size with redshift. This result is consistent with that obtained by Momose et al. (2014) with stacked LAEs at $z \simeq 2.2$–6.6, implying that the difference in redshift can be ignored in a comparison of the two studies. Indeed, there is no clear redshift evolution in the relations of MUSE LAEs shown by gray filled circles ($z <= 4.5$) and gray open circles ($z > 4.5$) in figure 5.1 described below.

In figure 5.1, we compare the stacked observational relation of LAEs at $z = 2.2$ in Momose et al. (2016) (black lines and red stars) with the individual results by Leclercq et al. (2017) (gray and black circles), where $\mathrm{X}(\mathrm{Ly}\alpha)_{x/y}$ indicates the Lyα luminosity ratio of the component x to the component y. Figure 5.1(a) is originally discussed in Leclercq et al. (2017), while figure 5.1(b) is used to determine the best-fit linear relation (equation 5.1) in Momose et al. (2016). Black lines in figures 5.1 (a), (c), and (d) are converted from one in figure 5.1(b). It is notable that the y-axis depends on the x-axis by construction[*16] in figures 5.1 (a), (b) and (d). We find that all five stacked data points (red stars) lie

[*15] They use images with the PSF matched to 1″.32 in FWHM. Here we have corrected a typo in their equation 2 and revised the range of $\log_{10}[L(\mathrm{Ly}\alpha)_{\mathrm{C}}]$. We conclude that this equation is valid over $41.7 < \log_{10}(L(\mathrm{Ly}\alpha)_{\mathrm{C}}) < 42.3$ from discussions below.

[*16] We regard $L(\mathrm{Ly}\alpha)_{\mathrm{C}}$ and $L(\mathrm{Ly}\alpha)_{\mathrm{H}}$ as two independent parameters in the measurements in Leclercq et al. (2017) and Momose et al. (2016). Even if objects are randomly distributed in the $L(\mathrm{Ly}\alpha)_{\mathrm{C}}$ and $L(\mathrm{Ly}\alpha)_{\mathrm{H}}$ plane (panel [c]), we will see a 'correlation' in the other three panels because the y axis of these panels is a combination of $L(\mathrm{Ly}\alpha)_{\mathrm{C}}$ and $L(\mathrm{Ly}\alpha)_{\mathrm{H}}$.

in the middle of the distribution of individual MUSE-LAEs (grey circles) over a range of $\log_{10}[L(\mathrm{Ly}\alpha)_{\mathrm{C}}(\mathrm{erg/s})] \simeq 41.7$–$42.6$ or $\log_{10}[L(\mathrm{Ly}\alpha)_{\mathrm{tot}}(\mathrm{erg/s})] \simeq 42.3$–$42.8$. It is also found that the median values of individual MUSE-LAEs (black filled circles in figures 5.1 [a] and [c]) are located near the stacked values. This means that the stacked results represent the average halo luminosities of LAEs despite the fact that there is a great variation in halo luminosity among objects. The best-fit relation shown by a black line traces well the stacked points except for the brightest one. This is because the brightest point already deviates from the best-fit linear relation determined in figure 5.1(b) while the other four are on the relation. Based on figure 5.1(a), Leclercq et al. (2017) have concluded that there is no significant correlation between $L(\mathrm{Ly}\alpha)_{\mathrm{tot}}$ and $\mathrm{X}(\mathrm{Ly}\alpha)_{\mathrm{H/tot}}$ on the basis of a Spearman rank correlation coefficient of -0.05 (see their figure 7 and their section 5.3.1). Although the existence of a correlation is not clear, and a further test is needed, figures 5.1 (a) and (c) indicate that the stacked results (red stars) also trace the median trend of individual MUSE LAEs (black filled circles).

5.3 Estimation of $L(\mathrm{Ly}\alpha)_{\mathrm{H}}$ from the empirical relation

In this thesis, we estimate average $L(\mathrm{Ly}\alpha)_{\mathrm{H}}$ and $L(\mathrm{Ly}\alpha)_{\mathrm{tot}}$ for each subsample from the stacked relation (equation 5.1) as well as average $L(\mathrm{Ly}\alpha)_{\mathrm{C}}$ by multiplying average $L(\mathrm{Ly}\alpha)_{ps}$ (in section 2.5.1) by 0.77 as an inverse aperture correction of $1''.32$ PSF (see table 6.6 in section 6.7.1). The $L(\mathrm{Ly}\alpha)_{\mathrm{C}}$ values of our subsamples are found to be within the range shown by skyblue inverted triangles in figures 5.1 (c) and (d) where the stacked relation traces well the stacked points. The typical 1σ uncertainties in the individual data points in Momose et al. (2016) are propagated to uncertainties in $L(\mathrm{Ly}\alpha)_{\mathrm{H}}$ and $L(\mathrm{Ly}\alpha)_{\mathrm{tot}}$ of $\sim 22\%$ and $\sim 16\%$, respectively. Momose et al. (2016) also present a stacked relation (anti-correlation) between $\mathrm{X}(L_{\mathrm{Ly}\alpha})_{\mathrm{tot/C}}$ and $EW_{0,ps}(L_{\mathrm{Ly}\alpha})$. Using this relation instead of equation 5.1 gives nearly the same $L(\mathrm{Ly}\alpha)_{\mathrm{H}}$ and $L(\mathrm{Ly}\alpha)_{\mathrm{tot}}$ values (see section 6.7.1).

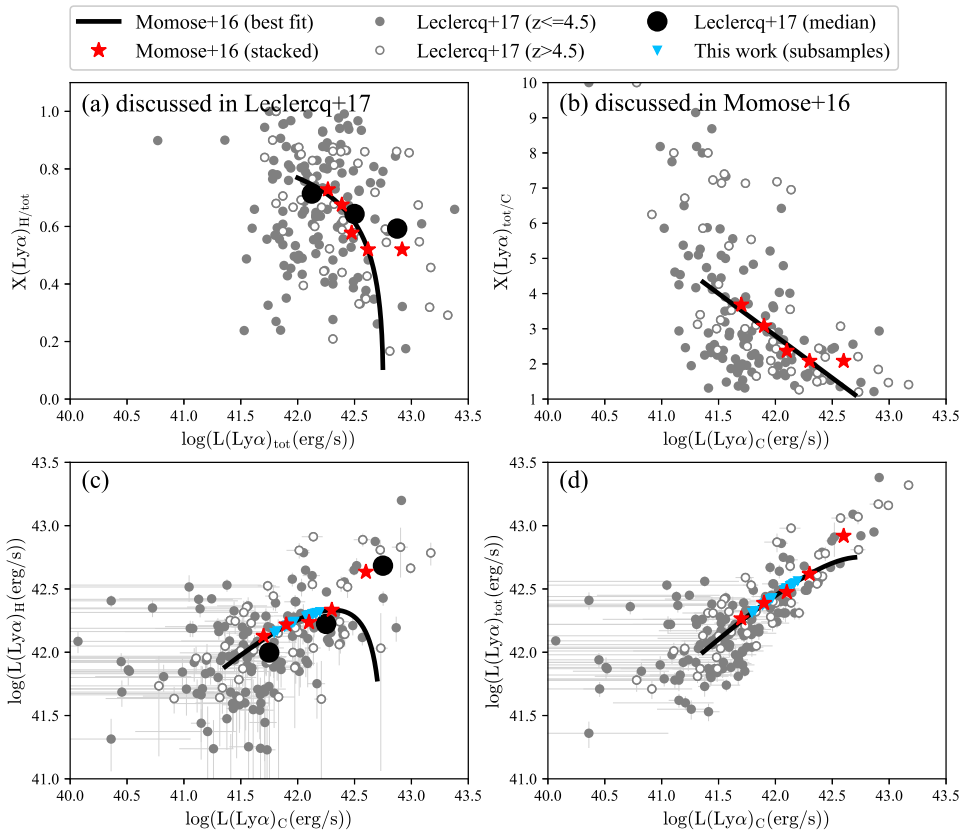

Figure 5.1 Relation between $L(\mathrm{Ly}\alpha)_\mathrm{H}$ and $L(\mathrm{Ly}\alpha)_\mathrm{C}$ in four different presentations. (a) $L(\mathrm{Ly}\alpha)_\mathrm{H}/L(\mathrm{Ly}\alpha)_\mathrm{tot}$ vs. $L(\mathrm{Ly}\alpha)_\mathrm{tot}$; (b) $L(\mathrm{Ly}\alpha)_\mathrm{tot}/L(\mathrm{Ly}\alpha)_\mathrm{C}$ vs. $L(\mathrm{Ly}\alpha)_\mathrm{C}$; (c) $L(\mathrm{Ly}\alpha)_\mathrm{H}$ vs. $L(\mathrm{Ly}\alpha)_\mathrm{C}$; and (d) $L(\mathrm{Ly}\alpha)_\mathrm{tot}$ vs $L(\mathrm{Ly}\alpha)_\mathrm{C}$. Red stars and black lines indicate, respectively, the stacked results and their best-fit relation given by Momose et al. (2016). The best-fit linear relation is determined in panel (b) and is shown in equation 5.1. The grey filled and open circles represent MUSE–LAEs at $z \sim 3-4.5$ and $z \sim 4.5-6$ in Leclercq et al. (2017), where errors are only shown in panels (c) and (d). The black filled circles in panels (a) and (c) show the median of the MUSE–LAEs over a range of $\log_{10}[L(\mathrm{Ly}\alpha)_\mathrm{tot}(\mathrm{erg/s})] \simeq 42.0$–$43.0$ and $\log_{10}[L(\mathrm{Ly}\alpha)_\mathrm{C}(\mathrm{erg/s})] \simeq 41.5$–$43.0$, respectively. Skyblue inverted triangles in panels (c) and (d) show the $L(\mathrm{Ly}\alpha)_\mathrm{H}$ and $L(\mathrm{Ly}\alpha)_\mathrm{tot}$ of our subsamples calculated from $L(\mathrm{Ly}\alpha)_\mathrm{C}$ using the stacked observational relation in Momose et al. (2016). Note that the y-axis depends on the x-axis by construction (see *16 for more details) in panels (a), (b) and (d), while panels (a) and (c) have independent axis.

Chapter 6

Results

In this chapter, we show our results of IR Luminosity and dust attenuation curve (in section 6.1), results of SED fitting (in section 6.2), results of clustering analysis (in section 6.3), IRX–$M_\star$ relation (in section 6.4), star formation mode (in section 6.5), $SHMR$ and BCE (in section 6.6), Lyα halo luminosity (in section 6.7), and Lyα escape fraction (in section 6.8).

6.1 IR Luminosity and dust attenuation curve

6.1.1 Individual detection

We match the 213 LAEs against the the MIPS[*6] and the PACS catalogs (Magnelli et al., 2013) within 1″ radius. None of the LAEs has a counterpart in either the MIPS and the PACS catalogs.

6.1.2 Stacking analysis

We derive IR luminosity through stack analysis of the MIPS/24μm, PACS/70 μm, 100 μm, and 160 μm band images at the position of the LAEs. Before stacking the MIPS/24μm images, we remove sources listed in the MIPS catalog with a similar method to Reddy et al. (2012a) and subtract a large-scale residual background following the procedure given in Wuyts et al. (2008). For each band, 50″ × 50″ cut-out images are median stacked. We then perform aperture photometry at the center of each stacked image on a radius of 3″.0, 3″.2, 4″.5, and 7″.4 for MIPS/24 μm, PACS/70 μm, 100 μm, and 160 μm, respectively. No significant signal is detected in any of the four stacked images, where the sky noise for each band is estimated from 1000 realizations generated by bootstrap resampling of the 213 objects as done by Wardlow et al. (2014). Thus, we derive the 3σ upper limit of the total flux density for each band by multiplying the 3σ sky noise by an aperture correction factor of 2.87, 2.45, 1.96, and 1.92 for MIPS/24 μm, PACS/70 μm, 100 μm, and 160 μm, respectively. The resulting 3σ total flux densities are 1.4, 56, 81, and 234 μJy, respectively.

[*6] http://irsa.ipac.caltech.edu/cgi-bin/Gator/nph-scan?mission=irsa&submit=Select&projshort=SPITZER

6.1.3 Scaling dust SED templates

We calculate two upper limits of the LTIR, one from the MIPS/24um 3sigma flux density and the other from the PACS (three bands) 3sigma flux densities, by scaling dust templates.

We calculate two upper limits of the infrared (3–1000μm) luminosity, $L_{\rm TIR}$, one from the MIPS/24μm 3σ flux density and the other from the PACS (three bands) 3σ flux densities, by scaling dust templates (Ciesla et al., 2014). While the PACS bands measure dust continuum emission for galaxies at $z \simeq 2.18$, the MIPS/24μm band measures $\simeq 8\mu$m PAH emission ($L_8 \equiv \nu_{8\mu{\rm m}} L_{\nu,\,8\mu{\rm m}}$). Although the MIPS/24$\mu$m band can reach fainter $L_{\rm TIR}$ than the PACS bands at $z \sim 1$–3 in general (see figure 4 in Elbaz et al., 2011), a MIPS-based $L_{\rm TIR}$ has an uncertainty because of a diverse relation between L_8 and $L_{\rm TIR}$. We discuss the reliability of the upper limit of the MIPS-based $L_{\rm TIR}$ for our LAEs using that of the PACS-based $L_{\rm TIR}$ in section 6.1.4.

In Ciesla et al. (2014), the dust SED templates of local galaxies binned over various properties are provided using 8 μm to 500 μm from Spitzer, WISE, IRAS and Herschel data, which are based on Draine & Li (2007) model. For the MIPS data, we scale the lowest-metallicity template to the 24μm limit to obtain $L^{3\sigma}_{\rm TIR} = 1.1 \times 10^{10} L_\odot$. We adopt this template because it gives the highest (i.e., most conservative) $L^{3\sigma}_{\rm TIR}$ among all. For the PACS data, we scale each template to each of the three data points to obtain each band's 3σ $L_{\rm TIR}$ upper limit for that template. We then statistically combine these three upper limits to derive a final 3σ upper limit which is lower than the individual bands[*17]. Among the final 3σ limits derived from all the templates, $L_{\rm TIR} = 1.4 \times 10^{11} L_\odot$ is the highest one. We adopt the MIPS-based $L^{3\sigma}_{\rm TIR}$ as the upper limit of our LAEs and use it in the following section. Below we discuss the possibility that this MIPS-based $L^{3\sigma}_{\rm TIR}$ may be optimistic.

6.1.4 Certainty of $L^{3\sigma}_{\rm TIR}$

A careful analysis and discussion on the IR luminosity is essential. There is a well-known trend that the relative contribution of PAH emission to $L_{\rm TIR}$ decreases with decreasing metallicity (Galliano, 2011). Hence, PAH-based $L_{\rm TIR}$is in general less reliable than that from longer wavelengths and MIPS-based $L^{3\sigma}_{\rm TIR}$ may be optimistic. However, the template we use to derive $L_{\rm TIR}$ is the lowest-metallicity one constructed from galaxies with $12 + \log {\rm O/H} \simeq 8.2$–$8.4$. This metallicity range is roughly consistent with those of LAEs: $12 + \log {\rm O/H} \simeq 8.0 - 8.8$ for bright LAEs with individual measurements (Nakajima & Ouchi, 2014) and $12 + \log {\rm O/H} \simeq 8.2 \pm 0.1$ for faint LAEs from stacking (Nakajima et al., 2012). Indeed, this template has a relatively high IR8 ($= L_{8-1000\mu{\rm m}}/L_8$ of 6.7, being close

[*17] We calculate the PACS-based final 3σ upper limit as $\frac{1}{\sqrt{1/\sigma^2_{70}+1/\sigma^2_{100}+1/\sigma^2_{160}}}$, where σ_{70}, σ_{100}, and σ_{160} are the 3σ $L_{\rm TIR}$ upper limit derived from the 3σ total flux limit of PACS/70 μm, 100 μm, and 160 μm band, respectively.

to those of $z \sim 2$ UV-selected galaxies, $\simeq$ 8–9 (Reddy et al., 2012a), and significantly higher than the typical value of $z < 2.5$ star-forming galaxies ($IR8 = 4$; Elbaz et al., 2011), and of Chary & Elbaz (2001) templates at the L_8 of our sample ($IR8 \sim 4$). It is also known that PAH emission is suppressed in starburst galaxies. Elbaz et al. (2011) shows that starburst galaxies, characterized by high projected IR densities, have high IR8. However, even when the PACS-based $L_{\rm TIR}$ is used, the IR surface density of our LAEs is lower than the threshold for the starburst regime, $\simeq 3 \times 10^{10}\ L_\odot\ {\rm kpc}^{-2}$, at which IR8 takes ~ 8. Here we assume our LAEs typically have a 1 kpc half-light radius following Malhotra et al. (2012) and Hagen et al. (2014).

In addition, Reddy et al. (2006) demonstrate from X-ray stacking analysis of MIPS/24um-undetected UV-selected galaxies at z∼2 that they are individually undetected in MIPS primarily because they have lower SFRs and not because they have deficient PAH emission (although we note that their objects are not as faint as ours, being detected in a stacked MIPS image).

Thus, it appears to be unlikely that the MIPS-based $L_{\rm TIR}^{3\sigma}$ is significantly underestimating the true value. Note that the PACS-based $L_{\rm TIR}^{3\sigma}$ divided by the L_8 of the lowest-metallicity template scaled to the MIPS photometry, gives $IR8 \sim 90$. However, we should keep in mind that the derivation of the MIPS-based $L_{\rm TIR}^{3\sigma}$ is based on two important assumptions. First, we are assuming that our LAEs have indeed low metallicities as suggested by previous studies. Second, the local calibration between the 8 μm emission and the dust SED shape and metallicity are assumed and applies at high redshifts.

In the next section, we compere the $L_{\rm TIR}^{3\sigma} (= 1.4 \times 10^{11} L_\odot)$ with that of previous work and derive the SFR of our LAEs. We then estimate a suitable dust attenuation curve for our LAEs from IRX–β relation.

6.1.5 IR luminosity and star formation rate

We obtain a robust upper limit of IR luminosity for our LAEs at $z \sim 2$, $L_{\rm TIR}^{3\sigma} = 1.1 \times 10^{10} L_\odot$, which is $\sim$ 1dex lower than those in previous work for bright LAEs at $z > 2$, $L_{\rm TIR}^{3\sigma} = 2$–$3 \times 10^{11} L_\odot$, in Wardlow et al. (2014). Our $L_{\rm TIR}^{3\sigma}$is 200 times lower than the 'knee' luminosity of the IR luminosity function at $z \sim 2$ (Magnelli et al., 2013), implying that the majority of $z \sim 2$ LAEs have very faint dust emission.

The 3σ upper limit of the dust obscured star formation rate (SFR) is calculated to be $SFR_{\rm IR} \leq 1.8\ M_\odot {\rm yr}^{-1}$ using the formula devised by Kennicutt (1998) [*18]. The unobscured SFR derived from the ultraviolet luminosity of the stacked SED, $L_{\rm UV} = 5.3^{+0.2}_{-0.2} \times 10^9\ L_\odot\ (= L_{\rm UV,typical})$, using the formula devised by Kennicutt (1998), is $SFR_{\rm UV} = 1.5^{+0.07}_{-0.07}\ M_\odot {\rm yr}^{-1}$. Thus, the ratio of obscured to unobscured SFRs is $SFR_{\rm IR}\ /\ SFR_{\rm UV} \leq 1.2$. This constraint is comparable or stronger than those for $z > 2$ LAEs obtained by Wardlow et al. (2014), $SFR_{\rm IR}\ /\ SFR_{\rm UV} \leq$2–14. The total SFR is

[*18] This formula assumes solar metallicity. It is notable that the conversion factor to SFR from UV luminosities does not depend on metallicity within the range of $\sim 0.1 Z_\odot$ to $1 Z_\odot$ as shown in figure 10 in Leitherer & Heckman (1995)

$1.5 \leq SFR_{\rm tot,IR+UV}\ M_{\odot}{\rm yr}^{-1} \leq 3.3$.

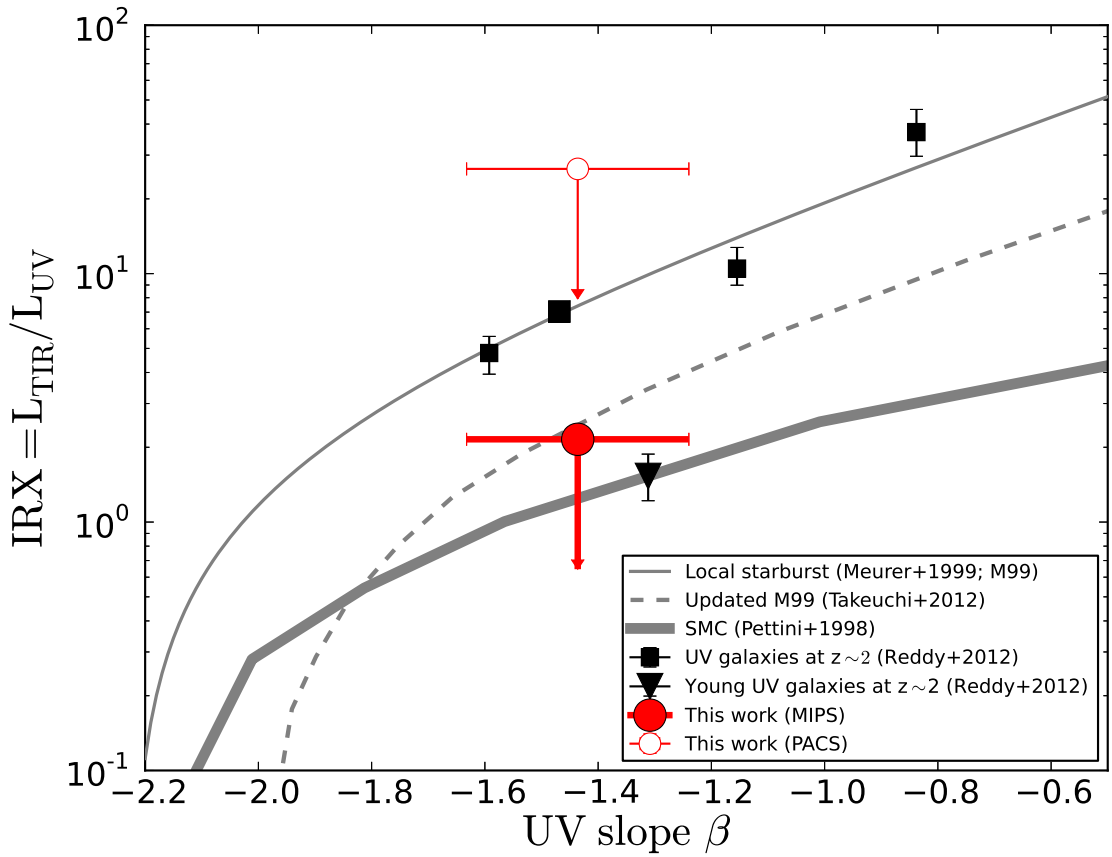

Figure 6.1 The $L_{\rm TIR}/L_{\rm UV}$ ratio, IRX, plotted against the UV slope, β. The red filled and open circles indicate our stacked LAE from the MIPS and PACS data, respectively. The black squares are for the stacking results for UV-selected galaxies binned according to various properties obtained by Reddy et al. (2012a) (largest symbol corresponding to the entire sample) and the black triangle for the stacking result for young galaxies (Reddy et al., 2012a). Three attenuation curves are overplotted: the local starburst relation (thin solid line; Meurer et al., 1999, M99); an updated M99 (dashed line; Takeuchi et al., 2012); an SMC-like attenuation curve (thick solid line; Pettini et al., 1998).

6.1.6 IRX-β relation and attenuation curve

The relation between the IR to UV luminosity ratio, $IRX \equiv L_{\rm TIR}\ /\ L_{\rm UV}$, and the slope of the UV continuum, β, is useful for constraining the attenuation curve of galaxies. Our stacked LAE has $\beta = -1.4^{+0.2}_{-0.2}$ and $IRX \leq 2.2$ using the MIPS/24 μm–based $L^{3\sigma}_{\rm TIR}$. This IRX corresponds to $A_{1600} \leq 0.9$ magnitude with the conversion formula by Overzier et al. (2011). This low IRX is in accord with the tendency seen in brighter UV-selected galaxies that IRX decreases with decreasing bolometric luminosity (e.g., Reddy et al.,

2012a). As found in Figure 6.1, these IRX and β are inconsistent with the relation for local starburst galaxies (Meurer et al., 1999) (M99, almost the same as the Calzetti curve) while consistent with an updated M99 given in Takeuchi et al. (2012) and an SMC-like attenuation curve (Pettini et al., 1998)[*19]. The original M99 gives a 3.8 times higher IRX at the observed β.

All three attenuation curves assume an intrinsic slope $\beta_{\rm int} \gtrsim -2.2$, while our best-fit SED model spectrum (shown in section 6.2.1) has $\beta_{\rm int} = -2.6$ and -2.4 with the Calzetti attenuation curve (M99 curve) and an SMC-like attenuation curves, respectively. Adopting these bluer $\beta_{\rm int}$ instead of $\gtrsim -2.2$ increases the inconsistency of the M99 in the IRX–β plot while an SMC-like attenuation curve is still consistent. The $z \sim 2$ UV selected galaxies of Reddy et al. (2012a) are distributed around the M99 except for those with very young ages. Recently, Reddy et al. (2018) find that galaxies at $z = 1.5$–2.5 prefer an SMC-like attenuation curve rather than the Calzetti curve with sub-solar metallicity stellar population models. Moreover, young/ low-$M_\star$ galaxies among their sample implies a attenuation curve even steeper than an SMC-like curve. Therefore, LAEs and young UV selected galaxies may have similar attenuation curves, which is steeper than the Calzetti curve. The PACS-based $L^{3\sigma}_{\rm TIR}$ gives a high $IRX = 28$ falling well above the M99. Indeed, the M99 is allowed in the case of $IRX \geq 8.4$. This happens if the MIPS-based $L^{3\sigma}_{\rm TIR}$ is a factor of ≥ 3.8 underestimate, i.e. the true IR8 is higher than 26. However, as discussed in section 6.1.4, such a high IR8 appears to be unlikely in our LAEs.

In chapter 3 and following chapters, we use an SMC-like curve as a fiducial attenuation curve, while we also examine the case with the M99 curve (i.e., the Calzetti attenuation curve). We discuss the IRX–$M_\star$ relation of our LAEs in section 6.4 and the origin of the dust attenuation of LAEs in section 7.2.

6.2 Results of SED fitting

The results of SED fitting to IR sample in CDFS field are shown in section 6.2.1. We compare the results with an SMC-like attenuation curve and those with the Calzetti curve. The results to the LAEs with $NB387_{\rm tot} \leq 25.5$ mag in the four fields are shown in section 6.2.2. In section 6.2.3, we show the results to subdivided LAEs in accordance with UV, Lyα and K band properties.

6.2.1 The IR-study sample in CDFS field

Table 6.1 summarizes the best-fit parameters and figure 6.2 compares the best-fit SEDs with the observed one. The two attenuation curves fit the data well. As expected from the results on the IRX–β plot, the fit using the Calzetti curve gives a 2 magnitude higher A_{1600} and a 10 times higher SFR than those calculated from the MIPS-based $L^{3\sigma}_{\rm TIR}$, while the results with an SMC-like curve are roughly consistent. The SFR from the SED fit with

[*19] We shift the original relation of Meurer et al. (1999) defined by $L_{\rm FIR}$(40-120μm) to 0.28 dex. See also footnote *11 for more details on an SMC-like attenuation curve.

the Calzetti curve is significantly larger than even the maximum $SFR_{\rm tot,IR+UV}$= 24 $M_\odot$ yr^{-1} from the PACS-based $L^{3\sigma}_{\rm TIR}$. Both curves give nearly the same stellar mass, because it is determined essentially from longer wavelengths ($\gtrsim$1 μm). The Calzetti curve gives an age less than 10 Myr, which is much shorter than dynamical times of LAEs, $\sim$ 60–260 Myr (Rhoads et al., 2014). We also note that the Calzetti curve gives too high an escape fraction of ionizing photons $f^{\rm ion}_{\rm esc}$ compared with observed values for LAEs, 10–30% (Nestor et al., 2013). These results suggest that an SMC-like curve is more appropriate than Calzetti for the majority of LAEs at $z \sim 2$. With an SMC curve, our stacked LAE has an relatively old age of 200 Myr.

Nakajima et al. (2012) have provided a stacked SED of $z \simeq 2.18$ LAEs in the Subaru/XMM-Newton Deep Field for which a less dust-sensitive SFR estimate from narrow-band Hα imaging is available. SED fitting to this stacked data finds that the $E(B-V)$ derived assuming the Calzetti curve gives an $SFR_{\rm UV,corr}$ ($\simeq$ 32 $M_\odot$yr^{-1}) which is two times higher than the Hα-based one ($SFR_{\rm H\alpha,corr}\simeq$ 14 $M_\odot$yr^{-1}), while adopting an SMC curve gives a consistent result ($SFR_{\rm UV,corr}\simeq$ 5.7 $M_\odot$yr^{-1}, $SFR_{\rm H\alpha,corr}\simeq$ 6.9 $M_\odot$yr^{-1}). Notice that $\rm E(B-V)_{gas} = E(B-V)_\star$ is assumed for modest dust-correction of the Hα luminosity. Thus we find here that an SMC-like curve is preferred. We discuss the IRX and the star formation mode in the sections 6.4 to 6.5 using the results with an SMC-like curve and the MIPS-based $L^{3\sigma}_{\rm TIR}$.

Table 6.1 Results of SED fitting for IR sample in CDFS field.

attenuation curve	$M_\star$ [$10^8 M_\odot$] (1)	$E(B-V)_\star[A_{1600}]$ [mag] (2)	Age [Myr] (3)	SFR [$M_\odot$yr^{-1}] (4)	$f^{\rm ion}_{\rm esc}$ (5)	χ^2_r (6)	$SFR_{\rm UV,corr}$ [$M_\odot$yr^{-1}] (7)
Calzetti	$3.7^{+0.1}_{-0.1}$	$0.3^{+0.00}_{-0.00}[3.0^{+0.0}_{-0.0}]$	$8.7^{+0.8}_{-1.1}$	43^{+4}_{-2}	$0.9^{+0.0}_{-0.0}$	1.02	25^{+1}_{-1}
SMC	$6.3^{+0.8}_{-2.0}$	$0.10^{+0.02}_{-0.01}[1.2^{+0.2}_{-0.1}]$	200^{+50}_{-100}	$3.7^{+1.2}_{-0.4}$	$0.4^{+0.3}_{-0.3}$	1.22	$4.9^{+1.7}_{-0.3}$

Note. — (1) The best fit stellar mass; (2) the best-fit color excess [UV attenuation]; (3) the best fit age; (4) the best fit SFR; (5) the best fit escape fraction of ionizing photons; (6) reduced chi-squared value; (7) the SFR derived from the dust-corrected UV luminosity using the best-fit A_{1600}. Metallicity and redshift are fixed to 0.2$Z_\odot$ and 2.18, respectively. The degree of freedom is 7. SFR is not a free parameter in the fit but calculated from $M_\star$ and age.

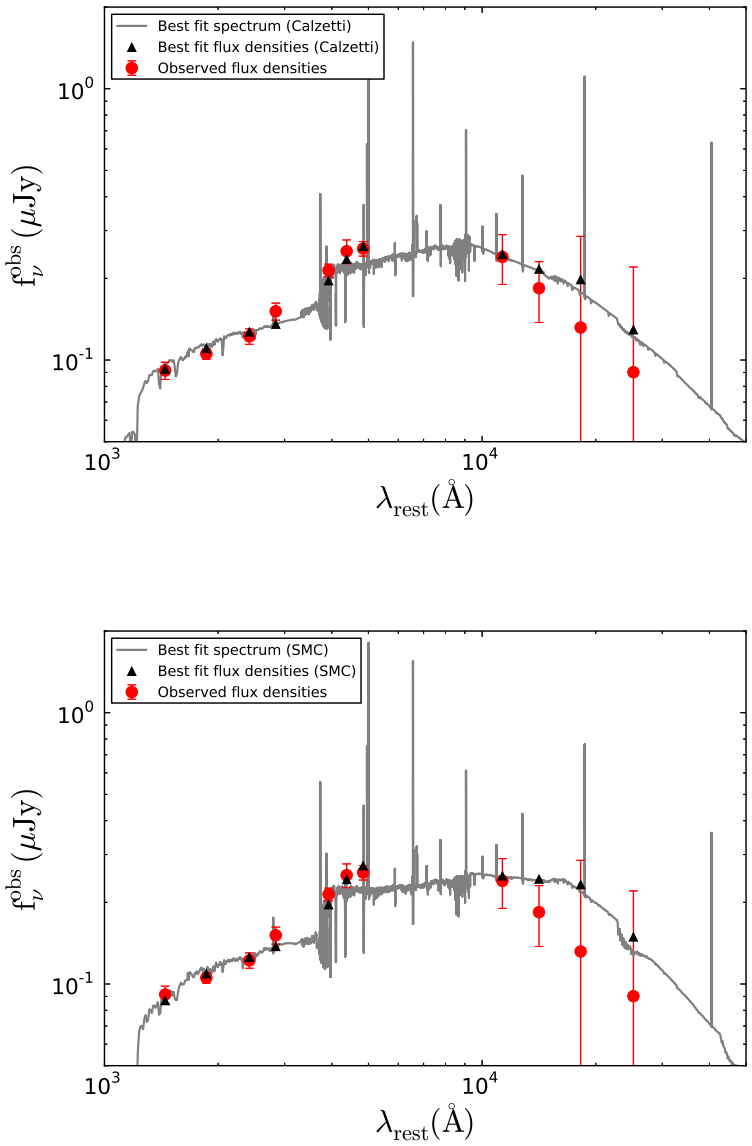

Figure 6.2 Results of SED fitting for the stacked IR sample in CDFS field (shown in Table 3.1) with the Calzetti curve (upper) and an SMC-like curve (lower). For each panel, the red filled circles show the observed flux densities, the gray lines the best-fit model spectrum, and the black filled triangles the flux densities calculated from the best-fit spectrum. The two attenuation curves fit the data well.

6.2.2 The sample with $NB387_{\rm tot} \leq 25.5$ in SXDS, COSMOS, HDFN, and CDFS fields

Table 6.2 summarizes the best-fit parameters and figure 6.3 compares the best-fit SEDs with the observed SEDs [*20] with the assumption of an SMC-like attenuation curve. The model fit the data well for each sample. The mean value for each parameter over the four fields is: $M_\star = 10.2 \pm 1.8 \times 10^8$ M$_\odot$, $A_{1600} = 0.6 \pm 0.1$ mag, age$= 3.8 \pm 0.3 \times 10^8$ yr, and $SFR = 3.4 \pm 0.4$ M$_\odot$ yr^{-1}. We discuss the IRX and the star formation mode in the sections 6.4 to 6.5 using the results with an SMC-like curve. The results with assumption of the Calzetti curve and those in the case without nebular emission, $f_{\rm esc}^{\rm ion} = 1$ are shown in appendix A.1 .

6.2.3 The subsample with UV, Lyα, K-band properties in SXDS and COSMOS fields

Figures A.3 and A.4 in appendix A.2 shows the best-fit SEDs and tables A.3 and A.4 in appendix A.2 summarize the results of the best-fit parameters in the two fields. The field-average values are shown in table 6.3 for the cases with assumption of an SMC-like attenuation curve and the Calzetti attenuation curve. The two attenuation curves fit the data equally well for each subsample. However, the best fit parameters are very different in most cases. These parameter dependencies are consistent with those in section 6.2.1.

We use the results with an SMC-like curve as our fiducial results to discuss the origin

Table 6.2 Results of SED fitting to stacked LAEs with $NB387_{\rm tot} \leq 25.5$ mag in SXDS, COSMOS, HDFN, and CDFS fields.

field	$M_\star$ (10^8M$_\odot$) (1)	$E(B-V)_\star$ [A_{1600}] (mag) (2)	Age (10^8 yr) (3)	SFR (M$_\odot$yr^{-1}) (4)	χ^2_r (5)
SXDS	$9.7^{+3.6}_{-1.7}$	$0.05^{+0.01}_{-0.02}$ [$0.6^{+0.1}_{-0.2}$]	$3.6^{+2.8}_{-1.1}$	$3.3^{+0.5}_{-0.7}$	0.604
COSMOS	$14.0^{+3.4}_{-3.6}$	$0.07^{+0.02}_{-0.02}$ [$0.8^{+0.2}_{-0.2}$]	$4.1^{+2.4}_{-1.8}$	$4.2^{+1.2}_{-0.8}$	0.473
HDFN	$7.6^{+4.0}_{-1.9}$	$0.06^{+0.02}_{-0.03}$ [$0.7^{+0.2}_{-0.4}$]	$3.2^{+4.0}_{-1.4}$	$2.9^{+0.8}_{-0.8}$	1.298
CDFS	$10.3^{+11.1}_{-9.7}$	$0.02^{+0.07}_{-0.01}$ [$0.2^{+0.8}_{-0.1}$]	$5.7^{+8.6}_{-5.7}$	$2.2^{+534}_{-0.4}$	0.120
Average	10.2 ± 1.8	0.06 ± 0.01 [0.6 ± 0.1]	3.8 ± 0.3	3.4 ± 0.4	

Note. — (1) The best fit stellar mass; (2) the best-fit color excess [UV attenuation]; (3) the best fit age; (4) the best fit SFR; (5) reduced chi-squared value. The UV attenuation is derived from an SMC-like attenuation curve. Metallicity, redshift, and $f_{\rm esc}^{\rm ion}$ are fixed to $0.2Z_\odot$, 2.18, and 0.2, respectively.

[*20] The uncertainties in the best fit parameters in the CDFS are large since the number of LAEs used in stacking analysis is smaller than those in the other fields as shown in table 2.5. Moreover, the i, z and H band images in this field are $\sim$ 0.5–2 mag shallower than those in the other fields.

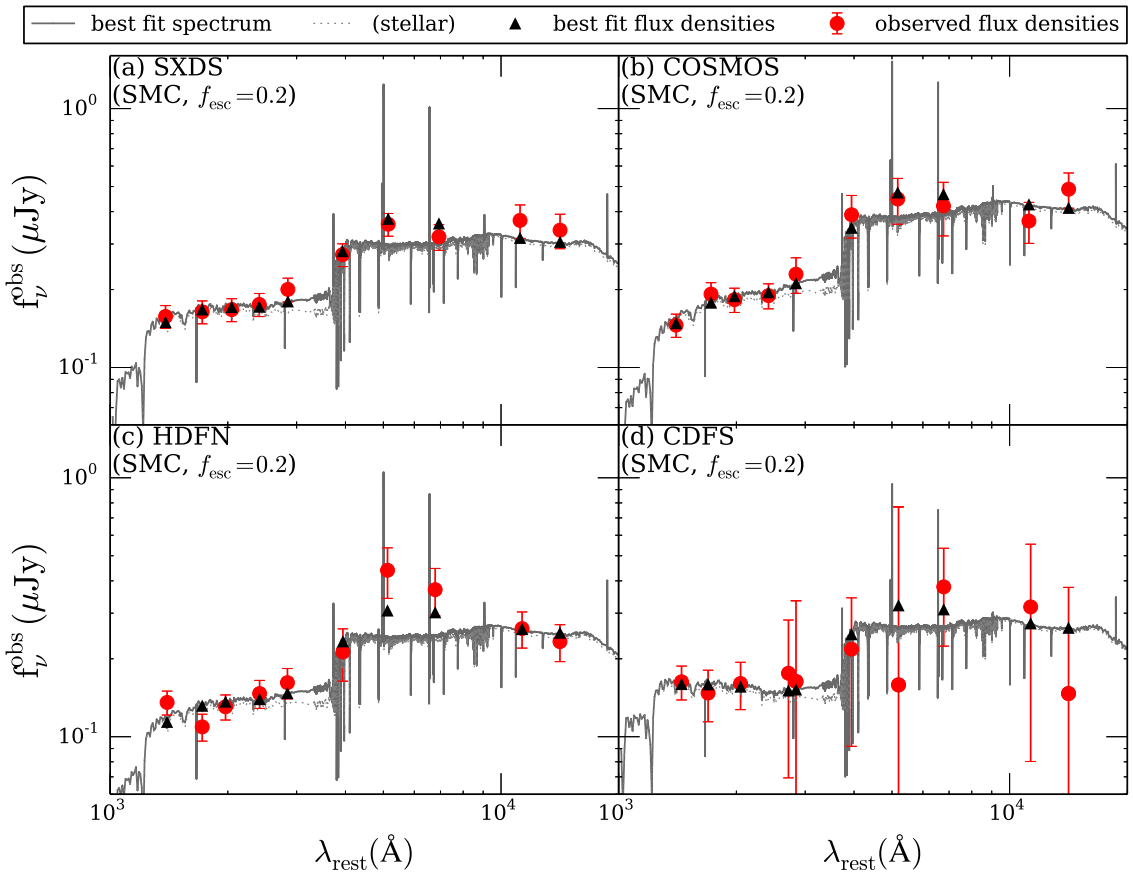

Figure 6.3 Results of SED fitting to stacked LAEs with $NB387_{tot} \leq 25.5$ mag in SXDS, COSMOS, HDFN, and CDFS fields from panels (a) to (d). For each panel, a gray solid line and a light gray dotted line show the best-fit model spectrum and its stellar continuum component, respectively. The difference of these two lines shows a contribution of its nebular continuum component. Red filled circles and black filled triangles represent the observed flux densities and the flux densities calculated from the best-fit spectrum, respectively.

of Lyα halo in chapter 8, while we use those with the Calzetti curve to compare them with previous results assuming the Calzetti curve as well as to discuss Lyα escape fraction conservatively in chapter 9. In sections 6.4.2 and 6.5.2, we compare the IRX and star formation mode of our subsamples with the average relations of star forming galaxies and examine whether they are normal galaxies in terms of these two properties, which will be employed in the discussion of the origin of LAHs in chapter 8.

Table 6.3 The field-average values of parameters obtained by SED fitting, $f_{\rm esc}({\rm Ly}\alpha)_{\rm tot}$, and the q-parameter for subsamples.

subsample	$M_\star$ ($10^8 M_\odot$) (1)	$E(B-V)_\star$ (mag) (2)	Age (Myr) (3)	SFR ($M_\odot {\rm yr}^{-1}$) (4)	$f_{\rm esc}({\rm Ly}\alpha)_{\rm tot}$ (5)	q-parameter (6)
SMC-like attenuation curve						
bright UV	14.1 ± 2.1	0.08 ± 0.01	240 ± 14	6.8 ± 1.3	0.37 ± 0.00	$0.80^{+0.11}_{-0.09}$
faint UV	4.1 ± 0.1	0.03 ± 0.01	280 ± 46	1.7 ± 0.3	1.43 ± 0.17	$-0.69^{+0.30}_{-0.62}$
blue β	4.8 ± 2.4	0.02 ± 0.00	246 ± 145	2.1 ± 0.0	1.21 ± 0.10	$-0.52^{+0.25}_{-0.27}$
red β	14.0 ± 0.9	0.10 ± 0.01	286 ± 0	5.8 ± 0.4	0.43 ± 0.08	$0.57^{+0.14}_{-0.11}$
bright Lyα	7.4 ± 0.8	0.04 ± 0.02	346 ± 80	2.2 ± 0.7	1.20 ± 0.35	$-0.28^{+0.57}_{-0.57}$
faint Lyα	12.3 ± 1.0	0.07 ± 0.01	360 ± 0	4.2 ± 0.3	0.49 ± 0.00	$0.64^{+0.10}_{-0.08}$
large EW	5.4 ± 1.6	0.04 ± 0.02	338 ± 19	1.8 ± 0.6	1.34 ± 0.42	$-0.46^{+0.60}_{-0.71}$
small EW	13.7 ± 3.4	0.07 ± 0.01	353 ± 40	5.0 ± 0.7	0.42 ± 0.02	$0.79^{+0.14}_{-0.11}$
bright K	18.3 ± 2.2	0.09 ± 0.01	265 ± 84	6.5 ± 1.2	0.36 ± 0.01	$0.72^{+0.09}_{-0.08}$
faint K	3.6 ± 0.4	0.04 ± 0.01	160 ± 44	2.3 ± 0.2	1.03 ± 0.04	$-0.04^{+0.06}_{-0.07}$
the Calzetti attenuation curve						
bright UV	12.9 ± 1.6	0.15 ± 0.02	118 ± 21	11.7 ± 3.4	0.20 ± 0.02	$0.96^{+0.16}_{-0.12}$
faint UV	2.9 ± 0.3	0.10 ± 0.03	73 ± 37	3.3 ± 1.3	0.74 ± 0.25	$0.27^{+0.46}_{-0.26}$
blue β	3.4 ± 2.4	0.06 ± 0.02	106 ± 112	2.9 ± 0.6	0.87 ± 0.08	$0.21^{+0.21}_{-0.14}$
red β	13.7 ± 2.6	0.18 ± 0.00	133 ± 30	11.8 ± 0.3	0.21 ± 0.02	$0.78^{+0.05}_{-0.05}$
bright Lyα	4.2 ± 0.6	0.14 ± 0.05	39 ± 24	6.1 ± 4.2	0.43 ± 0.29	$0.55^{+1.06}_{-0.34}$
faint Lyα	12.0 ± 1.2	0.14 ± 0.02	189 ± 11	7.1 ± 1.1	0.27 ± 0.02	$0.84^{+0.15}_{-0.11}$
large EW	3.7 ± 0.8	0.14 ± 0.03	60 ± 11	4.9 ± 2.6	0.50 ± 0.24	$0.46^{+0.51}_{-0.26}$
small EW	13.2 ± 3.6	0.14 ± 0.02	191 ± 11	8.8 ± 1.9	0.24 ± 0.03	$0.92^{+0.18}_{-0.13}$
bright K	11.2 ± 2.7	0.20 ± 0.02	46 ± 24	17.9 ± 6.4	0.13 ± 0.02	$0.93^{+0.14}_{-0.11}$
faint K	2.3 ± 0.9	0.11 ± 0.03	32 ± 25	4.1 ± 1.8	0.56 ± 0.18	$0.49^{+0.46}_{-0.25}$

Note. — (1) Stellar mass, (2) color excess, (3) age, (4) SFR, (5) $f_{\rm esc}({\rm Ly}\alpha)_{\rm tot}$ calculated from SFR and $L({\rm Ly}\alpha)_{\rm tot}$, and (6) q calculated from $f_{\rm esc}({\rm Ly}\alpha)_{\rm tot}$ and $E(B-V)_\star$.

6.3 Results of clustering analysis

The results of clustering analysis for the $NB387$ limiting magnitude samples in the four fields are described in sections 6.3.1 to 6.3.4. We compare our results with those in previous studies on LAEs and HAEs. We also evaluate an effect of cosmic variance on the results for our LAEs and previous results for LAEs. We also show the results for the subdivided LAEs in accordance with UV, LYα, and K-band properties in section 6.3.5.

6.3.1 The angular correlation function of the $NB387$ limiting samples

The best-fit ACFs are shown in figure 6.4. The data points for each subsamples are fitted well. The averages of the best-fit ACFs for the subsamples with $NB387_{\rm tot}\leq$25.0 mag, $NB387_{\rm tot}\leq$25.3 mag, and $NB387_{\rm tot}\leq$25.5 mag are derived over the four fields, while that with $NB387_{\rm tot}\leq$25.8 mag are derived over the two fields, CDFS and HDFN fields. For $NB387_{\rm tot}\leq$26.3 mag, we regard the result of the CDFS (shown in 6.4[d]) as the best-fit average since the other three fields have no data. The A_ω with $NB387_{\rm tot}\leq$26.3 mag is larger than the field-average A_ω with the other limiting magnitudes. It is possibly caused by cosmic variance due to the small survey area (see section 6.3.3 for more details). We do not include the $NB387_{\rm tot}\leq$26.3 subsample in the discussion in section 6.3.2. The value of the contamination-corrected correlation length, $r_{0,\,\rm corr}$ and its $1\,\sigma$ error are calculated from $A_{\omega,\,\rm corr}$ and $\Delta A_{\omega,\,\rm corr}$. Table 6.4 summarizes the results of the clustering analysis.

6.3.2 The bias factor for the $NB387$ limiting samples

Figure 6.5(a) shows $b_{\rm g,\,eff}$ for the cumulative subsamples in the four fields, where Lyα luminosity limits are calculated from the limiting $NB387$ magnitudes of the subsamples. We find that the average bias value of our LAEs (represented by black stars in panel (a) and also by red stars in panel (b)) does not significantly change with the Lyα luminosity limit. A possible change in $b_{\rm g,\,eff}$ over $L_{{\rm Ly}\alpha}\simeq 4$–$10\times10^{41}$ erg s^{-1} is less than 20% since the uncertainties in the average biases are $\sim$ 10–20%.

This weak dependence may be partly due to radiative transfer effects on Lyα photons. Star forming galaxies in more massive (i.e., larger bias) halos are thought to have higher $SFRs$ and thus brighter nebular emission lines. Indeed, Cochrane et al. (2017) have found a significant positive correlation between Hα luminosity and bias for bright $z=2.23$ HAEs, indicating a similarly strong correlation between intrinsic Lyα luminosity and bias for bright galaxies. However, such a strong correlation, if any, weakens when observed Lyα luminosity is used in place, because brighter (i.e., more massive) galaxies have lower Lyα escape fractions, $f_{\rm esc}^{{\rm Ly}\alpha}$ (e.g., Vanzella et al., 2009; Matthee et al., 2016). Indeed, our cumulative subsamples do not show a significant correlation between the observed Lyα luminosity and the total SFR (derived from SED fitting in the same manner as described in section 3.3) but rather show a positive correlation between the observed Lyα luminosity and the Lyα escape fraction, where the intrinsic Lyα luminosity is calcu-

Table 6.4 Clustering measurements of our LAE sample with $NB387$ limiting magnitudes.

Field $NB387_{\rm tot}$ (mag)	A_ω	$A_{\omega,\,\rm corr}$	$r_{0,\,\rm corr}$ ($\rm h_{100}^{-1}Mpc$)	$b_{\rm g,\,eff}$	$M_{\rm h}$ ($\times 10^{10}$ $\rm M_\odot$)	reduced χ^2_ν	IC
	(1)	(2)	(3)	(4)	(5)	(6)	(7)
SXDS							
≤25.0	4.70 ± 2.86	5.80 ± 3.75	$2.78^{+0.89}_{-1.22}$	$1.40^{+0.40}_{-0.57}$	$10.1^{+28.8}_{-10.1}$	1.74	0.0137
≤25.3	2.07 ± 1.27	2.56 ± 1.67	$1.77^{+0.57}_{-0.78}$	$0.93^{+0.27}_{-0.38}$	$0.4^{+3.2}_{-0.4}$	5.40	0.0060
≤25.5	3.35 ± 0.78	4.14 ± 1.33	$2.31^{+0.39}_{-0.45}$	$1.18^{+0.18}_{-0.21}$	$3.3^{+5.2}_{-2.7}$	3.02	0.0097
COSMOS							
≤25.0	3.88 ± 3.03	4.79 ± 3.88	$2.50^{+0.98}_{-1.51}$	$1.27^{+0.44}_{-0.72}$	$5.5^{+25.3}_{-5.5}$	0.89	0.0176
≤25.3	4.44 ± 1.81	5.48 ± 2.54	$2.70^{+0.64}_{-0.79}$	$1.36^{+0.29}_{-0.36}$	$8.5^{+16.6}_{-7.7}$	1.11	0.0201
≤25.5	3.32 ± 1.25	4.10 ± 1.79	$2.29^{+0.51}_{-0.63}$	$1.18^{+0.23}_{-0.29}$	$3.1^{+7.5}_{-2.9}$	0.62	0.0150
≤25.8	3.70 ± 0.70	4.57 ± 1.33	$2.44^{+0.37}_{-0.42}$	$1.24^{+0.17}_{-0.20}$	$4.7^{+6.0}_{-3.5}$	0.95	0.0168
HDFN							
≤25.0	6.89 ± 3.77	8.51 ± 5.03	$3.44^{+1.01}_{-1.35}$	$1.70^{+0.44}_{-0.61}$	$29.3^{+55.5}_{-27.6}$	0.81	0.0319
≤25.3	9.55 ± 2.28	11.79 ± 3.84	$4.13^{+0.70}_{-0.81}$	$2.00^{+0.30}_{-0.36}$	$62.9^{+52.0}_{-38.3}$	1.33	0.0441
≤25.5	5.18 ± 1.51	6.40 ± 2.34	$2.94^{+0.56}_{-0.66}$	$1.47^{+0.25}_{-0.30}$	$13.6^{+17.7}_{-10.5}$	0.95	0.0240
≤25.8	2.52 ± 0.75	3.11 ± 1.15	$1.97^{+0.38}_{-0.45}$	$1.03^{+0.18}_{-0.21}$	$1.0^{+2.6}_{-0.9}$	1.12	0.0116
CDFS							
≤25.0	3.78 ± 11.89	4.67 ± 14.72	$2.47^{+2.97}_{-2.47}$	$1.26^{+1.30}_{-1.26}$	$5.0^{+170.0}_{-5.0}$	0.71	0.0215
≤25.3	5.43 ± 8.12	6.70 ± 10.14	$3.02^{+2.02}_{-3.02}$	$1.51^{+0.88}_{-1.51}$	$15.5^{+117.8}_{-15.5}$	0.61	0.0309
≤25.5	5.47 ± 6.34	6.75 ± 7.97	$3.03^{+1.64}_{-3.03}$	$1.51^{+0.72}_{-1.51}$	$15.8^{+85.5}_{-15.8}$	1.07	0.0311
≤25.8	2.61 ± 3.43	3.22 ± 4.29	$2.01^{+1.21}_{-2.01}$	$1.04^{+0.55}_{-1.04}$	$1.2^{+20.0}_{-1.2}$	0.94	0.0148
≤26.3	8.62 ± 1.49	10.64 ± 2.99	$3.90^{+0.58}_{-0.65}$	$1.90^{+0.25}_{-0.29}$	$50.2^{+35.9}_{-28.0}$	1.66	0.0490
field average (#)							
≤25.0 (4)	4.69 ± 1.70	5.80 ± 2.46	$2.78^{+0.60}_{-0.74}$	$1.40^{+0.27}_{-0.34}$	$10.1^{+17.0}_{-8.8}$	0.75	
≤25.3 (4)	4.04 ± 0.90	4.99 ± 1.57	$2.56^{+0.42}_{-0.48}$	$1.30^{+0.19}_{-0.22}$	$6.3^{+8.3}_{-4.8}$	2.04	
≤25.5 (4)	3.55 ± 0.58	4.39 ± 1.21	$2.38^{+0.34}_{-0.39}$	$1.22^{+0.16}_{-0.18}$	$4.0^{+5.1}_{-2.9}$	1.01	
≤25.8 (3)	2.75 ± 0.45	3.40 ± 0.94	$2.07^{+0.30}_{-0.34}$	$1.07^{+0.14}_{-0.16}$	$1.5^{+2.4}_{-1.2}$	1.08	
≤26.3 (1)	8.62 ± 1.49	10.64 ± 2.99	$3.90^{+0.58}_{-0.65}$	$1.90^{+0.25}_{-0.29}$	$50.2^{+35.9}_{-28.0}$	1.66	

Note. — Note. (1) The best fit correlation amplitude without $f_{\rm c}$ correction; (2) the best fit correlation amplitude with $f_{\rm c}$ correction used to derive (3)–(5); (3) the best fit (contamination-corrected) correlation length; (4) the best fit effective bias factor (contamination-corrected); (5) the best fit effective dark matter halo mass (contamination-corrected); (6) reduced chi-squared value; (7) the best fit integral constant; The value in parentheses (#) shows the number of fields used to calculate the field-average correlation amplitude using equation 4.15.

lated from the total SFR (Brocklehurst, 1971; Kennicutt, 1998).

Moreover, some previous studies have found that high-redshift UV-selected galaxies with comparably faint UV luminosities ($L_{\rm UV}$) to our LAEs (the average absolute magnitude of our LAEs is $M_{\rm UV} \sim -19$ mag) have weak dependence of $b_{\rm g}$ on UV luminosity ($z \sim 3$–4 Lyman break galaxies (LBGs): Ouchi et al., 2004, 2005; Harikane et al., 2016; Bielby et al., 2016, see however, Lee et al. (2006) who find significant dependence for $z \sim 4$–5 LBGs), suggesting that the correlation between intrinsic Lyα luminosity and bias is not so strong for typical LAEs with modest Lyα luminosities.

The faintest limiting Lyα luminosity at which $b_{\rm g,\,eff}$ measurements are available for all four fields is $L_{{\rm Ly}\alpha} = 6.2 \times 10^{41}$ erg s^{-1} (corresponding to 25.5 mag in $NB387$). In order to reduce the uncertainty due to cosmic variance as much as possible, we adopt the average $b_{\rm g,\,eff}$ at this limiting luminosity, $b^{\rm ave}_{\rm g,\,eff} = 1.22^{+0.16}_{-0.18}$, as the average $b_{\rm g,\,eff}$ of our entire sample.

This average bias is lower than that of the previous work on narrow-band-selected LAEs at $z \sim 2.1$, $b_{\rm g,\,eff} = 1.8 \pm 0.3$ (Guaita et al., 2010, see the blue point in panel (b) of figure 6.5), with a probability of 96%. The median Lyα luminosity of their sample is $L_{{\rm Ly}\alpha} = 1.3 \times 10^{42}$ erg s^{-1} and their 5σ detection limit in Lyα luminosity is $L_{{\rm Ly}\alpha} = 6.3 \times 10^{41}$ erg s^{-1}, which is similar to the luminosity limit of our $NB387 \leq 25.5$ samples. Our clustering method is essentially the same as of Guaita et al. (2010) and in both studies the bias value is calculated at $r = 8\,h^{-1}_{100}$Mpc. Although we use a slightly different cosmological parameter set, ($\Omega_{\rm m}$, Ω_Λ, h, σ_8)=(0.3, 0.7, 0.7, 0.8), from theirs, ($\Omega_{\rm m}$, Ω_Λ, h, σ_8)=(0.26, 0.74, 0.7, 0.8), using Guaita et al. (2010)'s set changes $b_{\rm g,\,eff}$ only negligibly. Our contamination fraction, $f_{\rm c} = 10 \pm 10\%$, is comparable to or slightly conservative than theirs, $f_{\rm c} = 7 \pm 7\%$. The error in Guaita et al. (2010)'s $b_{\rm g,\,eff}$ is a quadrature sum of the uncertainty in $f_{\rm c}$ and the fitting error (statistical error), with the latter dominating because of the small sample size (250 objects). As discussed in section 4.4, their high $b_{\rm g,eff}$ value is attributable to cosmic variance since their survey area is approximately one third of ours (see figure 6.6(b)). Indeed, the sky distribution of their LAEs has a large scale excess at the north-west part and the ACF measurements seem to deviate to higher values from the best-fit power law at large scales because of it[*21].

[*21] We do not include the result of Guaita et al. (2010) when calculating the average bias.

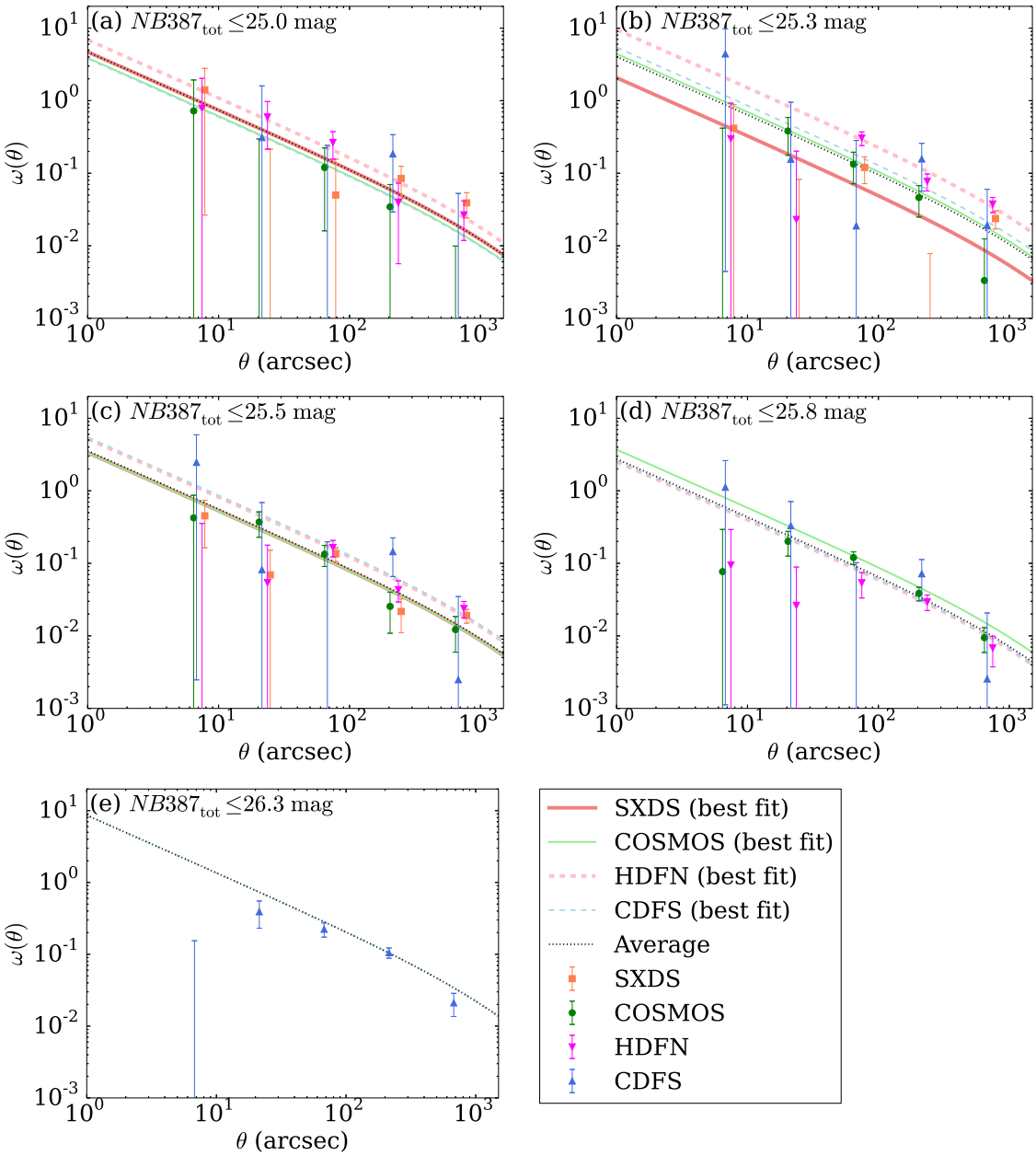

Figure 6.4 ACF measurements for LAEs with $NB387_{\rm tot}$≤25.0 mag (panel [a]), $NB387_{\rm tot}$≤25.3 mag ([b]), $NB387_{\rm tot}$≤25.5 mag ([c]), $NB387_{\rm tot}$≤25.8 mag ([d]), and $NB387_{\rm tot}$≤26.3 mag ([e]). For each panel, colored symbols (orange squares, green circles, magenta inverted triangles, and blue triangles) represent measurements in SXDS, COSMOS, HDFN, and CDFS, respectively. Colored lines, as labeled in the lower right panel, indicate the best-fit ACFs with fixed $\beta = 0.8$ in SXDS, COSMOS, HDFN, and CDFS, respectively. A dotted black line shows the average of the best-fit ACFs over the four fields. In panels (a)-(d), we slightly shift all data points along the abscissa by a value depending on the field for presentation purposes.

6.3.3 The cosmic variance on bias factor for the $NB387$ limiting samples

Our average effective bias value and that of Guaita et al. (2010) are not consistent within the $1\,\sigma$ uncertainties in spite of similar limiting Lyα luminosities. Biases derived from limited survey areas possibly suffer from cosmic variance due to spatial variations in the ACF of dark matter. In section 4.4, we analytically estimate cosmic variance in the bias value. We show the uncertainties in the amplitude of the dark matter ACF, $\frac{\Delta\omega_{\rm DM}}{\omega_{\rm DM}}$, as a function of survey area by a light gray solid line in figure 6.6 (a). We find $\frac{\Delta\omega_{\rm DM}}{\omega_{\rm DM}} \simeq 53\%$ for $\Omega_{\rm s} = 0.25$ deg^2, a typical area of the four survey fields, and $\simeq 26\%$ for the entire survey area ($\simeq 1$ deg^2).

Sobral et al. (2010) have empirically estimated relative uncertainties in ACF measurements for NB-selected $z = 0.85$ HAEs as a function of area by dividing their survey regions, $\simeq 1.3$ deg^2 in total, into sub regions with different sizes (green squares in figure 6.6(a)). This empirical relation has been used to estimate cosmic variance in ACF measurements in a $\simeq 2\,$deg^2 survey area of emission line galaxies at $z \sim 0.8$–4.7 in Khostovan et al. (2018). Our analytic method applied to the Sobral et al. (2010) survey with their own NB filter (over the same fitting range of θ as that for our LAEs for simplicity), however, gives larger uncertainties as shown by a green solid line in figure 6.6(a). This may be partly because the area of Sobral et al. (2010)'s survey is not large enough to catch the total variance. Our analytic estimation seems to be more conservative than theirs.

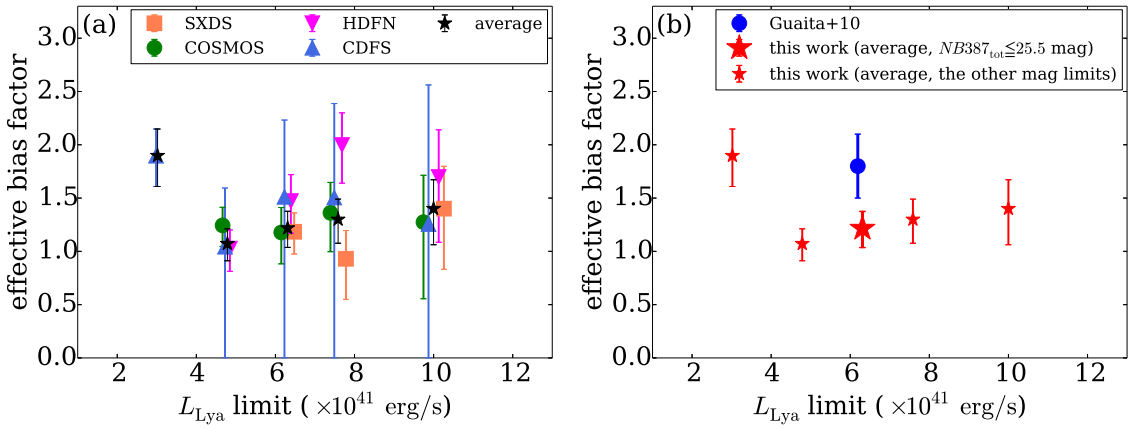

Figure 6.5 Bias value plotted against Lyα limiting luminosity for the $NB387$ limiting magnitude sample in the four fields. Panel (a). Orange squares, green circles, magenta inverted triangles, and blue triangles represent SXDS, COSMOS, HDFN, and CDFS fields, respectively. Black stars indicate the average (weighted mean) over available fields at each limiting luminosity (also shown by red stars in panel (b)). For presentation purposes, we slightly shift all of the points except for the black stars along the abscissa. Panel (b). The measurements shown by the small black stars in panel (a) are plotted by the small red stars except for the value at Lyα $_{\rm limit} \simeq 6 \times 10^{41}$ erg s^{-1} (or $NB387_{\rm tot} \leq 25.5$ mag) shown by a large red star. Guaita et al. (2010)'s measurement is also plotted by a blue circle.

We expect that Guaita et al. (2010)'s $b_{\mathrm{g,\ eff}}$ obtained from ~ 0.28 deg^2 area has also a $\simeq 51\%$ uncertainty using their $NB3727$ filter (solid blue line in figure 6.6(a)). The $1\,\sigma$ uncertainty in an observed bias including cosmic variance, $\Delta b_{\mathrm{g,\ eff,\,CV}}$, is given by:

$$\frac{\Delta b_{\mathrm{g,\ eff,\,CV}}}{b_{\mathrm{g,\ eff}}} \simeq \frac{1}{2}\sqrt{\left(\frac{\Delta A_\omega}{A_\omega}\right)^2 + \left(\frac{2\Delta f_c}{f_c}\right)^2 + \left(\frac{\Delta\omega_{\mathrm{DM}}}{\omega_{\mathrm{DM}}}\right)^2} \tag{6.1}$$

$$\simeq \frac{1}{2}\sqrt{\left(\frac{2\Delta b_{\mathrm{g,\,eff}}}{b_{\mathrm{g,\,eff}}}\right)^2 + \left(\frac{\Delta\omega_{\mathrm{DM}}}{\omega_{\mathrm{DM}}}\right)^2}, \tag{6.2}$$

where $\Delta b_{\mathrm{g,\,eff}}$ is the $1\,\sigma$ error in $b_{\mathrm{g,\,eff}}$.

By updating the errors using this equation (where for our $b_{\mathrm{g,\,eff}}$ the plus and minus errors are treated separately), our average effective bias and that of Guaita et al. (2010) are written as $b^{\mathrm{ave}}_{\mathrm{g,\,eff,\,CV}} = 1.22^{+0.23}_{-0.26}$ and $b_{\mathrm{g,\,eff,\,CV}} = 1.8 \pm 0.55$, respectively, thus becoming consistent with each other within the errors (see figure 6.6(b)). We also note that the relatively large scatter of $b_{\mathrm{g,\ eff}}$ among the four fields at each limiting Lyα luminosity seen

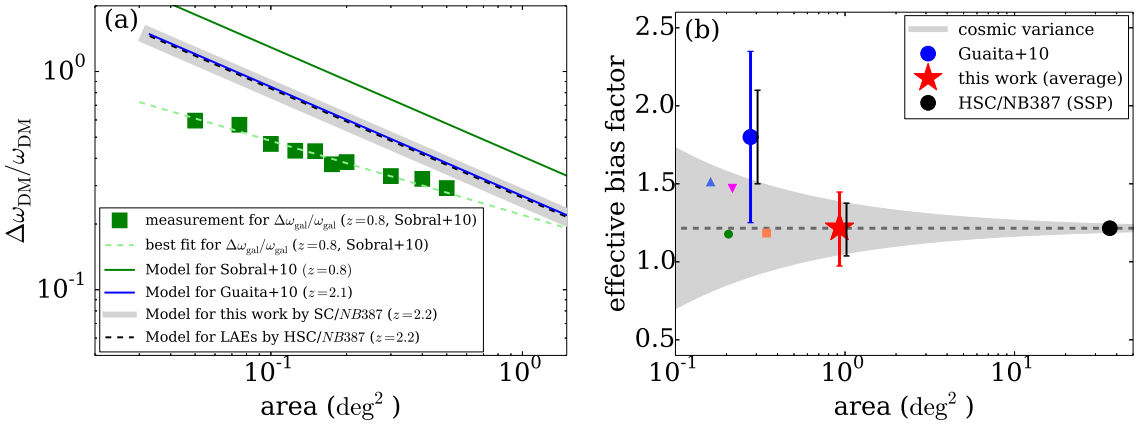

Figure 6.6 Effect of cosmic variance on clustering analysis. Panel (a). Uncertainties in the amplitude of the dark matter ACF as a function of survey area. Green squares and a light green dashed line denote the empirical measurements at $z \sim 0.8$ and the best-fit power law to them, respectively, by Sobral et al. (2010, : $\Delta\omega_{\mathrm{gal}}/\omega_{\mathrm{gal}}$). Other lines show our analytic calculations for four NB surveys: green solid line for Sobral et al. (2010), lightgray thick solid line for this study (Suprime-Cam/$NB387$), blue solid line for Guaita et al. (2010), and black dashed line for an on-going Hyper Suprime-Cam/$NB387$ survey. Panel (b). Effective bias factor as a function of survey area. The cosmic variance on $b^{\mathrm{ave}}_{\mathrm{g,\,eff}}$, which is indicated by a light gray thick solid line in panel (a), is shown by a light gray filled region around $b^{\mathrm{ave}}_{\mathrm{g,\,eff}}$ (fixed) shown by a dim gray dashed line. A red star and a blue circle indicate the $b^{\mathrm{ave\,CV}}_{\mathrm{g,\,eff}}$ in this work and the $b_{\mathrm{g,\,eff\,CV}}$ in Guaita et al. (2010), respectively, where colored error bars include the uncertainty due to cosmic variance while black bars next to them do not. A black circle corresponds to the expected HSC/$NB387$ survey area when completed. A small orange square, green circle, magenta inverted triangle, and blue triangle represent $b_{\mathrm{g,\,eff}}$ with $NB387 \leq 25.5$ mag from SXDS, COMOS, HDFN, and CDFS, respectively.

in figure 6.5(a) may be partly due to cosmic variance although the observational errors are too large to confirm it (see figure 6.6(b)). All the best-fit $b_{\mathrm{g,\ eff}}$ values for the four fields fall within the 1σ uncertainty range from cosmic variance shown by a shaded light gray region in figure 6.6(b).

6.3.4 The field-average dark matter halo mass for the sample with $NB387_{\mathrm{tot}} \leq 25.5$ mag

The effective halo mass of each sub-sample is listed in table 6.4. The field average of effective halo masses corresponding to the field average of effective biases of our LAEs with $NB387_{\mathrm{tot}} \leq 25.5$ mag, $b^{\mathrm{ave}}_{\mathrm{g,\,eff}} = 1.22^{+0.16}_{-0.18}$, is $4.0^{+5.1}_{-2.9} \times 10^{10}$ $\mathrm{M}_{\odot}$. This value is roughly comparable to previous measurements for $z \sim 3$–7 LAEs with similar Lyα luminosities, $M_{\mathrm{h}} \simeq 10^{10}$–$10^{12}$ $\mathrm{M}_{\odot}$ (e.g., Ouchi et al., 2005, 2010; Kovač et al., 2007; Gawiser et al., 2007; Shioya et al., 2009; Bielby et al., 2016; Diener et al., 2017; Ouchi et al., 2018), suggesting that the mass of dark haloes which can host typical LAEs is roughly unchanged with time.

The average M_{h} of our LAEs is smaller than those of HAEs at $z \sim 1.6$ (Kashino et al., 2017), $M_{\mathrm{h}} \sim 7 \times 10^{12}$ $\mathrm{M}_{\odot}$, and at $z \sim 2.2$, a few times 10^{12} $\mathrm{M}_{\odot}$ (Cochrane et al., 2017). The typical dust-corrected Hα luminosity, $L_{\mathrm{H}\alpha,\,\mathrm{corr}}$, of our LAEs is estimated to be $4.3 \pm 0.9 \times 10^{41}$ erg s^{-1} from the SFR obtained by SED fitting in section 6.2.2 using the conversion formula given in Kennicutt (1998) on the assumption of case B recombination. This Hα luminosity corresponds to an effective halo mass of $M_{\mathrm{h,eff}} = 5.2^{+4.8}_{-2.7} \times 10^{10}$ $\mathrm{M}_{\odot}$ according to the redshift independent relation between the normalized luminosity $L_{\mathrm{H}\alpha,\,\mathrm{corr}}/L^{\star}_{\mathrm{H}\alpha}(z)$ and $M_{\mathrm{h,eff}}$ found by Cochrane et al. (2017). The estimated halo mass of our LAEs, $M_{\mathrm{h}} = 4.0^{+5.1}_{-2.9} \times 10^{10}$ $\mathrm{M}_{\odot}$, is thus consistent with this relation. This result supports the result by Shimakawa et al. (2017) and Hagen et al. (2016) that the stellar properties of LAEs at $z \sim 2-3$ do not significantly differ from those of other emission galaxies such as HAEs and [O III] emitters. However, Cochrane et al. (2017) assume a constant dust attenuation against Hα luminosity, $A_{H\alpha} = 1.0$ mag, for all HAEs, which is larger than that of our LAEs, $A_{H\alpha} \sim 0.13 \pm 0.04$ mag, derived from the average $E(B-V)$ in table 6.2. If the (extrapolated) relation overestimates $L_{\mathrm{H}\alpha,\,\mathrm{corr}}$ at low halo masses owing to overestimation of $A_{\mathrm{H}\alpha}$, then the true log-log slope of $L_{\mathrm{H}\alpha,\,\mathrm{corr}}$ as a function of M_{h} would be steeper, implying that our LAEs would lie above the relation (see also section 6.6.2 and figure 6.12).

6.3.5 The field-average dark matter halo masses for the subdivided samples

Table 6.5 summarizes the results of the clustering analysis for the subdivided LAEs in accordance with UV, Lyα, and K-band properties. The value of the contamination-corrected correlation length, $r_{0,\,\mathrm{corr}}$ and its $1\,\sigma$ error are calculated from $A_{\omega,\,\mathrm{corr}}$ and $\Delta A_{\omega,\,\mathrm{corr}}$. The effective bias and the effective halo mass of each subsample are calculated in the same manner as for the $NB387$ limiting magnitude samples (as described in sections 4.2 and 4.3).

We do not perform clustering analysis for the K-divided subsamples as described in section 2.5.2. The best-fit ACFs for the two fields and their field-average values are shown in figure B.1 in appendix B.1. We do not plot the $M_{\rm h}$ of the UV bright and blue β subsamples (figures 6.13 and 8.1), since they are not constrained well. This is partly because at small r_0 values like those of these two subsamples, $M_{\rm h}$ depends very sensitively on r_0 according to the bias model (see appendix B in Khostovan et al., 2018). The differences in the ACF measurement (i.e., bias) between the two fields is described in section 6.3.2.

We use $M_{\rm h}$ to discuss the origin of Lyα halo in chapter 8. Here we do not include the effect of cosmic variance in the 1σ uncertainties of $M_{\rm h}$, because poisson errors are due to the poor sample sizes.

6.4 IRX–$M_\star$ relation

Star-forming galaxies have a positive correlation that more massive ones have higher IRXs. The $IRX \equiv L_{\rm IR}/L_{\rm UV}$ is an indicator of dustiness, where $L_{\rm IR}$ and $L_{\rm UV}$ are IR (8–1000μm) and UV (1530Å) luminosities, respectively (e.g., Reddy et al., 2010; Whitaker et al., 2014; Álvarez-Márquez et al., 2016; Fudamoto et al., 2017; McLure et al., 2018; Koprowski et al., 2018). The IRX can be calculated from the UV attenuation A_{1530} (e.g., Meurer et al., 1999). Buat et al. (2012) have found that high-z galaxies ($z \simeq 0.95 - 2.2$) follow the relation for local galaxies given in Overzier et al. (2011):

$$\log_{10} IRX = \log_{10}(10^{0.4A_{1530}} - 1) - \log_{10}(0.595), \tag{6.3}$$

Table 6.5 Clustering measurements for the eight subsamples.

subsamples	A_ω	$A_{\omega,\,\rm corr}$	$r_{0,\,\rm corr}$ ($\rm h_{100}^{-1}Mpc$)	$b_{\rm g,\,eff}$	$M_{\rm h}$ ($\times 10^{10}$ $\rm M_\odot$)	reduced χ^2
	(1)	(2)	(3)	(4)	(5)	(6)
bright UV	1.03 ± 0.82	1.28 ± 1.05	$1.20^{+0.48}_{-0.74}$	$0.66^{+0.23}_{-0.38}$	$< 0.2^{(7)}$	1.46
faint UV	3.65 ± 1.25	4.51 ± 1.84	$2.42^{+0.51}_{-0.61}$	$1.23^{+0.23}_{-0.29}$	$4.4^{+8.8}_{-4.0}$	1.34
blue β	1.12 ± 0.74	1.38 ± 0.97	$1.25^{+0.43}_{-0.61}$	$0.68^{+0.21}_{-0.31}$	$< 0.2^{(7)}$	0.91
red β	4.29 ± 1.37	5.29 ± 2.06	$2.65^{+0.53}_{-0.63}$	$1.34^{+0.24}_{-0.29}$	$7.6^{+12.4}_{-6.5}$	0.52
bright Lyα	3.96 ± 1.29	4.89 ± 1.93	$2.53^{+0.51}_{-0.62}$	$1.29^{+0.23}_{-0.29}$	$5.9^{+10.4}_{-5.1}$	0.85
faint Lyα	5.39 ± 1.27	6.65 ± 2.16	$3.00^{+0.51}_{-0.59}$	$1.50^{+0.23}_{-0.27}$	$15.2^{+16.8}_{-10.8}$	1.81
large EW	3.27 ± 1.27	4.04 ± 1.81	$2.28^{+0.52}_{-0.64}$	$1.17^{+0.24}_{-0.30}$	$3.0^{+7.4}_{-2.8}$	0.64
small EW	4.90 ± 1.26	6.05 ± 2.05	$2.85^{+0.50}_{-0.59}$	$1.43^{+0.23}_{-0.27}$	$11.5^{+14.3}_{-8.7}$	1.75

Note. — (1) Correlation amplitude without contamination correction; (2) contamination-corrected correlation amplitude used to derive (3)–(5); (3) correlation length; (4) effective bias factor, (5) dark matter halo mass; (6) reduced χ^2 value; and (7) $1\,\sigma$ upper limit of $M_{\rm h}$ (see appendix B.1). The field-average best fit values are calculated from equation 4.15.

as shown in their figure 14 [*22].

Average $M_\star$-IRX relations have been obtained by several studies at $z \sim 2$ (Heinis et al., 2014; Bouwens et al., 2016) as shown in figure 6.7. Bouwens et al. (2016) have obtained a 'consensus relation' from previous analyses for galaxies at $z \sim 2$–3 (Reddy et al., 2010; Whitaker et al., 2014; Álvarez-Márquez et al., 2016), which is consistent with their result using ALMA data. On the other hand, Heinis et al. (2014) derives a relation for UV-selected galaxies at $z \sim 1.5$ giving higher $IRXs$ than the 'consensus relation' at low-stellar masses regime, however it is consistent wit a new result of star forming galaxies at $2 < z < 3$ with ALMA data (McLure et al., 2018). At low-stellar masses with $M_\star \lesssim 3$–$5 \times 10^9\,\mathrm{M}_\odot$, the average relation has not been defined well but it is probably located between the two.

The dust emission of typical LAEs with $M_\star \sim 10^9$ $\mathrm{M}_\odot$ is too faint to be detected, although a few LAEs at $z \sim 2$–3 are detected by Herschel/PACS and Spitzer/MIPS (e.g., Pentericci et al., 2010; Oteo et al., 2012). In this thesis, we convert the $E(B-V)_\star$ derived from SED fitting of our LAEs into IRX and compare them with two average relations at $z \sim 2$ (Heinis et al., 2014; Bouwens et al., 2016). The IRXs with the TIR luminosity (3–1000μm) in the equation 6.3 are converted to those with IR luminosity (8–1000μm)[*23] for comparison of the average IRX for the LAEs in the four field in section 6.4.1 (Kusakabe et al., 2018b). Meanwhile, in section 6.4.2, we do not correct the $IRXs$ in the equation 6.3 for the subdivided LAEs (Kusakabe et al., 2018a) according to the result in Buat et al. (2012). Note that the correction factor of $\sim 10\%$ does not change the results for our LAEs. We also clarify the IRXs of our LAEs using the result with IR observations in CDFS field (Kusakabe et al., 2015).

6.4.1 The IRX at a fixed $M_\star$ of the LAEs with $NB387_{\mathrm{tot}} \leq 25.5$ mag at $z \sim 2$

Figure 6.7 shows the average IRX–$M_\star$ relation and those for our LAEs. We find that our LAEs are located near an extrapolation of the consensus relation (see filled color symbols). Their IRX values are also consistent with that ($\lesssim 2.0$ ($3\,\sigma$)) of the average LAEs in CDFS field who constrain the upper limit of the IR luminosity from stacked Spitzer/MIPS 24 μm images[*24] (Kusakabe et al., 2015). While unlikely, for our LAEs to require the Calzetti attenuation curve, they would be dusty galaxies whose values of IRX are more than 10 times higher than expected from the extrapolated consensus relation (see open colored

[*22] The equation 6.3 is originally derived with the total IR luminosity (3–1000μm, TIR) for local galaxies in Overzier et al. (2011), while Buat et al. (2012) adopt the IRXs with $L_{\mathrm{IR}} \equiv L_{8-1000\mu m}$ instead of $L_{\mathrm{TIR}} \equiv L_{3-1000\mu m}$ for high-z galaxies.

[*23] We shift the derived $IRXs$ downward by 10%. This conversion factor is calculated from the IR SED templates for low metal galaxies in Ciesla et al. (2014) adopted in sections 6.1.3 and 6.1.4. Although the PAH emission contribution to the total IR luminosity may vary over $\sim$ 1–30% (Shivaei et al., 2017; Dale et al., 2009, see also Galliano 2011), the variation does not change the results in this thesis.

[*24] This IRX has also been 10% corrected from the original value (see our footnote *23).

symbols) and comparable to those of 10 times more massive average galaxies.

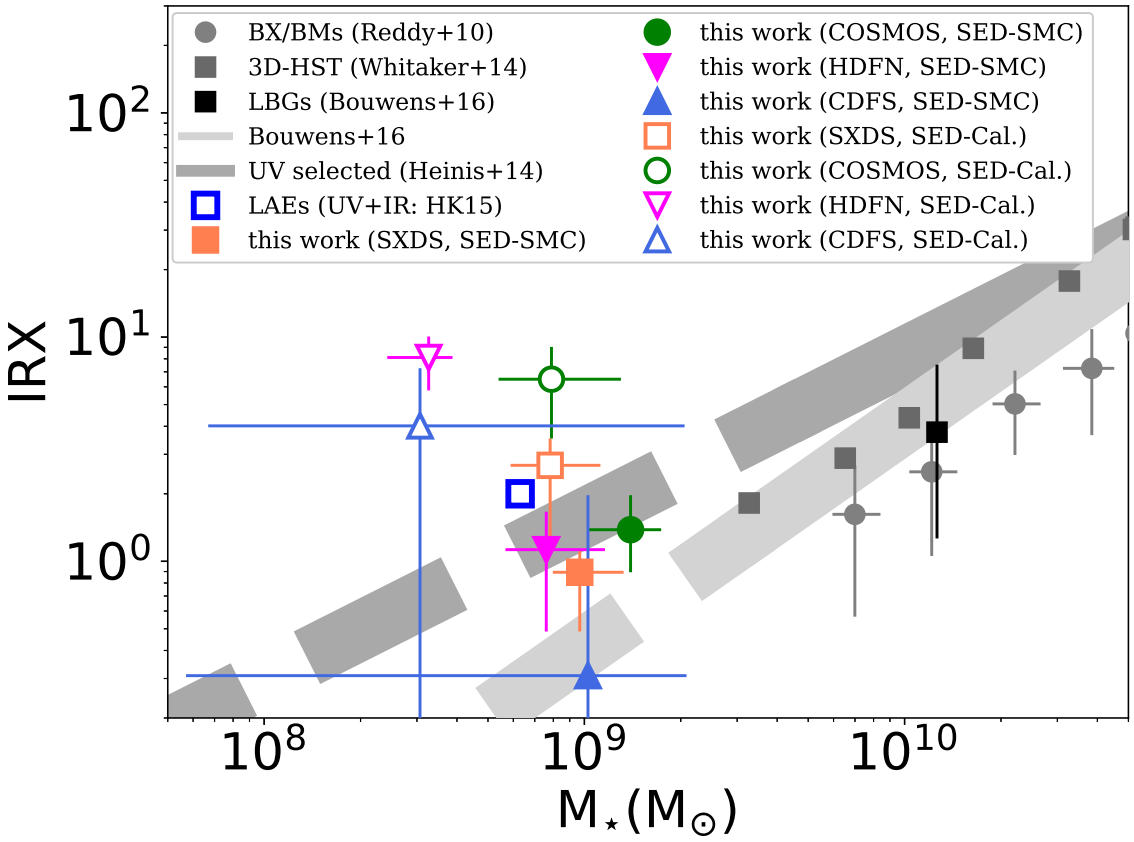

Figure 6.7 IRX plotted against $M_\star$ of the LAEs with $NB387_{\rm tot} \leq 25.5$ mag. Dim gray squares, dim gray circles, a black square, and a light gray solid band represent, respectively, 3D-HST galaxies at $z \sim 2$ in Whitaker et al. (2014), UV selected galaxies at $z \sim 2$ in Reddy et al. (2010), LBGs at $z \sim 2-3$ in Bouwens et al. (2016), and the consensus relation of them determined by Bouwens et al. (2016), with its extrapolation indicated by a lightt gray striped band (see also footnote ∗1). A light gray solid band represents the best-fit relation of UV-selected galaxies at $z \sim 1.5$ in Heinis et al. (2014) with its extrapolation indicated by a dark gray striped band. A filled (open) orange square, green circle, magenta inverted triangle, and blue triangle indicate SXDS, COSMOS, HDFN, and CDFS fields, respectively, on the assumption of an SMC-like attenuation curve (the Calzetti curve). An open blue square represents the 3σ upper limit of the average (stacked) LAEs in CDFS field (at $z \sim 2$) with IR observations (Kusakabe et al., 2015, hereafter HK15). All data are rescaled to a Salpeter IMF according to footnote ∗1.

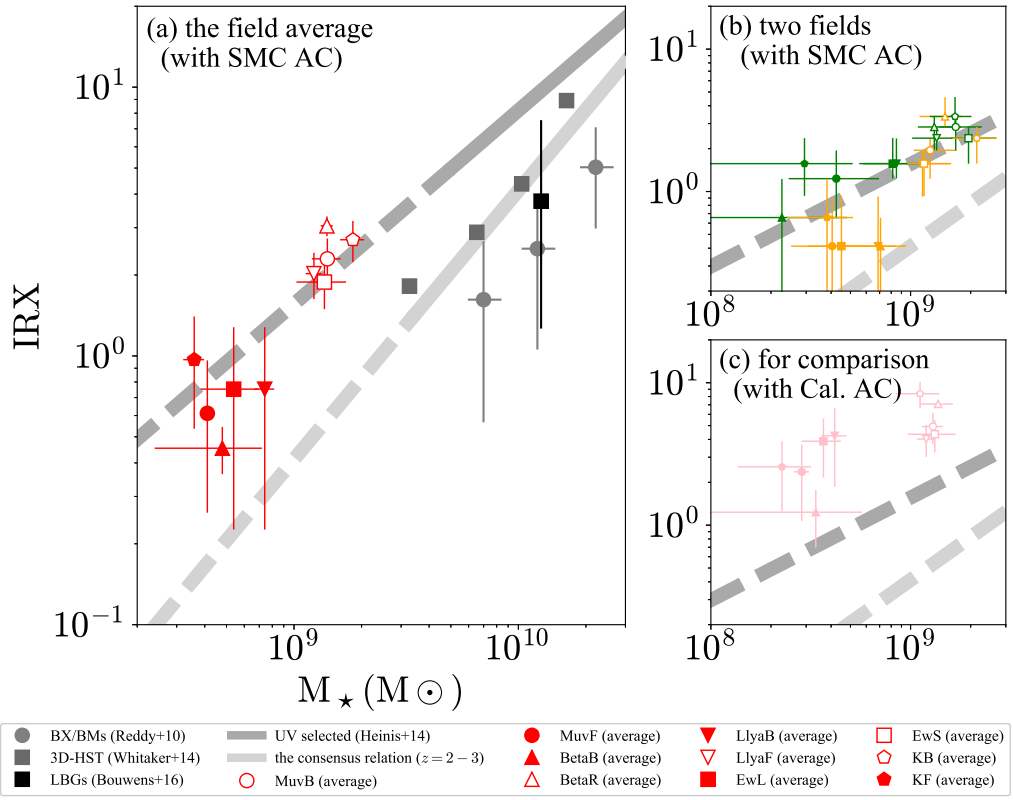

Figure 6.8 IRX plotted against $M_\star$ of the subdivided LAEs. (a) Field average values of our ten subsamples with an assumption of an SMC-like attenuation curve (red symbols), (b) results before averaging (green and orange symbols), and (c) field average values with an assumption of a Calzetti curve (pink symbols), plotted with some literature results. In panels (a) and (c), different subsamples are shown by different symbols: open (filled) circles for bright (faint) $M_{\rm UV}$, open (filled) triangles for red (blue) β, open (filled) inverted triangles for faint (bright) $L({\rm Ly}\alpha)_{ps}$, open (filled) squares for small (large) $EW_{0,ps}({\rm Ly}\alpha)$, and open (filled) pentagons for bright (faint) $m_{\rm K}$. Dark gray squares, dark gray circles, a black square, a dark gray solid line and a light gray solid line represent, respectively, 3D-HST galaxies at $z \sim 2$ in Whitaker et al. (2014), UV selected galaxies at $z \sim 2$ in Reddy et al. (2010), LBGs at $z \sim 2-3$ in Bouwens et al. (2016), UV-selected galaxies at $z \sim 1.5$ in Heinis et al. (2014) and the consensus relation of them determined by Bouwens et al. (2016). Dark and light gray dashed lines indicate extrapolations of gray solid lines. In panel (b), orange and green symbols indicate, respectively, the SXDS and COSMOS subsamples with an SMC-like attenuation curve (with SMC AC). All data are rescaled to a Salpeter IMF according to footnote *1.

6.4.2 The IRX at a fixed $M_\star$ of the subdivided LAEs at $z \sim 2$

Figure 6.8 (a) shows the field-average values of our subsamples with the assumption of an SMC-like attenuation curve (red symbols), which are calculated from the results for the two fields shown in panel (b) (orange and green symbols). The field-average results lie on an extrapolation of the relation for UV-selected galaxies at $z \sim 1.5$ in Heinis et al. (2014). Considering the relatively large uncertainties remaining in the two average relations, we conclude that our subdivided LAEs are not outliers but have normal dustinesses. This result is consistent with those obtained for the average (stacked) LAEs using Spitzer/MIPS 24μm data (in CDFS field Kusakabe et al., 2015) and from SED fitting (in the four field Kusakabe et al., 2018b). Note, however, that if we assume the Calzetti-like attenuation curve instead, our LAEs are expected to be dustier galaxies than ordinary galaxies at the same stellar masses as shown by pink symbols in panel (c).

6.4.3 Summary of the IRX of LAEs at $z \sim 2$

We find that the average LAEs in each of the four fields as well as the subdivided LAEs lie on the average IRX–$M_\star$ relation (Heinis et al., 2014; Bouwens et al., 2016) from SED fitting with an assumption of an SMC-like attenuation curve. This is consistent with the results with IR observations in CDFS field. It suggests that LAEs at $z \sim 2$ are normal galaxies at low-$M_\star$ regime in terms of dustiness. In chapter 8, we employ the result in the discussion of the origin of LAHs.

6.5 Star formation mode

The mode of star formation in star-forming galaxies can be divided into two categories: the main-sequence (MS) mode where galaxies form stars at moderate rates, making a well-defined sequence in the SFR-$M_\star$ plane (SFMS; e.g., Noeske et al., 2007; Elbaz et al., 2007; Speagle et al., 2014), and the burst mode where galaxies have much higher specific star formation rates, $sSFRs(= SFR/M_\star)$, than MS galaxies with similar masses (e.g., Rodighiero et al., 2011).

The SFMS itself at $z \sim 2$ has been determined well at $M_\star \gtrsim 10^{10}$ M$_\odot$ either from rest UV to FIR (MIR) data (e.g., Whitaker et al., 2014; Tomczak et al., 2016) or Hα and Hβ emission-line fluxes (balmer decrement; Shivaei et al., 2017). Below this stellar mass, the SFMS is suggested to continue at least down to $M_\star \sim 10^8$–10^9 M$_\odot$ keeping its power-law slope unchanged (e.g., by Santini et al., 2017, using gravitationally-lensed galaxies in the HST Frontier Fields), although SFRs have large uncertainties since without FIR data (or balmer decrement). Although these results are not consistent with each other at $M_\star \lesssim 10^{10}$ M$_\odot$ as shown in figure 6.9, the true SFMS probably lies somewhere between the Tomczak et al. (2016) and Shivaei et al. (2017)'s results.

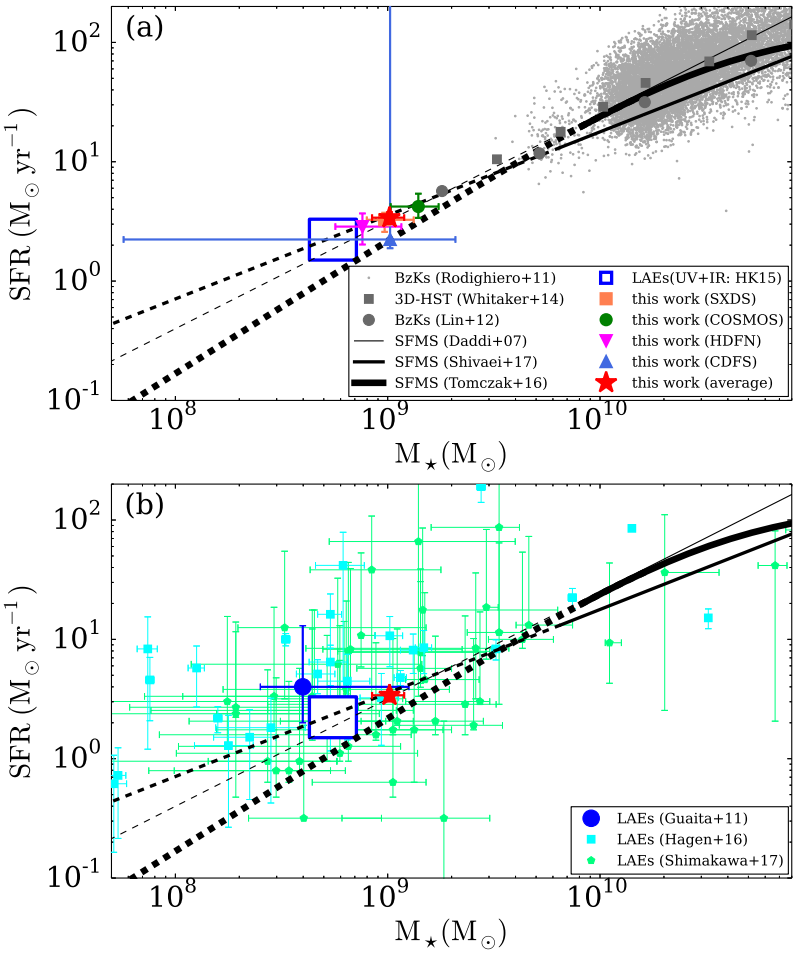

Figure 6.9 SFR plotted against $M_\star$ of the LAEs with $NB387_{\rm tot} \leq 25.5$ mag. Panel (a). An orange square, green circle, magenta inverted triangle, and blue triangle represent stacked LAEs with $NB387_{\rm tot} \leq 25.5$ mag in SXDS, COSMOS, HDFN, and CDFS fields, respectively, and a red star shows the average over the four fields. The orange square and the red star over lap with each other. A blue open rectangle denotes the permitted range for stacked LAEs from $L_{\rm UV}$ and $L_{\rm IR}$ in Kusakabe et al. (2015). Light gray dots, dim gray squares, and dim gray circles indicate BzKs from Rodighiero et al. (2011), BzKs from Lin et al. (2012), and 3D-HST galaxies from Whitaker et al. (2014), respectively. Black thin middle-width, and thick solid lines represent the star formation main sequence at $z \sim 2$ in Tomczak et al. (2016, hereafter T16), Shivaei et al. (2017, hereafter S17), and Daddi et al. (2007), respectively (determined well using $L_{\rm UV}$ and $L_{\rm IR}$), with extrapolated parts shown by dashed lines. (b) Same as panel (a) but LAEs taken from the literature are also plotted. Cyan squares and light green pentagons show individual LAEs at $z \sim 2$ in Hagen et al. (2016) and Shimakawa et al. (2017), respectively. A blue circle indicates stacked LAEs at $z \sim 2$ in Guaita et al. (2011). $SFRs$ in Hagen et al. (2016) and Shimakawa et al. (2017) are derived from the $IRX-\beta$ relation with the Calzetti curve (Meurer et al., 1999) and $SFRs$ in Guaita et al. (2011) are derived from SED fitting with the Calzetti curve, while $SFRs$ in this work are derived from SED fitting with an SMC-like curve. We also show our results with the $IRX-\beta$ and SED fitting with the Calzetti curve in figures D.1 and D.2. All data are rescaled to a Salpeter IMF according to footnote ∗1.

In this thesis, we simply extrapolate the SFMS, given in the literatures (Daddi et al., 2007; Tomczak et al., 2016; Shivaei et al., 2017) towards lower masses without changing the power-law slope. We compare our results for the average LAEs in the four field (Kusakabe et al., 2018b) and the subdivided LAEs (Kusakabe et al., 2018a) with the SFMS. When we derive SFR and $M_\star$, nebular emission is included in SED fitting unlike previous work for subdivided LAEs at $z \sim 2$ (Guaita et al., 2011). We also confirm our results using the result for the LAEs in CDFS field with IR observations (Kusakabe et al., 2015).

6.5.1 The star formation mode of the LAEs with $NB387_{\rm tot} \leq 25.5$ mag at $z \sim 2$

Figure 6.9(b) shows previous results for LAEs at $z \sim 2{-}2.5$. Hagen et al. (2016) have found that bright individually detected LAEs lie along or above the SFMS, while Shimakawa et al. (2017) have found that fainter, individually detected LAEs lie on the SFMS. Guaita et al. (2010)'s estimates based on stacking analysis have too large errors to distinguish the star formation mode although they are consistent with the MS mode.

The $M_\star$ and SFR of our LAEs averaged over the four fields (derived from SED fitting) are $M_\star = 10.2 \pm 1.8 \times 10^8$ M$_\odot$ and SFR$= 3.4 \pm 0.4$ M$_\odot$ yr^{-1}, respectively (Kusakabe et al., 2018b). Thus, our LAEs are on average placed near a lower-mass extrapolation of the SFMS as shown by a red star in figure 6.9(b). We also find in figure 6.9(a) that the LAEs in individual fields also lie on the extrapolated SFMS, although that in the CDFS has large uncertainties (blue triangle in figure 6.9(a)). This result is unchanged even when we stack all objects including those with $NB387_{\rm tot} \geq 25.5$ mag. We also derive the SFR from stacked IR and UV images for the LAEs in CDFS field (Kusakabe et al., 2015). The SF mode derived from IR and UV data is consistent with the field-average SFR derived from SED fitting with the assumption of an SMC-like attenuation curve for our LAEs at $z \sim 2$.

Hagen et al. (2016)'s sample is a mixture of two samples: bright spectroscopically-selected LAEs at $z = 1.90 - 2.35$ from the HETDEX survey ($L_{{\rm Ly}\alpha} > 10^{43}$ erg s^{-1}: Hagen et al., 2014) and bright NB-selected LAEs at $z \simeq 2.1$ from Guaita et al. (2010) and Vargas et al. (2014) with a counterpart in the 3D-HST catalog. They derive SFRs from the IRX-β relation with the Calzetti curve. Note that we also find our LAEs to have higher $sSFR$s similar to theirs if we use the Calzetti curve as shown in figures D.1 (a) – (c) and D.2 in appendix D. They also expect that their objects would move downward toward the SFMS in the $M_\star$–SFR plane if they adopt an SMC-like curve[*25]. Shimakawa et al. (2017) select LAEs using a narrow-band ($NB \leq 26.55$ mag (5σ)) and only include those with a counterpart in the 3D-HST catalogue (Skelton et al., 2014). They also derive SFRs from the $IRX - \beta$ with the Calzetti curve, while stellar masses are derived from SED fitting without IRAC photometry. Since their LAEs have blue β (~ -1.9 in average),

[*25] Hagen et al. (2016) suggest either that their LAEs are undergoing starbursts, that the SFMS becomes shallower at low stellar masses and their LAEs are distributed around it, or that their LAEs are biased towards high Lyα luminosities, not representing typical LAEs.

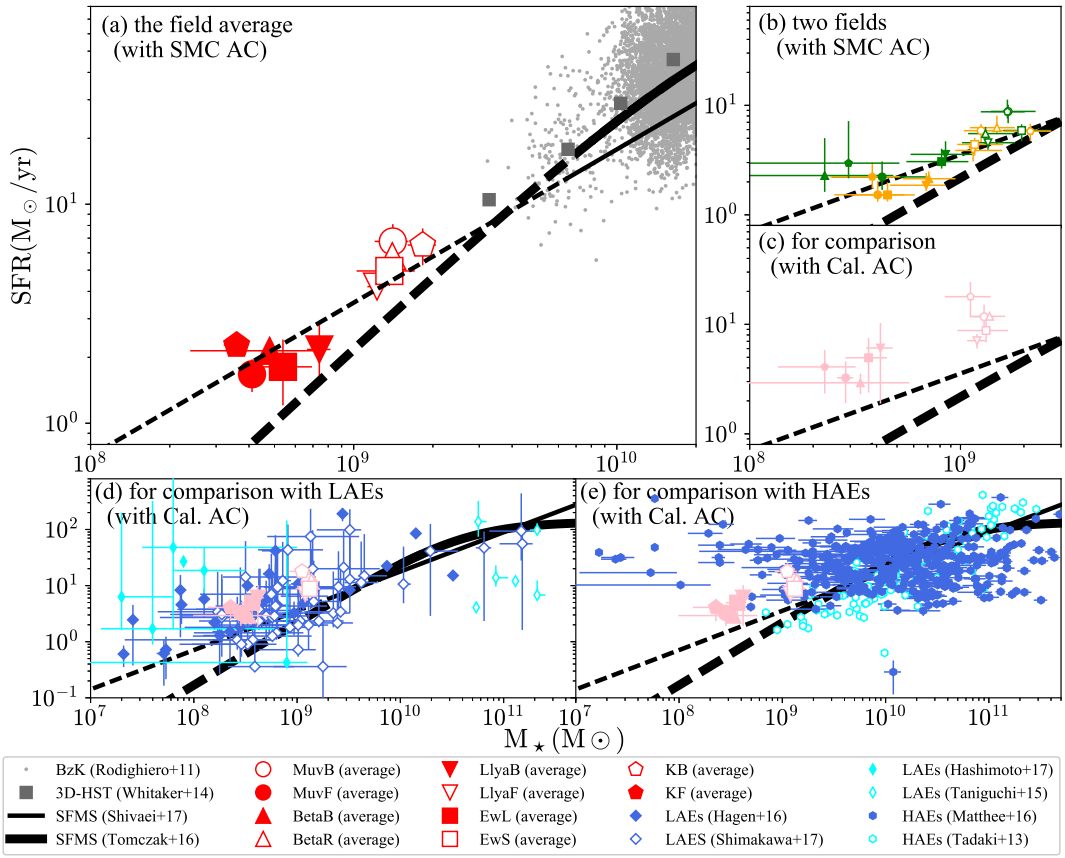

Figure 6.10 SFR plotted against $M_\star$ of the subdivided LAEs. (a) Field average values of our ten subsamples with an SMC-like attenuation curve (red symbols), (b) results before averaging (green and orange symbols), and (c)-(e) field average values with a Calzetti curve (pink symbols), plotted with some literature results. In panels (a) and (c)–(e), different subsamples are shown by different symbols: open (filled) circles for bright (faint) $M_{\rm UV}$, open (filled) triangles for red (blue) β, open (filled) inverted triangles for faint (bright) $L({\rm Ly}\alpha)_{ps}$, open (filled) squares for small (large) $EW_{0,ps}({\rm Ly}\alpha)$, and open (filled) pentagons for bright (faint) $m_{\rm K}$. In panel (b), orange and green symbols indicate, respectively, the SXDS and COSMOS subsamples with an SMC-like attenuation curve (with SMC AC). In panels (c)–(e), pink symbols show the average values of the subsamples over the two fields with a Calzetti attenuation curve (with Cal. AC). Dark gray squares, light gray dots, thick black solid lines, and thin black solid lines represent, respectively, 3D-HST galaxies at $z \sim 2$ in Whitaker et al. (2014), BzK galaxies at $z \sim 2$ in Rodighiero et al. (2011), the SFMS at $z \sim 2$ in Tomczak et al. (2016), and the SFMS at $z \sim 2$ in Shivaei et al. (2017). Thick and thin black dashed lines indicate extrapolations of the black solid lines. In panel (d), filled blue diamonds, open blue diamonds, filled cyan thin diamonds, and open cyan thin diamonds indicate LAEs at $z \sim 2$–3 in Hagen et al. (2016); Shimakawa et al. (2017); Hashimoto et al. (2017a) and Taniguchi et al. (2015), respectively. In panel (e), filled blue hexagons and open cyan hexagons show HAEs at $z \sim 2$–3 in Matthee et al. (2016) and Tadaki et al. (2013). All data are rescaled to a Salpeter IMF according to footnote *1.

their SFRs and stellar masses do not change so much if an SMC-like curve is used instead. Hashimoto et al. (2017a) have also examined six LAEs with $EW_0(\mathrm{Ly}\alpha) \simeq$ 200–400Å selected from the same sample as ours and found that they are starburst galaxies with $M_\star \sim 10^7$–10^8 $\mathrm{M}_\odot$. However, as suggested in Hashimoto et al. (2017a), their high $sSFR$s are probably a consequence of high $EW_0(\mathrm{Ly}\alpha)$s (because younger galaxies have a larger $EW_0(\mathrm{Ly}\alpha)$) and the stellar population properties of these six LAEs do not represent those of our LAE sample.

We infer that our sample better represents the majority of $z \sim 2$ LAEs because of a wide luminosity coverage (~ 0.1–$2 \times L^\star_{\mathrm{Ly}\alpha}$: see Konno et al., 2016) and a simple selection based only on $EW_0(\mathrm{Ly}\alpha) \geq$ 20–30Å, being less biased toward/against other quantities such as UV luminosity. The majority of $z \sim 2$ LAEs are probably normal star-forming galaxies with low stellar masses in terms of star formation mode.

6.5.2 The star formation mode of the subdivided LAEs at $z \sim 2$

Figure 6.10 (a) shows the field-average values for the ten subsamples with an SMC-like attenuation curve (red symbols) while figure 6.10 (b) the separate results for the two fields (orange and green symbols). All the field-average data points lie on the extrapolation of the SFMS in Tomczak et al. (2016), being only slightly above the Shivaei et al. relation. This result is also consistent with those obtained for the LAEs in CDFS field (Kusakabe et al., 2015) and the field-average LAEs (Kusakabe et al., 2018b) in section 6.5. We conclude that the majority of our subdivided LAEs are in a moderate star formation mode even after divided into two subsamples by various properties. In chapter 8, we use the relation in Shivaei et al. (2017) for the discussion of the origin of LAHs.

We also compare our results to previous studies on individual LAEs and Hα emitters (HAEs) at similar redshifts. For this comparison, we use the results based on a Calzetti attenuation curve (figure 6.10 [c]) following these previous studies. We find in figure 6.10 (d) that our ten subsamples (pink symbols) are distributed in the middle of individual LAEs with $M_\star$ and SFR measurements (Hagen et al., 2016; Shimakawa et al., 2017; Hashimoto et al., 2017a; Taniguchi et al., 2015, $z \sim$ 2–3)[*26]. In figure 6.10 (e), our LAEs are found to be located at the lower-mass regime of NB-detected HAEs (Tadaki et al., 2013; Matthee et al., 2016). While the HAEs in Tadaki et al. (2013) (open cyan hexagons) [*27] lie on the SFMS, those in Matthee et al. (2016) (filled blue hexagons)[*28] are widely

[*26] In Hagen et al. (2016) and Shimakawa et al. (2017), $M_\star$ are derived from SED fitting with the Calzetti curve and SFR from the IRX–β relation in Meurer et al. (1999). On the other hand, Taniguchi et al. (2015) and Hashimoto et al. (2017a) derive both quantities from SED fitting with the Calzetti curve.

[*27] They derive $M_\star$ from SED fitting with the Calzetti curve (see Tadaki et al., 2017, for more details), while deriving SFRs from Hα luminosities except for MIPS 24μm detected objects whose SFRs are estimated from UV and MIPS photometry (see also Tadaki et al., 2015). Note that SFRs calculated from PACS data are not plotted here.

[*28] When analyzing individual galaxies, they assume the Calzetti curve to derive $M_\star$ and assume $E(B-V)_\star = E(B-V)_g$ to correct Hα luminosities (and hence SFRs) for dust extinction(see SED fitting paper of HiZELS for more details, Sobral et al., 2014). However, when stacking, they use

scattered along the horizontal direction around the SFMS because they are essentially Hα luminosity selected. Some HAEs in Matthee et al. (2016) have similarly low stellar masses to our LAEs but with higher $SFRs$ due to this selection bias.

6.5.3 Summary of the star formation mode of LAEs at $z \sim 2$

We find that the average LAEs in each of the four fields as well as the subdivided LAEs lie on the SFMS at $z \sim 2$ (Tomczak et al., 2016; Shivaei et al., 2017) from SED fitting with an assumption of an SMC-like attenuation curve. This is consistent with the results with IR observations in CDFS field. It suggests that LAEs at $z \sim 2$ are normal star forming galaxies at low-$M_\star$ regime in terms of star formation mode. In chapters 8 and 7, we employe the results in the discussion of the origin of LAHs and star forming activity of LAEs, respectively.

6.6 SHMR and BCE

6.6.1 The stellar to halo mass ratio of LAEs at $z \sim 2$

The stellar to halo mass ratio ($= M_\star/M_{\rm h}$: $SHMR$) indicates the efficiency of star formation in dark matter halos integrated over time from the onset of star formation to the observed epoch, which we refer to as the integrated SF efficiency. The $SHMR$ as a function of halo mass is known to have a peak and the halo mass at the peak (pivot mass) is $\simeq 2-3\times10^{12}$ M$_\odot$ at $z \sim 2$ (e.g., Behroozi et al., 2013; Moster et al., 2013). The shape of the average relation show almost no evolution at $z \sim 0$–5, although the behavior of the $z \sim 2$ $SHMR$ below $M_{\rm h} \sim 10^{11}$ M$_\odot$ has not been constrained well. We plot the $SHMR$s of LAEs at $z \sim 2$ comparing them with the average relations for the first time and discuss the typical $SHMR$ of our LAEs with largest survey area so far.

Figure 6.11(a) shows $M_\star$ and $M_{\rm h}$ of our LAEs in each of the four fields (pink symbols) and those values averaged over the four fields: $M_\star = 10.2 \pm 1.8 \times 10^8$ M$_\odot$ and $M_{\rm h} = 4.0^{+5.1}_{-2.9} \times 10^{10}$ M$_\odot$ (a red star). Those of LAEs at $z \sim 2.1$ (Guaita et al., 2010)[*29], star forming galaxies based on clustering analysis (Lin et al., 2012; Ishikawa et al., 2016; Ishikawa, 2017)[*30], and the average relation based on abundance matching (Behroozi et al., 2013; Moster et al., 2013)[*31] at $z \sim 2$ are shown in figure 6.11 (a) and (b) for comparison. In contrast to Guaita et al.'s result (a blue circle), our LAEs averaged over

A(Hα) = 1 mag to correct Hα luminosities for all subsamples.

[*29] The SFR and stellar mass in Guaita et al. (2010, 2011) are derived from SED fitting to a median-stacked SED and their halo mass is a median halo mass. We plot them without any correction (see also section 6.3.2).

[*30] We recalculate halo masses in Lin et al. (2012) from the effective biases given in their table using the same method as ours.

[*31] The values of cosmological parameters adopted in Behroozi et al. (2013) and Moster et al. (2013) are slightly different from ours, but we have not corrected for those differences in this study. The $M_{\rm h}$ value in Behroozi et al. (2013) becomes ~ 0.15 dex higher at $M_{\rm h} \leq 10^{12}$ M$_\odot$ when our values are used (P. Behroozi 2017, private communication).

the four fields (a red star) lie above a simple lower-mass extrapolation (without changing the slope in the log-log space) of the $M_\star$-M_h relation of star forming galaxies and the average relation. Due to the high stellar mass and low halo mass, our LAEs have a $SHMR$ of $0.02^{+0.07}_{-0.01}$ as high as galaxies at the pivot mass, $M_\mathrm{h} \simeq 2-3\times10^{12}$ $\mathrm{M}_\odot$. Here, the errors in this $SHMR$ value indicate the $\pm1\sigma$ (68%) range. To examine a probability that our LAEs have a consistent $SHMR$ with that of the average relation, we calculate the two-dimensional probability distribution of our four-field average M_h and $SHMR$ from a Monte Carlo simulation with 500,000 trials. In each trial, we randomly select M_h and $M_\star$ from Gaussian profiles and calculate a $SHMR$ assuming that the probability distribution functions of our four-field average M_h and $M_\star$ are (asymmetric) Gaussian with (asymmetric) errors. We derive the 68% confidence interval from the 500,000 pair of M_h and $SHMR$. In the inset of figure 6.11(b), a magenta contour presents the 68% confidence interval, while brown dots indicate randomly selected 150,000 trials. Although the contour touches the $+1\sigma$ limit of the average relation, only $\sim$ 2.5% of the entire trials reach the $+1\sigma$ limit (an orange dashed line).

We discuss whether there are any systematic differences in $M_\star$ and/or M_h between our LAEs and the average relation, which result in the departure of our results from the relations. The average relation by Moster et al. (2013) expresses the mean stellar mass of the central galaxy as a function of halo mass and has a double power-law form, while that by Behroozi et al. (2013) uses the median stellar mass and has five fitting parameters, whose functional form at low halo masses is approximated by a power law[*32]. Although the definitions of stellar masses of the two relations are different, the relations are similar to one another. Our average stellar mass is a field-average median stellar mass since stellar masses are derived from SED fitting for median-stacked SEDs, which are commonly used to prevent contamination (see section 3.2.3). The field-average mean stellar mass of our sample is possibly higher than the field-average median. In fact, the mean value of K-band flux densities, which is an approximation of stellar mass, is approximately twice as high as the median one in SXDS field, the field with the deepest K data. We derive effective halo masses of our LAEs from effective biases directly (see section 4.3) assuming a one-to-one correspondence between galaxies and dark matter halos with a narrow range of halo mass. Our field-average effective halo mass probably corresponds to the true mean and/or median within the large uncertainty whose $1\,\sigma$ permitted range is $\sim$ 1 dex. Even though the uncertainty by cosmic variance discussed in section 6.3.3 is added to the total uncertainty in the field-average halo mass, by which the halo mass and $SHMR$ are written as $M_{\mathrm{h,\,cv}} = 4.0^{+8.4}_{-3.5}\times10^{10}$ $\mathrm{M}_\odot$ and $SHMR = 0.02^{+0.18}_{-0.01}$, respectively, our result is not consistent with the extrapolated average relations within $1\,\sigma$. Therefore, the departure of our field-average LAEs (a red star) from the average relation are not caused by neither a systematic difference of the definition of $M_\star$ nor $1\,\sigma$ cosmic variance on M_h.

[*32] The Behroozi et al. (2013) relations including extrapolated parts in figures 6.11–7.1 are taken from the website of P. Behroozi: http://www.peterbehroozi.com/data.html (see also footnote *31).

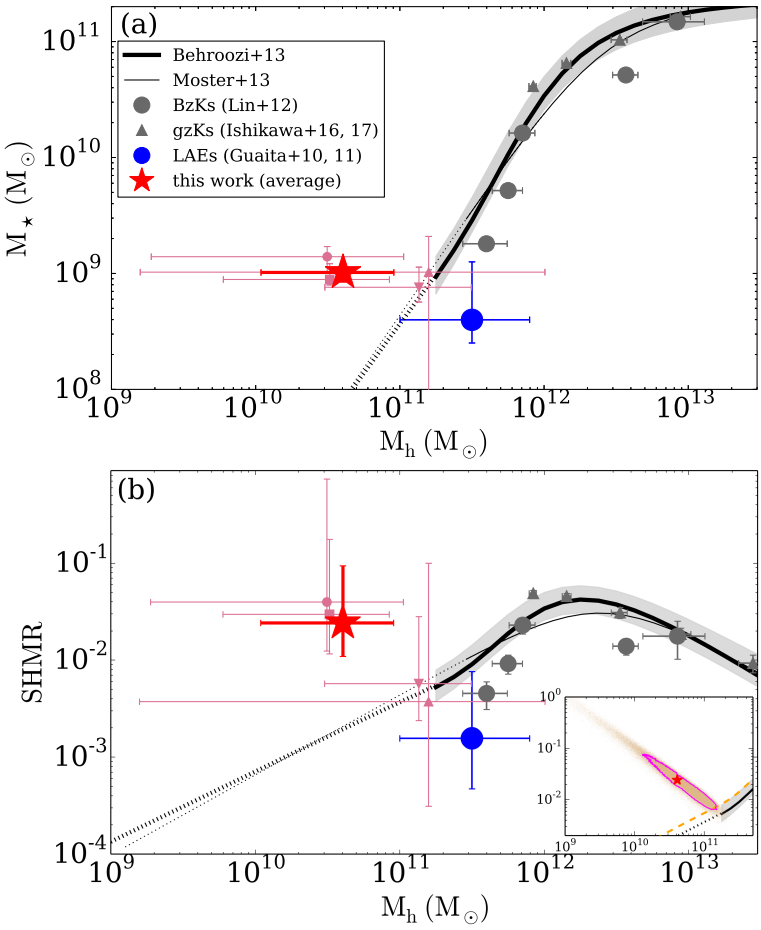

Figure 6.11 (a) $M_\star$ plotted against M_h and (b) $SHMR$ plotted against M_h. For each panel, a filled pink square, circle, inverted triangle, and triangle represent average (stacked) LAEs with $NB387_\mathrm{tot} \leq 25.5$ mag in SXDS, COSMOS, HDFN, and CDFS fields, respectively, and a large red star shows the average over the four fields. A blue circle indicates median (stacked) LAEs at $z \sim 2$ in Guaita et al. (2011). Black thick and thin solid lines represent the average relation of galaxies at $z \sim 2$ in Behroozi et al. (2013) and Moster et al. (2013), respectively; their extrapolations are shown by dotted black lines. A gray shaded region indicates the $1\,\sigma$ uncertainty in $M_\star$ in the relation in Behroozi et al. (2013). Gray circles and gray triangles denote BzK galaxies in Lin et al. (2012) and gzK galaxies in Ishikawa et al. (2016) and Ishikawa (2017), respectively. For each data point, the horizontal error bars indicate the $\pm1\sigma$ (68%) range of the M_h measurement, and the vertical error bars the $\pm1\sigma$ (68%) range of the $M_\star$ (panel [a]) and $SHMR$ ([b]) measurement. The inset of the panel (b) shows the two-dimensional probability distribution of our four-field average M_h and $SHMR$ values calculated from a Monte Carlo simulation with 500, 000 trials. A magenta contour presents the 68% confidence interval while brown dots indicate randomly selected 150, 000 trials for the presentation purpose. An orange dashed line indicates the $+1\sigma$ limit of the average relation. All data are rescaled to a Salpeter IMF according to footnote ⋆1. See also footnotes ⋆29–⋆32.

On the other hand, if LAEs represent average galaxies, the average $M_{\rm h}$–$SHMR$ relation must have an upturn at $M_{\rm h} \lesssim 10^{11}$ M$_\odot$. This, however, appears to be unphysical because no such upturn is seen at $z \sim 0$, the only epoch at which the average relation below $M_{\rm h} \sim 10^{11}$ M$_\odot$ has been constrained well (Behroozi et al., 2013), unless the low-mass slope of the average relation evolves drastically from $z \sim 2$ to ~ 0. Another possibility is that the scatter of the average relation become significantly larger at lower halo masses and the SHMR of our LAEs is within the scatter.

Note that the $SHMR$s in the HDFN and CDFS are consistent with the average relations although with large uncertainties. We obtain consistent stellar masses between the four fields and it is just the halo masses that are different. The difference in $M_{\rm h}$, and hence in $b_{\rm g,eff}$, among the four fields seen in figure 6.5 (see also sections 6.3.2 to 6.3.4) is not due to a difference in the limiting magnitude because all four fields have the same limit, $NB387_{\rm tot} = 25.5$. As shown in figure 6.11, fitting errors and contamination fraction errors possibly drive the offsets of $M_{\rm h}$ in the two fields to the average values. The difference is also explained by cosmic variance as shown in figure6.6(b) (see also section 6.3.3) and averaging over the four fields reduces the effect of cosmic variance.

6.6.2 The baryon conversion efficiency of LAEs at $z \sim 2$

The baryon conversion efficiency (BCE), defined as:

$$BCE = \frac{\dot{M}_\star}{\dot{M}_{\rm b}}, \tag{6.4}$$

measures the efficiency of star formation in dark matter halos at the observed time, where $\dot{M}_{\rm b}$ is the baryon accretion rate (BAR). Here we assume that most of the accreting baryons are in a (cold) gas phase (i.e., the BAR is equal to the inflow rate of cold gas). The average BAR at a fixed halo mass is proportional to the halo mass accretion rate, $\dot{M}_{\rm h}(z, M_{\rm h})$, which is estimated as a function of redshift and halo mass from cosmological simulations (Dekel et al., 2009a):

$$BAR = f_{\rm b} \times \dot{M}_{\rm h}(z,\ M_{\rm h}) \tag{6.5}$$

$$\sim 6 \times \left(\frac{M_{\rm h}}{10^{12} {\rm M}_\odot} \right)^{1.15} \times (1+z)^{2.25}\ {\rm M}_\odot\ {\rm yr}^{-1}, \tag{6.6}$$

where $f_{\rm b} \equiv \Omega_{\rm b}/\Omega_{\rm m} = 0.15$.

Figure 6.12 shows the BCE against halo mass. our LAEs have $BCE = 1.6^{+6.0}_{-1.0}$ and, as shown by a red star, lie above an extrapolation (keeping the slope unchanged) of the average relation by Behroozi et al. (2013) and most of the BzK galaxies in Lin et al. (2012). Here, the errors in our BCE value indicate the $\pm 1\sigma$ (68%) range. The inset of figure 6.12 shows the two-dimensional probability distribution of our four-field average $M_{\rm h}$ and BCE values calculated from a Monte Carlo simulation with 500, 000 trials in the same manner as in section 6.6.1. A magenta contour presents the 68% confidence interval, while brown dots indicate the 500, 000 trials. Only $\sim$ 0.3% of the entire trials reach the $+1\sigma$ limit of the average relation (an orange dashed line). On the other hand, Guaita et al. (2010,

2011)'s LAEs at $z \sim 2$ have a moderate BCE, although with large uncertainties, which is consistent with the average relation as shown by a blue circle. The average SFRs of both samples are nearly equivalent and it is the clustering measurements that differ and drive our BCE up. So the difference in the clustering affects the discrepancy in both axes in figure 6.12 making the offset worse.

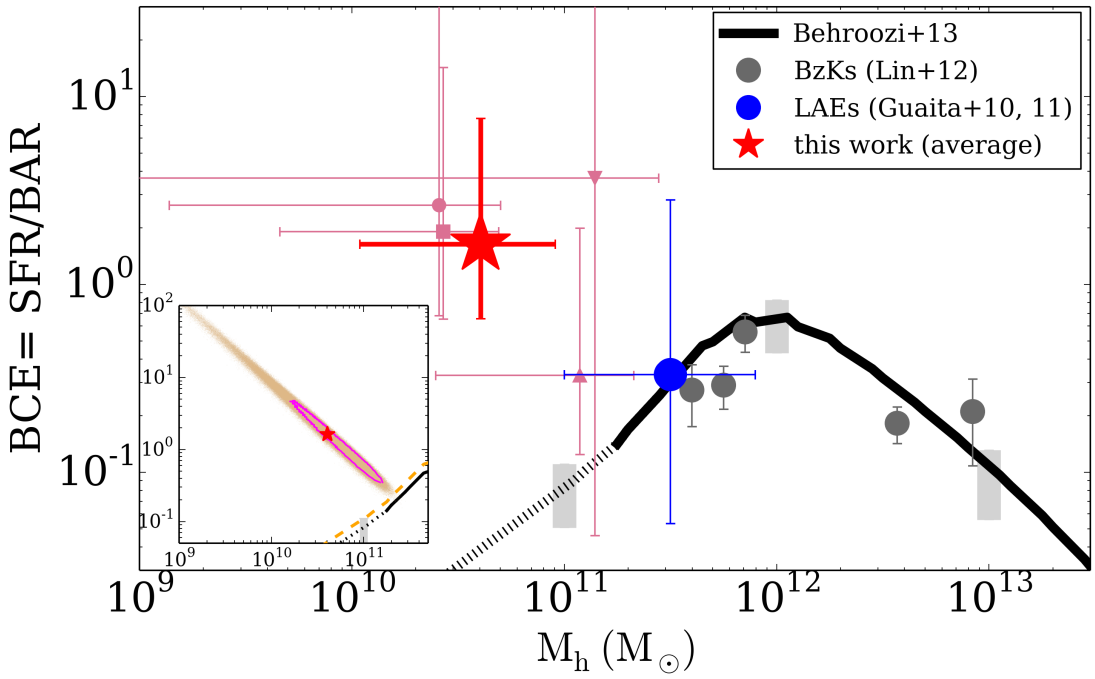

Figure 6.12 Baryon conversion efficiency (BCE) plotted against $M_{\rm h}$. A filled pink square, circle, inverted triangle, and triangle represent average (stacked) LAEs with $NB387_{\rm tot} \leq$ 25.5 mag in SXDS, COSMOS, HDFN, and CDFS fields, respectively, and a red star shows the average over the four fields. A blue circle indicates median (stacked) LAEs at $z \sim 2$ in Guaita et al. (2011). A black thick solid and gray circles show the average relation of galaxies at $z \sim 2$ in Behroozi et al. (2013) and measurements for BzK galaxies in Lin et al. (2012), respectively. For each data point, the horizontal (vertical) error bars indicate the $\pm 1\sigma$ (68%) range of the M_h (BCE) measurement. Extrapolations and 1 σ scatter of BCE at fixed $M_{\rm h}$ are shown by a dotted black line and vertical gray bands, respectively. The scatter of BCE is estimated from the scatter of SFRs at $M_{\rm h} = 1 \times 10^{11}$, 1×10^{12}, and 1×10^{13}. The inset shows the two-dimensional probability distribution of our four-field average Mh and BCE values calculated from a Monte Carlo simulation with 500,000 trials. A magenta contour presents the 68% confidence interval while brown dots indicate the entire trials. An orange dashed line indicates the $+1\sigma$ limit of the average relation. All data are rescaled to a Salpeter IMF according to footnote ∗1. See also footnotes ∗29–∗32.

We discuss whether there are any systematic differences in SFR and/or $M_{\rm h}$ between our LAEs and the average relation, which result in the departure of our results from the relations. The average relation by Behroozi et al. (2013) expresses the mean SFR as a function of halo mass. Our field-average SFR is derived from SED fitting for median-stacked SEDs and probably does not overestimate the true average SFR, since the median of B-band flux densities, which trace rest-frame UV, is similar to the average B-band flux density. Even when we neglect dust attenuation at UV, $A_{1600} = 0.6 \pm 0.1$ mag, the field-average SFR ($= 3.4 \pm 0.4$ M$_\odot$ yr^{-1}) decreases only a factor of ~ 2. Moreover, even when the uncertainty by cosmic variance discussed in section 6.3.3 is added to the measured value, $BCE = 1.6^{+6.0}_{-1.0}$, the $1\,\sigma$ lower limit of the field-average BCE is still larger than 0.4. Thus, it seems difficult for our LAEs to fall on the average relation shown in figure 6.12.

As described in section 6.6.1, logically we cannot rule out the possibilities that our LAEs lie indeed on or near the average relation which changes the slope and/or scatter below $M_{\rm h} \sim 1 \times 10^{11}$ M$_\odot$ for some reason.

6.7 Lyα halo luminosity

6.7.1 The halo and total Lyα luminosities for the subdivided LAEs at $z \sim 2$

The estimated $L({\rm Ly}\alpha)_{\rm H}$ and $L({\rm Ly}\alpha)_{\rm tot}$ from the empirical relation for individual subsample in the two fields are listed in table 6.6. To test the robustness of $L({\rm Ly}\alpha)_{\rm H}$ values derived from equation 5.1, we calculate $L({\rm Ly}\alpha)_{\rm H}$ from $EW_{0,ps}(L_{{\rm Ly}\alpha})$ using another stacked relation presented in Momose et al. (2016), an anti-correlation between ${\rm X}(L_{{\rm Ly}\alpha})_{\rm tot/C}$ and $EW_{0,ps}(L_{{\rm Ly}\alpha})$. We find that using this relation gives nearly the same $L({\rm Ly}\alpha)_{\rm H}$ values as those derived from equation 5.1, with differences being at most 0.09 dex. The typical 1σ uncertainties in the individual data points in Momose et al. (2016)'s $L({\rm Ly}\alpha)_{\rm C}$ - $L({\rm Ly}\alpha)_{\rm H}$ relation are propagated to uncertainties in $L({\rm Ly}\alpha)_{\rm H}$ and $L({\rm Ly}\alpha)_{\rm tot}$ of $\sim 22\%$ and $\sim 16\%$, respectively.

Figure 6.13 plots the field-average $L({\rm Ly}\alpha)_{\rm H}$ and $L({\rm Ly}\alpha)_{\rm tot}$ against SFR, $E(B-V)_\star$, $M_\star$, and $M_{\rm h}$. The ten subsamples have similar $L({\rm Ly}\alpha)_{\rm H}$ of $\sim 2 \times 10^{42}$ erg s^{-1}, and similar $L({\rm Ly}\alpha)_{\rm tot}$ of $\sim 2 \times 10^{42}$–4×10^{42} erg s^{-1} within a factor of 1.5. This is expected from the small difference in $L({\rm Ly}\alpha)_{ps}$ between the subsamples as described in the next paragraph. What we newly find is that $L({\rm Ly}\alpha)_{\rm H}$ and $L({\rm Ly}\alpha)_{\rm tot}$ remain almost unchanged when $M_\star$ increases by factor 2–5. This has not been confirmed with SED fitting (including nebular emission in models).

The nearly constant (or even slightly decreasing) $L({\rm Ly}\alpha)_{\rm H}$ against $M_\star$ is a result of two competing trends. One is that $L({\rm Ly}\alpha)_{\rm C}$ is constant or decreases with $M_\star$ as expected from the $L({\rm Ly}\alpha)_{ps}$ vs. $M_{\rm UV}$ plot (figure 2.3 [g]), and the other is that $L({\rm Ly}\alpha)_{\rm H}/L({\rm Ly}\alpha)_{\rm C}$ decreases with $L({\rm Ly}\alpha)_{\rm C}$ as found from equation (5.1). Let us take the $L({\rm Ly}\alpha)$–divided and K–divided subsamples as two examples. For the former subsamples, the $L({\rm Ly}\alpha)_{\rm C}$ of the massive subsample is factor 2.5 *lower* than that of the less massive one, but the difference

is reduced to factor 1.5 in $L(\mathrm{Ly}\alpha)_\mathrm{H}$ because objects with lower $L(\mathrm{Ly}\alpha)_\mathrm{C}$ have higher $L(\mathrm{Ly}\alpha)_\mathrm{H}/L(\mathrm{Ly}\alpha)_\mathrm{C}$. For the latter, the two subsamples have almost the same $L(\mathrm{Ly}\alpha)_\mathrm{C}$ and hence almost the same $L(\mathrm{Ly}\alpha)_\mathrm{H}$. The slightly decreasing trend of $L(\mathrm{Ly}\alpha)_\mathrm{tot}$ with mass is due to the fact that $L(\mathrm{Ly}\alpha)_\mathrm{tot}/L(\mathrm{Ly}\alpha)_\mathrm{C}$ decreases with $L(\mathrm{Ly}\alpha)_\mathrm{C}$ more mildly than $L(\mathrm{Ly}\alpha)_\mathrm{H}/L(\mathrm{Ly}\alpha)_\mathrm{C}$ does.

Figure 6.13 shows that $L(\mathrm{Ly}\alpha)_\mathrm{H}$ and $L(\mathrm{Ly}\alpha)_\mathrm{tot}$ are also nearly independent of SFR, $E(B-V)_\star$, and M_h, although the uncertainties in M_h are relatively large. The fact that differently defined subsamples follow a common trend in each panel indicates that the nearly constant $L(\mathrm{Ly}\alpha)_\mathrm{H}$ and $L(\mathrm{Ly}\alpha)_\mathrm{tot}$ against $M_\star$ and the other three parameters are real; it is unlikely that grouping the LAEs into two by the five quantities has erased strong mass dependence which otherwise would be visible. It is also unlikely that the NB-selection bias of our LAE sample causes the flat trend as described in appendices C.1 and C.2. We discuss the physical origins of diffuse Lyα halos from these results in chapter 8.

6.8 Lyα escape fraction

Following previous studies, we define the escape fraction of Lyα photons, $f_\mathrm{esc}(\mathrm{Ly}\alpha)$, as the ratio of observed Lyα luminosity, $L(\mathrm{Ly}\alpha)_\mathrm{obs}$, to intrinsic Ly$\alpha$ luminosity, $L(\mathrm{Ly}\alpha)_\mathrm{int}$, produced in the galaxy due to star formation (e.g., Atek et al., 2008; Kornei et al., 2010):

$$f_\mathrm{esc}(\mathrm{Ly}\alpha) = \frac{L(\mathrm{Ly}\alpha)_\mathrm{obs}}{L(\mathrm{Ly}\alpha)_\mathrm{int}} = \frac{SFR_{\mathrm{Ly}\alpha}}{SFR_\mathrm{tot}}, \tag{6.7}$$

where SFR_tot is the total (i.e., dust-corrected) star formation rate and $SFR_{\mathrm{Ly}\alpha}$ is the star formation rate converted from $L(\mathrm{Ly}\alpha)_\mathrm{obs}$ as below:

$$SFR_{\mathrm{Ly}\alpha}\,(\mathrm{M_\odot\,yr^{-1}}) = 9.1\times10^{-43}\,L(\mathrm{Ly}\alpha)_\mathrm{obs}\,(\mathrm{erg\,s^{-1}}) \tag{6.8}$$

(Brocklehurst, 1971; Kennicutt, 1998).

In this thesis, we constrain $f_\mathrm{esc}(\mathrm{Ly}\alpha)$ from $L^{3\sigma}_\mathrm{TIR}$of our LAEs in CDFS field (Kusakabe et al., 2015), which only take into account the observed Lyα photons from the main body of galaxies following previous studies (e.g., Blanc et al., 2011; Oteo et al., 2015) in section 6.8.1. We also derive $f_\mathrm{esc}(\mathrm{Ly}\alpha)$ from $L(\mathrm{Ly}\alpha)_\mathrm{tot}$ (total Lyα escape fraction, $f_\mathrm{esc}(\mathrm{Ly}\alpha)_\mathrm{tot}$; see table 6.3) in section 6.8.2 unlike previous studies which have ignored the contribution from the LAH (e.g., Blanc et al., 2011; Oteo et al., 2015). For SFR_tot we use the one obtained from the SED fitting. This definition of $f_\mathrm{esc}(\mathrm{Ly}\alpha)_\mathrm{tot}$ thus assumes that all Lyα photons including those of the LAH are produced from star formation in the central galaxy. We discuss the possibility of the existence of additional Lyα sources later (in section 9.2).

6.8.1 Lyα escape fraction for the main body of LAEs constrained with IR observations at $z\sim2$

The escape fraction of Lyα photons is robustly constrained from $L^{3\sigma}_\mathrm{TIR}$. By stacking the 52 LAEs in the $NB387$ band, we obtain $L(\mathrm{Ly}\alpha) = 5.9^{+0.6}_{-0.6}\times10^{41}$ erg s^{-1}, which is converted

Table 6.6 Lyα luminosities for the subsamples.

subsamples	$L(\mathrm{Ly}\alpha)_{\mathrm{C}}$ $10^{41}\,L_{\odot}$ (1)	$L(\mathrm{Ly}\alpha)_{\mathrm{H}}$ $10^{41}\,L_{\odot}$ (2)	$L(\mathrm{Ly}\alpha)_{\mathrm{tot}}$ $10^{41}\,L_{\odot}$ (3)
SXDS			
bright UV	$7.7^{+2.3}_{-1.5}$	$15.9^{+2.0}_{-1.7}$	$23.6^{+4.3}_{-3.2}$
faint UV	$9.4^{+1.8}_{-0.8}$	$17.5^{+1.4}_{-0.7}$	$26.9^{+3.2}_{-1.5}$
blue β	$9.1^{+2.1}_{-1.2}$	$17.3^{+1.6}_{-1.1}$	$26.4^{+3.7}_{-2.4}$
red β	$8.5^{+1.8}_{-0.9}$	$16.8^{+1.5}_{-0.9}$	$25.3^{+3.4}_{-1.8}$
bright Lyα	$13.8^{+2.4}_{-1.1}$	$20.2^{+0.8}_{-0.5}$	$34.0^{+3.3}_{-1.5}$
faint Lyα	$6.2^{+1.9}_{-1.0}$	$14.3^{+2.1}_{-1.4}$	$20.5^{+4.1}_{-2.4}$
large EW	$12.5^{+2.1}_{-0.8}$	$19.6^{+0.9}_{-0.4}$	$32.1^{+3.1}_{-1.2}$
small EW	$6.6^{+2.1}_{-1.3}$	$14.7^{+2.2}_{-1.7}$	$21.3^{+4.2}_{-3.0}$
bright K	$7.9^{+2.3}_{-1.2}$	$16.1^{+2.0}_{-1.3}$	$24.0^{+4.4}_{-2.5}$
faint K	$9.1^{+1.9}_{-0.9}$	$17.3^{+1.5}_{-0.8}$	$26.3^{+3.4}_{-1.7}$
COSMOS			
bright UV	$14.7^{+3.0}_{-1.4}$	$20.6^{+0.8}_{-0.6}$	$35.3^{+3.8}_{-2.0}$
faint UV	$11.9^{+2.0}_{-0.6}$	$19.2^{+1.0}_{-0.4}$	$31.1^{+2.9}_{-1.0}$
blue β	$13.5^{+2.4}_{-1.0}$	$20.1^{+0.9}_{-0.5}$	$33.5^{+3.2}_{-1.5}$
red β	$12.4^{+2.3}_{-0.9}$	$19.5^{+1.0}_{-0.5}$	$31.9^{+3.3}_{-1.5}$
bright Lyα	$15.7^{+2.5}_{-0.9}$	$20.9^{+0.5}_{-0.3}$	$36.6^{+3.1}_{-1.2}$
faint Lyα	$8.1^{+1.8}_{-0.8}$	$16.4^{+1.6}_{-0.8}$	$24.5^{+3.4}_{-1.7}$
large EW	$14.3^{+2.4}_{-0.7}$	$20.4^{+0.7}_{-0.3}$	$34.7^{+3.1}_{-0.9}$
small EW	$8.9^{+2.2}_{-1.2}$	$17.1^{+1.7}_{-1.1}$	$26.0^{+3.9}_{-2.3}$
bright K	$13.4^{+2.7}_{-1.1}$	$20.0^{+1.0}_{-0.6}$	$33.4^{+3.6}_{-1.7}$
faint K	$12.6^{+2.1}_{-0.8}$	$19.6^{+0.9}_{-0.4}$	$32.2^{+3.0}_{-1.2}$

Note. — (1) Lyα luminosity at the central part derived by multiplying $L(\mathrm{Ly}\alpha)_{ps}$ by 0.77; (2) Lyα luminosity of the LAH derived from equation 5.1; (3) total Lyα luminosity derived from equation 5.1.

into $\mathrm{SFR}_{\mathrm{Ly}\alpha} = 0.54^{+0.6}_{-0.6}\ M_{\odot}\mathrm{yr}^{-1}$. Here we have assumed that the $NB387$ photometry recovers the total Lyα luminosity. The escape fraction of Lyα is constrained as:

$$16\% = \frac{SFR_{\mathrm{Ly}\alpha}}{SFR_{\mathrm{UV}} + SFR^{3\sigma}_{\mathrm{IR}}} \leq f^{\mathrm{Ly}\alpha}_{\mathrm{esc}} \leq \frac{SFR_{\mathrm{Ly}\alpha}}{SFR_{\mathrm{UV}}} = 37\%. \tag{6.9}$$

This constraint on $f^{\mathrm{Ly}\alpha}_{\mathrm{esc}}$ is roughly consistent with those based on the Hα luminosity (Nakajima et al., 2012) and UV continuum (Blanc et al., 2011) as well as the lower limits obtained by Wardlow et al. (2014) from FIR stacking and by Zheng et al. (2012) from X-ray stacking. The $f^{\mathrm{Ly}\alpha}_{\mathrm{esc}}$ value is significantly higher than the cosmic averages at $z \sim 2$, $f^{\mathrm{Ly}\alpha}_{\mathrm{esc}} \simeq 2.8^{+2.6}_{-0.4}\%$ (Hayes et al., 2011) but comparable to those at $z \gtrsim 4$. In the next section, we include observed Lyα photons from LAHs to the calculation of the $f^{\mathrm{Ly}\alpha}_{\mathrm{esc}}$ and obtain higher higher $f^{\mathrm{Ly}\alpha}_{\mathrm{esc}}$ as $f_{\mathrm{esc}}(\mathrm{Ly}\alpha)_{\mathrm{tot}}$.

6.8.2 Lyα escape fraction including LAH of LAEs at $z \sim 2$

Figure 6.14 shows $f_{\rm esc}({\rm Ly}\alpha)_{\rm tot}$ as a functions of $M_\star$, SFR, and $E(B-V)$ for the ten subsamples. All values are field-average values. For a thorough discussion, results with the Calzetti curve are also shown (figures 6.14 [b], [d], and [f]) as well as those with an SMC-like curve (the other panels). Two interesting features are seen in these figures.

First, $f_{\rm esc}({\rm Ly}\alpha)_{\rm tot}$ anti-correlates with $M_\star$, SFR, and $E(B-V)$ regardless of the assumed curve. Similar anti-correlations have been found for HAEs by Matthee et al. (2016) who have measured total Lyα luminosities on a $6''$ diameter aperture, corresponding to 24 kpc in radius (blue crosses in the Calzetti-curve panels; see also footnote *28). Any galaxy population may have such anti-correlations. Indeed, an anti-correlation between $f_{\rm esc}({\rm Ly}\alpha)$ and $E(B-V)$ is found for star forming galaxies at $z \sim 0$–3 (e.g., Hayes et al., 2011; Blanc et al., 2011; Atek et al., 2014; Hayes et al., 2014). Although Lyα halos are not included in their calculations, these results imply an anti-correlation between $f_{\rm esc}({\rm Ly}\alpha)_{\rm tot}$ and $E(B-V)$ since $L({\rm Ly}\alpha)_{\rm tot}$ increases with $L({\rm Ly}\alpha)_{\rm C}$ as seen in figure 5.1(d).

Second, our LAEs have very high $f_{\rm esc}({\rm Ly}\alpha)_{\rm tot}$ values. For an SMC-like curve, they are higher than $\sim 30\%$, with some exceeding 100%. Using a Calzetti curve makes $f_{\rm esc}({\rm Ly}\alpha)_{\rm tot}$ lower but still in a range of $\sim$ 10–100%. The typical $f_{\rm esc}({\rm Ly}\alpha)_{\rm tot}$ of the LAE sample is ~ 1 dex higher than that of the HAE sample, which is similar to the result obtained in Sobral et al. (2017). More importantly, a large $f_{\rm esc}({\rm Ly}\alpha)_{\rm tot}$ difference is found even in comparison at a fixed $M_\star$, SFR, and $E(B-V)_\star$. We discuss mechanisms by which LAEs can achieve such high escape fractions in section 9.2.

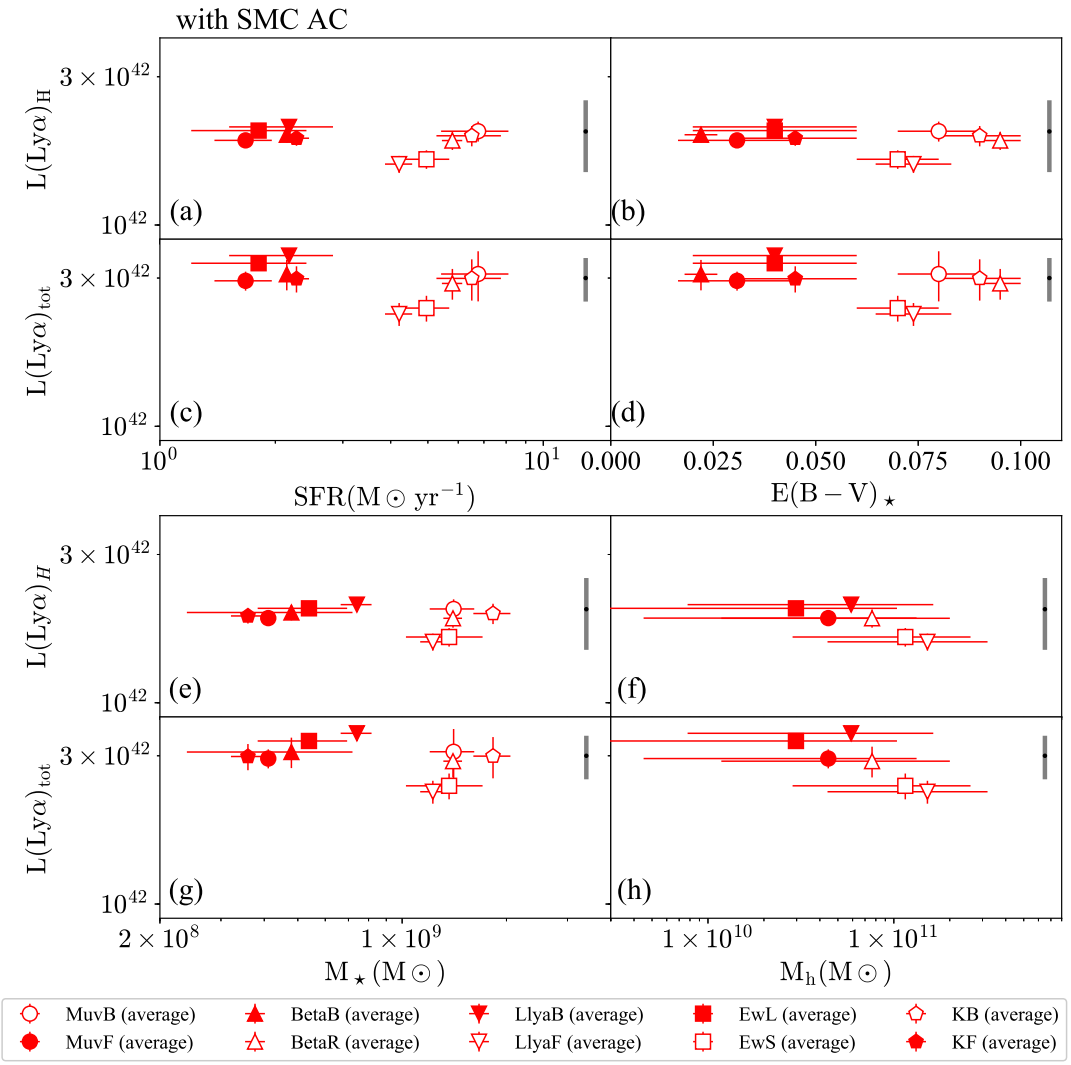

Figure 6.13 $L(\mathrm{Ly}\alpha)_{\mathrm{H}}$ and $L(\mathrm{Ly}\alpha)_{\mathrm{tot}}$ as a functions of stellar parameters and dark matter halo mass for an SMC curve: (a) $L(\mathrm{Ly}\alpha)_{\mathrm{H}}$ vs. SFR, (b) $L(\mathrm{Ly}\alpha)_{\mathrm{H}}$ vs. $E(B-V)_{\star}$, (c) $L(\mathrm{Ly}\alpha)_{\mathrm{tot}}$ vs. SFR, (d) $L(\mathrm{Ly}\alpha)_{\mathrm{tot}}$ vs. $E(B-V)_{\star}$, (e) $L(\mathrm{Ly}\alpha)_{\mathrm{H}}$ vs. $M_{\star}$, (f) $L(\mathrm{Ly}\alpha)_{\mathrm{H}}$ vs. M_{h}, (g) $L(\mathrm{Ly}\alpha)_{\mathrm{tot}}$ vs. $M_{\star}$, and (h) $L(\mathrm{Ly}\alpha)_{\mathrm{tot}}$ vs. M_{h}. All values are field average values. Different symbols indicate different subsamples: open (filled) circles for bright (faint) M_{UV}, open (filled) triangles for red (blue) β, open (filled) inverted triangles for faint (bright) $L(\mathrm{Ly}\alpha)_{ps}$, open (filled) squares for small (large) $EW_{0,ps}(\mathrm{Ly}\alpha)$, and open (filled) pentagons for bright (faint) m_{K}. The typical 1σ uncertainties in the individual data in Momose et al. (2016) are propagated to uncertainties in $L(\mathrm{Ly}\alpha)_{\mathrm{H}}$ and $L(\mathrm{Ly}\alpha)_{\mathrm{tot}}$ of $\sim 22\%$ and $\sim 16\%$, respectively. Gray error bars of black dots in panels (a)–(d) and (e)–(f) show those uncertainties at $L(\mathrm{Ly}\alpha)_{\mathrm{H}} = 2\times10^{42}\,\mathrm{erg\,s^{-1}}$ and $L(\mathrm{Ly}\alpha)_{\mathrm{tot}} = 3\times10^{42}\,\mathrm{erg\,s^{-1}}$, respectively. The vertical error bars of the red symbols are derived from the fitting errors in $L(\mathrm{Ly}\alpha)_{ps}$. M_{h} are not calculated for the m_K-divided subsamples. The M_{h} values for the bright M_{UV} and blue β subsamples are not shown because they are not constrained well owing to too weak clustering signals.

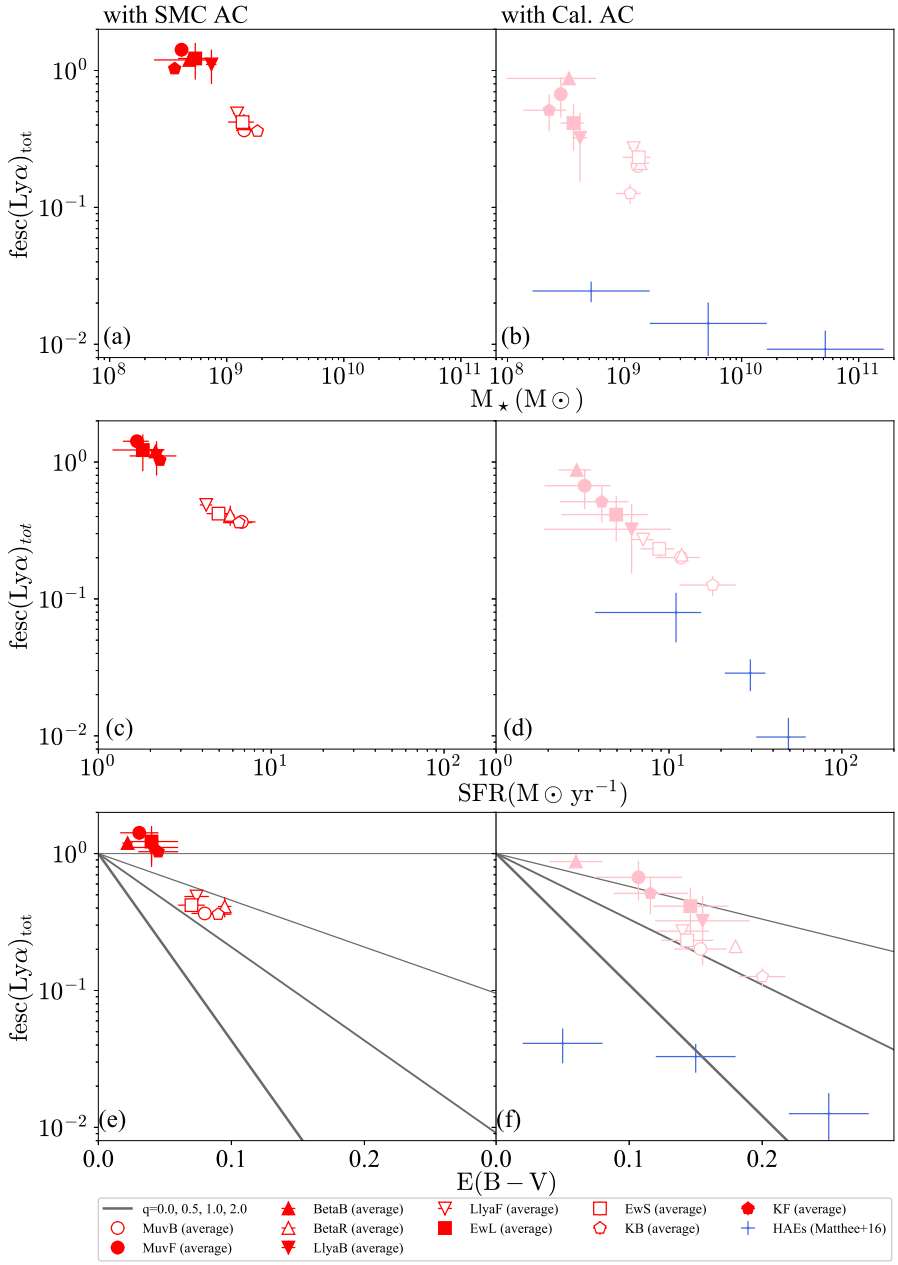

Figure 6.14 $f_{\rm esc}({\rm Ly}\alpha)_{\rm tot}$ as a functions of $M_\star$ (panels [a] and [b]), SFR ([c] and [d]), and $E(B-V)$ ([e] and [f]) for the two attenuation curves. All values are field average values. Different symbols indicate different subsamples: open (filled) circles for bright (faint) $M_{\rm UV}$, open (filled) triangles for red (blue) β, open (filled) inverted triangles for faint (bright) $L({\rm Ly}\alpha)_{ps}$, open (filled) squares for small (large) $EW_{0,ps}({\rm Ly}\alpha)$, and open (filled) pentagons for bright (faint) $m_{\rm K}$. Blue crosses indicate HAEs in Matthee et al. (2016), whose Lyα luminosities are derived from 6″ aperture photometry. Dark gray solid lines show models for four different q values, $q = 0.0, 0.5, 1.0$, and 2.0 with increasing thickness. Stellar parameters are derived with the assumption of $E(B-V)_\star = E(B-V)_g$.

Chapter 7

Discussion I. the origin of the properties of LAEs and the present-day descendants of LAEs

In this chapter, we interpret our results on LAEs in terms of the general evolution of galaxies. We discuss the physical origin of their high $SHMR$ and BCE as well as normal star formation mode (in section 7.1.1), the origin of the appropriate dust attenuation curve (in section 7.2), and the evolutionary path of our LAEs (in section 7.3). We compare our results with theoretical models.

We assume that the four average relations shown in figures 6.7, 6.9, 6.11, and 6.12 do not change either the slope (in log-log plane) or the scatter at low masses. We also assume that our LAEs are central galaxies. If they are satellite galaxies, their dark matter halo (sub halo) masses will be overestimated and their true $SHMR$ and BCE would be higher than reported in this thesis.

7.1 The physical origin of the star formation mode, $SHMR$, and BCE of LAEs at $z \sim 2$

Galaxies assemble their stellar mass through star formation and galaxy merging under the gravitational influence of their host dark matter halos, which also grow through mass accretion and merging (e.g., Somerville & Davé, 2015). The average baryon accretion rate (BAR, $\dot{M}_{\rm b}$) at a fixed halo mass is proportional to the halo mass accretion rate, which is estimated as a function of redshift and halo mass from cosmological simulation (Dekel et al., 2009a). The BCE ($= \dot{M}_\star/\dot{M}_{\rm b}$) means the efficiency of star formation in dark matter halos at the observed time with an assumption that most of the accreting baryons are in a (cold) gas phase (i.e., the BAR is equal to the inflow rate of cold gas). On the other hand,

the efficiency of star formation in dark matter halos integrated over time is indicated by SHMR ($= M_\star/M_{\rm h}$). They are suggested to depend on efficiency of star formation feed back including those due to AGNs and supernovae (SNe), which control the amount of cold gas, and (local) star formation efficiency. It is well known that SFR surface density correlates (cold) gas surface density (the Kennicutt-Schmidt law; e.g., Schmidt, 1959; Kennicutt & Evans, 2012, and references therein). It suggests that disk size of galaxy (or spin parameter of dark matter halo, Mo et al., 1998), is also an important parameter.

7.1.1 The possible origins of moderate star formation mode, high SHMR, and high BCE of LAEs at $z \sim 2$

Our LAEs have a higher $SHMR$ and a higher BCE than average galaxies but have a moderate SFR, being located on the (extrapolated) SFMS defined by average galaxies. Indeed, it is not trivial for galaxy formation models to reproduce these three properties simultaneously.

Dutton et al. (2010) have used a semi-analytic model to study the evolution of the SFMS and its dependence on several key parameters in the model. As shown in their figure 12

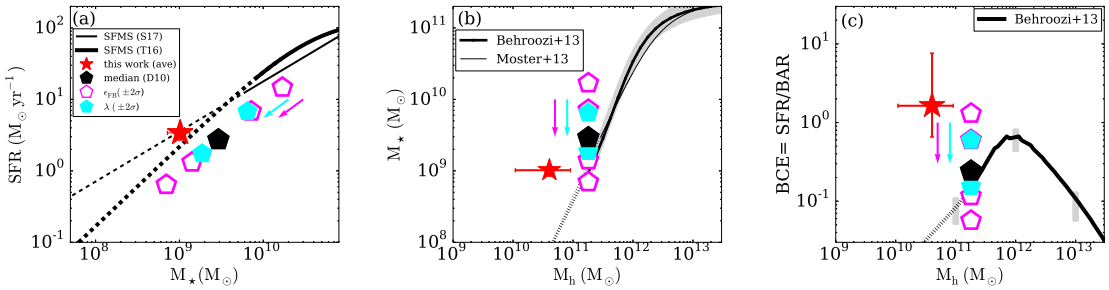

Figure 7.1 Changes in the position of model galaxies in the $M_\star$-SFR plane (panel (a)), $M_{\rm h}$-$M_\star$ plane ([b]), and $M_{\rm h}$-BCE plane ([c]) due to variations in the halo spin parameter, λ, and the feedback efficiency, $\epsilon_{\rm FB}$, calculated by Dutton et al. (2010, hereafter D10). Pentagons show D10' s model galaxies with a fixed halo mass ($M_{\rm h,\ z=0} = 4 \times 10^{11}{\rm M}_\odot$, corresponding to $\sim 2 \times 10^{11}{\rm M}_\odot$ at $z = 2$ according to figures 7 and 8 in Behroozi et al. (2013)), where black, cyan, and magenta colors denote, respectively, positions with median halo parameters, those with $\pm 2\sigma$ variation in λ, and those with $\pm 2\sigma$ variation in $\epsilon_{\rm FB}$. All model data of $M_\star$ and SFR are taken from figure 12 in D10 (In D10 four data points are shown as $\pm 2\sigma$ variation in $\epsilon_{\rm FB}$). The BARs of model galaxies are calculated from equation 6.6. Cyan and magenta arrows indicate the direction in which galaxies move when λ and $\epsilon_{\rm FB}$ increase. In all panels, red stars represent the average LAEs with $NB387_{\rm tot} \leq 25.5$ mag. In panel (a), several SFMS measurements in previous studies are shown by black lines in the same manner as figure 6.9. The average relations in Behroozi et al. (2013) and Moster et al. (2013) are plotted by black lines in panels (b) and (c), similar to figures 6.11 and 6.12. All data are rescaled to a Salpeter IMF according to footnote ∗1. See also footnotes ∗29–∗32.

and our figure 7.1, model galaxies (at $z \sim 2$) at a fixed halo mass move along the SFMS upward when the supernova (SN) feedback is weakened or the halos' spin parameter is reduced, thus having a higher $SHMR$ and a higher BCE on the SFMS. With a lower feedback efficiency, a larger amount of cold gas can be stored, thus resulting in a higher SFR and a higher stellar mass. A lower spin causes the gas density to be higher, thereby the SFR per unit gas mass is elevated. Although these results may not necessarily be applicable to our LAEs whose halo mass is ten times lower, it is interesting to note that there is a relatively simple way to explain MS galaxies with an elevated $SHMR$ and BCE.

It is beyond our scope to identify the mechanism(s) by which our LAEs acquire a high $SHMR$ and a high BCE. If, however, the high $SHMR$ and BCE of our LAEs are due to some systematic differences in one or more parameters controlling the star formation and/or internal structure of halos similar to Dutton et al. (2010)'s study, then it implies that not all but only a certain fraction of (low-mass) halos at $z \sim 2$ experience the LAE phase. This is consistent with a low duty cycle of LAEs and a low LAE fraction shown in section 9.1.

7.2 The origin of the dust attenuation of LAEs at $z \sim 2$

We find that our LAEs at $z \sim 2$ have a moderate IRX at a fixed $M_\star$, lying on the average (or 'consensus relation') of IRX–$M_\star$ as described in section 6.4. Our LAEs are also found to favor a steep attenuation curve like an SMC-like extinction curve as well as young/low-$M_\star$ galaxies at $z \sim 2$ as mentioned in section 6.1.6. These results implies a possibility that the physical origins of the amount of dust attenuation and wavelength dependence of dust attenuation of the LAEs are similar/common with those for young/low-$M_\star$ galaxies at the same redshift. This idea is not inconsistent with a higher Lyα escape fraction of our LAEs at a fixed $E(B-V)$ and $M_\star$ than those of the HAEs (see section 6.8.2). Below, we discuss the origin of the dust attenuation of the LAEs based on the theoretical model of dust evolution and galaxy evolution (e.g., Asano et al., 2013b, 2014).

7.2.1 Connection between attenuation curves and galaxy evolution

Attenuation curves of galaxies are thought to evolve with time because dust in galaxies changes its properties with galaxy evolution. We discuss aspects of attenuation curves reflecting galaxy evolution.

Physical properties of dust grains and relative spatial distributions of dust and stars (i.e., geometry) determine the dust attenuation of galaxies. The former corresponds to the abundance and size distribution of dust grains and is well modeled (e.g., Draine & Lee, 1984). Dust is usually assumed to be composed of a mixture of graphites and silicates. In a simple case that only dust "extinction" (not "attenuation") is taken into account, the dust extinction efficiency per unit mass, κ, depends on wavelength, λ, and the radius of dust grains, r_d. For $\lambda \lesssim 2\pi r_\mathrm{d}$, κ is nearly independent of λ and inversely proportional to r_d, while for $\lambda \gtrsim 2\pi r_\mathrm{d}$, κ decreases with increasing λ as λ^{-1} (see also figure 1(a) in Yajima & Nagamine, 2014). Consequently, if galaxies have dust of small

grains, κ at shorter wavelengths have larger values, making the extinction curve steeper. With regard to the latter, dust geometry, as summarized in table 1 of Calzetti (2001, and references therein), previous studies assume various geometries, e.g., a homogenous slab, a homogeneous sphere, and a clumpy distribution. It is suggested that nebular emission (from HII regions) is attenuated higher than continuum for some of galaxies (e.g., Calzetti, 1997; Kashino et al., 2013; Koyama et al., 2018). Koyama et al. (2018) suggest that more low-$M_\star$ galaxies (or hose with high $SFRs$) tend to have more uniformly distributed HII regions, while more massive galaxies tend to have more patchy distribution of dust. The properties of dust geometry and its evolution of high-z low-$M_\star$ galaxies are still open questions.

Recently, dust SED models have been proposed based on Draine & Li (2007) considering dust properties and geometry and they can reproduce multi-wavelength observations well. Theoretical models of dust evolution have been rapidly improving especially for physical properties of dust grains (Asano et al., 2013b, 2014). In the Asano model, dust is produced from type II supernovae (SNe II) and asymptotic giant branch (AGB) stars (e.g., Valiante et al., 2009; Hirashita & Kobayashi, 2013) and grows from metal accretion and grain-grain collisions (shattering and coagulation; e.g., Hirashita & Yan, 2009; Rémy-Ruyer et al., 2014), while being destroyed by SN shocks (e.g., Nozawa et al., 2007). Dust growth is expected to be a dominant process if metallicity becomes larger than a critical value (Asano et al., 2013a) and grain-grain collision becomes efficient if metallicity reaches a sub-solar value. Asano et al. (2014) introduce a simple evolutionary scenario of dust extinction curve as below.

(i) Early phase: formation of dust in SNe II and AGB stars
Large grains ($> 0.1\mu m$) are dominant and the extinction curve is flat.

(ii) Middle phase: shattering and grain growth due to gas accretion
Small grains ($< 0.03\mu m$) are produced and the extinction curve becomes steeper.

(iii) Late phase: coagulation of small grains
The peak of size distribution shifts and the extinction curve becomes flatter.

For instance, the Milky Way is chemically enriched ($\sim$ solar metallicity) and has a relatively flat extinction curve, being consistent with phase (iii). On the other hand, the SMC is a low-metal galaxy ($\sim$ a fifth of solar metallicity to sub-solar metallicities) and has a steep extinction curve. The SMC is probably expected to be just in phase (ii).

7.2.2 Possible origins of the steep attenuation curve of our LAEs

As mentioned in section 6.1.6, our LAEs favor an SMC-like extinction curve as the attenuation curve. With an assumption that the evolution of "attenuation" curve has the same tendency as of "extinction" curve, there is a possibility that our LAEs have just produced small grain dust with κ steeply increasing with wavelength (UV) and their dust has just started to grow with sub-solar metallicities (Nakajima et al., 2012; Nakajima & Ouchi, 2014) as in phase (ii). This is consistent with the young age of our LAEs, $\sim$ 100 Myr, and is also consistent with young UV-selected galaxies, which favor an SMC-like curve

according to Reddy et al. (2012a,b, their age derived with an SMC-like curve is $\sim$ 100 Myr). Recently, Reddy et al. (2018) find that galaxies at $z = 1.5$–2.5 prefer an SMC-like attenuation curve rather than the Calzetti curve with sub-solar metallicity stellar population models. Moreover, young/ low-$M_\star$ galaxies among their sample implies a attenuation curve even steeper than an SMC-like curve.

Consequently, our result for LAEs at $z \sim 2$ implies that the evolution of dust grains of LAEs probably causes the evolution of their attenuation curve as is the case for normal star-forming galaxies. It supports theoretical models of dust evolution, which suggests that dust attenuation curve reflects the degree of chemical evolution (i.e., metallicity) and the stellar assembly history such as age and the time scale of star formation (Asano et al., 2013b, 2014). Their normal IRXs at a fixed $M_\star$ as well as their high Lyα escape fractions at a fixed $E(B-V)$ and $M_\star$ implying that LAEs do not require an unique lower $E(B-V)$ and poor dust contents among low-$M_\star$ (faint) galaxies to have bright Lyα emission. These results of IRX and $fesc(\mathrm{Ly}\alpha)_{\mathrm{tot}}$ are not inconsistent with the implication for the origin of their steep attenuation curve.

7.3 The present-day descendants of LAEs at $z \sim 2$

LAEs are found to reside in low-mass halos with $M_{\mathrm{h}} \sim 10^{10}$–$10^{12}$ $\mathrm{M}_\odot$ over the wide redshift range $z \sim 2$–7 (e.g., Ouchi et al., 2005, 2010; Kovač et al., 2007; Gawiser et al., 2007; Shioya et al., 2009; Guaita et al., 2010; Bielby et al., 2016; Diener et al., 2017; Ouchi et al., 2017). In other words, the bias value of LAEs tends to decrease with decreasing redshift more rapidly than that of dark matter halos (see figure 7 in Ouchi et al., 2017). Although this trend may be biased because faint LAEs in lower-mass halos are missed at high redshifts, it implies that at lower redshifts, only galaxies with relatively lower masses in the halo mass function can be LAEs, which is analogous to and/or maybe related to downsizing (Cowie et al., 1996).

A roughly constant halo mass with redshift also implies that local descendants of LAEs vary depending on their redshift. The growth of dark matter halos is statistically predicted by the extended Press-Schehter (EPS: Press & Schechter, 1974; Bond et al., 1991; Bower, 1991) model. An application of the EPS model to distant galaxies can be found in, e.g., Hamana et al. (2006). Previous studies suggest that LAEs at $z \sim 4$–7 evolve into massive elliptical galaxies at $z = 0$ (Ouchi et al., 2005; Kovač et al., 2007; Ouchi et al., 2010), while LAEs at $z \sim 3$ are expected to be progenitors of present-day $L_\star$ galaxies (Gawiser et al., 2007; Ouchi et al., 2010). Guaita et al. (2010) show that LAEs at $z \sim 2$ could be progenitors of present-day $L_\star$ galaxies like the Milky Way (MW) and that they could also be descendants of $z \sim 3$ LAEs, depending on star formation and dust formation histories (see also Acquaviva et al., 2012).

With the EPS model[*33], we find that at $z = 0$ our LAEs are embedded in dark matter halos with a median mass similar to the mass of the Large Magellanic Cloud (LMC: $M_{\mathrm{h}} \sim 0.2$–3×10^{11} $\mathrm{M}_\odot$; van der Marel & Kallivayalil, 2014; Peñarrubia et al., 2016, and

[*33] We use a publicly released code by T. Hamana: http://th.nao.ac.jp/MEMBER/hamanatk/OPENPRO/index.html.

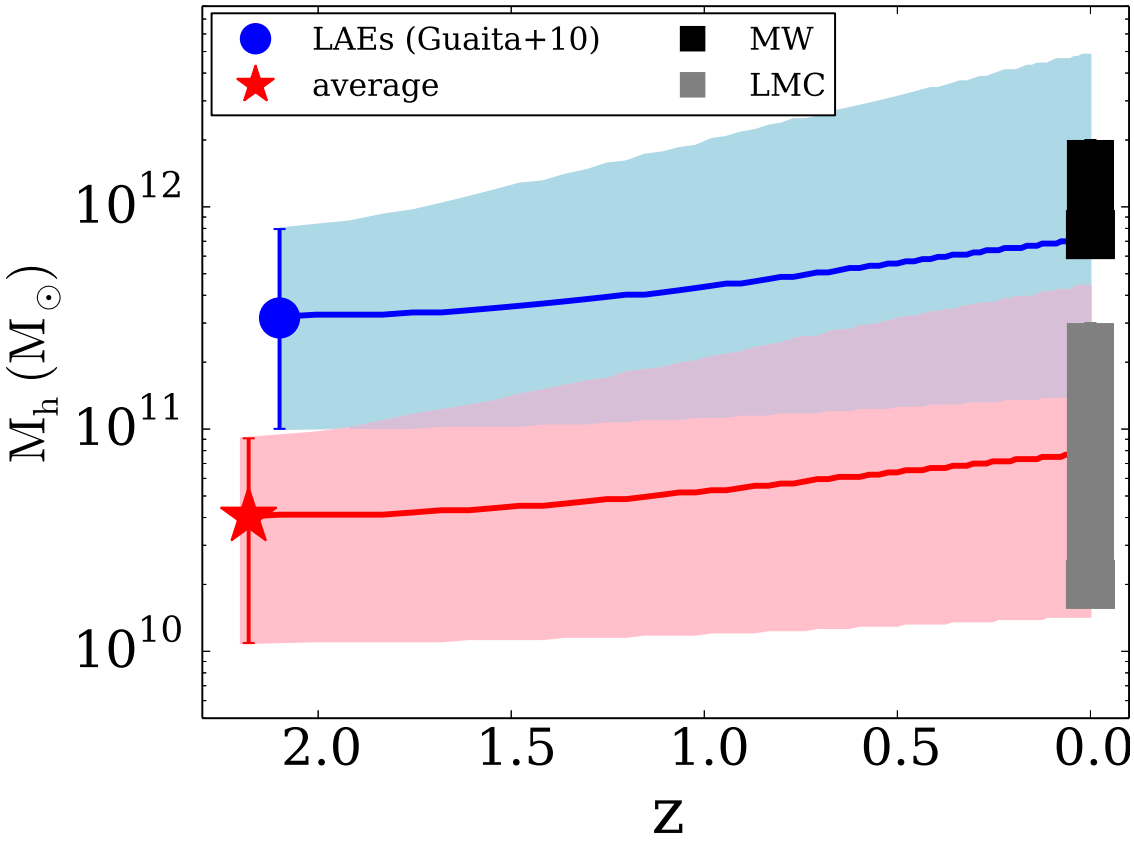

Figure 7.2 Dark matter halo mass evolution as a function of redshift predicted by the EPS formalism. A red (blue) curve indicates the evolution of the mode of the $M_{\rm h}$ distribution starting from the mass of our $z = 2.2$ LAEs shown by a red star (Guaita et al., 2010, 's $z = 2.1$ LAEs shown by a blue circle), with a shaded region indicating the 68% confidence interval of the distribution. Black and gray rectangles represent the measured halo mass ranges of the MW and the LMC, respectively (e.g., Wilkinson & Evans, 1999; Kafle et al., 2014; van der Marel & Kallivayalil, 2014; Eadie et al., 2015; Peñarrubia et al., 2016, see also Wang et al. 2015).

references therein), not in MW-like halos ($M_{\rm h} \sim 8 \times 10^{11}$–$2 \times 10^{12}$ $M_\odot$; e.g., Wilkinson & Evans, 1999; Kafle et al., 2014; Eadie et al., 2015, summarized in figure 1 in Wang et al. 2015), as shown in figure 7.2. This is consistent with the prediction by Acquaviva et al. (2012) from SED fitting that LAEs at $z \sim 3$, which are progenitors of present-day $L_\star$ galaxies, do not evolve into LAEs at $z \sim 2$. Combined with the previous studies, our result implies that the mass of present-day descendants of halos hosting LAEs depends on the redshift at which they are observed, with higher-z LAEs evolving into more massive halos.

Since the stellar mass of our LAEs, $10.2 \pm 1.8 \times 10^8$ $M_\odot$, is comparable to that of the LMC within only a factor of ~ 3 ($M_\star \sim 2.9 \times 10^9$ $M_\odot$: van der Marel et al., 2002), their star-formation has to be largely suppressed over most of the cosmic time until $z = 0$, or even be quenched, if they really become LMC-like galaxies. The star formation history

of the LMC has been inferred to have multiple components, i.e., an initial burst and subsequent periods with moderate or quiescent star formation (e.g., Harris & Zaritsky, 2009). For example, Rezaei Kh. et al. (2014) argue that it consists of two components: an initial burst of $\sim$ 10 Gyr ago, or at $z \sim 2$, with a $SFR \sim 2.4$ $M_\odot$ yr^{-1} assembling $\sim$90% of the total mass, and a much milder star formation with $SFR \sim 0.3$ $M_\odot$ yr^{-1} after that as shown in their figure 4 (see however Weisz et al. (2013), who obtained a much lower SFR). Interestingly, the estimated SFR for the LMC at $z \sim 2$ is similar to the SFR of our LAEs at $z \sim 2$, 3.4 ± 0.4 $M_\odot$ yr^{-1}. The high BCE ($= 1.6^{+6.0}_{-1.0}$) estimated for our LAEs also implies un-sustainable star formation after $z \sim 2$. If our LAEs follow such a history with suppressed star formation over $\sim 5 - 10 \times 10^9$ Gyr, they will grow to be LMC-like galaxies at $z = 0$. In this case, even if at $z \sim 2$ they lie above the average M_h–$SHMR$ relation, they will evolve into galaxies with an $SHMR$ consistent with the average relation at $z \sim 0$ (Behroozi et al., 2013; Moster et al., 2013).

Chapter 8

Discussion II. the origin of LAHs of LAEs

As described in section 1.4.2, theoretical studies have suggested three physical origins of LAHs around high–z star-forming galaxies: (a) cold streams (gravitational cooling), (b) star formation in satellite galaxies, and (c) resonant scattering of Lyα photons in the CGM which have escaped from the central galaxy. In origins (a) and (b), the Lyα photons of LAHs are produced in situ, while in origin (c) they come from central galaxies. The difference between (a) and (b) is how to produce Lyα photons. A flow chart and an illustration of these origins are shown in figure 6 in Mas-Ribas et al. (2017) and figure 15 in Momose et al. (2016), respectively. So far, observations have not yet identified the dominant origin(s) as explained below.

There are two observational studies on the origin of LAHs around star-forming galaxies. Leclercq et al. (2017) use 166 LAEs at $z \sim 3$–5 detected with the MUSE, while Momose et al. (2016) are based on a stacking analysis of ~ 3600 $z \simeq 2.2$ LAEs from a narrow-band survey, the same parent sample as we use in this study. Leclercq et al. (2017) have argued that a significant contribution from (b) star formation in satellite galaxies is somewhat unlikely since the UV component of MUSE-LAEs is compact and not spatially offset from the center of their LAH. However, they have not given a firm conclusion on the contributions from the remaining two origins. This is because while they have found a scaling relation of $L(\mathrm{Ly}\alpha)_{\mathrm{H}} \propto L_{\mathrm{UV}}^{0.45}$ which is not dissimilar to the scaling predicted from hydrodynamical simulations of cold streams by Rosdahl & Blaizot (2012), resonant scattering also prefers such a positive scaling relation if $f_{\mathrm{esc}}(\mathrm{Ly}\alpha)_{\mathrm{tot}}$ is constant. Moreover, they have also found that $\sim 80\%$ of their sample have a not-so-large total EW of Lyα emission, $EW_{0,tot}(\mathrm{Ly}\alpha) \lesssim 200$Å, not exceeding the maximum dust-free $EW_0(\mathrm{Ly}\alpha)$ of population II star formation, $\sim$ 50–240Å, with a solar metallicity and a Salpeter IMF (e.g., Charlot & Fall, 1993; Malhotra & Rhoads, 2002). If $EW_0(\mathrm{Ly}\alpha)$ is larger than ~ 200Å, Lyα radiation from cold streams would be responsible for LAHs.

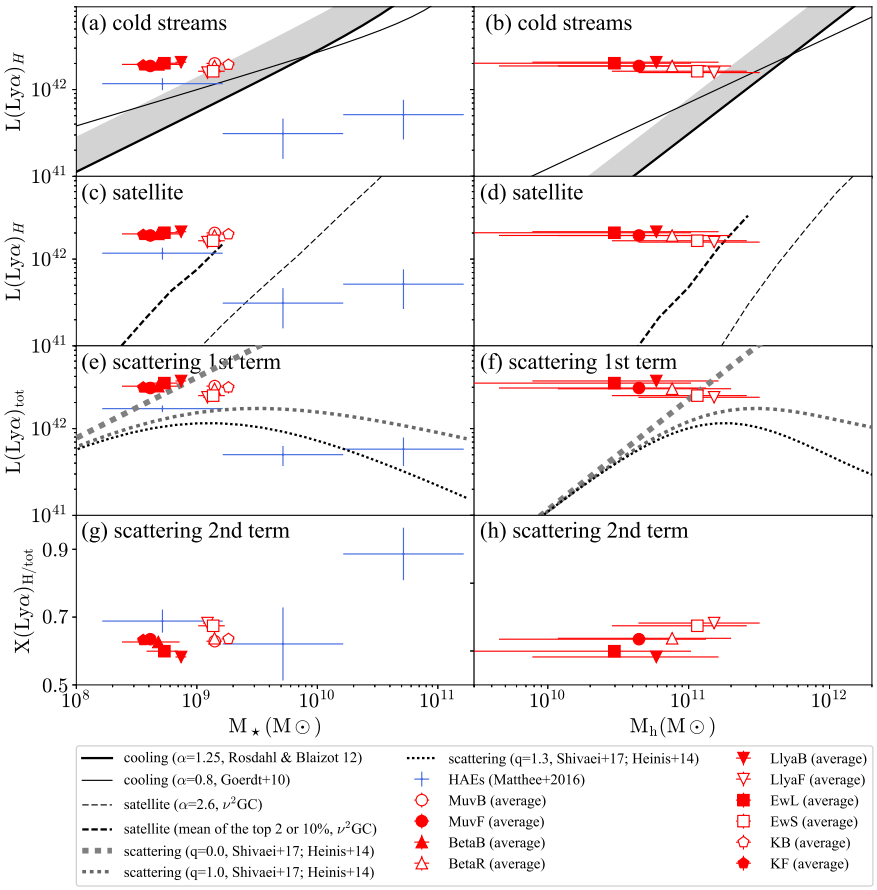

Figure 8.1 Test of the three LAH scenarios against the observed $L(\mathrm{Ly}\alpha)_\mathrm{H}$ and its mass dependence: (a) and (b) – cooling flow; (c) and (d) – satellite star formation; (e) and (h) – resonant scattering. Thick and thin solid black lines in panels (a) and (b) show the Lyα luminosity of cooling flows by theoretical models with a power law of $\alpha = 1.25$ (Rosdahl & Blaizot, 2012) and $\alpha = 0.8$ (Goerdt et al., 2010), respectively. Gray shaded regions above the solid black lines roughly indicate the distribution of Rosdahl & Blaizot (2012)'s simulated galaxies above the solid line, whose $L(\mathrm{Ly}\alpha)_\mathrm{H}$ reaches at most ~ 2.5 times higher than the line. A thin dashed black line indicates the mean Lyα luminosity from the star formation in satellite galaxies of ν^2GC (Makiya et al., 2016; Shirakata et al., 2018, Ogura et al. in prep.). A thick dashed black line indicates the mean of galaxies with the top 10% and 2% $L(\mathrm{Ly}\alpha)_\mathrm{H}$ at similar $M_\star$ and M_h in panels (c) and (d), respectively. Light gray, dark gray, and black dotted lines in (e) represent the Lyα luminosity escaping from the main body out to the CGM, with an absorption efficiency relative to UV continuum of $q = 0.0, 1.0$ and 1.3. We assume that all Ly*alpha* photons originate from star formation. Blue crosses indicate HAEs in Matthee et al. (2016), whose Lyα luminosities are derived from $3''$ and $6''$-diameter aperture photometry (see footnotes *28 and *34). Field average values of our ten subsamples are shown by symbols below: open (filled) circles for bright (faint) M_UV, open (filled) triangles for red (blue) β, open (filled) inverted triangles for faint (bright) $L(\mathrm{Ly}\alpha)_{ps}$, open (filled) squares for small (large) $EW_{0,ps}(\mathrm{Ly}\alpha)$, and open (filled) pentagons for bright (faint) m_K. Stellar parameters of our subsamples are derived with the assumption of a SMC-like attenuation curve. M_h are not calculated for the K-divided subsamples, and are not plotted for the bright M_UV and blue β subsamples because of extremely large uncertainties. All data are rescaled to a Salpeter IMF according to footnote *1.

Momose et al. (2016) have also found relatively low $EW_{0,tot}$(Lyα) and marginally ruled out the cold stream origin based on a similar discussion to Leclercq et al. (2017)'s. In these two observational studies, $EW_{0,tot}$(Lyα) are calculated by dividing the total Lyα luminosity by the UV luminosity of the *central* part. Therefore, the relatively low $EW_{0,tot}$(Lyα) values do not necessarily mean that the net EW_0 of LAHs are also low; they would even be extremely high if LAHs do not have UV emission. Thus, the cold stream scenario cannot be ruled out from the low $EW_{0,tot}$(Lyα) values alone. The discussion using the $L(\mathrm{Ly}\alpha)_\mathrm{H}$–$L_\mathrm{UV}$ relation assumes $L_\mathrm{UV} \propto M_\mathrm{h}^{0.5}$ because the simulations have calculated $L(\mathrm{Ly}\alpha)_\mathrm{H}$ against M_h. Since L_UV may not be a perfect tracer of M_h, it is more desirable to use directly the $L(\mathrm{Ly}\alpha)_\mathrm{H}$-$M_\mathrm{h}$ relation, or the $L(\mathrm{Ly}\alpha)_\mathrm{H}$–$M_\star$ relation as a better substitute. In addition, comparing the normalization of the relation as well as its power-law slope can better constrain this scenario. With regard to (b) satellite star formation, independent observations are desirable to strengthen the conclusion by Leclercq et al. (2017) since Momose et al. (2016) have not been able to rule out this origin. Finally, if resonant scattering is the dominant origin, LAH luminosities have to be explained by the properties of the main body of galaxies such as SFR and $E(B-V)$.

In section 6.7.1, we find that the $L(\mathrm{Ly}\alpha)_\mathrm{H}$ and $L(\mathrm{Ly}\alpha)_\mathrm{tot}$ of our LAEs remain unchanged with increasing stellar mass. We also obtain a constant or increasing $X(\mathrm{Ly}\alpha)_\mathrm{H/tot}$ with $M_\star$ (see figure 8.1[g]). In the following subsections, we use these relations to discuss the three origins with figure 8.1. We also use the results on HAEs obtained by Matthee et al. (2016)[*34] to strengthen the discussion. We also briefly examine the fluorescence scenario in appendix C.3, following the very recent study on fluorescence emission for star-forming LAEs by Gallego et al. (2018).

8.1 (a) Cold streams

Theoretical studies and simulations suggest that high-z ($z \gtrsim 2$) galaxies obtain baryons through the accretion of relatively dense and cold ($\sim 10^4$ K) gas known as cold streams (e.g., Fardal et al., 2001; Kereš et al., 2005; Dekel & Birnboim, 2006). The accreting gas releases the gravitational energy and emits Lyα photons, thus producing an extended Lyα halo without (extended) UV continuum emission (e.g., Haiman et al., 2000; Furlanetto et al., 2005; Dijkstra & Loeb, 2009; Lake et al., 2015).

The Lyα luminosity due to cold streams is suggested to increase with the M_h of host galaxies. A scaling of $L(\mathrm{Ly}\alpha)_\mathrm{H} \propto {M_\mathrm{h}}^{1.1}$-${M_\mathrm{h}}^{1.25}$ at $M = 10^{10}$–$10^{13}\,M_\odot$ has been predicted by (zoom-in) cosmological hydrodynamical simulations in Faucher-Giguère et al. (2010) and Rosdahl & Blaizot (2012). Dijkstra & Loeb (2009) have obtained a similar correlation to Faucher-Giguère et al. (2010)'s from an analytic model which reproduces the Lyα luminosities, Lyα line widths, and number densities of observed LABs at $M_\mathrm{h} \gtrsim 10^{11} M_\odot$. On the other hand, Goerdt et al. (2010) have derived a shallower power law slope ~ 0.8

[*34] They discuss the escape fraction using L(Lyα) on $r = 12$ kpc ($3''$ diameter) and 24 kpc ($6''$) apertures. Although the average profile of their LAHs extends to $r = 40$ kpc, we refer to $6''$ aperture luminosity as $L(\mathrm{Ly}\alpha)_\mathrm{tot}$ and to the difference in $3''$ and $6''$ aperture luminosities as $L(\mathrm{Ly}\alpha)_\mathrm{H}$.

for LAB-hosting massive ($M_{\rm h} \sim 10^{12}$–$10^{13} M_\odot$) halos from high-resolution cosmological hydrodynamical adaptive mesh refinement simulations.

We examine if our subsamples are consistent with these theoretical predictions by comparing the power-law slope and amplitude of the $L({\rm Ly}\alpha)_{\rm H}$-$M_{\rm h}$ relation. For a conservative discussion, we use Rosdahl & Blaizot (2012)'s relation which gives the steepest slope and Goerdt et al. (2010)'s relation giving the shallowest slope as shown in figure 8.1(b) [*35]:

$$L({\rm Ly}\alpha)_{\rm H} \sim 8 \times 10^{42} \left(\frac{M_{\rm h}}{10^{12} M_\odot} \right)^{1.25} \left(\frac{1+z}{1+3} \right)^{1.3}, \tag{8.1}$$

$$L({\rm Ly}\alpha)_{\rm H} = 9.72 \times 10^{42} \left(\frac{M_{\rm h}}{10^{12} M_\odot} \right)^{0.8} (1+z)^{1.3}. \tag{8.2}$$

In figure 8.1(a), we convert $M_{\rm h}$ to $M_\star$ using the average relation between $M_\star$ and $M_{\rm h}$ at $z \sim 2$ in Moster et al. (2013)[*36]. The constant $L({\rm Ly}\alpha)_{\rm H}$ with $M_\star$ and $M_{\rm h}$ seen in the LAEs is inconsistent with the increasing $L({\rm Ly}\alpha)_{\rm H}$ predicted by the theoretical models, although the uncertainties in our $M_{\rm h}$ estimates are large. The HAEs have also non-increasing $L({\rm Ly}\alpha)_{\rm H}$ over two orders of magnitude in $M_\star$, highlighting the inconsistency found for the LAEs. As for amplitude, the LAEs shown by red filled (open) symbols have $\sim$ 2–4 ($\sim$ 1–2) times higher $L({\rm Ly}\alpha)_{\rm H}$ than the two model predictions at the same $M_\star$ (figure 8.1[a]), and at least $\sim$ 1–10 ($\sim$ 1–10) times higher at the same $M_{\rm h}$ (figure 8.1[b]). Even when the individual distribution of Rosdahl & Blaizot (2012)'s galaxies is considered, low-$M_\star$ LAEs (red filled symbols) have more than $10\,\sigma$ brighter $L({\rm Ly}\alpha)_{\rm H}$ than the simulated galaxies with similar $M_\star$ (a gray shaded region). In other words, cold streams cannot produce as many Lyα photons in the CGM as observed.

Note that as mentioned in appendices C.1 and C.2, the $L({\rm Ly}\alpha)_{\rm H}$ values of the faint m_K and M_{UV} subsamples are possibly overestimated since they miss small $EW({\rm Ly}\alpha)$ (faint $L({\rm Ly}\alpha)_{\rm C}$) sources due to the NB-selection bias. If we derive $L({\rm Ly}\alpha)_{\rm H}$ conservatively from the M_{UV}–$L({\rm Ly}\alpha)_{\rm H}$ relation for individual MUSE-LAEs without such a selection bias in Leclercq et al. (2017), we obtain $\sim$ 1.5 times smaller $L({\rm Ly}\alpha)_{\rm H}$, which results in a slightly positive correlation between $M_\star$ and $L({\rm Ly}\alpha)_{\rm H}$. However, the power law index and the amplitude of the $M_\star$–$L({\rm Ly}\alpha)_{\rm H}$ correlation of the m_K subsamples is still shallower and higher than theoretical results at more than the $2\,\sigma$ and $10\,\sigma$ confidence levels, respectively (see more details in appendix C.2). Consequently, our study suggests that (a) cold streams are not the dominant origin of LAHs.

[*35] We shift the relation shown in figure 8 in Rosdahl & Blaizot (2012) at $z = 3$ to $z = 2$ by multiplying redshift-evolution term, $(1+z)^{1.3}$, given in figure 12 and equation 21 in Goerdt et al. (2010). We also note that the relation at $z \sim 3$ predicted in Faucher-Giguère et al. (2010) has a lower amplitude than that in Rosdahl & Blaizot (2012) typically about a factor of two (see appendix E in Rosdahl & Blaizot, 2012, for more details).

[*36] We have found that our LAEs are on average slightly offset from the average relation to lower $M_{\rm h}$ values in section 6.6.1 (Kusakabe et al., 2018b) . Our discussion is unchanged if we instead use $M_{\rm h}$ reduced by this offset.

8.2 (b) Satellite star formation

Satellite galaxies emit Lyα photons through star formation. If satellite star formation significantly contributes to LAHs, they will involve an extended UV emission from the star formation (e.g., Shimizu et al., 2011; Zheng et al., 2011; Lake et al., 2015; Mas-Ribas et al., 2017). Unfortunately, this emission is expected to be too diffuse to detect even by stacking of some 10^3 objects as mentioned in Momose et al. (2016).

The Lyα luminosity from satellite star formation can be interpreted as a function of the $M_{\rm h}$ and $M_\star$ of the central galaxy. In the local universe, the number of disk (i.e., star-forming) satellite galaxies is found to be described by a power law of the host halo mass of the central galaxy with a slope of 0.91 ± 0.11 for galaxies with $M_{\rm h} \sim 10^{12}$–$10^{14}\,M_\odot$ (see figure 14 and equation 6 in Trentham & Tully, 2009, see also figure 2 in Wang et al. 2014). At high redshifts, at least for massive central galaxies ($M_\star \sim 10^{11}\,M_\odot$ at $z \sim 1.4$), the radial number density profile of satellite galaxies is not significantly different from that at $z \sim 0$ (Tal et al., 2013). These local properties are reproduced by theoretical models (e.g., Nickerson et al., 2013; Sales et al., 2014; Okamoto et al., 2010). With an assumption that the total Lyα luminosity from satellite galaxies is proportional to the sum of their SFRs of satellite galaxies, $L({\rm Ly}\alpha)_{\rm H}$ can be calculated from cosmological galaxy formation models.

The "New Numerical Galaxy Catalogue" (ν^2GC) is a cosmological galaxy formation model with semi-analytic approach. It can reproduce not only the present-day luminosity functions (LF) and HI mass function but also the evolution of the LFs and the cosmic star formation history (Makiya et al., 2016; Shirakata et al., 2018, Ogura et al. in prep.). We use model galaxies at $z \sim 2.2$ in the ν^2GC-S with a box size of $280\,h^{-1}$cMpc (LAE NB selection is not applied). The number of central galaxies is $\sim 6 \times 10^6$. For each central galaxy, we calculate $L({\rm Ly}\alpha)_{\rm H}$ by summing the SFRs of the satellites with an assumption of case B recombination. We find that the average $L({\rm Ly}\alpha)_{\rm H}$ can be approximated as

$$L({\rm Ly}\alpha)_{\rm H} \sim 8.3 \times 10^{42} \left(\frac{M_{\rm h}}{10^{12} M_\odot} \right)^{2.58} \tag{8.3}$$

at $M_{\rm h} \sim 10^{10}$–$10^{12}\,M_\odot$ and

$$L({\rm Ly}\alpha)_{\rm H} \sim 1.9 \times 10^{42} \left(\frac{M_\star}{10^{10} M_\odot} \right)^{1.36} \tag{8.4}$$

at $M_\star \sim 10^8$–$10^{10}\,M_\odot$ as shown with a thin black dashed line in figures 8.1 (c) and (d). The power law of $M_{\rm h}$ for $L({\rm Ly}\alpha)_{\rm H}$ is steeper than that for the observed number of disk satellite galaxies.

We focus on the amplitude and slope of the $L({\rm Ly}\alpha)_{\rm H}$ – mass relations. The LAEs shown by red symbols have more than ~ 1 dex higher $L({\rm Ly}\alpha)_{\rm H}$ than the mean of the model galaxies at the same $M_\star$ and $M_{\rm h}$. However, observations show that LAEs occupy only $\sim 10\%$ ($\sim 2\%$) of all galaxies with the same $M_\star$ ($M_{\rm h}$) in section 9.1.(Kusakabe et al., 2018b). For a conservative comparison, we limit the model galaxies to those with

the top 10% (2%) $L(\mathrm{Ly}\alpha)_\mathrm{H}$ at a fixed $M_\star$ (M_h). We find that the mean $L(\mathrm{Ly}\alpha)_\mathrm{H}$ of these $L(\mathrm{Ly}\alpha)_\mathrm{H}$-bright model galaxies (thick dashed lines in figures 8.1 [c] and [d]) is still about three times lower than the observed values. Moreover, the positive correlations of $L(\mathrm{Ly}\alpha)_\mathrm{H}$ with $M_\star$ and M_h seen for the model galaxies are incompatible with the constant $L(\mathrm{Ly}\alpha)_\mathrm{H}$ of our LAEs and with the decreasing $L(\mathrm{Ly}\alpha)_\mathrm{H}$ of the HAEs in Matthee et al. (2016). These LAEs and HAEs span two orders of magnitude in $M_\star$. A non-increasing $L(\mathrm{Ly}\alpha)_\mathrm{H}$ over this wide mass range may be achieved if the Lyα photons from satellites of massive galaxies are heavily absorbed in the CGM, but the offset of $L(\mathrm{Ly}\alpha)_\mathrm{H}$ from our LAEs becomes larger. Such a heavy dust pollution in the CGM is probably unlikely.

As described in the previous subsection, using Leclercq et al. (2017)'s M_UV–$L(\mathrm{Ly}\alpha)_\mathrm{H}$ relation results in a slightly positive correlation. However, the power law index determined by the m_K subsamples is still shallower than that of the model (see appendix C.2 for detalis). In addition, it remains difficult for the model to explain the results of LAEs and HAEs in a unfied manner. From these results, we conclude that satellite star formation is unlikely to be the dominant origin.

8.3 (c) Resonant scattering of Lyα photons in the CGM which are produced in central galaxies

HI gas in the CGM can resonantly scatter Lyα photons which have escaped from the main body of the galaxy (e.g., Laursen & Sommer-Larsen, 2007; Barnes & Haehnelt, 2010; Zheng et al., 2011; Dijkstra & Kramer, 2012; Verhamme et al., 2012). However, there is no theoretical study that predicts $L(\mathrm{Ly}\alpha)_\mathrm{H}$ and its dependence on galaxy properties by solving the radiative transfer of Lyα photons in the CGM. In this subsection, we first describe the LAH luminosity of a galaxy assuming that all Lyα photons come from the main body. To do so, we introduce two parameters: the escape fraction out to the CGM and the scattering efficiency in the CGM. Then, we examine if resonant scattering can explain reasonably well the behavior of LAEs and HAEs shown in the previous section. Let $L(\mathrm{Ly}\alpha)_\mathrm{int}$ be the total luminosity of Lyα photons produced in the main body. Some fraction of $L(\mathrm{Ly}\alpha)_\mathrm{int}$ is absorbed by dust in the interstellar medium (ISM) and the rest escapes out into the CGM. With an assumption that dust absorption in the CGM is negligibly small, the escaping luminosity is equal to $L(\mathrm{Ly}\alpha)_\mathrm{tot}$ ($= L(\mathrm{Ly}\alpha)_\mathrm{C} + L(\mathrm{Ly}\alpha)_\mathrm{H}$), and the escape fraction into the CGM is calculated as $f_\mathrm{esc}(\mathrm{Ly}\alpha)_\mathrm{tot} = L(\mathrm{Ly}\alpha)_\mathrm{tot}/L(\mathrm{Ly}\alpha)_\mathrm{int}$. Then, a fraction, $X(\mathrm{Ly}\alpha)_\mathrm{H/tot}$, of the escaping photons are scattered in the CGM, being extended as a LAH with $L(\mathrm{Ly}\alpha)_\mathrm{H}$. Thus, $L(\mathrm{Ly}\alpha)_\mathrm{H}$ can be written as:

$$L(\mathrm{Ly}\alpha)_\mathrm{H} = L(\mathrm{Ly}\alpha)_\mathrm{int}\, f_\mathrm{esc}(\mathrm{Ly}\alpha)_\mathrm{tot}\, X(\mathrm{Ly}\alpha)_\mathrm{H/tot} \tag{8.5}$$

$$= L(\mathrm{Ly}\alpha)_\mathrm{tot}\, X(\mathrm{Ly}\alpha)_\mathrm{H/tot}. \tag{8.6}$$

In the following modeling, we assume that $L(\mathrm{Ly}\alpha)_\mathrm{int}$ originates only from star formation, and express it as a function of $M_\star$ using the SFMS:

$$L(\mathrm{Ly}\alpha)_\mathrm{int}\,(\mathrm{erg\,s^{-1}}) = SFR_\mathrm{MS}\,(\mathrm{M_\odot\,yr^{-1}})/9.1\times10^{-43}. \tag{8.7}$$

We then describe $f_{\rm esc}({\rm Ly}\alpha)_{\rm tot}$ as a function of $M_\star$ using the $M_\star$–IRX relation discussed in section 6.4.2. The dust attenuation for 1216 Å continuum, $A_{\rm 1216con}$, at a fixed $M_\star$ is calculated from $IRX(M_\star)$:

$$A_{\rm 1216con}(M_\star) = 2.5\log_{10}(0.595 IRX(M_\star) + 1.0)\left(\frac{\kappa_{1216}}{\kappa_{1500}}\right), \tag{8.8}$$

where κ_{1216} and κ_{1500} are the coefficients of the attenuation curve at $\lambda = 1216$ Å and 1500 Å, respectively. Introducing the relative efficiency of the attenuation of Lyα emission to the continuum at the same wavelength, $q = A_{\rm Ly\alpha}/A_{\rm 1216con}$ (e.g., Finkelstein et al., 2008), we can write $f_{\rm esc}({\rm Ly}\alpha)_{\rm tot}$ as:

$$f_{\rm esc}({\rm Ly}\alpha)_{\rm tot} = 10^{-0.4\,q\,A_{\rm 1216con}(M_\star)}, \tag{8.9}$$

where $q = 0$ and $q = 1$ correspond to the case without attenuation of Lyα emission and with the same attenuation as that of continuum. We thus obtain:

$$L({\rm Ly}\alpha)_{\rm tot}(M_\star) = \left(\frac{SFR_{\rm MS}(M_\star)}{9.1\times10^{-43}}\right) 10^{-0.4\,q\,A_{1216}(M_\star)}. \tag{8.10}$$

We use Shivaei et al. (2017)'s SFMS and Heinis et al. (2014)'s IRX-$M_\star$ relation because our LAEs are on these relations (see sections 6.4.2 and 6.5.2). We also assume a SMC-like attenuation curve.

Shown in figure 8.1(e) are three calculations with $q = 0.0$, 1.0, and 1.3 (gray (thick), dark gray, and black (thin) dotted lines, respectively). The constant $L({\rm Ly}\alpha)_{\rm tot}$ with increasing $M_\star$ seen in the LAEs is achieved if q increases with $M_\star$. We note that all LAEs require $q < 1$, with the less massive subsamples suggesting $q = 0$, meaning that Lyα photons escape much more efficiently than UV photons. We do not compare the HAEs with these models since they do not follow well the SFMS and the IRX-$M_\star$ relation (see section 6.5.3). As we show later, the HAEs can be explained by large q values. Further discussion of $f_{\rm esc}({\rm Ly}\alpha)_{\rm tot}$ and q for our LAEs and the HAEs is given in section 6.8.2. We also find that this result is unchanged even if we instead use a Calzetti attenuation curve, Tomczak et al. (2016)'s SFMS, and/or Bouwens et al. (2016)'s IRX-$M_\star$ relation.

The term $X({\rm Ly}\alpha)_{\rm H/tot}$ can be interpreted as the efficiency of resonant scattering in the CGM. More massive galaxies may have a larger amount of HI gas in the halo and thus have a higher $X({\rm Ly}\alpha)_{\rm H/tot}$ value. Figure 8.1(g) shows that this picture is consistent with our LAEs and Matthee et al. (2016)'s HAEs, because these two populations appear to follow a common, positive (although very shallow) correlation between $X({\rm Ly}\alpha)_{\rm H/tot}$ and $M_\star$. This picture is also consistent with the $X({\rm Ly}\alpha)_{\rm H/tot}$ – $M_{\rm h}$ plot for our LAEs (figure 8.1[h]) within the large uncertainties in $M_{\rm h}$. In this case, the LAHs of our LAEs ($\lesssim 40$ kpc in radius) are caused by HI gas roughly within the virial radius of hosting dark matter halos, $\sim$ 20–50 kpc, whose mass is estimated to be in the range $M_{\rm h} \sim 10^{10}$–$10^{11}\,M_\odot$. This relative extent of LAHs is close to those inferred for the LAHs of MUSE-LAEs by Leclercq et al. (2017), typically 60–90% of the virial radius, where they predict $M_{\rm h}$ from observed UV luminosities using the semi-analytic model of Garel et al. (2015).

Thus, in the resonant scattering scenario, the constant $L(\mathrm{Ly}\alpha)_{\mathrm{H}}$ observed is achieved by a combination of increasing $L(\mathrm{Ly}\alpha)_{\mathrm{int}}$, decreasing $f_{\mathrm{esc}}(\mathrm{Ly}\alpha)_{\mathrm{tot}}$, and (slightly) increasing $X(\mathrm{Ly}\alpha)_{\mathrm{H/tot}}$ with mass, and all three trends are explained reasonably well. Our study suggests that (c) resonant scattering is the dominant origin of the LAHs.

8.4 Summary of the three comparisons

It is found that resonant scattering most naturally explains the $L(\mathrm{Ly}\alpha)_{\mathrm{H}}$ and its dependence on galaxy properties seen in our LAEs and Matthee et al. (2016)'s HAEs. We, however, note that hydrodynamic cosmological simulations in Lake et al. (2015) show that scattered Lyα in the CGM can reach only out to $\sim$ 15 kpc, suggesting that cold streams or satellite star formation are also needed, although they slightly overestimate the observed radial Lyα profile at 15 kpc (by a factor of 2). On the other hand, Xue et al. (2017) have found for LAEs at $z \sim 4$ that the radial profile of LAHs is very close to a predicted profile by Dijkstra & Kramer (2012) who have only considered resonant scattering. Theoretical models discussing the contribution of scattering to $f_{\mathrm{esc}}(\mathrm{Ly}\alpha)_{\mathrm{tot}}$ and $X(\mathrm{Ly}\alpha)_{\mathrm{H/tot}}$ as a function of $M_\star$ and M_{h} are needed for a more detailed comparison. Mas-Ribas et al. (2017) show that different origins give different spatial profiles of Lyα, UV, and Hα emission. According to the best-effort observations of Lyα and Hα emission of LAEs in Sobral et al. (2017), Lyα photons of LAEs at $z \sim 2$ are found to escape over two times larger radii than Hα photons, which implies (a) cold stream scenario or (c) resonant scattering scenario, although their results are based on images with the PSF as large as $\sim$ 2 arcsecond (FWHM). Deep, spatially resolved observations of Hα emission with James Webb Space Telescope (JWST) would provide us with important clues to the origin of LAHs.

Chapter 9

Discussion III. the origins of the high Lyα escape fraction of LAEs at $z \sim 2$

In this chapter, we discuss the origin of the high Lyα escape fraction of LAEs, which causes the bright Lyα emission of LAEs. As we described in section 6.8.2, we find that our LAEs have a higher $f_{\rm esc}$(Lyα) than HAEs, implying that not all of the galaxies with low $M_\star$ and/or low $E(B-V)$ can be observed as LAEs. In the next section, we derive dusty cycle and LAE fraction at a fixed $M_{\rm h}$ or $M_\star$ and confirm the implication. Then we discuss the origins of the high Lyα escape fraction of LAEs at $z \sim 2$.

9.1 Duty cycle and LAE fraction

The duty cycle of LAEs, $f_{\rm duty}^{\rm LAEs}$, is defined as the fraction of dark mater halos hosting LAEs (Nagamine et al., 2010). Previous studies find that $f_{\rm duty}^{\rm LAEs}$ at $z \sim 3$ is $\sim$ 1–10% (Gawiser et al., 2007; Ouchi et al., 2010), which is similar to those at higher redshift (e.g., Ouchi et al., 2010, 2018), while $f_{\rm duty}^{\rm LAEs}$ is estimated to be relatively high, 43^{+113}_{30} % at $z \sim 2$ (Guaita et al., 2010). We estimate the duty cycle of our LAEs to be:

$$f_{\rm duty}^{\rm LAEs} = \frac{ND_{\rm LAE}}{ND_{\rm DMH}} \sim 2\%, \tag{9.1}$$

where $ND_{\rm LAE}$ and $ND_{\rm DMH}$ are the number density of LAEs with $NB_{\rm tot} \leq 25.5$ mag and that of dark matter halos estimated from the halo mass function at $z \sim 2$ using the calculator provided by Murray et al. (2013), respectively. For this calculation, we assume that dark matter halos hosting our LAEs have a one dex range of mass, 10^{10}–10^{11} $M_\odot$, since the K-band magnitudes, an approximation of stellar mass, of our LAEs are distributed with FWHM of $\sim$ 3.2 mag, or $\sim$ 1.3 dex. Our result is relatively lower than that in Guaita et al. (2010) as expected from the difference in $b_{\rm g,\,eff}$. However, it is comparable with those of previous studies at $z \sim 3$ and higher z.

We also estimate the fraction of galaxies in a given stellar mass (or luminosity) range

classified as LAEs (LAE fraction), $f_{\rm gals}^{\rm LAEs}$. Assuming that our LAEs have a one dex range of stellar mass, $10^{8.5}$–$10^{9.5}$ $M_\odot$, we obtain:

$$f_{\rm gals}^{\rm LAEs} = \frac{ND_{\rm LAE}}{ND_{\rm gal}} \sim 10\%, \tag{9.2}$$

where $ND_{\rm gal}$ is the number density of galaxies estimated by extrapolating Tomczak et al. (2014)'s stellar mass function at $z \sim 2$–2.5 below 10^9 $M_\odot$. This result is comparable with those of previous spectroscopic observations of star forming galaxies at $z \sim 2$–2.5 ($\sim 10\%$, Hathi et al., 2016) and BX galaxies at $z \sim 1.9$–2.7 ($\sim 12\%$ with $EW_{\rm Ly\alpha} \geqq 20$ Å; Reddy et al., 2008).

The low LAE fraction at $z \sim 2.2$ is in agreement with the general trend of LAE fraction found to increase from $z = 3$ to 6, and to decrease at $z > 6$, though uncertainties in the measurement of $f_{\rm gals}^{\rm LAEs}$ are still matters of debate (e.g., Stark et al., 2011; Tilvi et al., 2014; De Barros et al., 2017; Arrabal Haro et al., 2018). Recently, VLT/MUSE observations enable us to reveal the evolution of $f_{\rm gals}^{\rm LAEs}$ at $z \sim 3$ to 6 with homogeneous and complete samples (see appendix E for more details; Kusakabe et al. in prep., see also Caruana et al., 2018). Using MUSE and HST data, we derive $f_{\rm gals}^{\rm LAEs}$ with $EW_{0,ps}({\rm Ly}\alpha) \gtrsim 25$ Å and $M_{\rm UV} = -21.75$–-17.75 mag, which are similar to those of our LAE sample and have never been reached by previous work, among a photo-z sample in Hubble Ultra Deep Field (HUDF, Rafelski et al., 2015). We find that our $f_{\rm gals}^{\rm LAEs}$ at $z \sim 2$ locates near the extrapolation of the evolution of our $f_{\rm gals}^{\rm LAEs}$, $0.11z - 0.15$, at $z \sim 3$–6 fitted with a linear relation in appendix E.3.2 (see figure E.5).

Consequently, the low fractions obtained above for $z \sim 2$ imply that only a few fraction of galaxies within these mass ranges studied here can evolve into LAEs and/or that galaxies within these mass ranges can experience the LAE phase only for a very short time. It is notable that typical galaxies embedded in dark matter halos with $M_{\rm h} = 10^{10}$–10^{11} $M_\odot$ have lower stellar masses than $M_\star = 10^{8.5}$–$10^{9.5}$ $M_\odot$ because of the high $SHMR$ of our LAEs. In the next section, we discuss the origin of the high $f_{\rm esc}({\rm Ly}\alpha)_{\rm tot}$ of LAEs at $z \sim 2$, which results in such low $f_{\rm duty}^{\rm LAEs}$ and $f_{\rm gals}^{\rm LAEs}$. Although the origins of the continuous trend of $f_{\rm gals}^{\rm LAEs}$ against z ($z < 6$) are still an open question, the discussion below might give us some informations.

9.2 The origin of high Lyα escape fractions

By including $L({\rm Ly}\alpha)_{\rm H}$ in the total Lyα luminosity, we obtain very high $f_{\rm esc}({\rm Ly}\alpha)_{\rm tot}$ values for our LAEs as shown in section 6.14. These values are systematically higher than those obtained for LAEs in previous studies which have not considered $L({\rm Ly}\alpha)_{\rm H}$ (e.g., Song et al., 2014; Hayes et al., 2011). They are also about one order of magnitude higher than those of HAEs with the same $M_\star$ and $E(B-V)$ (figure 6.14), suggesting a large scatter in $f_{\rm esc}({\rm Ly}\alpha)_{\rm tot}$ among galaxies.

It is helpful to discuss $f_{\rm esc}({\rm Ly}\alpha)$ using $E(B-V)$, since additional mechanisms are needed to make $f_{\rm esc}({\rm Ly}\alpha)$ higher or lower than that expected from $E(B-V)$. The attenuation of

Lyα emission relative to that of continuum emission is evaluated by the q-parameter [*37] (e.g., Finkelstein et al., 2008, 2009), as discussed in section 8.3. Figure 9.1 shows q as a function of $E(B-V)$ for our LAEs and Matthee et al. (2016)'s HAEs, which are divided into subsamples in accordance with $E(B-V)$. Regardless of the attenuation curve, the LAEs have small q less than unity, which increases with $E(B-V)$. Remarkably, about a half of the subsamples, shown by red filled symbols, have $q<0$, meaning that the observed Lyα luminosity exceeds the one calculated from the SFR. On the other hand, the HAEs have larger q (>1) decreasing with $E(B-V)$. The difference in q between these two galaxy populations becomes larger at smaller $E(B-V)$. Note that if we calculate q of our LAEs from $L(\mathrm{Ly}\alpha)_{ps}$ instead of including $L(\mathrm{Ly}\alpha)_{\mathrm{H}}$, we obtain higher values, $q\sim1$, being closer to the values found in previous studies (e.g., Hayes et al., 2010; Nakajima et al., 2012).

Below, we discuss how LAEs can have low q and hence high $f_{\mathrm{esc}}(\mathrm{Ly}\alpha)_{\mathrm{tot}}$ than HAEs with the same $E(B-V)$, by grouping possible origins into three categories: (i) less efficient resonant scattering in a uniform ISM, (ii) less efficient resonant scattering in a clumpy ISM, (iii) additional Lyα sources, and (iv) hard ionizing spectra. We then discuss the difference in q and $f_{\mathrm{esc}}(\mathrm{Ly}\alpha)_{\mathrm{tot}}$ between the LAEs and HAEs. In this discussion, we assume that the contribution from cold streams and satellite galaxies to $L(\mathrm{Ly}\alpha)_{\mathrm{H}}$ is negligible.

9.2.1 (i) Less efficient resonant scattering in a uniform ISM

In a uniform ISM where dust and gas are well mixed, Lyα photons have a higher chance of dust absorption than continuum photons because of resonant scattering. To reduce the efficiency of resonant scattering in a uniform ISM, one needs to reduce the column density of HI gas (N_{HI}) or the scattering cross section ($\sigma_{\mathrm{Ly}\alpha}$) (e.g., Duval et al., 2014; Garel et al., 2015).

First, it appears that LAEs indeed have lower N_{HI} than average galaxies with the same $M_\star$ (and hence the same ($E(B-V)$ since average galaxies are expected to follow a common IRX-$M_\star$ relation). This is because our result suggests that LAEs at $z\sim2$ have lower M_{h} than expected from the average $M_\star$-M_{h} relation (in section 6.6.1, Kusakabe et al., 2018b). At a fixed $M_\star$, a lower M_{h} means a lower gas mass (M_{gas}), since the M_{gas} of a galaxy is written as $M_{\mathrm{gas}}\simeq f_{\mathrm{b}}M_{\mathrm{h}}-M_\star$. It is reasonable to expect that galaxies with a lower gas mass have a lower N_{HI}. The N_{HI} of LAEs is further reduced if they have a high

[*37] The q-parameter can be rewritten as: $q=\frac{-\log(f_{\mathrm{esc}}(\mathrm{Ly}\alpha))}{0.4E(B-V)\kappa_{1216}}=\frac{\kappa}{k\kappa_{1216}}-\frac{\log C}{0.4E(B-V)\kappa_{1216}}$, where κ and C are two parameters of a commonly used fitting formula of $f_{\mathrm{esc}}(\mathrm{Ly}\alpha)=C10^{-0.4E(B-V)\kappa}$ (e.g., Hayes et al., 2011). The two parameters are difficult to interpret physically, especially for a case with $C<1$. Hayes et al. (2011) and Atek et al. (2014) do not include $L(\mathrm{Ly}\alpha)_{\mathrm{H}}$ to calculate the $f_{\mathrm{esc}}(\mathrm{Ly}\alpha)$ and obtain $C=0.445$ with $\kappa=13.6$ and $C=0.22$ with $\kappa=6.67$, respectively. Although Matthee et al. (2016) include $L(\mathrm{Ly}\alpha)_{\mathrm{H}}$ to calculate $f_{\mathrm{esc}}(\mathrm{Ly}\alpha)_{\mathrm{tot}}$, their C is less than 1 ($C=0.08^{+0.02}_{-0.01}$ with $\kappa=7.64^{+1.38}_{-1.36}$), which is slightly larger than the value derived without $L(\mathrm{Ly}\alpha)_{\mathrm{H}}$ ($C=0.03^{+0.01}_{-0.01}$ with $\kappa=10.71^{+0.89}_{-1.01}$). Note that Atek et al. (2014) uses Balmer decrements to estimate $E(B-V)_{gas}$, while other studies use SED fitting.

ionizing parameter as suggested by e.g., Nakajima & Ouchi (2014), Song et al. (2014), and Nakajima et al. (2018a) or have a relatively face-on inclination (e.g., Verhamme et al., 2012; Yajima et al., 2012; Behrens & Braun, 2014; Shibuya et al., 2014a; Kobayashi et al., 2016; Paulino-Afonso et al., 2018).

The idea that LAEs have lower $N_{\rm HI}$ than average galaxies appears to be consistent with results based on observed Lyα profiles that LAEs have lower $N_{\rm HI}$ than LBGs (e.g., Hashimoto et al., 2015; Verhamme et al., 2006). This idea is also consistent with an anti-correlation between $M_{\rm HI}$ and $f_{\rm esc}$(Lyα) found for local galaxies, although their $f_{\rm esc}$(Lyα) values at a fixed $E(B-V)$ are lower than those of our LAEs (Lyα Reference Sample Hayes et al., 2013; Östlin et al., 2014).

The probability of the resonant scattering of Lyα photons is also reduced if the ISM is outflowing, because the gas sees redshifted Lyα photons (e.g., Kunth et al., 1998; Verhamme et al., 2006). This mechanism should work in LAEs because most LAEs have outflows (e.g., Hashimoto et al., 2013; Shibuya et al., 2014b; Hashimoto et al., 2015; Guaita et al., 2017). Outflowing gas is also needed to reproduce observed Lyα profiles characterized by a relatively broad, asymmetric shape with a redshifted peak. Note, however, that it is not clear whether LAEs have higher outflow velocities than average galaxies with the same $M_\star$ and $E(B-V)$.

To summarize, low HI column densities combined with some other mechanisms such as outflows appear to contribute to the high $f_{\rm esc}(\text{Ly}\alpha)_{\rm tot}$ seen in LAEs. However, none of these mechanisms can reduce q below unity as long as a uniform ISM is assumed.

9.2.2 (ii) Less efficient resonant scattering in a clumpy ISM

Lyα photons are not attenuated by dust if dust is confined in HI clumps (the clumpy ISMs; Neufeld, 1991; Hansen & Peng Oh, 2006) because Lyα photons are scattered on the surface of clumps before being absorbed by dust. Scarlata et al. (2009) find that the clumpy dust screen (ISMs) can reproduce observed line ratios of Lyα to Hα (or $f_{\rm esc}$(Lyα)), and Hα to Hβ (or$E(B-V)$) of local LAEs (see also Bridge et al., 2017). It is, however, not clear what causes such a clumpy ISM geometry especially for LAEs. Indeed, Laursen et al. (2013) argue that any real ISM is unlikely to give $q < 1$. Duval et al. (2014) also find that the clumpy ISM model (Neufeld, 1991) can achieve $q < 1$ only under unrealistic conditions: a large covering factor of clumps with high $E(B-V)$, a low HI content in interclump regions, and a uniform, constant, and slow outflow.

Consequently, the clumpy ISM scenario is unlikely for our LAEs, though we can not exclude the possibility completely.

9.2.3 (iii) Additional Lyα sources

If galaxies have other Lyα-photon sources in the main body besides star formation, the number of produced Lyα photons is larger than expected from the SFR, resulting in underestimation of q and overestimation of $f_{\rm esc}(\text{Ly}\alpha)_{\rm tot}$. We discuss two candidate sources: AGNs, and cold streams in the central part of galaxies.

First, the contribution of AGNs should be modest. This is because we have removed all objects detected in either X-ray, UV, or radio regarding them as AGNs, and because the fraction of obscured AGNs (AGNs without detection in either X-ray, UV, or radio) in the remaining sample is estimated to be only 2% (see section 2.2, Kusakabe et al., 2018b).

Second, Lake et al. (2015) have found from hydrodynamical simulations of galaxies with $M_{\rm h} = 10^{11.5}\,M_\odot$ at $z \sim 3$ that the Lyα luminosity from cold streams in the central part of galaxies amounts to as high as $\sim 45\%$ of that from star formation. This result may apply to our LAEs to some degree.

To summarize, cold streams in the central part of galaxies possibly achieve very low q values ($\lesssim 0$) seen in about half of our LAEs (red filled objects), while only ~ 2 % AGNs among LAE sample used to stack are unlikely to cause such very low q values.

9.2.4 (iv) Hard ionizing spectra

If our LAEs have a hard ionizing spectrum (in other words, the production efficiency of ionizing photons compared to the UV luminosity, $\xi_{\rm ion}$, is large) as suggested in previous studies on higher-z LAEs (at $z \sim 3$–7: e.g., Nakajima et al., 2016; Harikane et al., 2018; Nakajima et al., 2018b) and brighter LAEs at $z \sim 2.2$ (Sobral & Matthee, 2018), the intrinsic number of ionizing photons is larger than that assumed in equation 6.8. A hard ionizing spectrum arises from a young age, a low metallicity, a stellar population with a contribution of massive binary systems, an increasing star formation history, and/or a top-heavy IMF. If our LAEs have ~ 0.2 dex harder $\xi_{\rm ion}$ than the assumed fiducial value ($\log_{10}(\xi_{\rm ion}/{\rm Hz\,erg^{-1}}) \sim 25.11$), they have $f_{\rm esc}({\rm Ly}\alpha)_{\rm tot}$ lower than unity even in the case of the SMC-like curve. A much harder $\xi_{\rm ion}$ by ~ 0.4–1 dex would even help to explain the difference in $f_{\rm esc}({\rm Ly}\alpha)_{\rm tot}$ between LAEs and HAEs seen in figure 6.14 (right) in the case of the Calzetti curve.

To infer $\xi_{\rm ion}$ for our sample, we adopt an empirical relation presented by Sobral & Matthee (2018) in their figure 2[*38]. This relation implies a higher $f_{\rm esc}({\rm Ly}\alpha)$ and a harder $\xi_{\rm ion}$ for LAEs with a larger $EW_{0,ps}({\rm Ly}\alpha)$. Using this relation, we indeed obtain a harder $\xi_{\rm ion}$ of $\log_{10}(\xi_{\rm ion}/{\rm Hz\,erg^{-1}}) \sim 25.3$ for our large-EW LAE subsample whose typical $EW_{0,ps}({\rm Ly}\alpha)$ is ~ 70Å. This value is also comparable to those found for $z \sim 3$ LAEs in Nakajima et al. (2018b). In this case, their total Lyα escape fraction, $f_{\rm esc}({\rm Ly}\alpha)_{\rm tot}$, would become smaller than unity (~ 0.6–0.8) based on equation 5.1, suggesting that an additional Lyα source is not necessarily needed. However, the same relation gives a modest $\xi_{\rm ion}$ of $\log_{10}(\xi_{\rm ion}/{\rm Hz\,erg^{-1}}) \sim 25.1$ for the small-EW LAE subsample ($EW_{0,ps}({\rm Ly}\alpha) \sim 25$Å), resulting in $f_{\rm esc}({\rm Ly}\alpha)_{\rm tot} \sim 0.1$–0.3 which remains significantly higher than those of HAEs with the same $M_\star/SFR/E(B-V)$.

These calculations imply that it remains uncertain whether or not LAEs, especially those with a small $EW_0({\rm Ly}\alpha)$, typically have a hard ionizing spectrum. They also imply that another mechanism is possibly needed (in addition to hard ionizing spectra) to fully

[*38] Their $f_{\rm esc}({\rm Ly}\alpha)$ is derived from Hα luminosity with dust attenuation correction, 0.9 mag (see also Sobral et al., 2017), and Lyα flux measured as a point source with a 3″-diameter aperture.

explain the large $f_{\rm esc}({\rm Ly}\alpha)_{\rm tot}$ including the systematic difference from HAEs.

9.2.5 Summary of the mechanisms affecting the q-parameter

The origin of very high $f_{\rm esc}({\rm Ly}\alpha)_{\rm tot}$ and very low q found for LAEs is a long-standing problem. Song et al. (2014) have also found several bright LAEs with $q < 0$ as shown in their figure 14. This study makes this problem more serious by including $L({\rm Ly}\alpha)_{\rm H}$ in the calculation of these parameters. Remarkably, all of our subsamples have $q < 1$ and a half of them reach $q < 0$. Similaly, Song et al. (2014)'s q would decrease more if they include $L({\rm Ly}\alpha)_{\rm H}$ in the calculation of $f_{\rm esc}({\rm Ly}\alpha)_{\rm tot}$.

Low $N_{\rm HI}$ and small $\sigma_{{\rm Ly}\alpha}$ should help to increase $f_{\rm esc}({\rm Ly}\alpha)_{\rm tot}$ and reduce q to some degree. However, additional mechanisms are needed to reduce q less than unity, as highlighted by the very low q values, with some being negative, found for our LAE subsamples. Cold streams in the main body of LAEs and hard ionizing spectra are candidate mechanisms while a clumpy ISM and AGNs may be unlikely. The q value of galaxies is probably determined by the balance between the efficiency of resonant scattering and additional Lyα-photon sources. Spectroscopic observations of LAEs' Hα luminosities would provide more accurate measurements of $f_{\rm esc}({\rm Ly}\alpha)_{\rm tot}$ (q-parameters). They will also enable us to evaluate the spectral hardness from the UV to Hα luminosity ratio and to constrain the contribution of cold streams from the Lyα to Hα luminosity ratio.

Our LAEs have much lower q values than the HAEs in the lowest-$E(B-V)$ bin, which indicates that not all galaxies with small $E(B-V)$ (or equivalently, small $M_\star$) can be LAEs. A possible reason for this large difference is that our LAEs have lower $M_{\rm h}$ and hence lower $M_{\rm HI}$. Matthee et al. (2016)'s HAEs in the lowest-$M_\star$ bin ($M_\star \sim 3 \times 10^9$–$8 \times 10^9\,M_\odot$) used for clustering analysis by Cochrane et al. (2018) reside in massive dark matter halos of $M_{\rm h} \sim 7^{+9}_{-4} \times 10^{12}\,M_\odot$ (Cochrane et al., 2018), which is one dex larger than the average $M_{\rm h}$ of our LAEs [*39]. It would imply that the lowest-$E(B-V)$ HAEs in Matthee et al. (2016) have higher $M_{\rm h}$ than our LAEs, since the lowest-$E(B-V)$ HAEs should largely overlap with the lowest-$M_\star$ HAEs. Furthermore, a large fraction of low-$M_\star$ ($M_\star \lesssim 10^9\,M_\star$) HAEs are expected to be starburst galaxies as shown in figure 6.10, implying a large amount of gas (including HI) to fuel the starburst. However, the higher $M_{\rm h}$ also imply that they have brighter $L({\rm Ly}\alpha)$ from cold streams (in the main body). If the higher $M_{\rm HI}$ can reduce the $L({\rm Ly}\alpha)$ produced from both star formation and cold streams sufficiently, the higher q values of the HAEs can be reproduced.

[*39] We calculate this $M_{\rm h}$ value from the correlation length given in Cochrane et al. (2018) in the same manner as for our LAEs. Their r_0 and $M_{\rm h}$ are higher than those averaged over all the LAEs ($r_0 = 2.30^{+0.36}_{-0.41}\,h^{-1}\,Mpc$, i.e., $3.2^{+4.7}_{-2.5} \times 10^{10}\,M_\odot$), although their median $M_\star$ ($\sim 6 \times 10^9\,M_\odot$) is slightly higher than our average value ($\sim 1 \times 10^9\,M_\odot$).

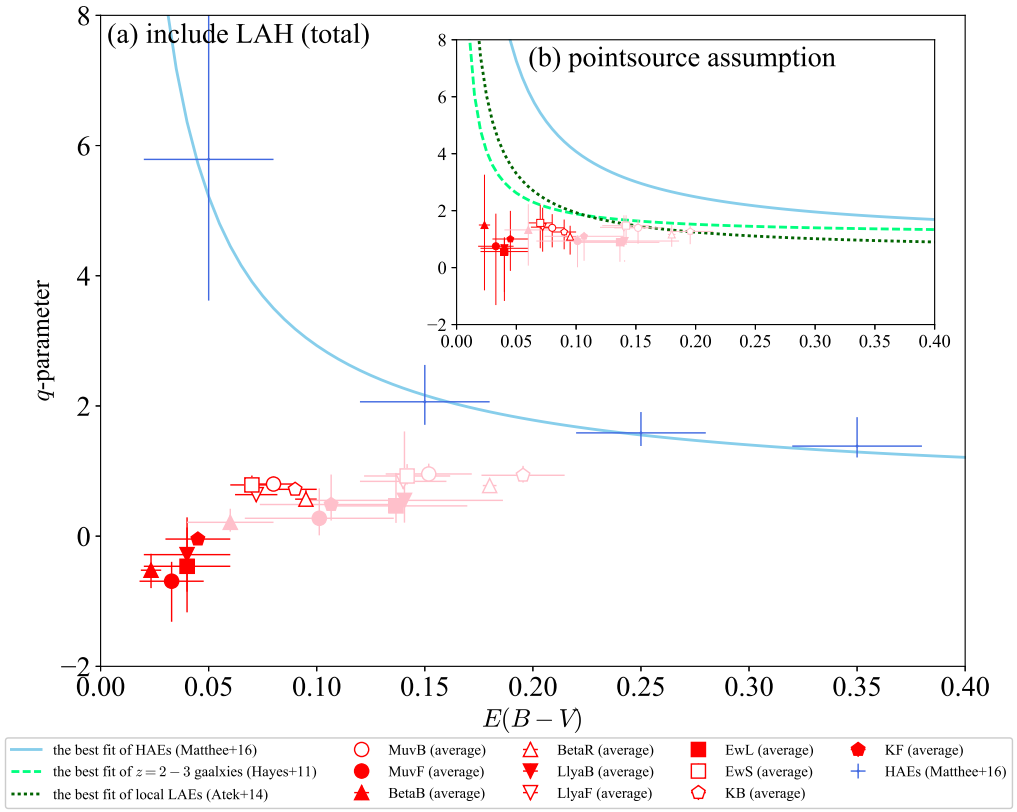

Figure 9.1 The q parameter vs. $E(B-V)$. The LAH is included in calculation of q in panel (a), while not included in panel (b). Blue crosses and a solid skyblue line show the values of $E(B-V)$-subdivided HAEs in Matthee et al. (2016) and the best fit two-parameter model to them as described in footnote *37 (see also footnotes *28 and *34); 12 kpc and 24 kpc apertures are used in panels (a) and (b), respectively. A light green dashed line and a dark green dotted line represent the best fit relation for LAEs, HAES, and UV-selected galaxies at $z \sim 2$–3 in Hayes et al. (2011) and local LAEs in Atek et al. (2014), respectively. Field average values of our ten subsamples with an assumption of an SMC-like attenuation curve are shown by red symbols below: open (filled) circles for bright (faint) $M_{\rm UV}$, open (filled) triangles for red (blue) β, open (filled) inverted triangles for faint (bright) $L({\rm Ly}\alpha)_{ps}$, open (filled) squares for small (large) $EW_{0,ps}({\rm Ly}\alpha)$, and open (filled) pentagons for bright (faint) $m_{\rm K}$. Shown by pink symbols are the results with the Calzetti curve. $E(B-V)_\star = E(B-V)_g$ is assumed to derive $E(B-V)$. All data are rescaled to a Salpeter IMF according to footnote *1.

Chapter 10

Conclusion

In this thesis, we have used 1249 narrow-band-selected LAEs from four deep survey fields with a total area of $\simeq 1$ deg^2. Among them, 213 LAEs with deep MIR/FIR data have been used to measure the dust emission of LAEs and to obtain an appropriate dust attenuation curve (Kusakabe et al., 2015). We have performed SED fitting to stacked imaging data of LAEs to measure stellar population parameters such as SFR, A_{1600}, and $M_\star$, while we derive M_h from clustering analysis. We have investigated star formation mode (or SFR–$M_\star$ relation), SHMR, BCE to discuss the star forming activity and the origin of LAHs of LAEs (Kusakabe et al., 2018b).

To discuss the origin of LAHs, we have studied the dependence of LAH luminosity on stellar properties and dark matter halo mass using 891 LAEs with deep optical/NIR data (Kusakabe et al., 2018a). We have divided our LAEs into subsamples in accordance with five physical quantities (m_K, M_UV, β, $L(\mathrm{Ly}\alpha)$ and $EW_0(\mathrm{Ly}\alpha)$), some of which are expected to correlate with $M_\star$ and M_h, and have estimated for each subsample the LAH luminosity from Momose et al. (2016)'s stacked observational relation. We have used the obtained dependence of LAH luminosity to test three candidate origins: cold streams, satellite star formation, and resonant scattering. We have also derived total Lyα escape fractions and q values by including the halo component, and discussed how LAEs can have high escape fractions.

The followings are the main results of this thesis.

i. The stacked LAE has the 3σ IR luminosity $L_\mathrm{TIR}^{3\sigma} = 1.1\times10^{10} L_\odot$. This, combined with $L_\mathrm{UV} = 5.3^{+0.2}_{-0.2}\times10^9 L_\odot$, gives $IRX \leq 2.2$, or $A_{1600} = 0.9$ mag, indicating remarkably low dust attenuation. An SMC-like attenuation curve is consistent with the stacked LAE in the IRX–β plane, while the Calzetti attenuation curve, which is assumed in most previous studies of LAEs, predicts a 3.8 times higher IRX at the observed $\beta = -1.4^{+0.2}_{-0.2}$. The PACS-based $L_\mathrm{TIR}^{3\sigma}$ allowing the Meurer's relation has also been discussed and it has been concluded that such a high value is unlikely. SED fitting using the Calzetti law also results in 10× overestimation of the true SFR derived from the L_TIR and L_UV.

ii. The mean of each stellar parameter over the four fields is: $M_\star = 10.2 \pm 1.8\times10^8$ M$_\odot$, $A_{1600} = 0.6 \pm 0.1$ mag, Age$= 3.8 \pm 0.3 \times 10^8$ yr, and SFR$= 3.4 \pm 0.4$ M$_\odot$ yr^{-1} for LAEs with $NB387{\leq}25.5$, which are derived from SED fitting with an assumption of

an SMC-like attenuation curve.

iii. The bias parameter of $NB387{\leq}25.5$ objects averaged over the four fields is $b^{\rm ave}_{\rm g,\,eff} = 1.22^{+0.16}_{-0.18}$, which is lower than that in Guaita et al. (2010) from 0.3 deg^2 with a probability of 96%. We estimate an external error from cosmic variance which inversely scales with the square root of the survey area. The high bias value obtained by Guaita et al. (2010) becomes consistent with our value if the uncertainties from cosmic variance, $\pm\,26\%$ and $\pm\,51\%$ for this work and Guaita et al. (2010), are considered. We have also found that $b_{\rm g,\,eff}$ does not significantly change with limiting NB387 magnitude, or limiting Lyα luminosity, which may be partly due to two trends canceling out with each other: galaxies in more massive halos have brighter intrinsic Lyα luminosities but lower Lyα escape fractions.

iv. The halo mass corresponding to the above $b^{\rm ave}_{\rm g,\,eff}$ value is $4.0^{+5.1}_{-2.9}\times10^{10}$ M$_\odot$. This value is roughly comparable to previous measurements for $z\sim3-7$ LAEs with similar Lyα luminosities, $M_{\rm h}\sim10^{10}$–10^{12} M$_\odot$ (e.g., Ouchi et al., 2010), suggesting that the mass of dark halos which can host typical LAEs is roughly unchanged with time.

v. Our LAEs are thus located near an extrapolation of the consensus relation of IRX against stellar mass (e.g., Heinis et al., 2014; Bouwens et al., 2016) with an assumption of an SMC-like attenuation curve. We have also found that our LAEs are on average placed near a lower-mass extrapolation of the SFMS (e.g., Tomczak et al., 2016; Shivaei et al., 2017), consistent with the results obtained from IR and UV observations. This suggests that the majority of LAEs are moderately forming stars in contrast to brighter LAEs which have been reported to fall above the SFMS.

vi. With $SHMR = 0.02^{+0.07}_{-0.01}$, our LAEs lie above a simple lower-mass extrapolation of the average $M_\star$-$M_{\rm h}$ relation. The higher $SHMR$ than average galaxies with the same $M_\star$ may make it easy for Lyα photons to escape since they are expected to have lower gas masses (baryon masses) and thus lower HI column densities. Our LAEs also have a high $BCE = 1.6^{+6.0}_{-1.0}$, lying above the average BCE-$M_{\rm h}$ relation. Thus, our LAEs have been converting baryons into stars more efficiently than average galaxies with similar $M_{\rm h}$ both in the past and at the observed epoch but with a moderate SF similar to average galaxies. Galaxies with weak SN feedback or small halos' spin parameters possibly have such properties according to the semi-analytic model by Dutton et al. (2010).

vii. We have calculated the dark matter halo mass evolution of our LAEs with the EPS model, to find that at $z = 0$ our LAEs are embedded in dark matter halos with a median halo mass similar to the mass of the Large Magellanic Cloud (LMC). If their star-formation is largely suppressed after the observed time until $z = 0$ similar to the star-formation history of the LMC, they would have a similar $SHMR$ to the present-day LMC.

viii. The duty cycle of LAEs (fraction of $M_{\rm h}\sim3\times10^{10}$ M$_\odot$ halos hosting LAEs) is estimated to be $\sim2\%$, and the LAE fraction (fraction of $M_\star\sim1\times10^9$ M$_\odot$ galaxies classified as LAEs) is found to be $\sim10\%$. These low fractions imply either that only a small fraction of all galaxies can evolve into LAEs and/or that even low-mass galaxies

can emit Lyα only for a very short time.

ix. We compare Momose et al. (2016)'s observational $L(\mathrm{Ly}\alpha)_\mathrm{C}$–$L(\mathrm{Ly}\alpha)_\mathrm{H}$ relation obtained from stacking analysis of essentially the same sample as ours, with the distribution of individual LAEs by VLT/MUSE in Leclercq et al. (2017). We find that their observational relation agrees well with the average trend of individual LAEs, ensuring the use of the relation for our analysis.

x. The ten subdivided LAE samples are found to have similar $L(\mathrm{Ly}\alpha)_\mathrm{H} \sim 2\times10^{42}\,\mathrm{erg\,s^{-1}}$ and $L(\mathrm{Ly}\alpha)_\mathrm{tot} \sim 2\times10^{42}$–$4\times10^{42}\,\mathrm{erg\,s^{-1}}$. Their $L(\mathrm{Ly}\alpha)_\mathrm{H}$ and $L(\mathrm{Ly}\alpha)_\mathrm{tot}$ remain almost unchanged or even decrease when $M_\star$ increases by factor 2–5. They are also nearly independent of SFR, $E(B-V)_\star$, and M_h, although the uncertainties in M_h are large. The HAEs in Matthee et al. (2016) also have non-increasing $L(\mathrm{Ly}\alpha)_\mathrm{H}$ and $L(\mathrm{Ly}\alpha)_\mathrm{tot}$. These results are inconsistent with the cold stream scenario and the satellite star formation scenario both of which predict a nearly linear scaling of $L(\mathrm{Ly}\alpha)_\mathrm{H}$ with mass. Specifically, the power law slope of the $M_\star$–$L(\mathrm{Ly}\alpha)_\mathrm{H}$ relation for the K-divided subsamples, the most stellar-mass sensitive subsamples, is shallower than predictions with more than the $2\,\sigma$ confidence level. The former scenario also fails to reproduce the bright $L(\mathrm{Ly}\alpha)_\mathrm{H}$ of low-mass subsamples at, e.g., a more than the 10σ level for the faint m_K subsample. The most likely is the resonant scattering scenario because it can naturally explain these results.

xi. The stacked LAEs are found to have $f_\mathrm{esc}^{\mathrm{Ly}\alpha}= 16-37\%$ without including LAHs from IR and UV observations. These values are significantly higher than the cosmic averages at $z\sim2$ but comparable to those at $z\gtrsim4$. When we include LAHs, the $f_\mathrm{esc}(\mathrm{Ly}\alpha)_\mathrm{tot}$ of all ten subsamples is higher than $\sim30\%$, with some exceeding 100%, with very low q values of $-1\lesssim q\lesssim1$. Using the Calzetti curve instead of an SMC-like curve makes $f_\mathrm{esc}(\mathrm{Ly}\alpha)_\mathrm{tot}$ lower but still in a range of 10–100% with $q\sim0$–1. The $f_\mathrm{esc}(\mathrm{Ly}\alpha)_\mathrm{tot}$ of the LAEs anti-correlates with $M_\star$, SFR, and $E(B-V)$ regardless of the assumed attenuation curve. Their $f_\mathrm{esc}(\mathrm{Ly}\alpha)_\mathrm{tot}$ and q are higher and lower, respectively, than those of HAEs with similar $M_\star$ and $E(B-V)$. The very low q values of the LAEs suggest the existence of an additional Lyα source in the main body; Lyα emission from cold streams and hard ionizing spectra are possible candidates. The difference in q between the LAEs and HAEs is possibly caused by a different balance between resonant scattering and additional Lyα-photon source(s).

Appendix A

SED fitting

A.1 The sample with $NB387_{\rm tot} \leq 25.5$ in the four fields

We show the results of SED fitting for the stacked LAEs with $NB387_{\rm tot} \leq 25.5$ in the four fields with the Calzetti curve and without nebular emission below.

A.1.1 The Calzetti Curve

We also examine the cases of the Calzetti curve for comparison. The best-fit parameters with an SMC-like curve and the Calzetti curve are listed in table A.1. Figure A.1 shows the best-fit SEDs with the observed ones in the case with the Calzetti curve as well as figure 6.3 for an SMC-like curve. We compare the best-fit parameters in section 6.2.2.

A.1.2 Without nebular emission

It is well known that considering nebular emission generally leads to a lower stellar mass (e.g., de Barros et al., 2014). To obtain upper limits of stellar mass and determine the star formation mode of our LAEs, we also examine the case without nebular emission, $f_{\rm esc}^{\rm ion} = 1$. The best-fit parameters with an SMC-like curve and the Calzetti curve are listed in table A.2. Figure A.2 shows the best-fit SEDs with the observed ones in the case with an SMC-like curve and the Calzetti curve.

When we assume an SMC-like curve, the average stellar mass and SFR without nebular emission, $M_\star = 11.2 \pm 1.2 \times 10^8$ M$_\odot$ and $SFR = 3.2 \pm 0.6$ M$_\odot$ yr^{-1}, are consistent with those with nebular emission, $M_\star = 10.2 \pm 1.8 \times 10^8$ M$_\odot$ and $SFR = 3.4 \pm 0.4$ M$_\odot$ yr^{-1}. This means that the average stellar mass and star formation mode of our LAEs are insensitive to $f_{\rm esc}^{\rm ion}$ when an SMC-like curve is used. On the other hand, if we assume the Calzetti curve, the average SFR without nebular emission, $SFR = 51.8 \pm 4.5$ M$_\odot$ yr^{-1}, is about four times higher than that with nebular emission, $SFR = 12.7 \pm 1.0$ M$_\odot$ yr^{-1}. Their average stellar mass without nebular emission, $M_\star = 4.7 \pm 0.7 \times 10^8$ M$_\odot$ is slightly higher than that with nebular emission, $M_\star = 3.4 \pm 0.8 \times 10^8$ M$_\odot$. With this high SFR, our LAEs lie above the SFMS at $z \sim 2$. However, this case seems unrealistic because our LAEs have Lyα emission, one of nebular emission lines. Indeed, the reduced χ square values in the case without nebular emission are larger than those with nebular emission in

all the fields except SXDS. In addition, results with $f_{\rm esc}^{\rm ion} = 1$ give a high UV attenuation of $A_{1600} = 2.9 \pm 0.2$ mag and hence a high IRX ($= 22^{+5}_{-4}$), which is significantly higher than predicted by the consensus relation (see figure 6.4.1).

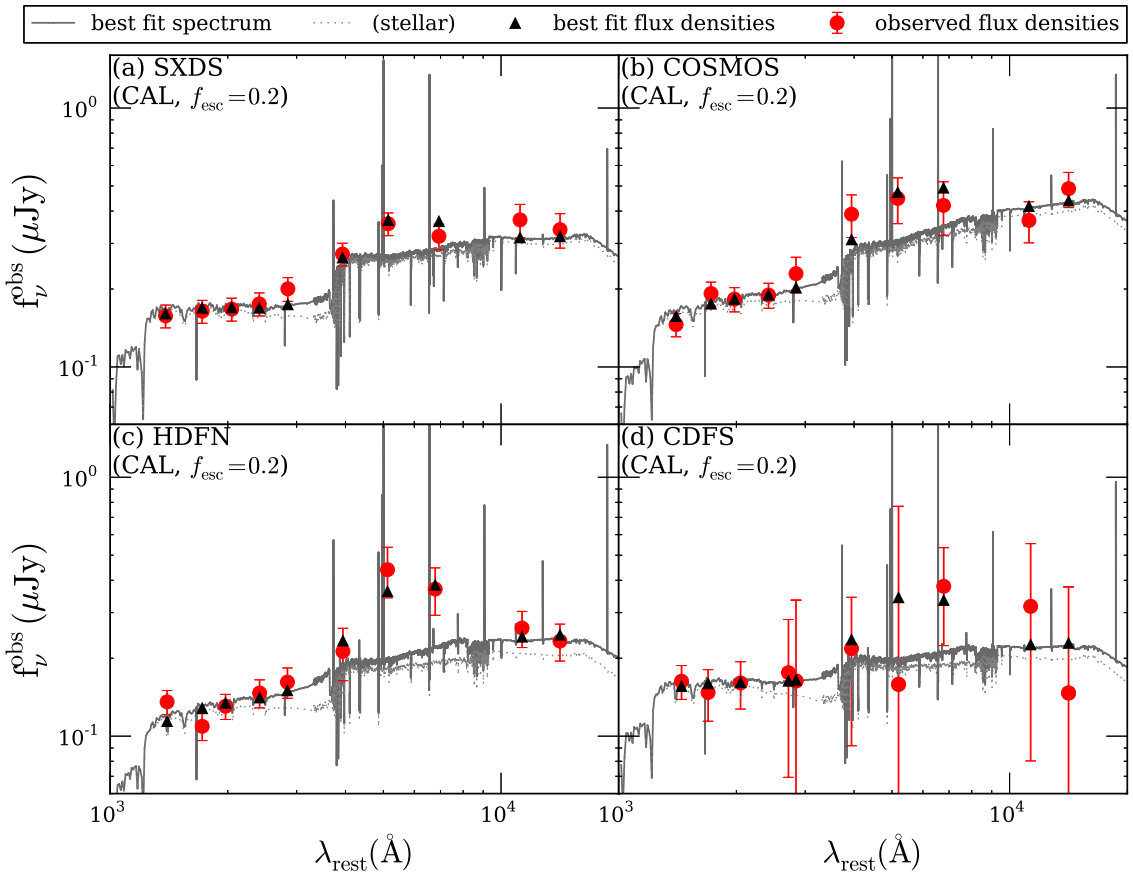

Figure A.1 Same as figure 6.3 but with the Calzetti curve. Panels (a) to (d) show results for SXDS, COSMOS, HDFN, and CDFS, respectively.

Table A.1 Results of SED fitting with an SMC-like curve and the Calzetti curve ($f_{\rm esc}^{\rm ion} = 0.2$).

attenuation curve	$M_\star$ ($10^8 {\rm M}_\odot$) (1)	$E(B-V)_\star$ [A_{1600}] (mag) (2)	Age (10^8 yr) (3)	SFR (${\rm M}_\odot {\rm yr}^{-1}$) (4)	χ_r^2 (5)
SXDS					
SMC	$9.7^{+3.6}_{-1.7}$	$0.05^{+0.01}_{-0.02}$ [$0.6^{+0.1}_{-0.2}$]	$3.6^{+2.8}_{-1.1}$	$3.3^{+0.5}_{-0.7}$	0.604
Calzetti	$7.8^{+3.4}_{-1.9}$	$0.11^{+0.02}_{-0.05}$ [$1.1^{+0.2}_{-0.5}$]	$1.6^{+2.4}_{-0.7}$	$5.7^{+1.7}_{-2.3}$	0.665
COSMOS					
SMC	$14.0^{+3.4}_{-3.6}$	$0.07^{+0.02}_{-0.02}$ [$0.8^{+0.2}_{-0.2}$]	$4.1^{+2.4}_{-1.8}$	$4.2^{+1.2}_{-0.8}$	0.473
Calzetti	$7.9^{+5.1}_{-2.5}$	$0.18^{+0.03}_{-0.05}$ [$1.8^{+0.3}_{-0.5}$]	$0.7^{+1.6}_{-0.4}$	$12.3^{+6.4}_{-5.5}$	0.648
HDFN					
SMC	$7.6^{+4.0}_{-1.9}$	$0.06^{+0.02}_{-0.03}$ [$0.7^{+0.2}_{-0.4}$]	$3.2^{+4.0}_{-1.4}$	$2.9^{+0.8}_{-0.8}$	1.298
Calzetti	$3.2^{+0.6}_{-0.8}$	$0.20^{+0.02}_{-0.03}$ [$2.0^{+0.2}_{-0.3}$]	$0.3^{+0.2}_{-0.1}$	$13.3^{+5.1}_{-3.9}$	0.866
CDFS					
SMC	$10.3^{+11.1}_{-9.7}$	$0.02^{+0.07}_{-0.01}$ [$0.2^{+0.8}_{-0.1}$]	$5.7^{+8.6}_{-5.7}$	$2.2^{+534}_{-0.4}$	0.120
Calzetti	$3.1^{+17.5}_{-2.4}$	$0.14^{+0.05}_{-0.13}$ [$1.4^{+0.5}_{-1.3}$]	$0.4^{+14.0}_{-0.3}$	$9.0^{+23.4}_{-7.1}$	0.101
Average					
SMC	10.2 ± 1.8	0.06 ± 0.01 [0.6 ± 0.1]	3.8 ± 0.3	3.4 ± 0.4	
Calzetti	3.4 ± 0.4	0.19 ± 0.01 [1.9 ± 0.1]	0.3 ± 0.04	12.7 ± 0.6	

Note. — (1) The best fit stellar mass; (2) the best-fit color excess [UV attenuation]; (3) the best fit age; (4) the best fit SFR; (5) reduced chi-squared value. The UV attenuation is derived from the attenuation curve listed in the first column. Metallicity, redshift, and $f_{\rm esc}^{\rm ion}$ are fixed to $0.2 Z_\odot$, 2.18, and 0.2, respectively.

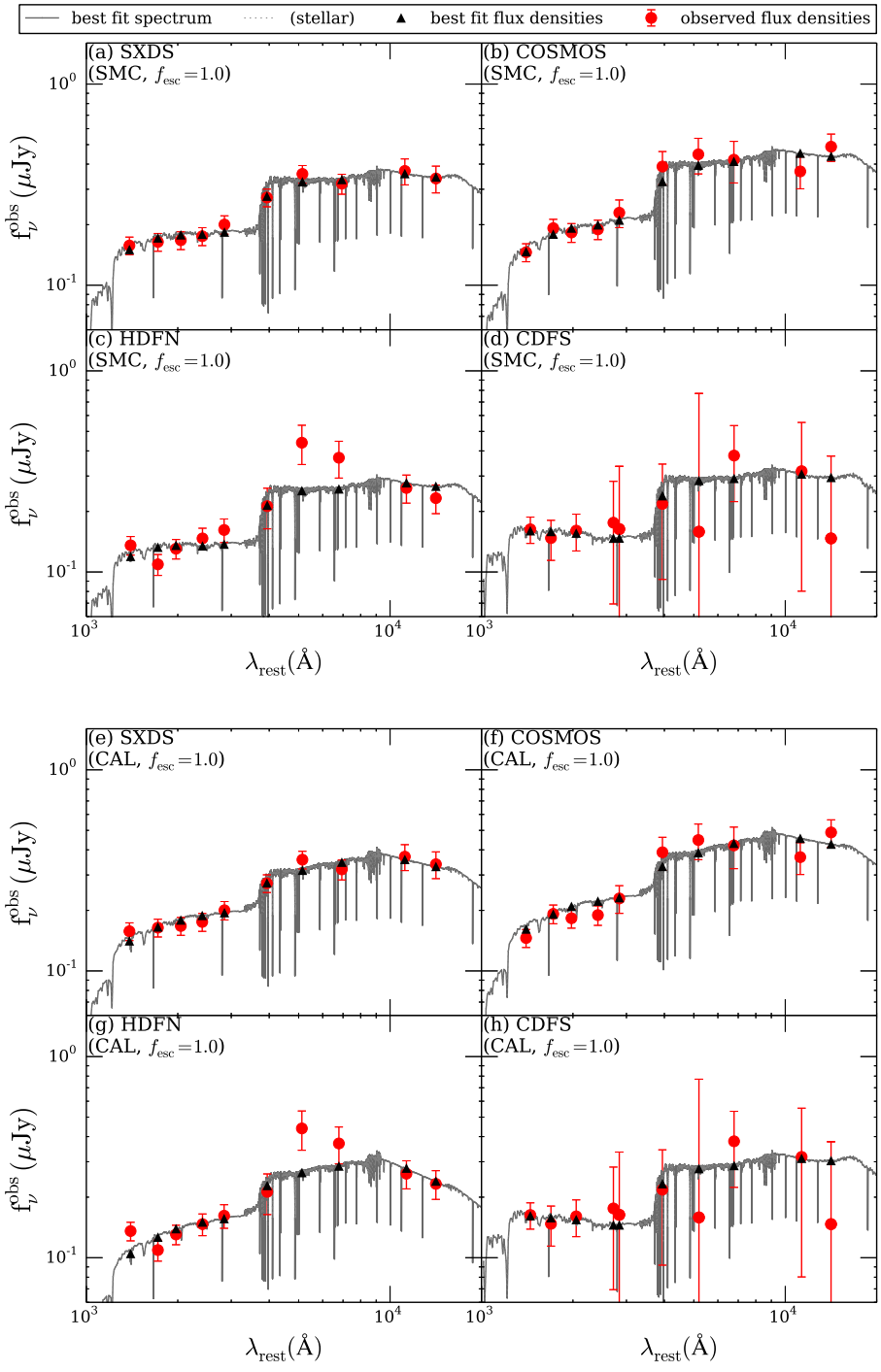

Figure A.2 Same as figure 6.3 but without nebular emission, $f_{esc}^{ion} = 1$. Panels (a) to (d) show results with an SMC-like curve for SXDS, COSMOS, HDFN, and CDFS, respectively. Panels (e) to (h) show results with the Calzetti curve for SXDS, COSMOS, HDFN, and CDFS, respectively.

Table A.2 Results of SED fitting without nebular emission, $f_{\rm esc}^{\rm ion} = 1$.

attenuation curve	$M_\star$ ($10^8 {\rm M}_\odot$) (1)	$E(B-V)_\star$ [A_{1600}] (mag) (2)	Age (10^8 yr) (3)	SFR (${\rm M}_\odot {\rm yr}^{-1}$) (4)	χ_r^2 (5)
SXDS					
SMC	$11.4^{+2.7}_{-1.3}$	$0.06^{+0.02}_{-0.02}$ [$0.7^{+0.2}_{-0.2}$]	$3.6^{+2.1}_{-1.1}$	$3.9^{+0.9}_{-0.8}$	0.350
Calzetti	$5.1^{+7.1}_{-0.4}$	$0.27^{+0.02}_{-0.16}$ [$2.7^{+0.2}_{-1.6}$]	$0.1^{+2.4}_{-0.0}$	$45.3^{+12.0}_{-40.0}$	0.586
COSMOS					
SMC	$14.6^{+5.2}_{-2.7}$	$0.08^{+0.02}_{-0.02}$ [$1.0^{+0.2}_{-0.2}$]	$3.6^{+2.8}_{-1.3}$	$4.9^{+1.3}_{-1.1}$	0.611
Calzetti	$6.6^{+1.5}_{-0.7}$	$0.29^{+0.01}_{-0.04}$ [$2.9^{+0.1}_{-0.4}$]	$0.1^{+0.2}_{-0.0}$	$56.2^{+12.8}_{-26.4}$	0.821
HDFN					
SMC	$9.8^{+2.4}_{-2.5}$	$0.05^{+0.03}_{-0.02}$ [$0.6^{+0.4}_{-0.2}$]	$4.5^{+2.7}_{-2.0}$	$2.7^{+1.0}_{-0.5}$	1.865
Calzetti	$4.4^{+0.0}_{-0.8}$	$0.30^{+0.00}_{-0.04}$ [$3.0^{+0.0}_{-0.4}$]	$0.09^{+0.03}_{-0.01}$	$51.8^{+5.9}_{-18.9}$	1.653
CDFS					
SMC	$13.1^{+10.9}_{-8.9}$	$0.02^{+0.06}_{-0.01}$ [$0.2^{+0.7}_{-0.1}$]	$7.1^{+8.9}_{-6.2}$	$2.3^{+3.0}_{-0.3}$	0.148
Calzetti	$12.1^{+12.7}_{-10.0}$	$0.05^{+0.25}_{-0.04}$ [$0.5^{+2.5}_{-0.4}$]	$5.1^{+11.9}_{-5.1}$	$2.9^{+135.8}_{-1.0}$	0.157
Average					
SMC	11.2 ± 1.2	0.06 ± 0.01 [0.6 ± 0.1]	4.1 ± 0.5	3.2 ± 0.6	
Calzetti	4.7 ± 0.4	0.29 ± 0.02 [2.9 ± 0.2]	0.09 ± 0.01	51.8 ± 4.5	

Note. — (1) The best fit stellar mass; (2) the best-fit color excess [UV attenuation]; (3) the best fit age; (4) the best fit SFR; (5) reduced chi-squared value. The UV attenuation is derived from the attenuation curve listed in the first column. Metallicity, redshift, and $f_{\rm esc}^{\rm ion}$ are fixed to $0.2 Z_\odot$, 2.18, and 1, respectively.

A.2 The subsample in accordance with UV, Lyα and K-band properties in SXDS and COSMOS fields

Figures A.3 and A.4 show the best-fit SEDs and tables A.3 and A.4 summarize the results of the best-fit parameters in SXDS field and COSMOS field, respectively. The field-average values are shown in table 6.3 in section 6.2.3.

Table A.3 Best-fit parameters of SED fitting in SXDS field.

subsample	$M_\star$ ($10^8 M_\odot$) (1)	$E(B-V)_\star$ (mag) (2)	Age (Myr) (3)	SFR ($M_\odot \mathrm{yr}^{-1}$) (4)	χ^2_r (5)
SXDS field/ SMC-like attenuation curve					
bright UV	$12.5^{+4.5}_{-2.1}$	$0.07^{+0.01}_{-0.02}$	255^{+198}_{-74}	$5.9^{+0.9}_{-1.3}$	0.538
faint UV	$4.1^{+1.4}_{-1.5}$	$0.02^{+0.02}_{-0.01}$	321^{+188}_{-178}	$1.5^{+0.5}_{-0.2}$	0.139
blue β	$7.1^{+2.4}_{-1.8}$	$0.02^{+0.01}_{-0.01}$	404^{+236}_{-149}	$2.1^{+0.4}_{-0.3}$	0.588
red β	$14.9^{+3.2}_{-3.8}$	$0.10^{+0.02}_{-0.01}$	286^{+118}_{-125}	$6.2^{+1.8}_{-0.8}$	2.282
bright Lyα	$6.9^{+1.6}_{-2.3}$	$0.02^{+0.02}_{-0.01}$	453^{+187}_{-226}	$1.9^{+0.5}_{-0.2}$	0.289
faint Lyα	$11.5^{+4.3}_{-2.0}$	$0.06^{+0.01}_{-0.02}$	360^{+280}_{-105}	$3.9^{+0.6}_{-0.8}$	1.461
large EW	$4.5^{+1.6}_{-1.5}$	$0.02^{+0.02}_{-0.01}$	360^{+211}_{-180}	$1.5^{+0.5}_{-0.2}$	0.255
small EW	$11.7^{+4.3}_{-2.0}$	$0.06^{+0.01}_{-0.02}$	321^{+250}_{-94}	$4.4^{+0.7}_{-0.9}$	0.775
bright K	$21.5^{+5.5}_{-5.3}$	$0.08^{+0.01}_{-0.02}$	453^{+265}_{-167}	$5.8^{+1.0}_{-1.1}$	0.680
faint K	$3.8^{+1.3}_{-1.4}$	$0.03^{+0.02}_{-0.02}$	203^{+158}_{-112}	$2.2^{+0.8}_{-0.5}$	0.692
SXDS field/ the Calzetti attenuation curve					
bright UV	$12.0^{+3.0}_{-3.8}$	$0.13^{+0.03}_{-0.03}$	143^{+112}_{-79}	$9.7^{+4.5}_{-2.7}$	0.902
faint UV	$3.1^{+2.3}_{-1.8}$	$0.06^{+0.05}_{-0.05}$	161^{+348}_{-128}	$2.3^{+2.3}_{-1.0}$	0.114
blue β	$6.7^{+2.7}_{-2.4}$	$0.04^{+0.05}_{-0.03}$	321^{+320}_{-207}	$2.5^{+1.8}_{-0.7}$	0.581
red β	$16.0^{+3.7}_{-4.0}$	$0.18^{+0.02}_{-0.02}$	161^{+94}_{-70}	$11.6^{+3.5}_{-2.4}$	2.978
bright Lyα	$5.2^{+3.3}_{-3.3}$	$0.07^{+0.06}_{-0.06}$	203^{+438}_{-174}	$3.0^{+4.0}_{-1.4}$	0.268
faint Lyα	$10.9^{+3.2}_{-2.7}$	$0.12^{+0.02}_{-0.04}$	203^{+202}_{-89}	$6.4^{+1.9}_{-2.1}$	1.550
large EW	$2.8^{+3.3}_{-1.9}$	$0.09^{+0.04}_{-0.08}$	102^{+469}_{-85}	$3.1^{+2.8}_{-1.8}$	0.212
small EW	$11.1^{+2.9}_{-2.9}$	$0.12^{+0.03}_{-0.03}$	181^{+141}_{-90}	$7.2^{+3.0}_{-2.0}$	1.016
bright K	$16.1^{+5.8}_{-4.2}$	$0.17^{+0.03}_{-0.04}$	143^{+143}_{-72}	$13.0^{+5.5}_{-4.4}$	1.012
faint K	$3.6^{+1.3}_{-1.5}$	$0.06^{+0.03}_{-0.03}$	143^{+143}_{-91}	$2.9^{+1.5}_{-0.8}$	0.673

Note. — (1) Stellar mass; (2) color excess; (3) age; (4) SFR; and (5) reduced χ^2 value. Metallicity is fixed to $0.2\mathrm{Z}_\odot$, redshift to 2.18, and $f_{\mathrm{esc}}^{\mathrm{ion}}$ to 0.2.

Table A.4 Best-fit parameters of SED fitting in COSMOS field.

subsample	$M_\star$ ($10^8 M_\odot$) (1)	$E(B-V)_\star$ (mag) (2)	Age (Myr) (3)	SFR ($M_\odot \mathrm{yr}^{-1}$) (4)	χ^2_r (5)
COSMOS field/ SMC-like attenuation curve					
bright UV	$16.8^{+5.9}_{-2.9}$	$0.09^{+0.01}_{-0.02}$	227^{+177}_{-66}	$8.8^{+1.3}_{-1.9}$	0.377
faint UV	$4.2^{+2.7}_{-1.8}$	$0.05^{+0.02}_{-0.02}$	227^{+282}_{-137}	$2.2^{+0.9}_{-0.5}$	0.244
blue β	$2.3^{+2.5}_{-1.8}$	$0.03^{+0.02}_{-0.02}$	114^{+246}_{-105}	$2.3^{+2.7}_{-0.7}$	0.458
red β	$13.1^{+4.8}_{-2.3}$	$0.09^{+0.01}_{-0.02}$	286^{+223}_{-84}	$5.5^{+0.8}_{-1.2}$	0.560
bright Lyα	$8.5^{+2.8}_{-2.7}$	$0.06^{+0.02}_{-0.01}$	286^{+167}_{-143}	$3.6^{+1.1}_{-0.5}$	0.257
faint Lyα	$13.5^{+4.6}_{-3.3}$	$0.08^{+0.01}_{-0.01}$	360^{+211}_{-133}	$4.6^{+0.8}_{-0.6}$	2.238
large EW	$8.1^{+2.8}_{-2.6}$	$0.06^{+0.02}_{-0.01}$	321^{+188}_{-160}	$3.1^{+1.0}_{-0.4}$	0.311
small EW	$19.5^{+7.3}_{-3.5}$	$0.08^{+0.01}_{-0.02}$	404^{+315}_{-118}	$5.9^{+0.8}_{-1.2}$	3.052
bright K	$16.7^{+3.5}_{-4.2}$	$0.10^{+0.02}_{-0.01}$	227^{+94}_{-99}	$8.7^{+2.5}_{-1.1}$	0.208
faint K	$2.9^{+2.2}_{-2.4}$	$0.06^{+0.02}_{-0.02}$	114^{+172}_{-107}	$3.0^{+4.2}_{-0.8}$	0.278
COSMOS field/ the Calzetti attenuation curve					
bright UV	$15.5^{+5.5}_{-5.6}$	$0.17^{+0.02}_{-0.03}$	102^{+101}_{-57}	$17.4^{+6.7}_{-5.1}$	1.185
faint UV	$2.6^{+2.5}_{-1.1}$	$0.13^{+0.02}_{-0.05}$	57^{+170}_{-32}	$5.1^{+2.1}_{-2.4}$	0.213
blue β	$1.7^{+2.6}_{-1.0}$	$0.08^{+0.02}_{-0.06}$	47^{+239}_{-35}	$3.9^{+1.9}_{-2.1}$	0.413
red β	$10.9^{+5.1}_{-3.4}$	$0.18^{+0.02}_{-0.03}$	102^{+126}_{-52}	$12.2^{+4.2}_{-3.8}$	1.305
bright Lyα	$3.8^{+3.0}_{-1.0}$	$0.17^{+0.01}_{-0.04}$	35^{+79}_{-12}	$11.8^{+2.4}_{-5.0}$	0.377
faint Lyα	$13.4^{+3.5}_{-3.5}$	$0.16^{+0.03}_{-0.03}$	181^{+141}_{-90}	$8.7^{+3.7}_{-2.4}$	2.609
large EW	$4.4^{+3.4}_{-1.4}$	$0.16^{+0.02}_{-0.04}$	57^{+123}_{-28}	$8.6^{+3.1}_{-3.5}$	0.368
small EW	$19.3^{+5.1}_{-4.8}$	$0.16^{+0.02}_{-0.03}$	203^{+158}_{-89}	$11.2^{+3.3}_{-3.0}$	3.267
bright K	$9.7^{+4.2}_{-1.4}$	$0.21^{+0.02}_{-0.02}$	40^{+41}_{-11}	$26.3^{+6.0}_{-7.0}$	1.057
faint K	$1.7^{+1.2}_{-0.7}$	$0.13^{+0.02}_{-0.01}$	26^{+38}_{-14}	$6.7^{+1.9}_{-1.7}$	0.279

Note. — (1) Stellar mass; (2) color excess; (3) age; (4) SFR; and (5) reduced χ^2 value. Metallicity is fixed to $0.2\mathrm{Z}_\odot$, redshift to 2.18, and $f_{\mathrm{esc}}^{\mathrm{ion}}$ to 0.2.

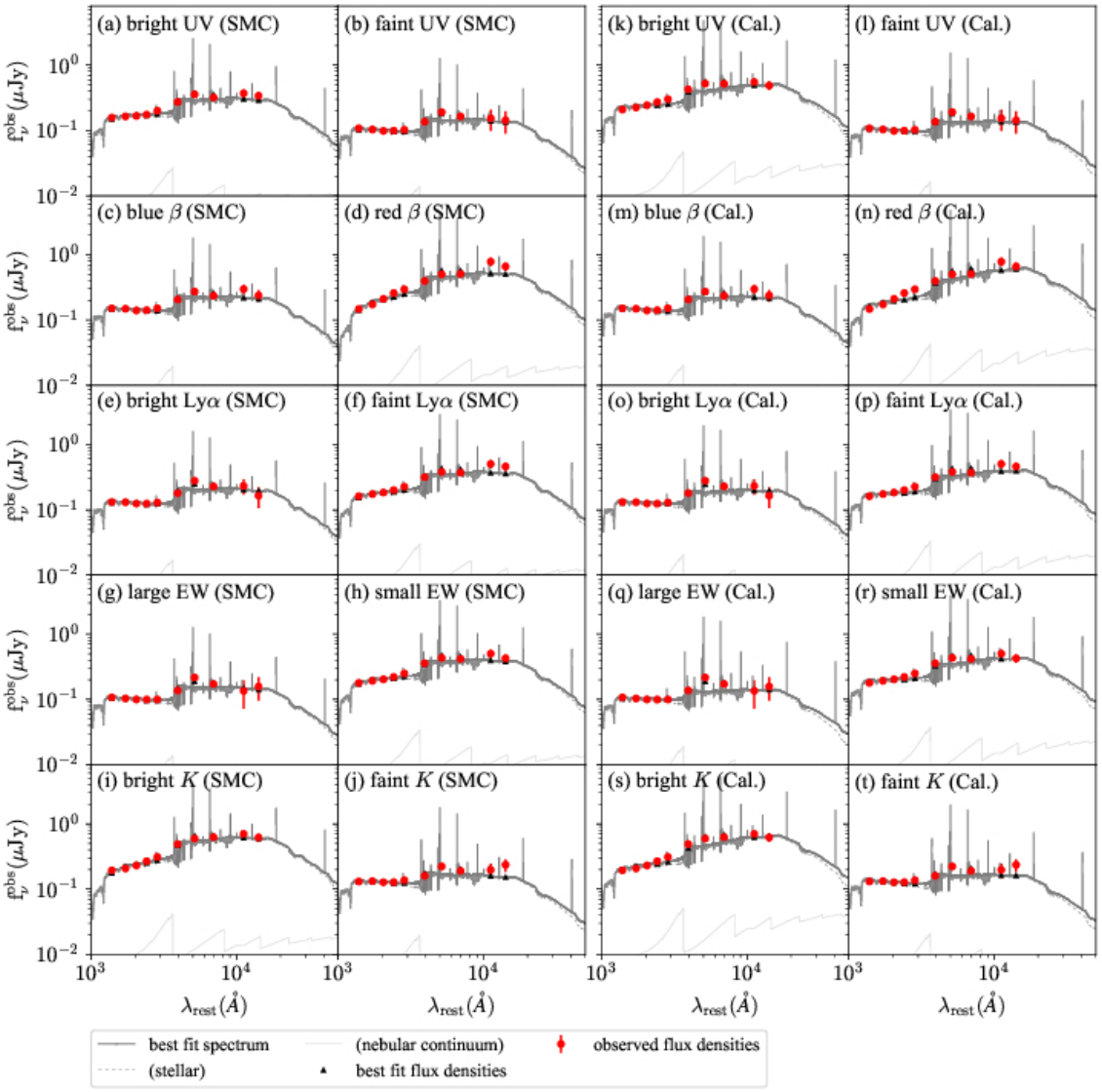

Figure A.3 Best-fit SEDs for the ten subsamples in SXDS field. Panels (a)–(j) show results with an assumption of an SMC-like attenuation curve: (a) bright UV, (b) faint UV, (c) blue β, (d) red β, (e) bright Lyα, (f) faint Lyα, (g) large EW_0(Lyα), (h) small EW_0(Lyα), (i) bright K, and (j) faint K, while panels (k)–(t) show those with an assumption of Calzetti curve. For each panel, a gray solid line, a light gray solid line and a light gray dotted line show the best-fit model spectrum, its nebular continuum component and its stellar continuum component, respectively. Red filled circles and black filled triangles represent the observed flux densities and the flux densities calculated from the best-fit spectrum, respectively.

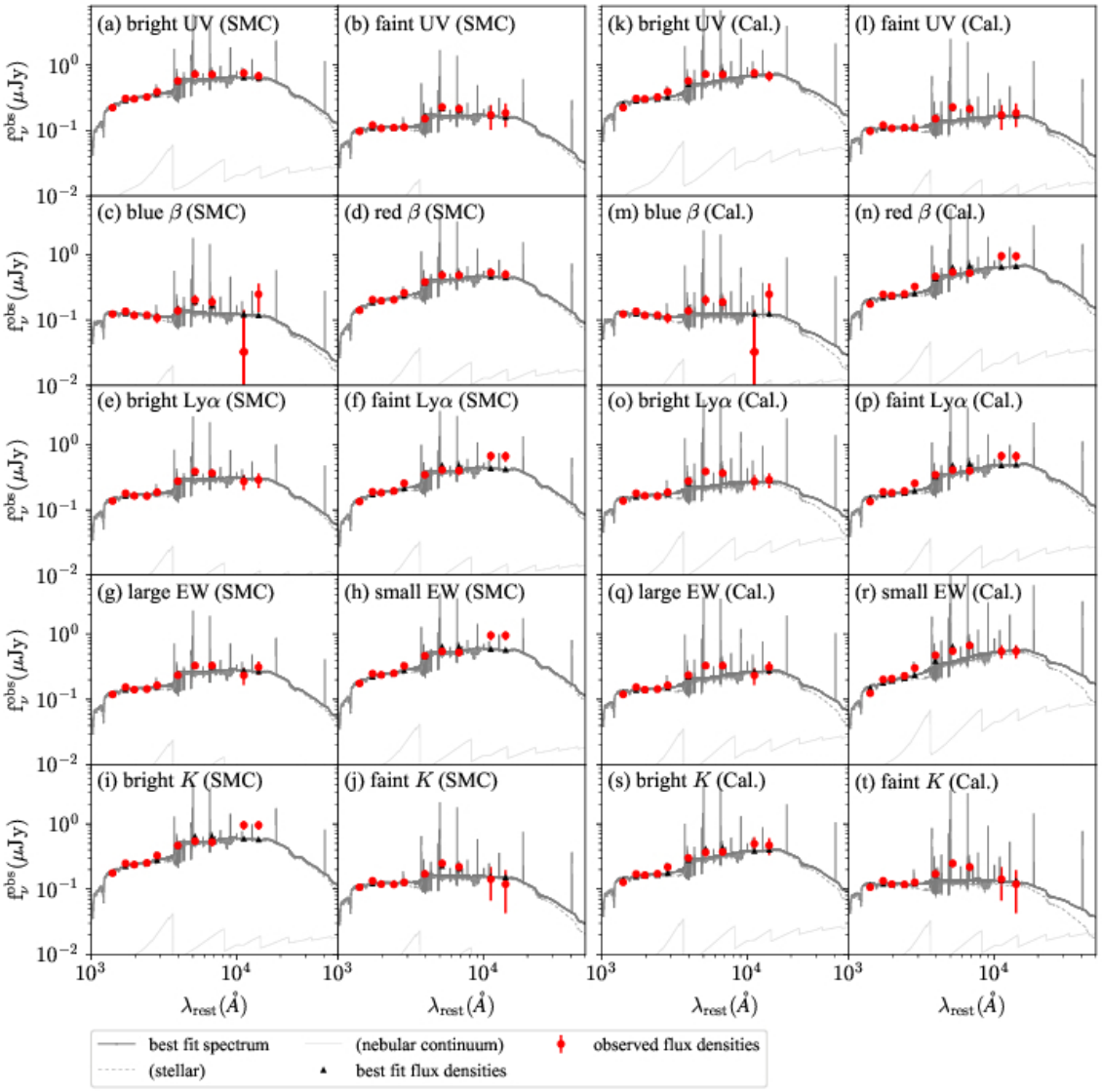

Figure A.4 Best-fit SEDs for the ten subsamples in COSMOS field. Panels (a)–(j) show results with an assumption of an SMC-like attenuation curve: (a) bright UV, (b) faint UV, (c) blue β, (d) red β, (e) bright Lyα, (f) faint Lyα, (g) large EW_0(Lyα), (h) small EW_0(Lyα), (i) bright K, and (j) faint K, while panels (k)–(t) show those with an assumption of Calzetti curve. For each panel, a gray solid line, light gray solid line and a light gray dotted line show the best-fit model spectrum, its nebular continuum component and its stellar continuum component, respectively. Red filled circles and black filled triangles represent the observed flux densities and the flux densities calculated from the best-fit spectrum, respectively.

Appendix B

Clustering analysis

B.1 The best fit ACFs for the subdivided LAEs

We show the best-fit ACFs for the subdivided LAEs in accordance with UV, Lyα, and K-band properties in the two fields and their field-average values in figure B.1. We do not perform clustering analysis for the K-divided subsamples as described in section 2.5.2. The differences in the ACF measurement (i.e., bias) between the two fields is described in section 6.3.2.

B.2 Cosmic variance

Biases and dark matter halo masses derived from limited survey areas suffer from cosmic variance due to spatial variations in the ACF of dark matter. One of the commonly used techniques to estimate the uncertainties due to cosmic variance is "Jackknife method", which divides a survey field into sub-fields and calculates the ACF without including one of the sub-fields, repeating the procedure as the same times as the number of sub-fields (e.g., Quenouille, 1956; Tukey, 1958; Shao, 1986). Other general technique is "Bootstrap method", which is similar to Jackknife method but calculates the ACF from randomly selected (overlapping) sub-fields (e.g., Efron, 1979). Norberg et al. (2009) suggest that Bootstrap method overestimates the variance of spacial correlation function by 40% on all scales, while Jackknife method reproduces the correct variance on large scales but significantly overestimates on smaller scales, if a survey area is large enough. However, it is also well known that it can not include cosmic variance beyond observed area (e.g., Norberg et al., 2009).

According to Cohn (2006), cosmic variance in ACF arises from fluctuations of dark matter distribution and the number of limited sample size (shot noise), and it can be analytically calculated from cosmological structure formation model. The idea is similar to the one used to predict cosmic variance in number density (e.g., Moster et al., 2011). This formalism in Cohn (2006) has been used to estimate uncertainties, for instance, in angular power spectrum of Sunyaev-Zel'dovich selected galaxy clusters (e.g., Cohn & Kadota, 2005) and in baryon acoustic oscillations correlation function in the matter power spectrum and correlation function (e.g., Taruya et al., 2009). In this section, we

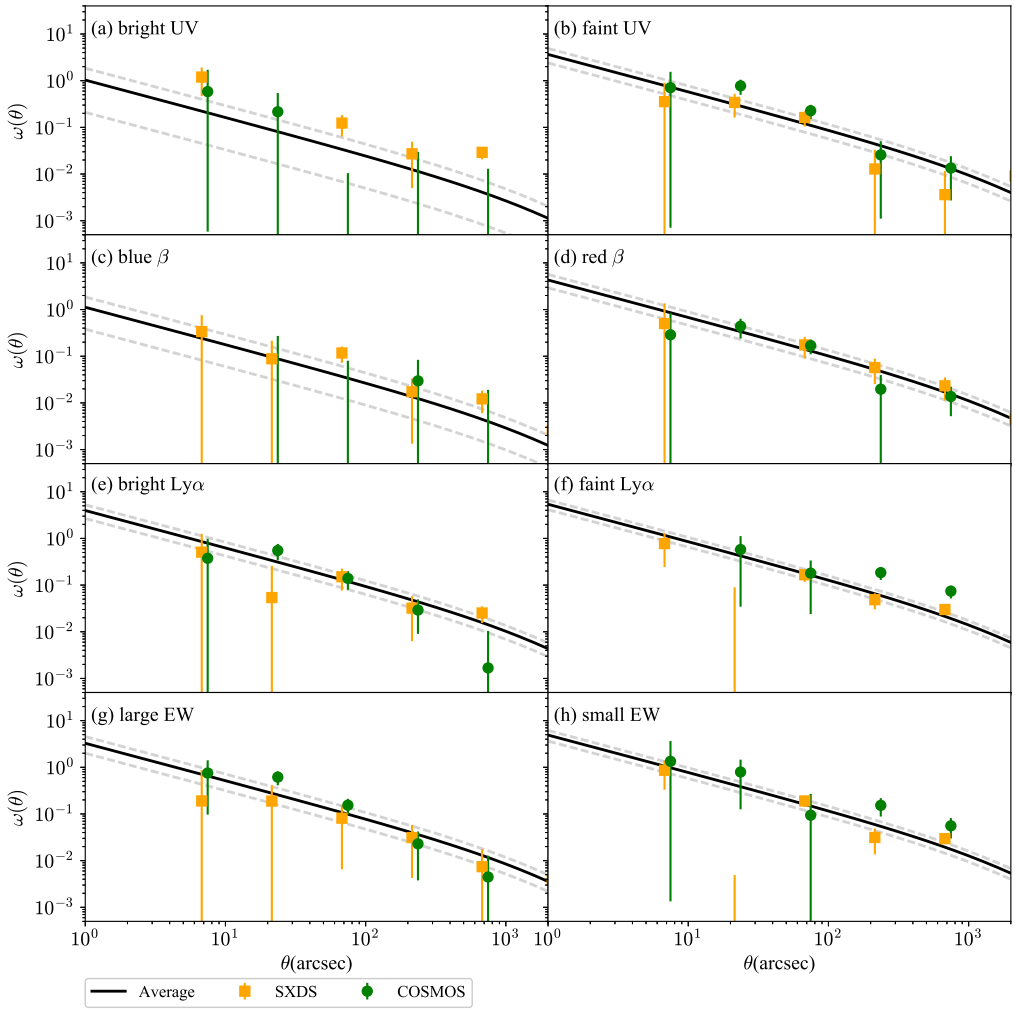

Figure B.1 ACF measurements for the eight subsamples: (a) bright UV, (b) faint UV, (c) blue β, (d) red β, (e) bright Lyα, (f) faint Lyα, (g) large EW_0(Lyα), and (h) small EW_0(Lyα). For each panel, orange filled squares and green filled circles represent measurements in SXDS and COSMOS fields. A black solid line and light gray dotted line indicate the field-average best-fit ACFs with fixed $\beta = 0.8$, whose fitting range is 40–1000″. we slightly shift all data points along the abscissa by a value depending on the field for presentation purpose.

analytically estimate cosmic variance in bias value and thus dark matter halo mass for the first time for high-z clustering analysis (at $z \gtrsim 2$). We describe relative uncertainty of ACF as a function of z, survey area, bias, and number density of sample in section B.2.1, convert it to relative uncertainty of bias parameter in section B.2.2.

B.2.1 Covariance and relative uncertainty of ACF

Covariance on angular correlation function, $\omega(\theta)$, between $\theta = \theta1(\neq 0)$ and $\theta = \theta2(\neq 0)$ is given in Cohn (2006):

$$\mathrm{cov}(\omega(\theta1), \omega(\theta2)) = \frac{1}{\Omega_{\rm sr}\pi}\int KdK\, J_0(K\theta1)\, J_0(K\theta2)P_2(K)^2 + \frac{2}{\Omega_{\rm sr}\pi\, N_{\rm sr}}\int KdK\, J_0(K\theta1)\, J_0(K\theta2)P_2(K) + \frac{(1+\omega(\theta1))^2}{0.5N_{\rm sr}^2(1+\omega(\theta1))\Omega_{\rm sr}d\Omega_{\rm sr}}\delta_{\theta1,\,\theta2}, \tag{B.1}$$

where K, $P_2(K)$, $J_0(K\theta)$, $\Omega_{\rm sr}$, and $N_{\rm sr}$ are the Fourier transform of θ, power spectrum (i.e., the Fourier transform of $\omega(\theta)$), the zeroth-order Bessel function of the first kind, survey area in steradians, and surface number density of galaxies per steradians, respectively.

We introduce F and G to normalize the equation B.1 at $z \sim$ 2–6[*40]:

$$F(z,\, \Omega_0 = 1\,\mathrm{deg}^2,\, \Delta z_0 = 0.5,\; b_0 = 1)_{\theta1,\,\theta2} = \frac{1}{\Omega_0\pi}\int KdK\, J_0(K\theta1)\, J_0(K\theta2)P_2(K)^2_{z,\,\Delta z_0,\,b_0}\, X_{\rm unit}, \tag{B.2}$$

and

$$G(z,\, \Omega_0 = 1\,\mathrm{deg}^2,\, \Delta z_0 = 0.5,\, N_0\Delta z_0 = 5000,\, b_0 = 1)_{\theta1,\,\theta2} = \frac{2}{\Omega_0\pi\, N_0\Delta z_0}\int KdK\, J_0(K\theta1)\, J_0(K\theta2)P_2(K)_{z,\,\Delta z_0,\,b_0}, \tag{B.3}$$

where $P_2(K)_{z,\,\Delta z_0,\,b}$ is Fourier transform of $\omega(\theta)$ as a function of z with $\Delta z_0 = 0.5$ and $b_0 = 1$. N_0 and $X_{\rm unit}$ are number density of galaxies per $1\,\mathrm{deg}^2$ per z and conversion factor from deg^2 to sr, respectively. We introduce PE, which is interpreted as a poisson error:

$$PE = \frac{(1+\omega(\theta1))^2}{0.5N^2\Delta z^2(1+\omega(\theta1))\Omega d\Omega}\delta_{\theta1,\,\theta2}, \tag{B.4}$$

where N, Δz and Ω are number density of galaxies per deg^2 per z, width of redshift, and survey area with deg^2, respectively. The equation B.1 is converted to be

$$\mathrm{cov}(\omega(\theta1), \omega(\theta2))(z,\, \Omega,\, \Delta z,\; b,\; N) \simeq \frac{\Omega_0}{\Omega}\left(\frac{\Delta z_0}{\Delta z}\right)^2\left(\frac{b}{b_0}\right)^4 F(z,\, \Omega_0,\, \Delta z_0,\, b_0)_{\theta1,\,\theta2} + \frac{\Omega_0\, N_0}{\Omega\, N}\left(\frac{\Delta z_0}{\Delta z}\right)^2\left(\frac{b}{b_0}\right)^2 G(z,\, \Omega_0,\, \Delta z_0,\; b_0, N)_{\theta1,\,\theta2} + \mathrm{PE}. \tag{B.5}$$

Hearafter, we define the first and the second terms in equation B.5 as cosmic variance, $\mathrm{cov}_{\omega,\,\mathrm{CV}}(\theta1,\, \theta2,\, z,\, \Omega,\, \Delta z,\; b,\; N)$. F is a term with square of power spectrum, meaning fluctuation of dark matter distribution, while G is a term with power spectrum and number density, implying the coupling of dark matter fluctuation to limited sample size.

[*40] Redshift dependences of $P_2(K)$ and $J_0(K\theta)$ are small at $z \sim$ 2–6, at which clustering analysis of high-z galaxies is usually applied.

At $z \sim 2$–6, $\omega(\theta)$ can be approximated as $\frac{\Delta z_0\, b^2}{\Delta z\, b_0^2}\, \omega_{b_0, \Delta z_0}(\theta)$ (see footnote *40). Therefore, relative uncertainties (1σ) of $\omega(\theta)$ caused by cosmic variance at $z \sim 2$–6 is

$$
\begin{aligned}
&\frac{\sqrt{\mathrm{cov}_{\omega,\,\mathrm{CV}}(\theta 1,\, \theta 2,\, z,\, \Omega,\, \Delta z,\, b,\, N)}}{\sqrt{\omega(\theta 1)\, \omega(\theta 2)}} \\
&= \left(\frac{\Omega_0}{\Omega}\right)^{0.5} \frac{\Delta z_0\, b^2}{\Delta z\, b_0^2\, \sqrt{\omega(\theta 1)\, \omega(\theta 2)}} \left(F(z,\, \Omega_0,\, \Delta z_0,\, b_0)_{\theta 1,\, \theta 2} + \frac{N_0\, b_0^2}{N b^2}\, G(z,\, \Omega_0,\, \Delta z_0,\, b_0, N_0)_{\theta 1,\, \theta 2}\right)^{0.5} \\
&\simeq \frac{1}{\sqrt{\omega_{b_0, \Delta z_0}(\theta 1)\, \omega_{b_0, \Delta z_0}(\theta 2)}} \left(\frac{\Omega_0}{\Omega}\right)^{0.5} \left(F(z,\, \Omega_0,\, \Delta z_0,\, b_0)_{\theta 1,\, \theta 2} + \frac{N_0\, b_0^2}{N b^2}\, G(z,\, \Omega_0,\, \Delta z_0,\, b_0, N_0)_{\theta 1,\, \theta 2}\right)^{0.5} \\
&= \left(\frac{\Omega_0}{\Omega}\right)^{0.5} \left(\frac{F(z,\, \Omega_0,\, \Delta z_0,\, b_0)_{\theta 1,\, \theta 2}}{\omega_{b_0, \Delta z_0}(\theta 1)\, \omega_{b_0, \Delta z_0}(\theta 2)} + \frac{N_0\, b_0^2}{N b^2}\, \frac{G(z,\, \Omega_0,\, \Delta z_0,\, b_0, N_0)_{\theta 1,\, \theta 2}}{\omega_{b_0, \Delta z_0}(\theta 1)\, \omega_{b_0, \Delta z_0}(\theta 2)}\right)^{0.5} \\
&= \left(\frac{\Omega_0}{\Omega}\right)^{0.5} \left(f(z,\, \Omega_0)_{\theta 1,\, \theta 2} + \frac{N_0\, b_0^2}{N b^2}\, g(z,\, \Omega_0,\, b_0, N_0)_{\theta 1,\, \theta 2}\right)^{0.5}, \qquad \text{(B.6)}
\end{aligned}
$$

where we define constant parameters, f and g, as

$$
f(z,\, \Omega_0)_{\theta 1,\, \theta 2} = \frac{F(z,\, \Omega_0,\, \Delta z_0,\, b_0)_{\theta 1,\, \theta 2}}{\omega_{b_0, \Delta z_0}(\theta 1)\, \omega_{b_0, \Delta z_0}(\theta 2)} \qquad \text{(B.7)}
$$

and

$$
g(z,\, \Omega_0,\, b_0, N_0)_{\theta 1,\, \theta 2} = \frac{G(z,\, \Omega_0,\, \Delta z_0,\, b_0, N_0)_{\theta 1,\, \theta 2}}{\omega_{b_0, \Delta z_0}(\theta 1)\, \omega_{b_0, \Delta z_0}(\theta 2)}, \qquad \text{(B.8)}
$$

respectively. A relative uncertainty of $\omega(\theta)$ caused by cosmic variance can be written as a function of Ω, N, and b. It is found to be proportional to square of the survey area (Ω) and to be independent of width of redshift (at $z \sim 2$–6, see footnote *40). It is almost independent of redshift.

B.2.2 Relative uncertainties of bias parameter

A relative uncertainty of b_{eff} due to cosmic variance can be written as:

$$
\frac{\Delta b_{\mathrm{eff}}}{b_{\mathrm{eff}}} = 0.5 \frac{\Delta \mathrm{A}_\omega}{\mathrm{A}_\omega} \propto \Omega^{-0.5} \qquad \text{(B.9)}
$$

As seen in equations B.6 and B.9, $\frac{\Delta b_{\mathrm{eff}}}{b_{\mathrm{eff}}}$ is found to be proportional to $\Omega^{-0.5}$. It is independent of width of redshift (at $z \sim 2$–6) and is almost independent of redshift. In section 4.4, we only include the first term in equation B.6 when we calculate cosmic variance in effective bias since the contribution of the second term is small as described in footnote *14.

Appendix C

Lyα Halo Luminosity

C.1 NB selection bias

In this Appendix, we first describe the NB-selection bias of our LAE sample, and then discuss the effect of this bias on the obtained $M_\star$ (M_h) –$L(\mathrm{Ly}\alpha)_H$ relations. As shown in figures 2.3 (g) and (h), our sample misses UV-faint LAEs ($M_{UV} \gtrsim -19$ mag) with faint $L(\mathrm{Ly}\alpha)_{ps}$ and small $EW_{0,\,ps}(\mathrm{Ly}\alpha)$. This selection bias has the following effects on subsample properties.

M_{UV} and m_K subsamples The UV-faint ($M_{UV} > -19.2$ mag) subsample is biased toward brighter $L(\mathrm{Ly}\alpha)_{ps}$ and larger $EW_{0,\,ps}(\mathrm{Ly}\alpha)$. The K-faint subsample ($m_K > 25.0$ mag) is probably biased similarly. Although the $L(\mathrm{Ly}\alpha)_H$ of these subsamples is probably overestimated, we find in appendix C.2 that it does not change our results. This selection bias probably does not change $M_\star$ values since m_K and M_{UV} are a good tracer of $M_\star$. The bright m_K and M_{UV} subsamples are almost free from this bias.

β subsamples Galaxies with fainter UV luminosities generally have smaller β (e.g., Alavi et al., 2014). Although our β subsamples are probably biased to some degree, it is difficult to evaluate the effects on $M_\star$ and $L(\mathrm{Ly}\alpha)_H$ estimates quantitatively. However, the effects should be smaller than those on the UV and K subsamples, since the M_{UV}–β correlation has a large scatter (see figure 2.3 [f]).

$L(\mathrm{Ly}\alpha)_{ps}$ and $EW_{0,ps}(\mathrm{Ly}\alpha)$ subsamples The faint $L(\mathrm{Ly}\alpha)$ and small $EW(\mathrm{Ly}\alpha)$ subsamples are biased toward bright UV magnitudes. Although their $L(\mathrm{Ly}\alpha)_H$ values are probably not affected by the selection bias, their $M_\star$ values are expected to be overestimated to some degree. The bright $L(\mathrm{Ly}\alpha)$ and large $EW(\mathrm{Ly}\alpha)$ subsamples are not biased. If the $M_\star$ of the faint $L(\mathrm{Ly}\alpha)$ and small $EW(\mathrm{Ly}\alpha)$ subsamples decreases, the power-law slope of the $M_\star$–$L(\mathrm{Ly}\alpha)_H$ relation becomes shallower, enlarging the descrepancy from the models of cold streams and satellite star formation.

In the next appendix, we use the MUSE sample to evaluate the robustness of $L(\mathrm{Ly}\alpha)_H$ estimates for our faint m_K and M_{UV} subsamples. The MUSE sample is complementary to our sample, because it is essentially UV-limited but contains much fewer objects than ours.

C.2 Robustness of the relations of $L(\mathrm{Ly}\alpha)_H$

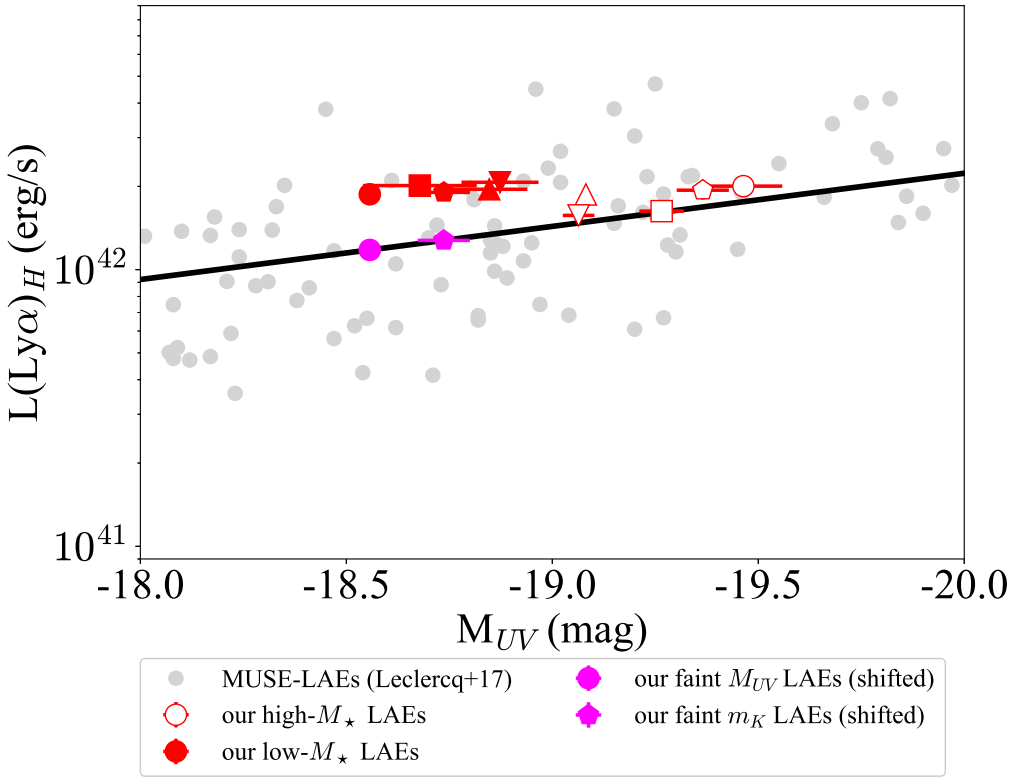

Figure C.1 $L(\mathrm{Ly}\alpha)_H$ as a function of M_{UV}. Grey points represent MUSE-LAEs at $z \sim 3-6$ and a black solid line the best fit of a linear function to them (Leclercq et al., 2017). The field average values of our ten subsamples using the stacked relation (equation 5.1) are shown by red symbols below: open (filled) circles for bright (faint) M_{UV}, open (filled) triangles for red (blue) β, open (filled) inverted triangles for faint (bright) $L(\mathrm{Ly}\alpha)_{ps}$, open (filled) squares for small (large) $EW_{0,ps}(\mathrm{Ly}\alpha)$, and open (filled) pentagons for bright (faint) m_{K}. Results using Leclercq et al. (2017)'s relation for two subsamples are shown by filled magenta symbols: a circle for the faint M_{UV} subsample and a pentagon for the faint m_K subsample.

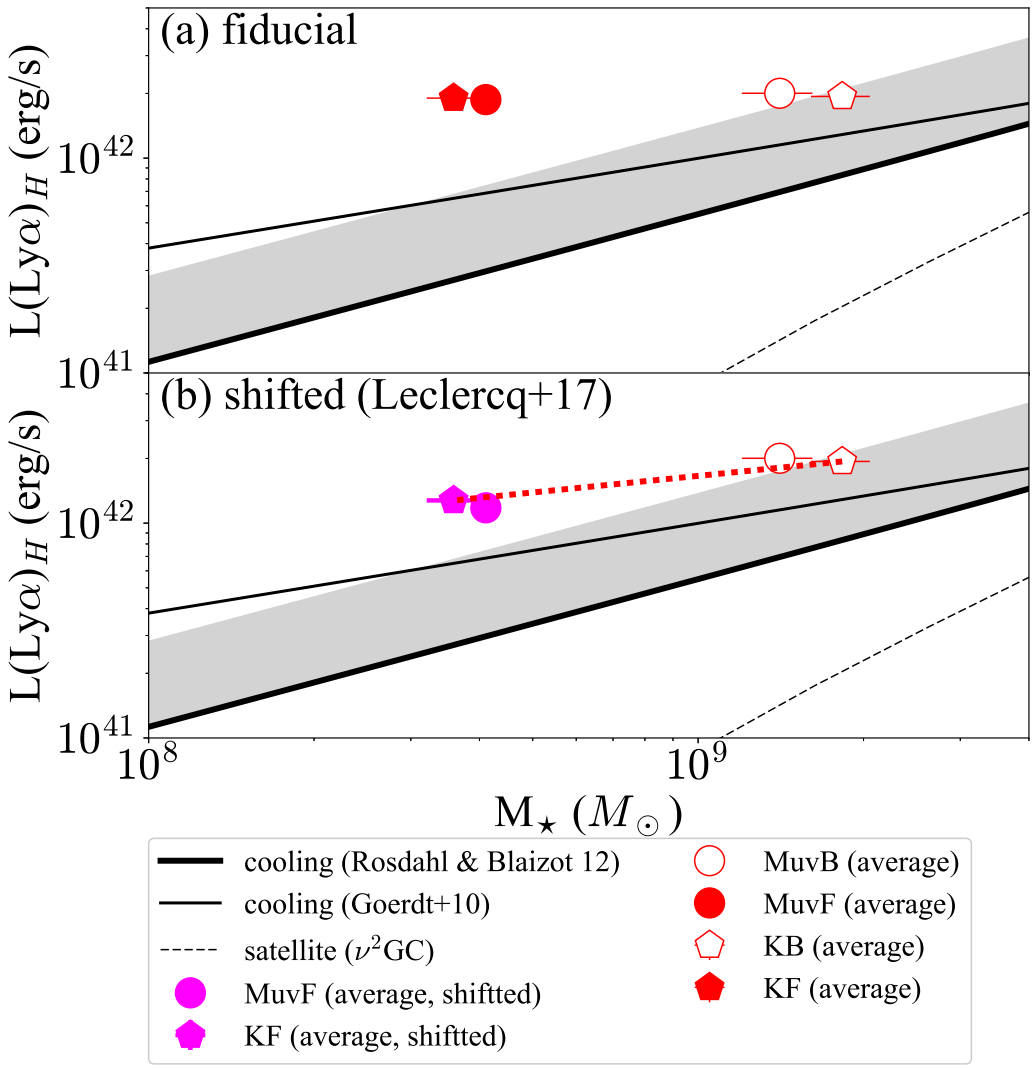

Figure C.2 $L(\mathrm{Ly}\alpha)_H$ vs. $M_\star$: (a) the fiducial results and (b) NB-selection bias corrected results using the M_{UV}–$L(\mathrm{Ly}\alpha)_H$ relation in Leclercq et al. (2017). The field average values of our M_{UV} and m_K subsamples using the stacked relation (equation 5.1) are shown by red symbols below: open (filled) circles for bright (faint) M_{UV}, and open (filled) pentagons for bright (faint) m_{K}. Results using Leclercq et al. (2017)'s relation for two subsamples are shown by filled magenta symbols: a circle for the faint M_{UV} subsample and a pentagon for the faint m_K subsample. Thick and thin solid black lines show the Lyα luminosities from cooling flows by theoretical models in Rosdahl & Blaizot (2012) and Goerdt et al. (2010), respectively, which are converted from original $M_\star$–$L(\mathrm{Ly}\alpha)_H$ relations using the $M_\star$–M_{h} relation in Moster et al. (2013). Gray shaded regions above the solid black lines roughly indicate the distribution of Rosdahl & Blaizot (2012)'s simulated galaxies above the solid line, whose $L(\mathrm{Ly}\alpha)_H$ reaches at most ~ 2.5 times higher than the line. A black dashed line shows the Lyα luminosities from satellite star formation calculated by a theoretical model (ν^2GC Makiya et al., 2016; Shirakata et al., 2018, Ogura et al. in prep.). A dotted red line in panel (b) shows the slope determined by the m_K subsamples.

We evaluate the effects of the NB-selection bias on the m_K and M_{UV} subsamples. We re-estimate $L(\mathrm{Ly}\alpha)_H$ with a complementary result of the MUSE-LAEs in Leclercq et al. (2017) which is essentially free from this kind of bias: the relation between M_{UV} and $L(\mathrm{Ly}\alpha)_H$. They have found $L(\mathrm{Ly}\alpha)_H$ anti-correlates with L_{UV} (see their figure 16). As shown in figure C.1, our high-$M_\star$ LAEs (red filled objects), which are not affected by the NB-bias, are consistent with the best-fit relation of MUSE-LAEs (black solid line), while the faint m_K and M_{UV} subsamples are found to lie alightly above the relation. As a result, the power-law slopes of the m_K and M_{UV} subsamples become positive as shown in figure C.2. However, they are still shallow. For example, the m_K-divided subsamples give a power-law index of 0.26 ± 0.05, which is more than $2\,\sigma$ shallower than those of the cold stream models in Goerdt et al. (2010) and Rosdahl & Blaizot (2012), ~ 0.38 and ~ 0.75, respectively. This slope is also more than $20\,\sigma$ shallower than that of the satellite star formation model, ~ 1.36. Moreover, the $L(\mathrm{Ly}\alpha)_H$ values of the faint m_K and M_{UV} subsamples also remain higher than predicted from the cold stream models at a $> 10\,\sigma$ level. We conclude that the conclusions obtained in section 6 are robust.

C.3 The fluorescence scenario

Some of the ionizing photons produced in central galaxies are converted to fluorescence Lyα emission due to recombination of neutral hydrogen gas in the CGM. We do not include the fluorescence scenario in the discussion of LAHs (chapter 8), since this scenario has been favored for QSOs' LAHs (e.g., Hennawi & Prochaska, 2013; Cantalupo et al., 2014). Recently, however, the fluorescence emission of star forming LAEs has been discussed with MUSE data (Gallego et al., 2018; Leclercq et al., 2017). In this appendix, we briefly examine this scenario on the basis of the minimum amount of ionizing photons, $N(\mathrm{ion})$ (photon s^{-1}), and hense ξ_{ion}, required to maintain the LAH of LAEs with fluorescence while reproducing the nebular emission of the main bodies.

Our LAEs in a sub region in the SXDS field have been observed with a narrow band targeting Hα emission (Nakajima et al., 2012). The stacked Hα luminosity as a point source is $L(\mathrm{H}\alpha)_{ps,tot} \sim 8.4 \times 10^{41}\,L_\odot$ with dust attenuation correction ($E(B-V) \sim 0.1$ in appendix D.2, Kusakabe et al., 2015). The number of ionizing photons that are produced by star formation and then converted to nebular emission in the LAEs is $N(\mathrm{ion})_{H\alpha,corr} = L(\mathrm{H}\alpha)_{ps,tot}/1.36 \times 10^{-12} \sim 6.1 \times 10^{53}$ photon s^{-1} following Kennicutt (1998).

The LAH luminosity is calculated as $L(\mathrm{Ly}\alpha)_H \sim 2.0 \times 10^{42}\,L_\odot$ from the stacked $L(\mathrm{Ly}\alpha)_{ps} \sim 1.8 \times 10^{42}\,L_\odot$. It is converted to the number of Lyα photons, $N(\mathrm{Ly}\alpha)_{\mathrm{LAH}} = L(\mathrm{Ly}\alpha)_H/h\nu_{\mathrm{Ly}\alpha} \sim 1.3 \times 10^{53}$ photon s^{-1} with the Planck constant (h) and the frequency of Lyα ($\nu_{\mathrm{Ly}\alpha}$). The fraction of recombinations which results in Lyα photons in the optically thick case (case B) is $\eta_{\mathrm{thick}} = 0.66$, which is larger than the fraction for the optically thin limit, $\eta_{\mathrm{thin}} = 0.42$ (e.g., Osterbrock & Ferland, 2006; Hennawi & Prochaska, 2013). The minimum number of ionizing photons that escape from the ISM to the CGM required to maintain the observed LAHs is $N(\mathrm{ion})_{\mathrm{LAH}} = N(\mathrm{Ly}\alpha)_{\mathrm{LAH}}/\eta_{\mathrm{thick}} \sim 1.8 \times 10^{53}$ photon s^{-1}. It is notable that the LAH luminosity (surface brightness, more accurately) is independent

of the luminosity of ionizing radiation in the highly-ionized, optical thin regime (Hennawi & Prochaska, 2013) which requires larger number of $N(\mathrm{ion})_{\mathrm{LAH}}$ than that in optically thick case at a fixed hydrogen gas distribution. Ionizing radiation is attenuated by dust in the ISM before escaping out to the CGM. The dust-attenuation corrected $N(\mathrm{ion})_{\mathrm{LAH}}$, $N(\mathrm{ion})_{\mathrm{LAH,corr}}$, is estimated roughly to be 1.1×10^{54} photon s^{-1} with an underestimated correction with $\kappa \sim 20$ from the SMC-like attenuation curve at ~ 1000Å (> 912 Å). This part gives the largest uncertainty in the whole calculation.

The minimum value of the intrinsic $N(\mathrm{ion})$ produced in the galaxy is $N(\mathrm{ion})_{H\alpha,corr} + N(\mathrm{ion})_{\mathrm{LAH,corr}} \sim 1.8 \times 10^{54}$ photon s^{-1}. Here, we do not consider ionizing photons escaping out to the IGM, although LAEs (at $z \sim 3$) are found to have high escape fractions of ~ 10–30% (e.g., Nestor et al., 2013; Fletcher et al., 2018).

Our LAEs are estimated to have the total $SFR = 5.7\,M_{\odot}\mathrm{yr}^{-1}$ on average from SED fitting in appendix D.2 (Kusakabe et al., 2015) and to have $EW_{0,ps}(\mathrm{Ly}\alpha) \sim 60$Å (Nakajima et al., 2012). With the fiducial ξ_{ion} value of $\sim 1.3 \times 10^{25}$ Hz erg^{-1} (Kennicutt, 1998; Sobral & Matthee, 2018), this SFR is converted into $N(\mathrm{ion}) \sim 5.3 \times 10^{53}$ photon s^{-1}, which is three times lower than the minimum required value obtained above. In order for $N(\mathrm{ion})$ to reach $\sim 1.8 \times 10^{54}$ photon s^{-1}, ξ_{ion} must be as high as $\sim 4 \times 10^{25}$ Hz erg^{-1}. The minimum value of the required ξ_{ion} is higher than the estimated ξ_{ion} ($\sim 2 \times 10^{25}$ Hz erg^{-1}) for the large-EW LAEs ($EW_{0,ps}(\mathrm{Ly}\alpha) \sim 70$Å) from Sobral & Matthee (2018)'s relation (see section 9.2.4). Note that the required ξ_{ion} is consistent with a high ξ_{ion} estimated for LAEs at $z \sim 3$ in Nakajima et al. (2018a). We can also estimate the minimum value of the escape fraction of ionizing photons from the ISM as $\sim 10\%$ from $N(\mathrm{ion})_{\mathrm{LAH}}/(N(\mathrm{ion})_{\mathrm{LAH,corr}}+N(\mathrm{ion})_{H\alpha,corr})$. This is larger than 2% for LAEs at $z \sim 3.5$ in Gallego et al. (2018).

The fluorescence scenario requires a high ξ_{ion} and a high escape fraction of ionizing photons for the LAEs in subregion of SXDS field with Hα observation even without including ionizing photons escaping out to the IGM. However, we can not exclude the fluorescence scenario completely because of the lack of direct observations of ξ_{ion} and a high escape fraction of ionizing photons. Further observational and theoretical studies are required to examine the fluorescence scenario for star forming galaxies.

Appendix D

SF mode

D.1 SFMS based on the IRX-β relation with the Calzetti curve

In the discussion of the star formation mode of LAEs at $z \sim 2$ in section 6.3, we derive the average SFR of our LAEs using SED fitting with an SMC-like curve, while Hagen et al. (2016) and Shimakawa et al. (2017) derive SFRs using the $IRX - \beta$ relation with the Calzetti curve. For a fair comparison, figure D.1(c) shows our results with the $IRX - \beta$ relation with the Calzetti curve (Meurer et al., 1999). We find our LAEs to have higher sSFRs similar to LAEs in Hagen et al. (2016). Note that the selections of these three samples are different as described in section 6.3. We also compare our results with those by the three different methods discussed in appendix A.1 in figures D.1(a) and (b).

D.2 SFMS based on SED fitting with the Calzetti curve

We also compare results of star formation mode using LAE sample with NB observations of Hα emission in Nakajima et al. (2012). We correct dust attenuation of SFR derived from Hα emission using the A_{1600} obtained by the SED fitting with an SMC-like curve and the Calzetti curve, respectively. The obtained dust-attenuation corrected SFRs ($SFR_{H\alpha,corr}$) for an SMC-like curve and the Calzetti curve are shown in figure D.2. We confirm that the star formation mode of the LAEs is misunderstood as star burst with the Calzetti curve even we use Hα emission, which is a more robust estimator of SFR than UV. This procedure supports our results of their star formation mode.

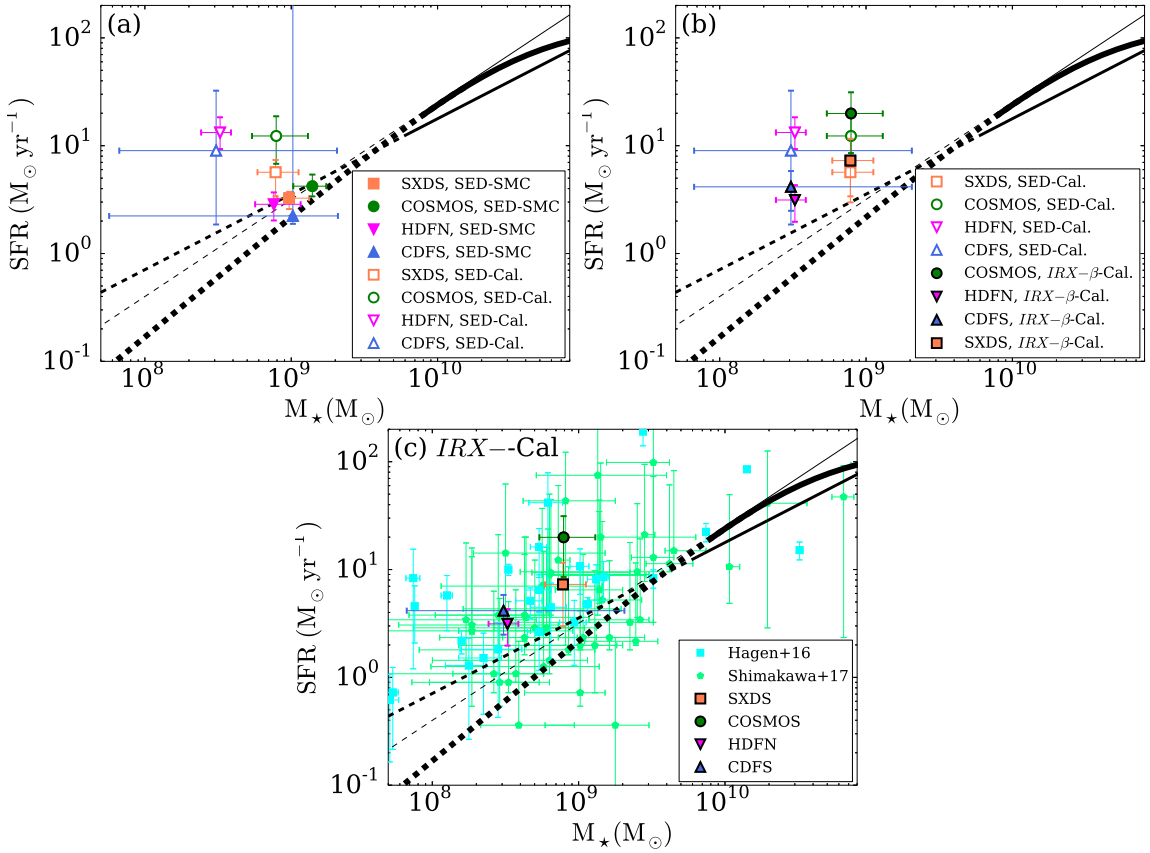

Figure D.1 SFR plotted against $M_\star$. Panels (a) and (b) compare different SFR calculation methods for our LAEs; in panel (a) $SFRs$ calculated from SED fitting with two different attenuation curves are compared; in panel (b) $SFRs$ from SED fitting are compared with those from the $IRX - \beta$ relation, where the Calzetti curve is used in both calculations. Panel (c) uses the $IRX - \beta$ relation with the Calzetti curve and compares our LAEs with Hagen et al. (2016)'s and Shimakawa et al. (2017)'s. In panel (a), orange squares, green circles, magenta inverted triangles, and blue triangles represent stacked LAEs with $NB387_{\rm tot} \leq 25.5$ mag in SXDS, COSMOS, HDFN, and CDFS fields, respectively; filled and open symbols are for an SMC-like curve and the Calzetti curve, respectively. In panel (b), encircled symbols indicate that $SFRs$ are derived from the $IRX - \beta$ relation with the Calzetti curve (Meurer et al., 1999). In panel (c), cyan squares and light green pentagons show individual LAEs at $z \sim 2$ in Hagen et al. (2016) and Shimakawa et al. (2017), respectively; in both studies, $SFRs$ are derived from the $IRX - \beta$ relation with the Calzetti curve (Meurer et al., 1999). Our results based on the $IRX - \beta$ relation with the Calzetti curve are also plotted (encircled symbols). In all panels, several SFMS measurements in previous studies are shown by black lines in the same manner as figure 6.9. All data are rescaled to a Salpeter IMF according to footnote *1.

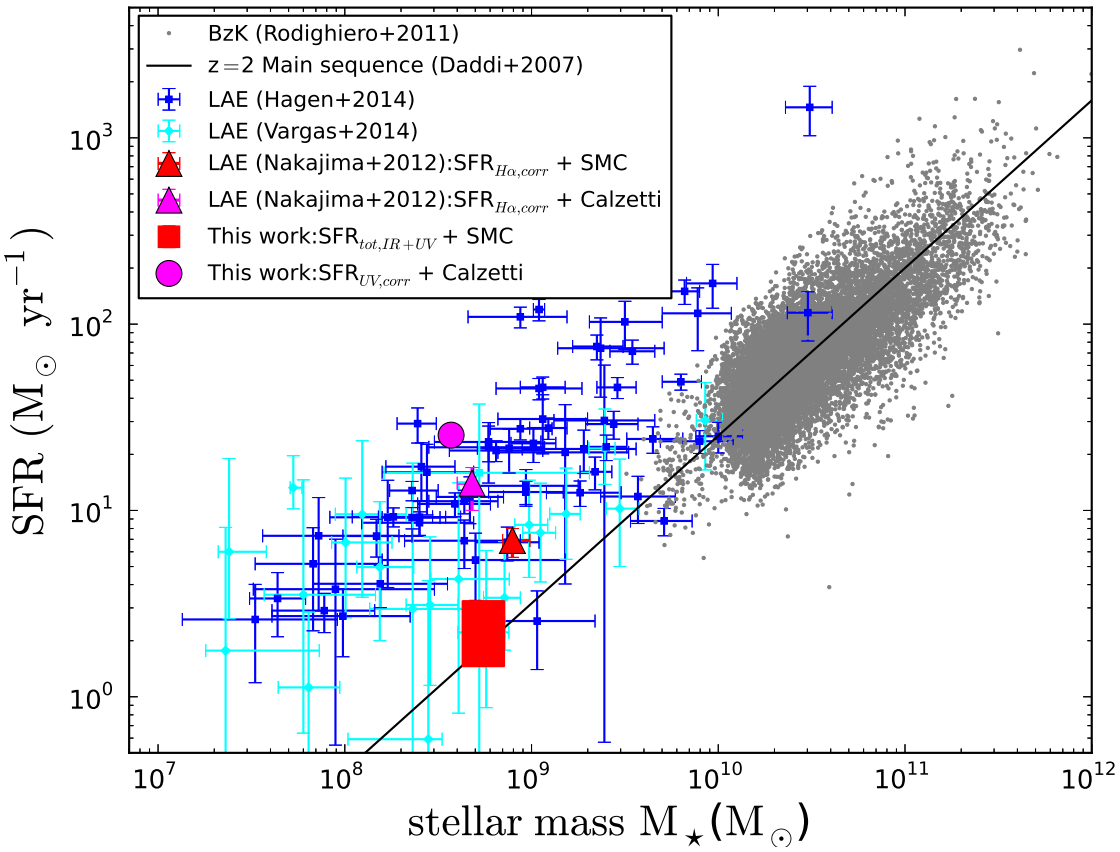

Figure D.2 $SFR_{\rm tot}$ plotted against M$_\star$. The red rectangular region represents our stacked LAE with $M_\star = 6.3^{+0.8}_{-2.0}$ $M_\odot$ from an SMC-like curve and $SFR_{\rm tot,IR+UV}$= 1.5–3.3 $M_\odot$ yr^{-1}, while the magenta filled circle corresponds to the result from the SED fitting with the Calzetti curve (SFR =$SFR_{\rm UV,corr}$). The red and magenta triangles represent LAE from Nakajima et al. (2012), calculated from SFR$_{H\alpha,corr}$ using the A_{1600} obtained by the SED fitting with an SMC-like curve and the Calzetti curve, respectively. The black line shows the star formation main sequence at $z = 2$ (Daddi et al., 2007) and the gray dots represent BzK galaxies (Rodighiero et al., 2011). The blue and cyan dots are for LAEs given in Hagen et al. (2014) and Vargas et al. (2014), respectively; for both samples the Calzetti curve has been used to derive A_{1600}.

Appendix E

The evolution of LAE fraction

The redshift evolution of LAE fraction among galaxies, X(LAE), has been used to probe the evolution of the HI gas fraction of the IGM at the end of reionization. X(LAE) has been found to increase from $z = 3$ to 6, and to decrease at $z > 6$ (e.g., Stark et al., 2010, 2011; Pentericci et al., 2011; Tilvi et al., 2014; Schenker et al., 2014; Arrabal Haro et al., 2018). However, uncertainties in the measurement and interpretation of X(LAE) are still matters of debate (e.g., Stark et al., 2011; Garel et al., 2015; Caruana et al., 2018; De Barros et al., 2017, see also Jung et al. 2018). In this appendix, we show X(LAE) using optical IFU spectroscopic data of VLT/MUSE in the HUDF survey (Bacon et al., 2017). The broad wavelength coverage and the wide FoV IFU of MUSE as well as the unprecedented depth of MUSE-HUDF data allow us to obtain the most homogeneous and complete sample of LAEs at $z = 2.9$–6.6 compared with any other earlier studies (~ 700 LAEs, Inami et al., 2017), which reaches as faint as UV magnitude, M_{1500}, of -17.75 mag. We construct a UV-selected galaxy sample from a HST catalog (Rafelski et al., 2015), and evaluate the redshift evolution of X(LAE) as a function of M_{1500}. In section 9.1, we compare the LAE fraction at $z \sim 2$ derived from our NB-selected LAEs with those at $z \sim 3$–6 derived from MUSE-selected LAEs.

E.1 Data and sample construction

We use a continuum-selected catalog in Rafelski et al. (2015) for constructing parent sample with photometric redshift, z_p, from 2.91 to 6.12.

We show the distribution of z_p and M_{1500} of our sample in figure E.1. Their UV magnitude is derived from two or three HST bands in Rafelski et al. (2015). We fit a power law spectrum with UV continuum slope β and flux density at $\lambda = 1500$Å, $f_{\nu,\lambda=1500}$,

$$f_\nu = f_{\nu,\lambda=1500} \left(\frac{\lambda}{1500} \right)^{\beta+2}, \tag{E.1}$$

where f_ν is flux density and then convert f_ν to M_{1500} (mag) as follows:

$$M_{1500} = -2.5 \log (f_{\nu,\lambda=1500}) - 48.6 - 5 \log (d_{\rm L}/10{\rm pc}) + 2.5 \log (1 + z_{\rm p}), \tag{E.2}$$

where $d_{\rm L}$ and $z_{\rm p}$ are luminosity distance and photometric redshift, respectively. We chose passbands following in Hashimoto et al. (2017b) so that Lyα emission and IGM absorption

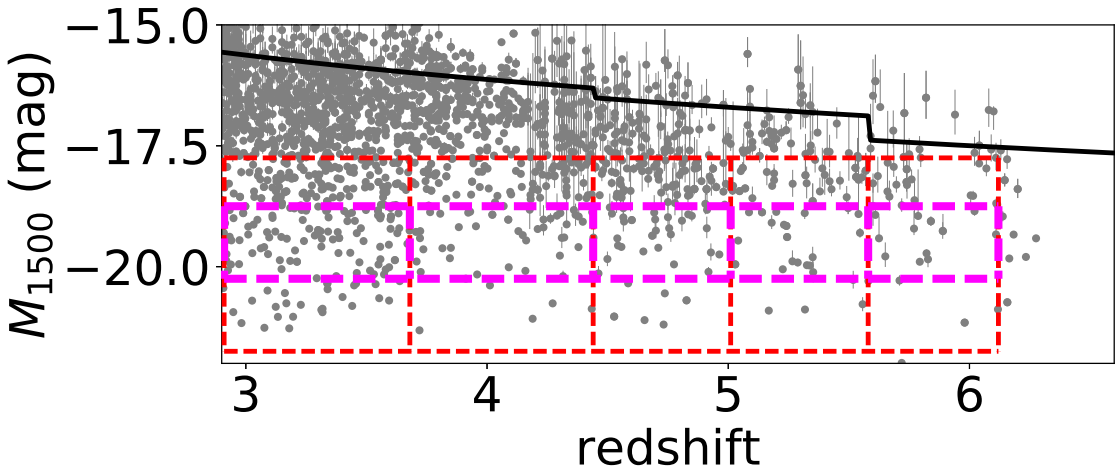

Figure E.1 M_{1500} of our sample and the limiting magnitude of M_{1500} as a function of z_p. Grey circles indicate the sample at $z_p = 2.91$–6.12 in Rafelski et al. (2015). A black solid line, red dashed line, and magenta thick dashed line represent M_{1500} limit cut, M_{1500} range for investigating the evolution of X(LAE), M_{1500} range for comparing our X(LAE) with those in previous studies, corresponding to "faint sample" in Stark et al. (2011).

are not included in the photometry: HST/F775W, F850LP, and F105W are used for objects at $2.91 \leq z \leq 4.44$; F105W, F125W, and F140W are used for objects at $4.44 < z \leq 5.58$; F125W, F140W, and F160W are used for objects at $5.58 < z \leq 6.12$.

We adopt M_{1500} limit cut to our HST sample so that objects are detected at least two HST bands among the rest-frame UV HST bands with $S/N > 2$. The sample is divided into subsample in accordance with M_{1500} and z with criteria shown in table E.1. We derive the number of galaxies $N_{1500}(z_p, M_{1500})$ based on photometric redshift. Each derived subsample is contaminated by sources whose photometric redshifts are misunderstood to be in a given range of z and does not include sources in the redshift range that have wrong photometric redshifts. We include such uncertainties of $N_{1500}(z_p, M_{1500})$ into uncertainties of X(Lyα) later. In figure E.2, we show the histogram of UV magnitude distribution, and find that our sample is more complete compared with that of previous work in Stark et al. (2011) and roughly comparable with that estimated from UV luminosity functions (Bouwens et al., 2015).

We detect Lyα emission line from 1D spectra, which are convolved with HST segmentation map and MUSE PSF following Inami et al. (2017) using a software, updated version of MARZ (Hinton et al., 2016). We cut out a small datacube for each object from a preliminary version of MUSE datacube DR2 instead of public released DR1, and then create a 1D spectrum as an input file. It is notable that we do not include Lyα halo in this procedure because of the HST segmentation map. Then we use automatic spectral fitting of MARZ with LAE templates (optical SED templates with Lyα emission) as a detector. It gives us redshift, MARZ's quality flag (QOP) and type of objects (TYPE). We only include objects with QOP more than 1 (i.e., more than 95% confidence) and TYPE of

Table E.1 Subsample criteria.

z range	mean z	M_{1500} range	sample size
$2.91 < z \leq 3.68$	3.30	$-21.75 < M_{1500} \leq -17.75$	247
$3.68 < z \leq 4.44$	4.06	$-21.75 < M_{1500} \leq -17.75$	131
$4.44 < z \leq 5.01$	4.73	$-21.75 < M_{1500} \leq -17.75$	105
$5.01 < z \leq 5.58$	5.30	$-21.75 < M_{1500} \leq -17.75$	53
$5.58 < z \leq 6.12$	5.85	$-21.75 < M_{1500} \leq -17.75$	37
$2.91 < z \leq 4.44$	3.30	$-20.25 < M_{1500} \leq -18.75$	143
$4.44 < z \leq 5.58$	5.01	$-20.25 < M_{1500} \leq -18.75$	58
$5.58 < z \leq 6.12$	5.85	$-20.25 < M_{1500} \leq -18.75$	13

Note. — Subsample criteria of redshift and M_{1500} for parent sample. The mean redshift and sample size are also shown.

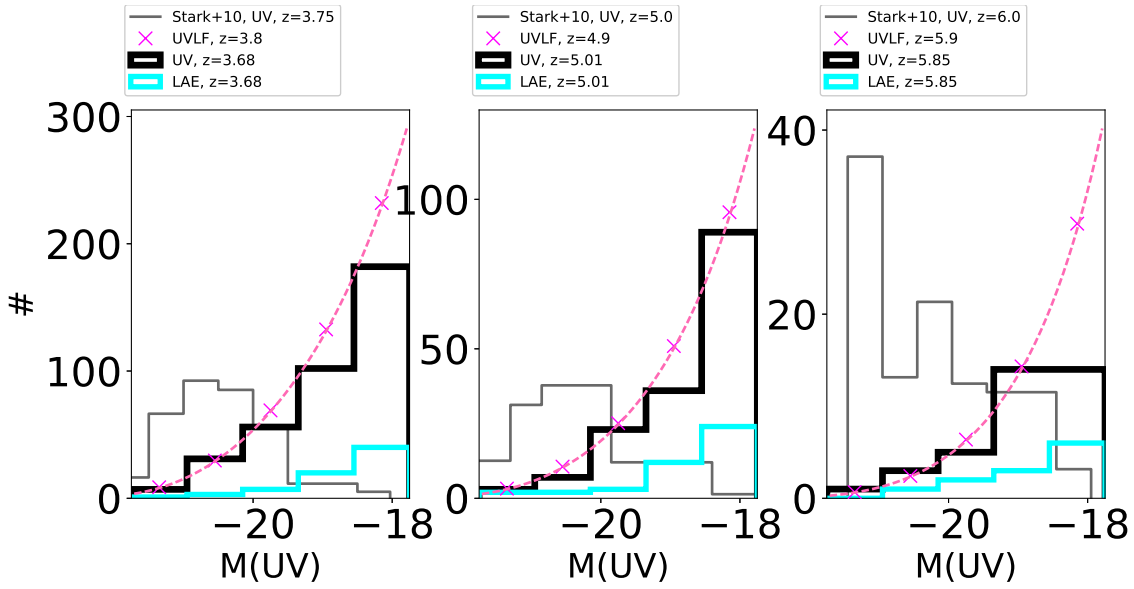

Figure E.2 Histograms of M_{1500} for our subsamples at $z \sim 3.7$ (2.91–4.44), 5.0 (4.44–5.58), and 5.9 (5.58–6.12). Thick black and cyan solid lines represent the number of our parent UV sample and our LAEs with EW(Lyα)$>$ 25 Å respectively. Thin gray solid and magenta dotted lines show the number of the sample in Stark et al. (2011) and the number of the sample expected from UV luminosity function in Bouwens et al. (2015) for our UV parent sample.

6 (LAEs) as LAE candidates. We than remove contaminants using visual inspection of spectrum, UV color (dropout), photometric redshift, and images to construct LAE sample among photo-z parent sample. We then measure Lyα flux of each LAE using PLATEFIT (multiple Gaussian fitting code) in Inami et al. (2017). Rest-frame EW of Lyα emission is derived from Lyα flux and M_{1500}.

E.2 Calculation of X(LAE)

Lyα emitter fraction is defined as:

$$X(\mathrm{LAE}) = \frac{N_{\mathrm{LAE}}^{\mathrm{corr}}(z_s = z,\, M_{1500},\, EW)}{N_{1500}(z_p = z,\, M_{1500})}, \tag{E.3}$$

where $N_{1500}(z_p = z,\, M_{1500})$ and $N_{\mathrm{LAE}}^{\mathrm{corr}}(z_s = z,\, M_{1500},\, EW)$ are the number of galaxies with a given range of M_{1500} and z, and the number of LAEs among them with a given range of EW, respectively. To derive X(LAE) accurately, we correct completeness of spectroscopic observation of Lyα emission as described below.

We add fake Lyα emission to 1D spectrum which does not have clear spectroscopic features in the procedure above and extract the fake emission using MARZ in the same manner as that for true sources. We generate 40 fake Lyα profile per each wavelength pixel with three parameters, flux of Lyα emission, total FWHM, and FWHM ratio of red wing to blue wing of spectra. The later two are drawn randomly from measured profiles of Lyα emission in Bacon et al. (2015) and Hashimoto et al. (2017b). Completeness in each of the two fields (udf-10 and the other part of mosaic) for a given Lyα flux (f) and redshift, $C_z(f)$, is calculated as:

$$C_z(f) = \frac{N_{\mathrm{det,\,fake\,Ly}\alpha\mathrm{,\,f,\,z_s=z}}}{N_{\mathrm{fake\,Ly}\alpha\mathrm{,\,f,\,z_s=z}}}, \tag{E.4}$$

where $N_{\mathrm{det,\,fake\,Ly}\alpha\mathrm{,\,f,\,z_s=z}}$ and $N_{\mathrm{fake\,Ly}\alpha\mathrm{,\,f,\,z_s=z}}$ are the number of detected fake Lyα emission and the number of fake Lyα emission, respectively. We fit an S/N normalized $C_z(f)$ with an error function (e.g., Rykoff et al., 2015) and compute the redshift-bin-averaged completeness, $C_z^{\mathrm{bf,av}}(S/N)$. We convert $C_z^{\mathrm{bf,av}}(S/N)$ to completeness as a function of flux $C_z^{\mathrm{bf,av}}(f)$ for each flux. We correct the number of LAEs using $C_z^{\mathrm{bf,av}}(f)$.

The uncertainties of X(LAE) arise from three component: uncertainty due to contaminants and missed objects in $N_{1500}(z_p = z,\, M_{1500})$, the Poisson error for $N_{1500}(z_p = z,\, M_{1500})$, uncertainty due to completeness correction of $N_{\mathrm{LAE}}^{\mathrm{corr}}(z_s = z,\, M_{1500},\, EW)$, and the Poisson error of $N_{\mathrm{LAE}}^{\mathrm{corr}}(z_s = z,\, M_{1500},\, EW)$. We estimate the relative uncertainty of X(LAE) from error propagation.

The fraction of objects whose z_{p} is different from the true redshift more than 15 % is estimated to be $\sim$ 10% in Brinchmann et al. (2017). We assume that both of the ratio of contaminants and missed objects among the UV sample is 10% and the relative uncertainty of the two error is $\sqrt{2 \times 0.1^2}$. The Poisson error of $N_{1500}(z_p = z,\, M_{1500})$ and $N_{\mathrm{LAE}}^{\mathrm{corr}}(z_s = z,\, M_{1500},\, EW)$ are basically derived from the square root of the number of objects. In the case of the number of objects is less than 10, we use the values in columns

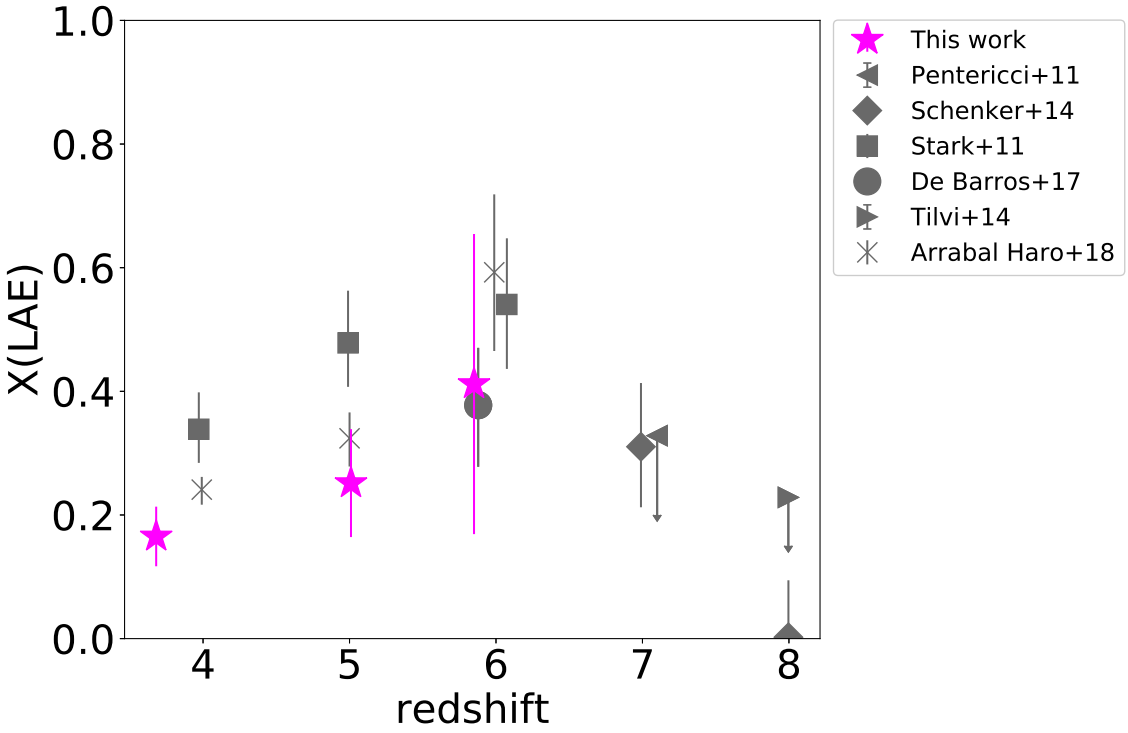

Figure E.3 X(LAE) vs. z with bright M_{1500} (= −20.25– −18.75 mag) and $EW > 25$Å compared with previous results. Our X(LAE) is indicated by a magenta star, while those in Pentericci et al. (2011), Stark et al. (2011), Schenker et al. (2014), Tilvi et al. (2014), De Barros et al. (2017), and Arrabal Haro et al. (2018) are shown by a gray triangle (left), square, diamond, triangle (right), circle, and cross.

in tables 1 and 2 in Gehrels (1986) for the upper and lower limits of the Poisson errors, respectively. The uncertainties of the completeness estimation is ∼ 20% in average. The relative uncertainties of X(LAE), $\frac{\Delta X(\mathrm{LAE})}{X(\mathrm{LAE})}$, is given by the square root of the summed square of the four relative uncertainties.

E.3 Result

E.3.1 Comparison with previous studies

We compare our X(LAE) for $M_{1500} = -20.25$–-18.75 mag at $z = 2.9$–6.1 with those in previous studies (corresponding to the faint sample in Stark et al. (2011) in figure E.3). We confirm the low values from Arrabal Haro et al. (2018) at $z \sim 4$–5 as well as from De Barros et al. (2017) at $z \sim 6$, though the error bars of our sample at $z \sim 6$ is large. Our X(LAE) is lower than those in Stark et al. (2011) at $z \sim 4$ and ~ 5. It is also found that the slope of X(LAE) is positive to redshift, which is consistent with that in Stark et al. (2011) and Arrabal Haro et al. (2018), not with a plateau slope in Caruana et al. (2018).

The difference in X(LAE) between ours and previous studies possibly arise from (1) different distribution of UV magnitude, (2) different selection bias, and (3) different method

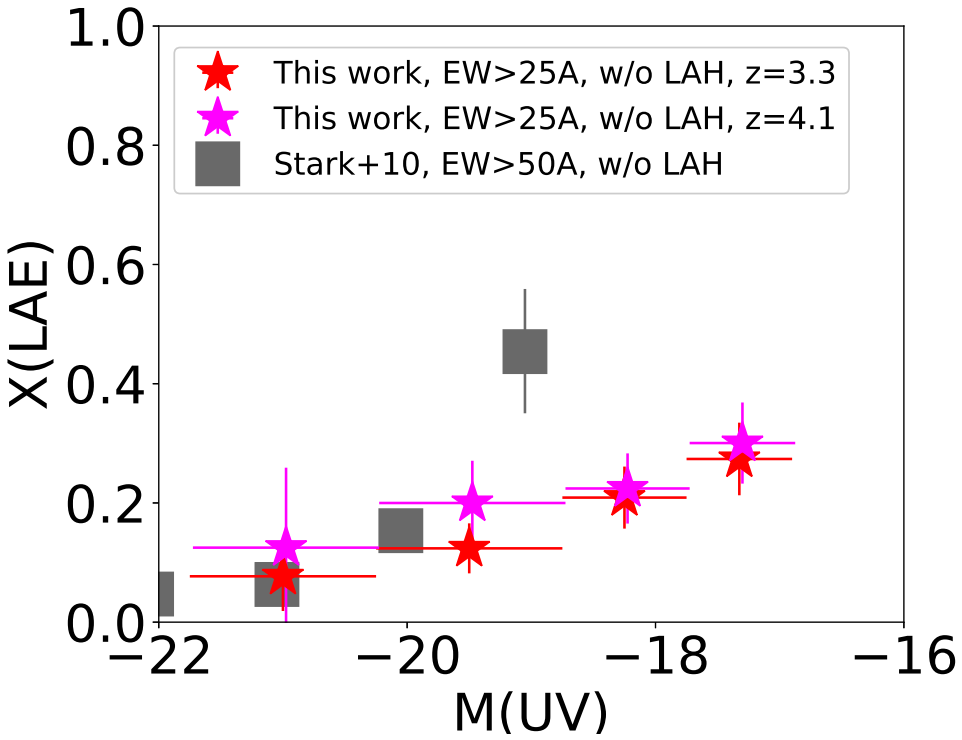

Figure E.4 X(LAE) vs. M_{1500}. Our X(LAE) with $EW > 25$Å at $z \sim 2.9$–3.7 and $z \sim 3.7$–4.4 are indicated by red stars and magenta stars, respectively. The X(LAE) with $EW > 50$Å at $z \sim 3.75$ in Stark et al. (2011) is shown by gray squares.

(including slit loss, aperture correction, and completeness correction). It is generally expected that X(LAE) is higher for UV faint galaxies than that for UV bright galaxies (e.g., Stark et al., 2010). As shown in figure E.4, our X(LAE) for $EW > 25$Å is still lower or similar to those for $EW > 50$Å even at the same UV magnitude. We can exclude the scenario (1) different distribution of UV magnitude. As shown in figure E.2, our photo-z parent sample is suggested to be more complete than that in Stark et al. (2011). The selection bias of Lyman break galaxies is discussed in previous studies (e.g., Inami et al., 2017; De Barros et al., 2017). Existence of strong Lyα emission in a UV spectrum can avoid to be selected by dropout method, when Lyα emission is within a redder band. On the other hand, strong Lyα emission can causes Lyman break less significant, when it is within a bluer band. In addition, the IGM transmission also affect on dropout method (Brinchmann et al., 2017; Inami et al., 2017). Their effect is unclear, and we can not exclude the scenario (2) selection bias. With regard to (3), Lyα emission of our sample is measured by IFU (without including Lyα halo) and less affected by uncertainties due to slit loss, slit-loss correction, and aperture correction. Completeness correction for our sample is expected to be measured more accurately, since our photo-z sample is less affected by the selection bias of dropout method as described above. Consequently, the cause of the difference in X(LAE) is suggested to be (2) different selection bias, and (3) different method. Thanks to the MUSE observations and the HST photo-z sample, our X(LAE) is probably derived from the most homogeneous and complete sample.

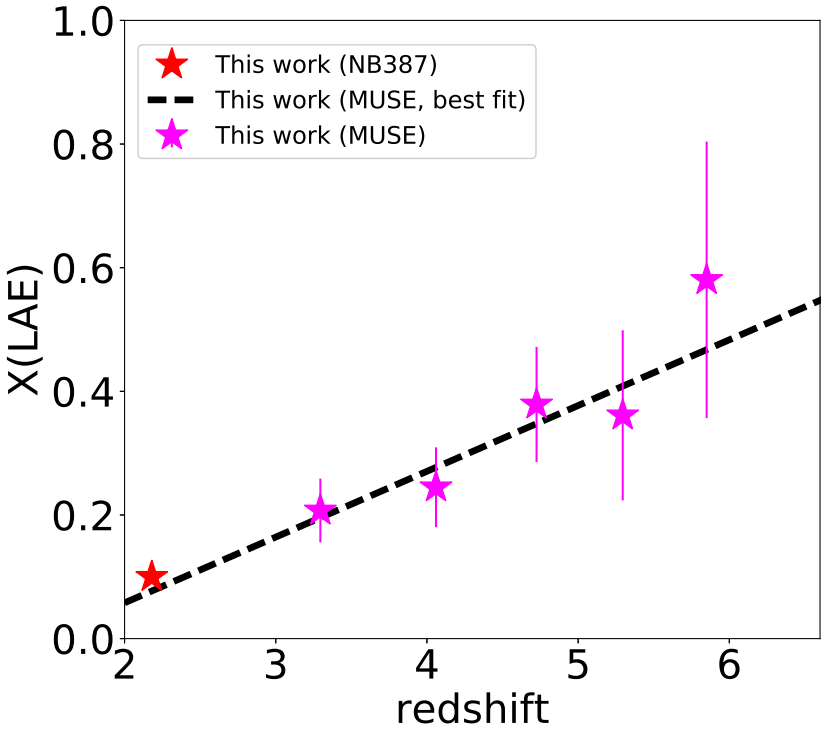

Figure E.5 X(LAE) vs. z with $M_{1500} = -21.75$– -17.75 mag. The X(LAE) derived from MUSE data at $z \sim 3$–6 and that derived from $NB387$-selected LAEs at $z \sim 2$ are indicated by magenta stars and a red star, respectively. The best fit relation of X(LAE) is shown by a black dashed line: $X(\mathrm{LAE}) = 0.11\mathrm{z} - 0.15$ (at $z \sim 3$–6).

E.3.2 The evolution of X(LAE)

We derive the redshift evolution of X(LAE) with $EW > 25$Å from $M_{1500} = -21.75$ mag to a faint UV magnitude, -17.75 mag, which is similar to our LAE sample and has never been reached by previous work. We find a gentle rise of$X$(LAE) from $z \sim 3$ to 6 as well as those with $M_{1500} = -20.25$– -18.75 mag as shown in figure E.5. The X(LAE) for $M_{1500} = -21.75$– -17.75 mag can be fitted well by a linear relation: $X(\mathrm{LAE}) = 0.11\mathrm{z} - 0.15$ at $z \sim 3$–6. We also find that our X(LAE) at $z \sim 2$ derived from $NB387$ follows the evolution of X(LAE) (as described in section 9.1). The result suggests that only $\sim$ 10 % of galaxies within these luminosity (mass) ranges can evolve into LAEs and/or that galaxies within these luminosity (or mass) ranges can experience the LAE phase only for a very short time at $z \sim 2$. The origins of well-known increasing trend of X(LAE) against z ($z < 6$) is still an open question. Accurate measurements of SFR, $M_\star$, M_h, IRX, ξ and Lyα halo of LAEs at a wide range of redshift would give us deeper insights into their origin and their evolution.

Bibliography

Acquaviva, V., Vargas, C., Gawiser, E., & Guaita, L. 2012, The Astrophysical Journal, 751, L26

Aird, J., Coil, A. L., & Georgakakis, A. 2018, Monthly Notices of the Royal Astronomical Society, 474, 1225

Alavi, A., Siana, B., Richard, J., et al. 2014, The Astrophysical Journal, 780, 143

Alexander, D. M., Bauer, F. E., Brandt, W. N., et al. 2003, The Astronomical Journal, 126, 539

Álvarez-Márquez, J., Burgarella, D., Heinis, S., et al. 2016, Astronomy & Astrophysics, 587, A122

Ando, M., Ohta, K., Iwata, I., et al. 2006, The Astrophysical Journal, 645, L9

—. 2007, Publications of the Astronomical Society of Japan, 59, 717

Arrabal Haro, P., Rodríguez Espinosa, J. M., Muñoz-Tuñón, C., et al. 2018, Monthly Notices of the Royal Astronomical Society, 478, 3740

Asano, R. S., Takeuchi, T. T., Hirashita, H., & Inoue, A. K. 2013a, Earth, Planets and Space, 65, 213

Asano, R. S., Takeuchi, T. T., Hirashita, H., & Nozawa, T. 2013b, Monthly Notices of the Royal Astronomical Society, 432, 637

—. 2014, Monthly Notices of the Royal Astronomical Society, 440, 134

Ashby, M. L. N., Willner, S. P., Fazio, G. G., et al. 2013, The Astrophysical Journal, 769, 80

Atek, H., Kunth, D., Hayes, M., Östlin, G., & Mas-Hesse, J. M. 2008, Astronomy and Astrophysics, 488, 491

Atek, H., Kunth, D., Schaerer, D., et al. 2014, Astronomy & Astrophysics, 561, A89

Bacon, R., Brinchmann, J., Richard, J., et al. 2015, Astronomy & Astrophysics, 575, A75

Bacon, R., Conseil, S., Mary, D., et al. 2017, Astronomy & Astrophysics, 608

Barnes, L. A., & Haehnelt, M. G. 2010, Monthly Notices of the Royal Astronomical Society, 403, 870

Behrens, C., & Braun, H. 2014, Astronomy and Astrophysics, 572, A74

Behroozi, P. S., Wechsler, R. H., & Conroy, C. 2013, The Astrophysical Journal, 770, 57

Bielby, R. M., Tummuangpak, P., Shanks, T., et al. 2016, Monthly Notices of the Royal Astronomical Society, 456, 4061

Blanc, G. a., Adams, J. J., Gebhardt, K., et al. 2011, The Astrophysical Journal, 736, 31

Bond, J. R., Cole, S., Efstathiou, G., & Kaiser, N. 1991, The Astrophysical Journal, 379, 440

Bouwens, R. J., Illingworth, G. D., Oesch, P. A., et al. 2015, Astrophysical Journal, 803, 1

Bouwens, R. J., Aravena, M., Decarli, R., et al. 2016, The Astrophysical Journal, 833, 72

Bower, R. G. 1991, MNRAS, 248, 332

Brammer, G. B., van Dokkum, P. G., Franx, M., et al. 2012, The Astrophysical Journal Supplement Series, 200, 13

Bridge, J. S., Hayes, M., Melinder, J., et al. 2017, The Astrophysical Journal, 852, 9

Brinchmann, J., Inami, H., Bacon, R., et al. 2017, Astronomy & Astrophysics, 608, A3

Brocklehurst, M. 1971, MNRAS, 153, 471

Bruzual, G., & Charlot, S. 2003, Monthly Notices of the Royal Astronomical Society, 344, 1000

Buat, V., Noll, S., Burgarella, D., et al. 2012, Astronomy & Astrophysics, 545, A141

Burgarella, D., Buat, V., Gruppioni, C., et al. 2013, Astronomy & Astrophysics, 554, A70

Calzetti, D. 1997, The Astronomical Journal, 113, 162

—. 2001, CHICAGO JOURNAL, 113, 84

Calzetti, D., Armus, L., Bohkin, R., et al. 2000, ApJ, 533, 682

Cantalupo, S., Arrigoni-battaia, F., Prochaska, J. X., Hennawi, J. F., & Madau, P. 2014, Nature, 506, 63

Cantalupo, S., Porciani, C., Lilly, S. J., & Miniati, F. 2005, The Astrophysical Journal, 628, 61

Capak, P., Cowie, L. L., Hu, E. M., et al. 2004, The Astronomical Journal, 127, 180

Capak, P., Aussel, H., Ajiki, M., et al. 2007, The Astrophysical Journal Supplement Series, 172, 99

Cardamone, C. N., van Dokkum, P. G., Urry, C. M., et al. 2010, The Astrophysical Journal Supplement Series, 189, 270

Caruana, J., Wisotzki, L., Herenz, E. C., et al. 2018, Monthly Notices of the Royal Astronomical Society, 473, 30

Chabrier, G., & Chabrier, G. 2003, PASP, 115, 763

Charlot, S., & Fall, S. M. 1993, Astrophysical Journal v.415, 415, 580

Chary, R., & Elbaz, D. 2001, ApJ, 556, 562

Ciardullo, R., Gronwall, C., Wolf, C., et al. 2012, The Astrophysical Journal, 744, 110

Ciardullo, R., Gronwall, C., Adams, J. J., et al. 2013, The Astrophysical Journal, 769, 83

Ciesla, L., Boquien, M., Boselli, A., et al. 2014, A&A, 565, 128

Cochrane, R. K., Best, P. N., Sobral, D., et al. 2018, Monthly Notices of the Royal Astronomical Society, 475, 3730

—. 2017, MNRAS, 469, 2913

Cohn, J. D. 2006, New Astronomy, 11, 226

Cohn, J. D., & Kadota, K. 2005, The Astrophysical Journal, 632, 1

Cowie, L. L., Barger, A. J., & Hu, E. M. 2010, The Astrophysical Journal, 711, 928

Cowie, L. L., & Hu, E. M. 1998, The Astronomical Journal, 115, 1319

Cowie, L. L., Songaila, A., Hu, E. M., & Cohen, J. G. 1996, The Annals of Statistics, 112, 839

Curtis-Lake, E., McLure, R. J., Pearce, H. J., et al. 2012, Monthly Notices of the Royal Astronomical Society, 422, 1425

Daddi, E., Cimatti, a., Renzini, a., et al. 2004, The Astrophysical Journal, 617, 746

Daddi, E., Dickinson, M., Morrison, G., et al. 2007, ApJ, 670, 156

Dale, D. a., Cohen, S. a., Johnson, L. C., et al. 2009, The Astrophysical Journal, 703, 517

Damen, M., Labbé, I., van Dokkum, P. G., et al. 2011, The Astrophysical Journal, 727, 1

de Barros, S., Schaerer, D., & Stark, D. P. 2014, Astronomy & Astrophysics, 563, A81

De Barros, S., Pentericci, L., Vanzella, E., et al. 2017, Astronomy & Astrophysics, 608, A123

Dekel, A., & Birnboim, Y. 2006, Monthly Notices of the Royal Astronomical Society, 368, 2

Dekel, A., Birnboim, Y., Engel, G., et al. 2009a, ArXiv e-prints, ArXiv:0808, 1

—. 2009b, Nature, 457, 451

Dickinson, M., Giavalisco, M., & Team, f. t. G. 2003, Proceedings of the ESO Workshop held in Venice, 324

Diemer, B., & Kravtsov, A. V. 2015, The Astrophysical Journal, 799, 108

Diener, C., Wisotzki, L., Schmidt, K. B., et al. 2017, MNRAS, 471, 3186

Dijkstra, M. 2014, Publications of the Astronomical Society of Australia, 31, arXiv:arXiv:1406.7292v1

Dijkstra, M., & Kramer, R. 2012, Monthly Notices of the Royal Astronomical Society, 424, 1672

Dijkstra, M., & Loeb, A. 2009, Monthly Notices of the Royal Astronomical Society, 400, 1109

Draine, B. T., & Lee, H. 1984, APJ, 285, 89

Draine, B. T., & Li, A. 2007, ApJ, 657, 810

Dressler, A., Martin, C. L., Henry, A., Sawicki, M., & McCarthy, P. 2011, ApJ, 71, arXiv:1104.2900

Drinkwater, M. J., Gregg, M. D., & Colless, M. 2001, The Astrophysical Journal, 548, L139

Dutton, A. A., van den Bosch, F. C., & Dekel, A. 2010, Monthly Notices of the Royal Astronomical Society, 405, 1690

Duval, F., Schaerer, D., Östlin, G., & Laursen, P. 2014, Astronomy & Astrophysics, 562, A52

Eadie, G. M., Harris, W. E., & Widrow, L. M. 2015, The Astrophysical Journal, 806, 54

Efron, B. 1979, The Annals of Statistics, 7, 1

Eisenstein, D. J., & Hu, W. 1998, The Astrophysical Journal, 496, 605

—. 1999, the Astrophysical Journal, 511, 5

Elbaz, D., Daddi, E., Borgne, D. L., et al. 2007, A&A, 468, 33

Elbaz, D., Dickinson, M., Hwang, H. S., et al. 2011, A&A, 533, 119

Elvis, M., Civano, F., Vignali, C., et al. 2009, The Astrophysical Journal Supplement Series, 184, 158

Erb, D. K., Steidel, C. C., Shapley, A. E., et al. 2006, The Astrophysical Journal, 647,

128
Erb, D. K., Steidel, C. C., Trainor, R. F., et al. 2014, ApJ, 795, 33
Fan, X., Strauss, M. A., Becker, R. H., et al. 2006, The Astronomical Journal, 132, 117
Fardal, M. A., Katz, N., Gardner, J. P., et al. 2001, Astrophysical Journal, 562, 605
Faucher-Giguère, C. A., Kereš, D., Dijkstra, M., Hernquist, L., & Zaldarriaga, M. 2010, Astrophysical Journal, 725, 633
Feldmeier, J. J., Hagen, A., Ciardullo, R., et al. 2013, Astrophysical Journal, 776, 75
Finkelstein, S. L., Rhoads, J. E., Malhotra, S., & Grogin, N. 2009, The Astrophysical Journal, 691, 465
Finkelstein, S. L., Rhoads, J. E., Malhotra, S., Grogin, N., & Wang, J. 2008, ApJ, 678, 655
Fletcher, T. J., Robertson, B. E., Nakajima, K., et al. 2018, arXiv:, 1806.01741, arXiv:1806.01741
Fudamoto, Y., Oesch, P. A., Schinnerer, E., et al. 2017, MNRAS, 472, 483
Furlanetto, S. R., Schaye, J., Springel, V., & Hernquist, L. 2005, The Astrophysical Journal, 622, 7
Furusawa, H., Kosugi, G., Akiyama, M., et al. 2008, ApJs, 176, 1
Gallego, S. G., Cantalupo, S., Lilly, S., et al. 2018, Monthly Notices of the Royal Astronomical Society, 475, 3854
Galliano, F. 2011, EAS Publications Series, 46, 43
Garel, T., Blaizot, J., Guiderdoni, B., et al. 2015, Monthly Notices of the Royal Astronomical Society, 450, 1279
Gawiser, E., van Dokkum, P. G., Gronwall, C., et al. 2006, The Astrophysical Journal, 642, L13
Gawiser, E., Francke, H., Lai, K., et al. 2007, ApJ, 671, 278
Gehrels, N. 1986, The Astrophysical Journal, 303, 336
Giacconi, R., Rosati, P., & Tozzi, P. 2001, The Astrophysical Journal, 551, 624
Giallongo, E., Grazian, A., Fiore, F., et al. 2015, Astronomy & Astrophysics, 578, A83
Giavalisco, M., Ferguson, H. C., Koekemoer, A. M., et al. 2004, ApJ, 600, 93
Goerdt, T., Dekel, A., Sternberg, A., et al. 2010, Monthly Notices of the Royal Astronomical Society, 407, 613
Gordon, K. D., Clayton, G. C., Misselt, K. A., Landolt, A. U., & Wolff, M. J. 2003, ApJ, 594, 279
Goto, T., Utsumi, Y., Furusawa, H., Miyazaki, S., & Komiyama, Y. 2009, Monthly Notices of the Royal Astronomical Society, 400, 843
Grogin, N. a., Kocevski, D. D., Faber, S. M., et al. 2011, The Astrophysical Journal Supplement Series, 197, 35
Gronwall, C., Ciardullo, R., Hickey, T., et al. 2007, The Astrophysical Journal, 667, 79
Guaita, L., Gawiser, E., Padilla, N., et al. 2010, The Astrophysical Journal, 714, 255
Guaita, L., Acquaviva, V., Padilla, N., et al. 2011, The Astrophysical Journal, 733, 114
Guaita, L., Talia, M., Pentericci, L., et al. 2017, Astronomy & Astrophysics, 606, A19
Gunn, J. E., & Peterson, B. A. 1965, The Astrophysical Journal, 142, 1633

Gunn, J. E., & Stryker, L. L. 1983, Astrophysical Journal Supplement Series, 52, 121
Hagen, A., Ciardullo, R., Gronwall, C., et al. 2014, The Astrophysical Journal, 786, 59
Hagen, A., Zeimann, G. R., Behrens, C., et al. 2016, The Astrophysical Journal, 817, 79
Hagen, L. M. Z., Siegel, M. H., Hoversten, E. A., et al. 2017, MNRA, 466, 4540
Haiman, Z., Spaans, M., & Quataert, E. 2000, Astrophysical Journal, 537, L5
Hamana, T., Yamada, T., Ouchi, M., Iwata, I., & Kodama, T. 2006, MNRAS, 1938, 1929
Hansen, M., & Peng Oh, S. 2006, Monthly Notices of the Royal Astronomical Society, 367, 979
Harikane, Y., Ouchi, M., Ono, Y., et al. 2016, The Astrophysical Journal, 821, 123
Harikane, Y., Ouchi, M., Shibuya, T., et al. 2018, The Astrophysical Journal, 859, 84
Harris, J., & Zaritsky, D. 2009, The Astronomical Journal, 138, 1243
Hashimoto, T., Ouchi, M., Shimasaku, K., et al. 2013, The Astrophysical Journal, 765, 70
Hashimoto, T., Verhamme, A., Ouchi, M., et al. 2015, The Astrophysical Journal, 812, 157
Hashimoto, T., Ouchi, M., Shimasaku, K., et al. 2017a, MNRAS, 465, 1543
Hashimoto, T., Garel, T., Guiderdoni, B., et al. 2017b, Astronomy & Astrophysics, 608, A10
Hathi, N. P., Fevre, O. L., & Team, t. V. 2016, A&A, 588, A26
Hayashino, T., Matsuda, Y., Tamura, H., et al. 2004, The Astrophysical Journal Letters, 128, 2073
Hayes, M., Östlin, G., Mas-Hesse, J., et al. 2005, Astronomy and Astrophysics, 438, 71
Hayes, M., Schaerer, D., Östlin, G., et al. 2011, The Astrophysical Journal, 730, 8
Hayes, M., Östlin, G., Schaerer, D., et al. 2010, Nature, 464, 562
—. 2013, The Astrophysical Journal, 765, L27
Hayes, M., Östlin, G., Duval, F., et al. 2014, ApJ, 782, 6
Heckman, T. T. M., & Best, P. N. P. 2014, Annual Review of Astronomy and Astrophysics, 52, 589
Heinis, S., Buat, V., Béthermin, M., et al. 2014, Monthly Notices of the Royal Astronomical Society, 437, 1268
Hennawi, J. F., & Prochaska, J. X. 2013, The Astrophysical Journal, 766, 58
Hildebrandt, H., Erben, T., Dietrich, J., et al. 2006, A&A, 452, 1121
Hinton, S. R., Davis, T. M., Lidman, C., Glazebrook, K., & Lewis, G. F. 2016, Astronomy and Computing, 15, 61
Hirashita, H., & Kobayashi, H. 2013, Earth, Planets and Space, 65, 1083
Hirashita, H., & Yan, H. 2009, Monthly Notices of the Royal Astronomical Society, 394, 1061
Hopkins, A. M., & Beacom, J. F. 2006, The Astrophysical Journal, 651, 142
Hopkins, P. F., Richards, G. T., & Hernquist, L. 2007, The Astrophysical Journal, 654, 731
Hsieh, B. B.-C., Wang, W.-H. W., Yan, H., et al. 2012, ApJs, 203, 23
Hsu, L.-T., Lin, L., Dickinson, M., et al. 2019, arXiv, 1901.00013, arXiv:1901.00013

Hu, E. M., Cowie, L. L., Barger, A. J., et al. 2010, The Astrophysical Journal, 725, 394
Hu, E. M., & McMahon, R. G. 1996, Nature, 382, 231
Hubble, E. P. 1936, ealm of the Nebulae (New Haven: Yale University Press)
Inami, H., Bacon, R., Brinchmann, J., et al. 2017, Astronomy & Astrophysics, 608, A2
Ishikawa, S. 2017, PhD thesis, SOKENDAI (The Graduate University for Advanced Studies)
Ishikawa, S., Kashikawa, N., Hamana, T., Toshikawa, J., & Onoue, M. 2016, Monthly Notices of the Royal Astronomical Society, 458, 747
Itoh, R., Ouchi, M., Zhang, H., et al. 2018, The Astrophysical Journal, 867, 46
Jung, I., Finkelstein, S. L., Livermore, R. C., et al. 2018, The Astrophysical Journal, 864, 103
Kafle, P. R., Sharma, S., Lewis, G. F., & Bland-Hawthorn, J. 2014, ApJ, 794, 59
Karman, W., Caputi, K. I., Caminha, G. B., et al. 2017, A&A, 599, A28
Kashikawa, N., Shimasaku, K., Malkan, M. A., et al. 2006, ApJ, 2, 7
Kashikawa, N., Shimasaku, K., Matsuda, Y., et al. 2011, ApJ, 734, 119
Kashino, D., Silverman, J. D., Rodighiero, G., et al. 2013, The Astrophysical Journal, 777, L8
Kashino, D., More, S., Silverman, J. D., et al. 2017, The Astrophysical Journal, 843, 138
Keel, W. C., Cohen, S. H., Windhorst, R. A., & Waddington, I. 1999, The Astrophysical Journal Letters, 118, 2547
Kennicutt, R. C. 1998, STAR FORMATION IN GALAXIES ALONG THE HUBBLE SEQUENCE
Kennicutt, R. C., & Evans, N. J. 2012, Annual Review of Astronomy and Astrophysics, 50, 531
Kereš, D., Katz, N., Weinberg, D. H., & Davé, R. 2005, Monthly Notices of the Royal Astronomical Society, 363, 2
Khostovan, A. A., Sobral, D., Mobasher, B., et al. 2018, Monthly Notices of the Royal Astronomical Society, 478, 2999
Kobayashi, M. A. R., Murata, K. L., Koekemoer, A. M., et al. 2016, The Astrophysical Journal, 819, 0
Koekemoer, A. M., Faber, S. M., Ferguson, H. C., et al. 2011, The Astrophysical Journal Supplement Series, 197, 36
Kojima, T., Ouchi, M., Nakajima, K., et al. 2017, PASJ, 69, 44
Kollmeier, J. A., Zheng, Z., Davé, R., et al. 2010, Astrophysical Journal, 708, 1048
Konno, A. 2014, ApJ, 797, 16
Konno, A., Ouchi, M., Nakajima, K., et al. 2016, The Astrophysical Journal, 823, 20
Konno, A., Ouchi, M., Shibuya, T., et al. 2018, Publications of the Astronomical Society of Japan, 70, arXiv:1705.01222
Koprowski, M. P., Coppin, K. E., Geach, J. E., et al. 2018, Monthly Notices of the Royal Astronomical Society, 479, 4355
Kornei, K. a., Shapley, A. E., Erb, D. K., et al. 2010, The Astrophysical Journal, 711, 693
Kovač, K., Somerville, R. S., Rhoads, J. E., Malhotra, S., & Wang, J. 2007, The Astro-

physical Journal, 668, 15
Koyama, Y., Shimakawa, R., Yamamura, I., Kodama, T., & Hayashi, M. 2018, PASJ, 00, 1
Kroupa, P. 2001, Monthly Notices of the Royal Astronomical Society, 322, 231
Kubo, J. M., Stebbins, A., Annis, J., et al. 2007, The Astrophysical Journal, 671, 1466
Kunth, D., Leitherer, C., Mas-Hesse, J. M., Östlin, G., & Petrosian, A. 2003, The Astrophysical Journal, 597, 263
Kunth, D., Mas-Hesse, J. M., Terlevich, E., et al. 1998, Astronomy and Astrophysics, 334, 11
Kurk, J., Cimatti, A., Daddi, E., et al. 2013, A&A, 549, 63
Kusakabe, H., Shimasaku, K., Nakajima, K., & Ouchi, M. 2015, The Astrophysical Journal, 800, L29
Kusakabe, H., Shimasaku, K., Momose, R., et al. 2018a, arXiv, 1803.10265, 1
Kusakabe, H., Shimasaku, K., Ouchi, M., et al. 2018b, Publications of the Astronomical Society of Japan, 70, 1
Lai, K., Huang, J.-s., Fazio, G., et al. 2008, ApJ, 674, 70
Laigle, C., McCracken, H. J., Ilbert, O., et al. 2016, The Astrophysical Journal Supplement Series, 224, 1
Lake, E., Zheng, Z., Cen, R., et al. 2015, The Astrophysical Journal, 806, 46
Landy, S. D., & Szalay, A. S. 1993, The Astrophysical Journal, 412, 64
Laursen, P., Duval, F., & Östlin, G. 2013, Astrophysical Journal, 766, 124
Laursen, P., & Sommer-Larsen, J. 2007, The Astrophysical Journal, 657, L69
Lawrence, A., Warren, S. J., Almaini, O., et al. 2007, Monthly Notices of the Royal Astronomical Society, 379, 1599
Leclercq, F., Bacon, R., Wisotzki, L., et al. 2017, Astronomy & Astrophysics, 608, A8
Lee, K., Giavalisco, M., Gnedin, O. Y., et al. 2006, The Astrophysical Journal, 642, 63
Leitherer, C., & Heckman, T. M. 1995, The Astrophysical Journal Supplement Series, 96, 9
Lilly, S. J., Carollo, C. M., Pipino, A., Renzini, A., & Peng, Y. 2013, The Astrophysical Journal, 772, 119
Lin, L., Dickinson, M., Jian, H.-y., et al. 2012, The Astrophysical Journal, 756, 71
Livermore, R. C., Finkelstein, S. L., & Lotz, J. M. 2017, The Astrophysical Journal, 835, 113
Lutz, D., Poglitsch, A., Altieri, B., et al. 2011, A&A, 532, 90
Madau, P. 1995, The Astrophysical Journal, 441, 18
Madau, P., & Dickinson, M. 2014, Annual Review of Astronomy and Astrophysics, 52, 415
Madau, P., & Haardt, F. 2015, Astrophysical Journal Letters, 813, L8
Madden, S. C., Rémy-Ruyer, A., Galametz, M., et al. 2013, Publications of the Astronomical Society of the Pacific, 125, 600
Magnelli, B., Elbaz, D., Chary, R. R., et al. 2011, A&A, 528, 35
Magnelli, B., Popesso, P., Berta, S., et al. 2013, A&A, 553, 132

Makiya, R., Enoki, M., Ishiyama, T., et al. 2016, Publications of the Astronomical Society of Japan, 68, 25

Malhotra, S., & Rhoads, J. E. 2002, ApJ, 565, L71

Malhotra, S., Rhoads, J. E., Finkelstein, S. L., et al. 2012, The Astrophysical Journal, 750, L36

Malkan, M. A., Cohen, D. P., Maruyama, M., et al. 2017, The Astrophysical Journal, 850, 5

Mallery, R. P., Mobasher, B., Capak, P., et al. 2012, ApJ, 760, 128

Mas-Ribas, L., & Dijkstra, M. 2016, The Astrophysical Journal, 822, 84

Mas-Ribas, L., Dijkstra, M., Hennawi, J. F., et al. 2017, The Astrophysical Journal, 841, 19

Matsuda, Y., Yamada, T., Hayashino, T., et al. 2011, Monthly Notices of the Royal Astronomical Society: Letters, 410, 13

—. 2012, Monthly Notices of the Royal Astronomical Society, 425, 878

Matsuoka, Y., Strauss, M. A., Kashikawa, N., et al. 2018, arXiv:1811.01963, arXiv:1811.01963

Matthee, J., Sobral, D., Oteo, I., et al. 2016, Monthly Notices of the Royal Astronomical Society, 458, 449

McCracken, H. J., Milvang-Jensen, B., Dunlop, J., et al. 2012, Astronomy & Astrophysics, 544, A156

McGreer, I. D., Mesinger, A., & D'Odorico, V. 2015, Monthly Notices of the Royal Astronomical Society, 447, 499

McLure, R. J., Dunlop, J. S., Cullen, F., et al. 2018, Monthly Notices of the Royal Astronomical Society, 476, 3991

Mehta, V., Scarlata, C., Capak, P., et al. 2018, The Astrophysical Journal Supplement Series, 235, 36

Meurer, G. R., Heckman, T., & Calzetti, D. 1999, ApJ, 521, 64

Miller, N. a., Bonzini, M., Fomalont, E. B., et al. 2013, The Astrophysical Journal Supplement Series, 205, 13

Miyazaki, S., Sekiguchi, M., Imi, K., et al. 1998, in Proc. SPIE, ed. S. D'Odorico, Vol. 3355, 363–374

Miyazaki, S., Komiyama, Y., Nakaya, H., et al. 2012, in Ground-based and Airborne Instrumentation for Astronomy IV. Proceedings of the SPIE, ed. I. S. McLean, S. K. Ramsay, & H. Takami, Vol. 8446, 84460Z

Mo, H. J., Mao, S., & White, S. D. 1998, Monthly Notices of the Royal Astronomical Society, 295, 319

Momose, R., Ouchi, M., Nakajima, K., et al. 2014, MNRAS442, 442, 110

—. 2016, Monthly Notices of the Royal Astronomical Society, 457, 2318

Mori, M., & Umemura, M. 2006, Nature, 440, 644

Moster, B. P., Naab, T., & White, S. D. M. 2013, Monthly Notices of the Royal Astronomical Society, 428, 3121

Moster, B. P., Somerville, R. S., Newman, J. A., & Rix, H.-W. 2011, The Astrophysical

Journal, 731, 113
Moy, E., Barmby, P., Rigopoulou, D., et al. 2003, a&a, 403, 493
Muratov, A. L., Kereš, D., Faucher-Giguère, C. A., et al. 2015, Monthly Notices of the Royal Astronomical Society, 454, 2691
Murray, S., Power, C., & Robotham, A. 2013, Astronomy and Computing, 3, 23
Nagamine, K., Ouchi, M., Springel, V., & Hernquist, L. 2010, Publications of the Astronomical Society of Japan, 62, 1455
Nakajima, K., Ellis, R. S., Iwata, I., et al. 2016, The Astrophysical Journal, 831, L9
Nakajima, K., Fletcher, T., Ellis, R. S., Robertson, B. E., & Iwata, I. 2018a, ArXiv:1801.03085, 13, 1
Nakajima, K., & Ouchi, M. 2014, Monthly Notices of the Royal Astronomical Society, 442, 900
Nakajima, K., Ouchi, M., Shimasaku, K., et al. 2013, The Astrophysical Journal, 769, 3
—. 2012, The Astrophysical Journal, 745, 12
Nakajima, K., Schaerer, D., Le Fèvre, O., et al. 2018b, Astronomy & Astrophysics, 612, A94
Nestor, D. B., Shapley, A. E., Kornei, K. a., Steidel, C. C., & Siana, B. 2013, The Astrophysical Journal, 765, 47
Neufeld, d. A. 1991, ApJ, 370, 85
Nickerson, S., Stinson, G., Couchman, H. M. P., Bailin, J., & Wadsley, J. 2013, Monthly Notices of the Royal Astronomical Society, 429, 452
Niida, M., Nagao, T., Ikeda, H., et al. 2016, The Astrophysical Journal, 832, 1
Nilsson, K. K., & Møller, P. 2009, Astronomy and Astrophysics, 508, L21
Nilsson, K. K., Östlin, G., Møller, P., et al. 2011, A&A, 529, 9
Noeske, K. G., Kassin, S. a., Weiner, B. J., et al. 2007, ApJ, 10, 35
Nonino, M., Dickinson, M., Rosati, P., et al. 2009, The Astrophysical Journal Supplement Series, 183, 244
Norberg, P., Baugh, C. M., Gaztañaga, E., & Croton, D. J. 2009, Monthly Notices of the Royal Astronomical Society, 396, 19
Nordon, R., Lutz, D., Saintonge, a., et al. 2013, The Astrophysical Journal, 762, 125
Nozawa, T., Kozasa, T., Habe, A., et al. 2007, ApJ, 666, 955
Oesch, P. A., Bouwens, R. J., Illingworth, G. D., et al. 2015, Astrophysical Journal, 808, 104
Okamoto, T., Frenk, C. S., Jenkins, A., & Theuns, T. 2010, Monthly Notices of the Royal Astronomical Society, 406, 208
Oke, J. B., & Gunn, J. E. 1983, The Astrophysical Journal, 266, 713
Ono, Y., Shimasaku, K., Dunlop, J., et al. 2010a, The Astrophysical Journal, 724, 1524
Ono, Y., Ouchi, M., Shimasaku, K., et al. 2010b, Monthly Notices of the Royal Astronomical Society, 402, 1580
Osterbrock, D. E., & Ferland, G. J. 2006, Astrophysics of gaseous nebulae and active galactic nuclei
Östlin, G., Hayes, M., Kunth, D., et al. 2009, The Astronomical Journal, 138, 923

Östlin, G., Hayes, M., Duval, F., et al. 2014, The Astrophysical Journal, 797, 11

Ota, K., Iye, M., Kashikawa, N., et al. 2008, Apj, 677, 12

—. 2017, The Astrophysical Journal, 844, 85

Oteo, I., Sobral, D., Ivison, R. J., et al. 2015, Monthly Notices of the Royal Astronomical Society, 452, 2018

Oteo, I., Bongiovanni, A., Cepa, J., et al. 2012, A&A, 541, A65

Ouchi, M., Shimasaku, K., Furusawa, H., et al. 2003, The Astrophysical Journal, 582, 60

Ouchi, M., Shimasaku, K., Okamura, S., et al. 2004, The Astrophysical Journal, 611, 685

Ouchi, M., Hamana, T., Shimasaku, K., et al. 2005, The Astrophysical Journal, 635, L117

Ouchi, M., Shimasaku, K., Akiyama, M., et al. 2008, The Astrophysical Journal Supplement Series, 176, 301

Ouchi, M., Shimasaku, K., Furusawa, H., et al. 2010, The Astrophysical Journal, 723, 869

Ouchi, M., Harikane, Y., Shibuya, T., et al. 2017, arXiv, 00, 1704.07455v1

—. 2018, Publications of the Astronomical Society of Japan, 70, 1

Overzier, R. a., Heckman, T. M., Wang, J., et al. 2011, The Astrophysical Journal, 726, L7

Partridge, R. B., & Peebles, P. J. E. 1967, The Astrophysical Journal, 147, 868

Pascarelle, S. M., Windhorst, R. A., Keel, W. C., & Odewahn, S. C. 1996, Nature, 383, 45

Paulino-Afonso, A., Sobral, D., Ribeiro, B., et al. 2018, Monthly Notices of the Royal Astronomical Society, arXiv:1709.04470

Pei, Y. C. 1992, Astrophysical Journal, 395, 130

Peñarrubia, J., Gómez, F. A., Besla, G., Erkal, D., & Ma, Y. Z. 2016, Monthly Notices of the Royal Astronomical Society: Letters, 456, L54

Pentericci, L., Grazian, A., Scarlata, C., et al. 2010, Astronomy and Astrophysics, 514, A64

Pentericci, L., Fontana, A., Vanzella, E., et al. 2011, The Astrophysical Journal, 743, 132

Pettini, M., Ellogg, M. E. K., Teidel, C. H. C. S., & Delberger, K. U. R. T. L. A. 1998, Apj, 508, 539

Pirzkal, N., Malhotra, S., Rhoads, J. E., & Xu, C. 2007, The Astrophysical Journal, 667, 49

Planck Collaboration. 2016, A&A, 594, 13

Press, W. H., & Schechter, P. 1974, The Astrophysical Journal, 187, 425

Quenouille, M. H. 1956, Biometrika, 43, 353

Rafelski, M., Teplitz, H. I., Gardner, J. P., et al. 2015, Astronomical Journal, 150, arXiv:1505.01160

Rauch, M., Haehnelt, M., Bunker, A., et al. 2008, The Astrophysical Journal, 681, 856

Reddy, N., Dickinson, M., Elbaz, D., et al. 2012a, The Astrophysical Journal, 744, 154

Reddy, N. a., Erb, D. K., Pettini, M., Steidel, C. C., & Shapley, A. E. 2010, The Astrophysical Journal, 712, 1070

Reddy, N. a., Pettini, M., Steidel, C. C., et al. 2012b, The Astrophysical Journal, 754, 25

Reddy, N. A., Steidel, C. C., Fadda, D., et al. 2006, ApJ, 644, 792

Reddy, N. A., Steidel, C. C., Pettini, M., et al. 2008, The Astrophysical Journal Supplement Series, 175, 48

Reddy, N. A., Kriek, M., Shapley, A. E., et al. 2015, Astrophysical Journal, 806, 259

Reddy, N. A., Oesch, P. A., Bouwens, R. J., et al. 2018, The Astrophysical Journal, 853, 56

Rémy-Ruyer, A., Madden, S. C., Galliano, F., et al. 2014, A&A, 563, A31

Rezaei Kh., S., Javadi, A., Khosroshahi, H., & Van Loon, J. T. 2014, Monthly Notices of the Royal Astronomical Society, 445, 2214

Rhoads, J. E., Malhotra, S., Dey, A., et al. 2000, The Astrophysical Journal, 545, L85

Rhoads, J. E., Malhotra, S., Richardson, M. L. a., et al. 2014, The Astrophysical Journal, 780, 20

Ricci, F., Marchesi, S., Shankar, F., La Franca, F., & Civano, F. 2017, Monthly Notices of the Royal Astronomical Society, 465, 1915

Robertson, B. E., Ellis, R. S., Furlanetto, S. R., & Dunlop, J. S. 2015, Astrophysical Journal Letters, 802, L19

Rodighiero, G., Daddi, E., Baronchelli, I., et al. 2011, The Astrophysical Journal, 739, L40

Rodríguez-Puebla, A., Primack, J. R., Avila-Reese, V., & Faber, S. M. 2017, Monthly Notices of the Royal Astronomical Society, 470, 651

Rosdahl, J., & Blaizot, J. 2012, Monthly Notices of the Royal Astronomical Society, 423, 344

Rykoff, E. S., Rozo, E., & Keisler, R. 2015, arXiv.org, astro-ph.I, 1509.00870

Sales, L. V., Vogelsberger, M., Genel, S., et al. 2014, Monthly Notices of the Royal Astronomical Society: Letters, 447, L6

Salpeter, E. E. 1955, Astrophysical Journal, 121, 161

Sandberg, A., Guaita, L., Östlin, G., Hayes, M., & Kiaeerad, F. 2015, A&A, 580, A91

Santini, P., Fontana, A., Grazian, A., et al. 2009, A&A, 504, 751

Santini, P., Fontana, A., Castellano, M., et al. 2017, The Astrophysical Journal, 847, 76

Scarlata, C., Colbert, J., Teplitz, H. I., et al. 2009, The Astrophysical Journal, 704, L98

Schenker, M. A., Ellis, R. S., Konidaris, N. P., & Stark, D. P. 2014, The Astrophysical Journal, 795, 20

Schinnerer, E., Carilli, C. L., Bondi, M., et al. 2007, The Astrophysical Journal Supplement Series, 172, 46

Schlegel, D. J. D., Finkbeiner, D. P. D., & Davis, M. 1998, The Astrophysical Journal, 500, 525

Schmidt, M. 1959, The Astrophysical Journal, 129, 243

Scoville, N., Abraham, R. G., Aussel, H., et al. 2007, ApJs, 172, 38

Shao, J. 1986, Annals of Statistics, 14, 1322

Shapley, A. E., Steidel, C. C., Adelberger, K. L., et al. 2001, The Astrophysical Journal, 562, 95

Shapley, A. E., Steidel, C. C., Pettini, M., & Adelberger, K. L. 2003, The Astrophysical Journal, 588, 65

Shibuya, T., Ouchi, M., Nakajima, K., et al. 2014a, The Astrophysical Journal, 785, 64
—. 2014b, The Astrophysical Journal, 788, 74
Shibuya, T., Ouchi, M., Konno, A., et al. 2018a, Publications of the Astronomical Society of Japan, 70, 1
Shibuya, T., Ouchi, M., Harikane, Y., et al. 2018b, Publications of the Astronomical Society of Japan, 70, 1
Shimakawa, R., Kodama, T., Shibuya, T., et al. 2017, MNRAS, 468, 1123
Shimasaku, K., Kashikawa, N., Doi, M., et al. 2006, Publications of the Astronomical Society of Japan, 58, 313
Shimizu, I., Yoshida, N., & Okamoto, T. 2011, Monthly Notices of the Royal Astronomical Society, 418, 2273
Shioya, Y., Taniguchi, Y., Sasaki, S. S., et al. 2009, The Astrophysical Journal, 696, 546
Shirakata, H., Okamoto, T., Kawaguchi, T., et al. 2018, Monthly Notices of the Royal Astronomical Society, doi:10.1093/mnras/sty2958
Shivaei, I., Reddy, N., Shapley, A., et al. 2017, The Astrophysical Journal, 837, 157
Simon, P. 2007, Astronomy & Astrophysics, 473, 711
Simpson, C., Martínez-Sansigre, A., Rawlings, S., et al. 2006, Monthly Notices of the Royal Astronomical Society, 372, 741
Skelton, R. E., Whitaker, K. E., Momcheva, I. G., et al. 2014, The Astrophysical Journal Supplement Series, 214, 24
Sklias, P., Zamojski, M., Schaerer, D., et al. 2014, A&A, 561, A149
Sobral, D., Best, P. N., Geach, J. E., et al. 2010, Monthly Notices of the Royal Astronomical Society, 404, 1551
Sobral, D., Best, P. N., Smail, I., et al. 2014, Monthly Notices of the Royal Astronomical Society, 437, 3516
Sobral, D., & Matthee, J. 2018, ArXiv:, 1803.08923, arXiv:1803.08923
Sobral, D., Matthee, J., Best, P., et al. 2017, Monthly Notices of the Royal Astronomical Society, 466, 1242
Somerville, R. S., & Davé, R. 2015, Annual Review of Astronomy and Astrophysics, 53, 51
Song, M., Finkelstein, S. L., Gebhardt, K., et al. 2014, The Astrophysical Journal, 791, 3
Speagle, J. S., Steinhardt, C. L., Capak, P. L., & Silverman, J. D. 2014, The Astrophysical Journal Supplement Series, 214, 15
Stark, D. P., Ellis, R. S., Chiu, K., Ouchi, M., & Bunker, A. 2010, Monthly Notices of the Royal Astronomical Society, 408, 1628
Stark, D. P., Ellis, R. S., & Ouchi, M. 2011, Astrophysical Journal Letters, 728, arXiv:1009.5471
Steidel, C. C., Bogosavljević, M., Shapley, A. E., et al. 2011, The Astrophysical Journal, 736, 160
Stern, D., Assef, R. J., Benford, D. J., et al. 2012, The Astrophysical Journal, 753, 30
Tadaki, K.-i., Kodama, T., Tanaka, I., et al. 2013, The Astrophysical Journal, 778, 114
Tadaki, K. I., Kohno, K., Kodama, T., et al. 2015, Astrophysical Journal Letters, 811, L3

Tadaki, K.-i., Genzel, R., Kodama, T., et al. 2017, The Astrophysical Journal, 834, 135
Takeuchi, T. T., Yuan, F.-T., Ikeyama, A., Murata, K. L., & Inoue, A. K. 2012, The Astrophysical Journal, 755, 144
Tal, T., van Dokkum, P. G., Franx, M., et al. 2013, The Astrophysical Journal, 769, 31
Taniguchi, Y., & Shioya, Y. 2000, Astrophysical Journal Letters v.489, 532, L13
Taniguchi, Y., Ajiki, M., Nagao, T., et al. 2005, Publications of the Astronomical Society of Japan, 57, 165
Taniguchi, Y., Scoville, N., Murayama, T., et al. 2007, The Astrophysical Journal Supplement Series, 172, 9
Taniguchi, Y., Kajisawa, M., Kobayashi, M. A. R., et al. 2015, The Astrophysical Journal, 809, L7
Taruya, A., Nishimichi, T., Saito, S., & Hiramatsu, T. 2009, Physical Review D - Particles, Fields, Gravitation and Cosmology, 80, 1
Taylor, E. N., Franx, M., van Dokkum, P. G., et al. 2009, The Astrophysical Journal Supplement Series, 183, 295
Tilvi, V., Papovich, C., Finkelstein, S. L., et al. 2014, Astrophysical Journal, 794, 1
Tinker, J. L., Robertson, B. E., Kravtsov, A. V., et al. 2010, The Astrophysical Journal, 724, 878
Tomczak, A., Quadri, R., & Tran, K. 2014, ApJ, 783, 85
Tomczak, A. R., Quadri, R. F., Tran, K.-V. H., et al. 2016, The Astrophysical Journal, 817, 118
Totani, T., Kawai, N., Kosugi, G., et al. 2006, Proceedings of the International Astronomical Union, 2, 265
Totsuji, H., & Kihara, T. 1969, Publications of the Astronomical Society of Japan, 21, 221
Trentham, N., & Tully, R. B. 2009, Monthly Notices of the Royal Astronomical Society, 398, 722
Tukey, J. W. 1958, Ann. Math. stat, 29, 614
Ueda, Y., Watson, M. G., Stewart, I. M., et al. 2008, The Astrophysical Journal Supplement Series, 179, 124
Valiante, R., Schneider, R., Bianchi, S., & Andersen, A. C. 2009, Monthly Notices of the Royal Astronomical Society, 397, 1661
van der Marel, R. P., Alves, D. R., Hardy, E., Suntzeff, N. B., & Al, V. A. N. D. E. R. M. E. T. 2002, ApJ, 124, 2639
van der Marel, R. P., & Kallivayalil, N. 2014, The Astrophysical Journal, 781, 121
Vanzella, E., Giavalisco, M., Dickinson, M., et al. 2009, The Astrophysical Journal, 695, 1163
Vargas, C. J., Bish, H., Acquaviva, V., et al. 2014, The Astrophysical Journal, 783, 26
Verhamme, A., Dubois, Y., Blaizot, J., et al. 2012, A&A, 546, 111
Verhamme, A., Schaerer, D., & Maselli, A. 2006, Astronomy and Astrophysics, 460, 397
Wang, W., Cowie, L. L., Barger, A. J., Keenan, R. C., & Ting, H. 2010, The Astrophysical Journal Supplement, 187, 251

Wang, W., Han, J., Cooper, A. P., et al. 2015, Monthly Notices of the Royal Astronomical Society, 453, 377

Wang, W., Sales, L. V., Henriques, B. M. B., & White, S. D. M. 2014, Monthly Notices of the Royal Astronomical Society, 442, 1363

Wardlow, J. L., Malhotra, S., Zheng, Z., et al. 2014, The Astrophysical Journal, 787, 9

Weisz, D. R., Dolphin, A. E., Skillman, E. D., et al. 2013, Monthly Notices of the Royal Astronomical Society, 431, 364

Whitaker, K. E., Franx, M., Leja, J., et al. 2014, ApJ, 795, 104

Wilkinson, M. I., & Evans, N. W. 1999, Monthly Notices of the Royal Astronomical Society, 310, 645

Wisotzki, L., Bacon, R., Blaizot, J., et al. 2016, A&A, 587, 98

Wisotzki, L., Bacon, R., Brinchmann, J., et al. 2018, Nature, 562, 229

Wuyts, S., Labbe, I., Fo, N. M., et al. 2008, ApJ, 682, 985

Xue, R., Lee, K.-S., Dey, A., et al. 2017, The Astrophysical Journal, 837, 172

Xue, Y. Q., Brandt, W. N., Luo, B., et al. 2010, The Astrophysical Journal, 720, 368

Xue, Y. Q., Luo, B., Brandt, W. N., et al. 2011, The Astrophysical Journal Supplement Series, 195, 10

Yagi, M., Suzuki, N., Yamanoi, H., et al. 2013, PASJ, 65, 22

Yajima, H., Li, Y., & Zhu, Q. 2013, The Astrophysical Journal, 773, 151

Yajima, H., Li, Y., Zhu, Q., et al. 2012, Astrophysical Journal, 754, 118

Yajima, H., & Nagamine, K. 2014, MN, 439, 3073

Yamada, T., Nakamura, Y., Matsuda, Y., et al. 2012, ApJ, 79, 143

Zamojski, M. A., Schiminovich, D., Rich, R. M., et al. 2007, The Astrophysical Journal Supplement Series, 172, 468

Zehavi, I., Weinberg, D. H., Zheng, Z., et al. 2004, The Astrophysical Journal, 608, 16

Zheng, Z., Cen, R., Weinberg, D., Trac, H., & Miralda-Escudé, J. 2011, The Astrophysical Journal, 739, 62

Zheng, Z.-Y., Malhotra, S., Wang, J.-X., et al. 2012, The Astrophysical Journal, 746, 28